ABSTRACT

Title of Dissertation: PROPULSION PERFORMANCE OF REPEATED, HIGHLY FOCUSED LASER ABLATION

Eric Sesto Smith, Doctor of Philosophy, 2019

Dissertation directed by: Associate Professor Raymond J. Sedwick
Department of Aerospace Engineering

Space debris is a growing concern for satellites. While most of the debris are small, though still extremely dangerous, nearly all of the mass currently on orbit is contained in relatively few large objects, waiting to be released by collisions with both large and small debris. To prevent an exponential growth in the number of debris, a tug spacecraft could be sent to deorbit all of the large objects. Unfortunately, the fuel required for any single tug to deorbit multiple debris grows exponentially with the number of objects deorbited. Laser ablation, which uses a laser to create a jet of high speed plasma from any solid material, provides an elegant solution – the necessary propellant is drawn from the mass of the debris object, rather than carried to it by the tug. To successfully deorbit large debris will require maximizing use of the debris mass. Other laser ablation propulsion schemes can address propellant efficiency issues by selecting both the ablated materials and their configuration, for example a strip of material the exact width of the laser and one laser pulse thick. By moving the ablation target, they are able to avoid questions about how damage done to the surface by one ablation event will affect the next ablation event. A laser ablation tug

cannot afford to ablate its targets only once. This work used time-of-flight mass spectrometry to investigate how laser ablation propulsion performance changes with repeated ablation of the same location on an aluminum plate. The variation of performance metrics was considered as a function of the number of laser pulses applied to a given location, whether they were applied with a short or long delay between pulses, and whether the laser was slightly mis-aligned. It was found that, for up to 25 laser pulses, repeated ablation of the same location significantly improves the thrust-to-power ratio but makes only a small improvement to mass efficiency. After 25 pulses, a crater formed by repeated ablation deflects the plume towards the laser. The time delay between pulses and a slight mis-alignment of the laser had no significant effect.

PROPULSION PERFORMANCE OF REPEATED, HIGHLY FOCUSED LASER ABLATION

by

Eric Sesto Smith

Dissertation submitted to the Faculty of the Graduate School of the
University of Maryland, College Park, in partial fulfillment
of the requirements for the degree of
Doctor of Philosophy
2019

Advisory Committee:
Professor Raymond J. Sedwick, Chair
Professor David Akin
Professor Christopher Cadou
Professor Mark Lewis
Professor Michael Zachariah

Acknowledgements

I begin by thanking my advisor, Dr. Sedwick. He accepted me as a student, even though I was working full time, and he was understanding of the limitations that entailed, such as not being able to take certain classes or make mid-day meetings. He provided lab space, grant funding for equipment, and room for me to grow and develop my own research. Without his support I could not even have gotten started.

I also thank Drs. Akin, Cadou, Lewis, and Zachariah, who served on my committee, and Dr. Ott who served on my comprehensive exam committee. My passing is only as meaningful as the test they provided.

Many thanks to my lab partner Josh. I've worked with assistants for various tasks over the years, but few would I consider partners in our effort. A reliable partner is a precious thing and I could not have asked for better. It would have been impossible to manage both my work and my research without his help.

Thanks to my fellows at the UMD Space Power and Propulsion lab, who helped me prepare for the various examinations and presentations, and some of whom were companions in many of my most challenging classes. When I struggled, it was helpful to know I was not alone.

I am also grateful for the understanding and flexibility of my managers and coworkers when my academic pursuits interfered with work; when I needed to take classes mid-day, when late nights at lab made me all but useless in the morning, and when I had to go part-time to finish my dissertation.

Thanks to my family. I know they don't understand what I do, but that never stopped them from being supportive. Thanks to my friends. They kept me social through the years when work and research threatened to consume my waking hours. Particular thanks to John, who took the time to review my dissertation. Thanks to my girlfriend/fiancée/wife Danielle. She met me during my busiest period and somehow didn't flee. I look forward to a long and successful partnership. All these believed I would succeed, even, and most importantly, when I was doubtful.

Catherine Miller and the MIT Space Propulsion Laboratory supplied the ionic liquids and associated ion source used in this work. Her assistance with setup and operation was greatly appreciated. Josh's efforts were supported, in part, under the National Science Foundation Graduate Research Fellowship Program [Grant No. DGE 1322106]. The Air Force Office of Scientific Research provided equipment funding [FA9550-11-1-0158]. Scanning electron microscope imaging was performed by the Maryland NanoCenter and its AIMLab.

Table of Contents

List of Tables

List of Figures

List of Abbreviations

EMI-BF_4	1-ethyl-3-methylimidazolium tetrafluoroborate
EMI-Im	1-ethyl-3-methylimidazolium bis(trifluoromethylsulfonyl)imide
EMI-$GaCl_4$	1-ethyl-3-methylimidazolium tetrachlorogallate
FWHM	full width at half maximum
KE	kinetic energy
PMT	photomultiplier
RPA	retarding potential analyzer
SEM	scanning electron microscope
TOF	time-of-flight

Chapter 1: Introduction

1.1 Motivation

Orbital debris has been a growing problem since the beginning of the space age. End-of-life planning is now common, but cannot address the debris already in orbit or the inevitable premature failures. There are many proposals to deal with both large and small debris objects, but no active removal has yet been implemented. Of interest herein is the laser ablation tug [2], which uses a laser ablation propulsion system to remove large debris objects in a controlled fashion before they become small debris through collisions or other deterioration. During disposal, thrust is generated by ablating mass from the debris object, propelling both the debris object and the attached tug to the destination orbit. Since each debris object provides propellant for its own disposal, the tug need only enough to travel between targets, allowing multiple disposals with minimal increase in launch mass. In the most extreme case, such a tug could retain material from its most recent disposal with which to reach the next object, thus needing to launch with only enough propellant to reach the first disposal.

The most critical factor in the feasibility of a laser ablation tug is the ability to use a sufficient portion of the debris mass. A feasibility assessment indicated that, with a specific impulse of about 1000 seconds, the tug could deorbit a typical LEO object using approximately 6% of the object's mass, while a GEO object could be sent to the graveyard for about 0.2% of the object's mass. Satellites and rocket bodies are complex structures and may not offer convenient access to their full mass. It is, therefore, critical to make maximum use of each available surface.

Maximizing target usage efficiency begins with maximizing specific impulse. Prior laser ablation propulsion research has focused on thrust-to-power efficiency, preferring lower fluence, less strongly focused lasers, up to several times the ablation threshold, and short laser pulses, often nanoseconds to microseconds. Increasing fluence should increase specific impulse, reducing the amount of the debris object that must be ablated [3,4]. Shorter pulses should lead to less energy conducted to the surroundings of the ablation site, making more efficient use of the laser power, but also reducing heat damage to the surrounding region of the target. Such damage could be an issue when trying to ablate a neighboring area. Increasing fluence comes with increased potential for nanoparticles [5], which may be harmful to the tug or laser, and will generally reduce propulsive efficiency. It will be necessary to strike a balance between higher ion velocity and the presence of low-velocity, high-mass particles in the plume.

To protect the laser optics from the ablation plume it will be necessary to fire the laser from an angle. Although the initial plume will be normal to the target surface, eventually the laser will drill into the target, causing the plume to veer away from the surface normal and back towards the laser source [6]. A non-debris laser propulsion system could simply make the target thickness match the depth of a single laser pulse. For the tug, it will be critical to maximize the impulse derived from a single ablation site. Repeated ablation was reported to produce a performance improvement for a polyacetal target near the thrust maximizing fluence using a weakly focused laser normal to the target surface [7]. Whether the performance improvement occurs for orbital debris remediation depends on the relative influence

of material properties (metal being more reflective and having faster heat conduction away from the ablation site) and the more rapid crater development that results from using a highly focused laser. Before the crater begins to rotate towards the laser, the walls may provide some performance enhancement by containing sideways expansion near the surface, similar to [8]. Simultaneously, the slanted crater walls may reduce the effective fluence and direct some ablated material towards the center crater rather than normally to the original surface. Whether and for how long the performance improves with repeated pulses will determine how quickly the laser should be moved across the target surface.

It has been reported in the literature that bursts of laser pulses applied to a surface result in increased material removal per pulse [9-13]. If the extra material has the same or higher energy than the non-burst material, bursts should be included in any design. If the extra material's energy is lower, it may be always detrimental or perhaps a viable and valuable mechanism to trade between thrust and specific impulse in-flight.

1.2 Instrument

A custom mass spectrometer was designed to make the majority of the measurements in this work. The design is presented in the next chapter. The most common thrust measurement technique for laser ablation is an impulse pendulum. The pendulum moves as a part of its operation, which would cause the next laser pulse to land in a different location from the previous. Since repeated ablation of the same sites is of primary interest, an impulse pendulum is not suitable. Using a mass spectrometer to observe the plume, on the other hand, allows a rigid target, stationary

during an observation. The same site may be reliably ablated multiple times, alternating single pulses and short bursts. Even if there is variance between one ablation site and the next, the variation with pulse number and between short bursts and single shots will be well captured. Estimating specific impulse requires removing the target from the chamber to determine the mass removal (e.g. weighing the target). Every time the target is touched it may shift position relative to the laser focus, changing the fluence. Both specific impulse and thrust may be derived from the plume composition, eliminating the need to remove and weigh targets.

More measurements would increase the accuracy of thrust estimates; however, the accuracy of the thrust and specific impulse is less critical, at this point, than the precision of the relative performance measurements. It is anticipated that a final ablation tug design will not use exactly the laser from this work, nor ablate only aluminum as this study does. It is reasonable to expect, however, that a similar laser and similar materials will be used. Thus the performance estimates will be roughly appropriate while the relative performance due to bursts and development of the ablation crater (changes with pulse number) should remain fully appropriate.

Measuring the plume composition has additional benefits compared to direct thrust and specific impulse measurements. For example, with a plume composition it is possible to assess the benefit of applying additional plume acceleration, as proposed by [14], or to assess the impact the plume is likely to have where it impinges on the tug or on other satellites in the vicinity.

One of the primary drivers of the spectrometer design used here-in was an ability to distinguish between particles with different masses but identical mass-to-

charge ratio. This can be significant for assessing specific impulse if there are sufficient quantities of multiply-charged clusters. As higher mass ions produce higher sputter and secondary particle yields for a given velocity [15-18], a capability for mass determination is perhaps most important for assessing the risk of plume related damage to objects nearby an ablation propulsion system. The tug will need to operate near, and possibly within, the ablation plume of a target it is moving for very long durations.

A scanning electron microscope (SEM) was used to evaluate the development of the ablation crater with repeated laser pulses. The primary purpose is to determine when the crater begins to rotate back towards the laser. For shallow craters, the 3-D shape of the crater may be reconstructed from angled SEM observations. The 3-D shape permits an estimate of the total material removed, which is used to account for neutral plume components when estimating specific impulse based on the ionized plume composition. The electron microscope was also used to scan a collecting surface for any visible nanoparticles, providing an independent estimate of nanoparticle flux.

A time-resolved retarding potential analyzer (RPA) was also used to measure the plume composition, as a complement to the spectrometer. The spectrometer is best suited for high energy species where the RPA is best suited for lower energies. The overlap in their energy ranges provides a point for comparison.

1.3 Goals

The first goal of this work is to assess the performance of the spectrometer/particle detector design. Its ability to observe heavy cluster ions and

nanoparticles will be evaluated. Finally, its ability to identify particle mass in addition to mass-to-charge ratio will be assessed. Improvements will be suggested for any deficiencies discovered.

The second goal of this work is to consider two ablation thruster design options of particular interest to a laser ablation tug for orbital debris removal. The first design option is repeated ablation of the same site. The second design option is firing the laser in bursts. The mass spectrometer will be used to observe plume behavior over a number of laser pulses per ablation site. Single laser pulses, short bursts of 5 laser pulses, and long bursts of laser pulses will be compared to determine whether the reported increase in mass removal translates to increased propulsive efficiency. Variation of performance metrics will also be evaluated against the number of laser pulses to see whether beneficial effects like plume confinement by the crater wall or surface morphology changes outweigh detrimental effects like the reduced fluence on sloped crater walls or parts of the plume being directed normal to the crater wall rather than the main surface.

The third goal is to assess the sensitivity of performance to precise alignment of the laser focal point. Insofar as higher laser fluence is desirable, whatever laser system is used for a tug will include strong focusing. The spectrometer will be used to assess the ablation plume at two slightly different locations near the laser focal spot, one as close as possible to the focus and the other slightly offset. The significance of the difference will guide how much effort should be put into the laser focusing system vs. other system enhancements.

The fourth goal of this work is to estimate propulsion performance metrics (thrust, specific impulse, and efficiency). The results will be compared against the nearest similar work [1], which used pulses 7x longer at $1/9^{th}$ the intensity with less extreme focusing. The comparison will determine whether shorter, higher intensity pulses produce the anticipated performance improvements. The propulsion metrics will also be used for the comparisons in the second and third goals.

This work uses a higher fluence and shorter pulse laser for benefits described, about 140x to 560x the ablation threshold and just under 1 ns (0.23 J/cm^2 based on [19] scaled for pulse duration according to Eq. (3)). Fig. 1 shows the laser parameters of this work, those common in propulsion literature [3,7,20-29], and the closest examples of energy and mass-to-charge resolved spectra for aluminum ablation in the broader literature [1,30].

Given the high fluence, it is probable that there is some nanoparticle content in the plume. The final goal is to estimate the nanoparticle content. Ideally the mass spectrometer will observe the nanoparticles. A SEM will be used to independently evaluate the size distribution and flux of nanoparticles in the plume.

All results in this work are applicable to other laser ablation thrusters, though such systems are generally designed to avoid repeated ablation of the same site and misalignment of the laser focus.

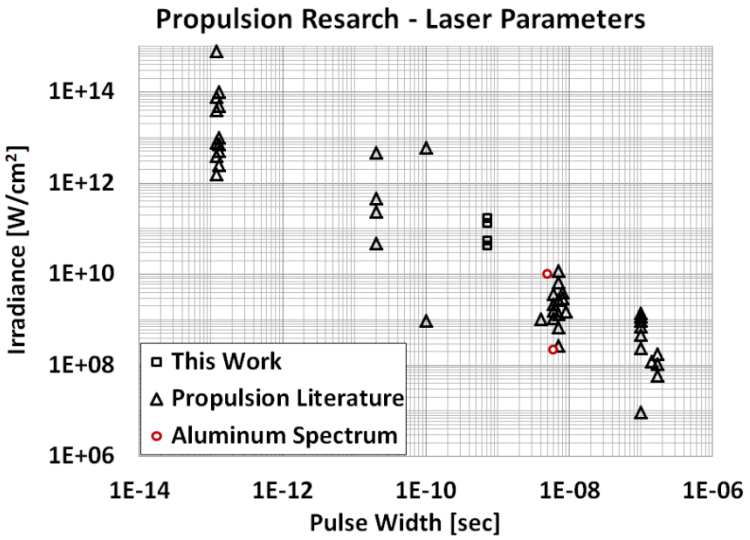

Fig. 1 Laser Parameters of This Work in Context

1.4 Summary of Contributions

1. A low complexity mass spectrometer design for observation and sizing of heavy ions.

   Secondary particle emission is used for signal magnification. It provides a kinetic energy dependent signal, similar to cryodetectors but with less stringent design and operating requirements. Ion kinetic energy per charge at the detector is fixed by voltages applied within the spectrometer, so all particles of the same charge state produce approximately the same signal. The more typical microchannel plate detector has velocity dependence, so for a fixed set of system biases the signal strength falls off for heavier ions. The discrete nature of charge states helps counter the variability in secondary particle emission. Secondary ion emission is available for particles with a low penetration depth, where the secondary electron signal may saturate.

2. Propulsion performance characterization for aluminum at 140x the ablation threshold.

   Laser ablation propulsion research has focused on low laser intensities, just a few multiples above the ablation threshold, near the maximum momentum coupling coefficient. This work verifies that significantly higher laser intensities provide an increase in specific impulse. This provides a path for laser ablation propulsion to be applied to missions that demand high propellant efficiency.

3. Assessment of the variation of propulsion performance with repeated ablation by a highly focused laser.

   This work evaluated repeated ablation when applied for strongly focused lasers, whose crater development and heat dissipation behavior is significantly different from the materials and laser conditions used in prior works studying the performance impact of repeated ablation.

4. Nanoparticle content at a laser intensity of 90 GW/cm^2 and a pulse duration of 0.7 ns.

   These laser conditions, in both intensity and pulse duration, are at the border of a significant increase in nanoparticle generation. These data help to define the range of laser conditions at which significant nanoparticle generation begins.

5. Variation of secondary ion and secondary electron yields with primary ion impact energy for four previously uncharacterized ionic liquid ions at low impact energies.

   These data are necessary for operation of particle detectors like that used in this work. They are also useful for assessing the risk from

plume impingement by ionic liquid based thrusters on nearby satellites.

6. Variation of scintillator response to low energy electrons and aluminum ions. Scintillation type detectors are most commonly applied at high particle energies, often 100 keV or greater. Data on the response of scintillators below 5 keV is rare, particularly the response to heavier ions like aluminum. The data provided from this work allows instrument designers expand the usable energy range of scintillation type detectors.

Chapter 2: Background

2.1 Laser Ablation- phenomena and models

2.1.1 Laser Ablation Timescales and Phenomena

Laser ablation consists of four primary processes, which may or may not overlap depending primarily on the laser pulse duration.

At the start of the process, the laser is absorbed primarily by the electrons in the target. This can include both electrons that are free before the laser pulse and electrons freed as a result of the pulse. Some of the laser energy will be reflected off the surface and some may interact with any material above the surface (for example the plume from the current or previous ablation event). Initially the electrons may have a non-thermal distribution with a relaxation time up to about 1 ps [31-34], which is lower for higher energy electrons. Next, energy is transferred from the electrons to the material lattice with a relaxation time around 1-10 ps [31,35-39]. Then some region of the target area undergoes phase change and is expelled from the surface, generally in some combination of liquid, vapor, and/or plasma. The phase change time scale depends on the specific mechanism, but is generally on the order of several 10s of picoseconds to 10s of nanoseconds [31,40-46]. Finally, the expelled material (the plume) expands out from the surface. Particle velocities can vary widely, from as low as 10s or 100s of m/s for particle clusters and liquid droplets or as high as 10,000s of m/s for some expelled ions [3,4,8,24,25,36,37,47-6063]. All these may be present in the plume from a single ablation event. Typical post-ablation surface topography is discussed in [11,64,65].

2.1.2 Analytic Model

The depth of ablation craters in metals (after a single pulse) has routinely been observed to vary as the logarithm of the incident fluence [9,35,66-69]. This leads to the equation

$$z = z_0 \ln\left(\frac{\Phi}{\Phi_{th}}\right) \tag{1}$$

Where z is the depth of the ablation crater, Φ is the applied fluence, and z_0 and Φ_{th} are the characteristic ablation depth and threshold fluence for ablation, both of which are often determined experimentally. The applied fluence quoted in literature is typically measured before any reflection or attenuation – assuming a transmissivity of unity. Two regimes of ablation are often observed as a function of fluence, gentle and strong, with each having its own values of z_0 and Φ_{th} [10,42,66,67,69,70]. Phase change details are neglected except insofar as they affect z_0 and Φ_{th}.

With repeated pulses the ablation threshold drops and the ablation depth per pulse increases [7,9-13]. This is commonly referred to as incubation or incubation effects. Some are time dependent (e.g. residual heat near the ablation spot) while others are independent of inter-shot delay (e.g. surface roughening). Incubation effects are treated, in this simplified model, by making Φ_{th} dependent on the current pulse number (N) [10]:

$$\Phi_{th,N} = \Phi_{th,0} N^{\xi} \tag{2}$$

Where ξ is called the incubation coefficient and is typically determined experimentally. Incubation effects begin to accumulate even below the single pulse ablation threshold, so that the ablation crater expands as incubation effects lower the

ablation threshold below the wings of the laser profile [10,11]. The above treatment of incubation effects does a good job of matching both the increased depth and width observed experimentally [11]. As the crater gets deeper, wall slope and intra-cavity reflections become significant [9,71], reducing the validity of the above incubation model. In particular, Li [72] experimentally observed a maximum value of N, above which incubation effects appear saturated.

The material specific parameters are most often determined experimentally [66,67], but attempts have also been made to estimate them from more complex models [37,72]. The ability to predict ablation depth as a function of fluence is very often used as the measure of the accuracy of an ablation model.

First estimates of z_0 and Φ_{th} can be made from a combination of laser and material properties. From [35,66] for nanosecond pulses:

$$\Phi_{th} = \rho\Omega\sqrt{\frac{k_0\tau_L}{C_i}} \tag{3}$$

The characteristic depth comes from the heat penetration depth:

$$z_0 \approx \sqrt{\frac{k_0 t}{\rho C_i}} \tag{4}$$

From [35,66] for femtosecond pulses:

$$\Phi_{th} = \frac{\rho\Omega}{\alpha} \tag{5}$$

The characteristic depth comes from the skin depth:

$$z_0 = \alpha^{-1} = \frac{\delta}{2} \tag{6}$$

In the above equations, ρ is the material density, α is the inverse of half the material skin depth (δ), Ω is the specific heat of vaporization, k_0 and C_i are the thermal

conductivity and specific heat of the bulk material, τ_L is the laser pulse width, and t is the time from the start of the laser pulse through the end of the ablation event. In both cases, the specific heat of ablation is taken to be the normal specific heat of vaporization.

2.1.3 Two-Temperature Model

The two temperature model is the baseline continuum model for ultrafast laser ablation. The lower mass free/valence/conduction-band electrons are treated as a separate but coupled system with the higher mass ions or material lattice. The electrons are assumed to absorb the incoming laser energy, then deposit that energy into the lattice based on an electron-phonon coupling coefficient, the latter generally occurring (for femtosecond ablation) over a much longer time scale than the laser pulse. Additional factors are often considered to improve accuracy and the most significant will be mentioned later. The most basic form of the two temperature model uses the following two equations [73]:

$$\begin{aligned} C_e \frac{\partial T_e}{\partial t} &= \frac{\partial}{\partial x}\left(k_e \frac{\partial T_e}{\partial x} \right) - G\left(T_e - T_i\right) + S \\ C_i \frac{\partial T_i}{\partial t} &= \frac{\partial}{\partial x}\left(k_i \frac{\partial T_i}{\partial x} \right) + G\left(T_e - T_i\right) \end{aligned} \tag{7}$$

Where S is laser input power, G is the electron-phonon coupling coefficient, k_u is the subsystem thermal conductivity, T_u is the subsystem temperature, C_u is the subsystem specific heat, and the indices e and i refer to the electron and ion subsystems respectively. The laser input power is typically assumed to decay exponentially with depth into the target following the Beer-Lambert law. Any reflection or plume-based attenuation of the beam is accounted by reducing the laser intensity at the surface.

Longer (nanosecond) pulses and the later stages of ultrafast ablation (after electron-lattice equilibrium) can be modeled with a comparable single temperature model. In this situation more care must be given to modeling laser attenuation and other effects of having simultaneous laser heating, phase change, and plume development. The two temperature model is also extendable into, at least, the low picosecond region - as attempted by Cheng [73] (10 ps) with moderate success and Yang [70] (7.6 ps) with notable success. In this region the laser pulse is too long to allow separation of the laser input and phase change mechanisms, but too fast to consider the electron and lattice in thermal equilibrium.

2.1.4 Two Temperature Model Improvements

The single most common improvement is to account for temperature dependence of the electron-phonon coupling coefficient [41,74]. It is also beneficial to include the effect of electron-electron (as well as electron-phonon) collisions on the electron relaxation rate [41]. Yang [70] showed that these two effects and phase explosion could account for both the gentle and strong ablation regions observed using the log model. During the literature review, no other paper clearly demonstrated this result.

Several works [40,74,75] add momentum equations to the thermal equations Eq. (7) in an attempt to improve accuracy of ablated depth. The addition of these equations leads to shock/rarefaction waves and the possibility of mechanically induced material failure rather than melting and vaporization. There is no obvious improvement in the ablation depth calculation.

Although the two temperature model is most often used for metals, it is capable, with sufficient adjustments, to model short pulse ablation of semi-conductors and dielectrics. Wu [76] adapts it for semi-conductors and dielectrics, primarily by including multi-photon and avalanche ionization. These two phenomena result in a higher than typical number of free electrons in the material, causing it to behave like a metal and absorb most of the laser energy very near the surface rather than deeper in the material.

Huang [43] suggests, based on past experiments with exploding metal wires, that the propagation of the liquid/vapor front (i.e. the ablation rate) is limited by the speed of sound in the material. Mazhukin [74] also limits the phase change front propagation rate to the material speed of sound. This results in a higher material temperature at the liquid/vapor and liquid/solid interface than otherwise predicted. Unfortunately no direct comparison to experimental data was provided. Again, there is no obvious improvement to the ablation depth calculation.

Some efforts [72,77] have been made to evaluate laser ablation in 2 and 3 dimensions, accounting for a non-uniform (typically Gaussian) laser profile and/or lateral thermal conduction. These are uncommon and so far deal only with a single pulse, applied normal to the target surface. Li [72] presents results from a 3-D solution using a predefined material removal temperature. It suggests that, for high fluences, the ablation depth may be proportionally dependent rather than logarithmically dependent on incident fluence. The results are not carried to a high enough fluence to demonstrate this is a truly linear regime rather than the strong logarithmic ablation regime mentioned previously.

The two temperature model has occasionally been used in conjunction with molecular dynamics or single temperature model simulations, generally to save processing time. A two temperature simulation simplifies to single temperature naturally after electron-phonon equilibrium is reached, which is relatively fast compared to other phenomena; thus processing effort can be saved by reducing to the single equation. When combined with molecular dynamics simulation [45,78], the two temperature model is used to determine material interactions with the laser. The molecular dynamics simulation begins after the laser pulse, focusing on phase change phenomena, which are assumed to initiate after the completion of the laser pulse.

Some effort has also been given to extending the model to multiple pulses [7,9-13] by accounting for incubation effects, most typically residual heat.

2.1.5 Molecular Dynamics Simulations

Molecular dynamics simulations are typically performed to try to understand what physical processes are behind laser ablation, particularly the nature of phase change/material expulsion [38,46,50,79]. No particular phase change mechanism needs to be assumed, but that which occurs may be deduced by following the thermodynamic trajectories of groups of modeled particles. Based on MD simulations, [44] concluded that multiple phase change mechanisms can occur within a single ablation event, based upon the total energy deposited in a given region of the target material.

2.1.6 Phase Change

While the two-temperature model is widely accepted, the mechanisms of phase changes are still under discussion. While traditional vaporization does occur, it

is generally not dominant for ultra-short pulses [44]. MD simulations, post-ablation surface topology, and plume analysis all show that it is common to have at least some solid/liquid droplets expelled from the ablated surface [38,46,50,54,60,79-81]. For sufficiently long or high-energy pulses it is common to have a significant region of melted material [35,62,66] which, if expelled, can significantly reduce the average specific impulse. The amount of reduction (i.e. fraction of low velocity melt vs. high velocity gas) depends on the specifics of the phase change process. For shorter pulses there are two common explanations for bulk material removal (including droplets): phase explosion (aka. explosive boiling or homogeneous nucleation) and mechanical cavitation (aka. negative pressure, spallation, or mechanical failure). Although generally not considered, Coulomb explosion may also occur.

For longer pulses (nanosecond), traditional vaporization is typically assumed. Generally a combination of the Clausius-Clapeyron relation [43,47,82] and the Hertz-Knudsen equation [43,82] is used to determine the vapor pressure and initial vapor expansion velocity at the liquid-vapor interface, based on the local temperature. Another relation is needed to define and track the location of the liquid/solid and liquid/vapor interfaces, which can be made difficult by the potential for superheated states.

Coulomb explosion occurs when the high electric fields force a significant number of electrons out of the surface, leaving a large surface charge. The charge separation pulls the material apart, accelerating the ejected ions to high velocity. This is not frequently used in ablation models, but significant ejection of electrons out of the surface can occur for sufficiently short laser pulses [83].

Phase explosion occurs when a material is heated well above the normal phase change temperature. The material enters a meta-stable region wherein any notable fluctuation in density will cause rapid homogenous nucleation. This bubble growth draws heat from the surrounding liquid, leading to a mixed phase plume. As the material temperature approaches a critical level, the likelihood of sufficient density fluctuation goes up. The critical temperature values are a material property. Arguments for phase explosion typically involve small droplets frozen (after the ablation event) in the act of leaving the surface and models showing material temperatures well into the meta-stable regime [41,42,64,77]. Typically the numerical algorithm takes advantage of the difference in time scale between electron-lattice relaxation and meta-stable phase relaxation – the temperature distribution is determined before any material has been removed.

Critical point phase separation is a specific implementation of phase change modeling that has shown high potential for predicting ablation depths, particularly for high fluences [73]. A critical temperature is defined (before the simulation) such that any region of material surpassing that temperature is considered ablated and any region not reaching that point is considered left behind. As with phase explosion, critical point phase separation considers energy deposition and material removal to be on sufficiently different time scales that they can be considered as sequential rather than concurrent events.

Mechanical cavitation results from a rarefaction wave propagating into the target, generally in the wake of a much stronger shock wave [40,74,75,84]. The rarefaction wave produces high negative pressures, pulling the material apart and/or

causing formation of bubbles which then expand and expel the broken material. This seems comparable (at least to me) to phase explosion. Phase explosion and CPPS model thermal behavior but may not include a momentum (pressure) model (which is potentially reasonable for a solid).

Polymers also show photochemical decomposition, where the incoming photons directly break chemical bonds leading to material expulsion. This is confirmed by studies of plume constituents, which can demonstrate the particular bonds that are broken [20,85].

It has been observed that two pulses applied in rapid succession, rather than separated by microseconds, seem to interfere such that the total ablated mass is less for the two pulses than for the first pulse alone. Povarnitsyn [40,86] explains this as an interaction of successive shock/rarefaction waves – the second pulse's shock wave reduces the intensity of the first pulse's rarefaction wave, reducing the maximum negative pressure and causing less material to be expelled. This phenomenon seems the best argument for the shock/rarefaction wave phase change mechanism; however it may also be compatible with the phase explosion removal mechanism and the evaluation performed in [86] was not entirely convincing. The phenomenon has not thus far been addressed in terms of phase explosion.

2.2 Laser Ablation – Phenomena specific to a Laser Ablation Tug

This section presents several results from materials science research which are likely relevant to laser ablation propulsion, particularly where high target usage is required. Incubation effects tend to reduce the threshold fluence for ablation. Laser reflection and attenuation reduces the amount of laser energy deposited in the target

material, reducing the ablated mass and, in the case of plume-based attenuation, adding additional heat to the plume. Ablating deep into a surface leads to a steep-walled crater, with a wide variety of competing effects including reduced fluence, laser reflections within the crater, and lateral confinement of the early plume.

2.2.1 Incubation Effects

Hu [12] investigated the results of incubation effects by comparing the ablated depth after a five pulse burst vs. after a single pulse (of equivalent total fluence) and finds a significant increase in ablated depth for the burst case. A two temperature model with CPPS was used successfully to model the ablated depth. Vorobyev [87] measured residual heat left in the target after one or more laser pulses, reporting 12-70% of the input laser energy still in the target after the target reached internal thermal equilibrium. Both of these, and other burst ablation mode studies, suggest residual heat in the target surface is a probable source of incubation effects.

Several papers investigate the surface topography left behind after laser ablation [11,64,65]. Obona [64] shows that low accumulated fluences show bubbling, higher but still low fluences show frequent (spaced about a wavelength apart), low height ripples oriented perpendicular to the laser's polarization. As the fluence increases, the surface becomes dominated by lower frequency but higher ripples, again oriented perpendicular to the laser's polarization, with the low-fluence (high frequency) ripples occurring between and perpendicular to the larger ripples [64]. These surface nanostructures are another possible explanation for observed incubation effects. They have also been used as evidence of phase explosion.

Ahmad [88] looked at ablation of a surface impregnated with nanoparticles, as a stand-in for the surface roughness common after laser pulses. Models typically use an adjusted surface reflectivity to account for the results (on laser absorption) of such surface details [77].

Cristoforetti [89] investigated the specific case of dual pulses in a background gas. The first pulse creates a low density region just above the target location either by significantly heating the near-surface background gas or as a result of the high temperature plume from the initial pulse. With the reduced background gas density, the ablation is more comparable to ablation in vacuum than ablation with a significant background gas (i.e. more material is removed). Some propulsion researchers have also investigated a two-pulse scheme (this time in vacuum) where the first pulse sets up for the second pulse, resulting in higher overall performance. This is discussed under "Propulsion characterization."

2.2.2 Deep drilling

As the crater depth increases, the previously discussed models lose applicability. There have been a few experimental studies of the behavior of deep craters, noting several new phenomena: angled drilling, near vertical crater walls, additional (somewhat random) widening of parts of the hole, and a potential maximum depth (based on applied fluence) [9,71].

Leitz [9] observed a raised rim around the crater after the initial pulses, which disappeared with additional pulses, while others [35,71] do not show this feature. Chichkov [35] does observe deposits forming around the crater rim (but apparently

low height), and the images from Doring [71] are not appropriate to show low height deposits.

A few plausible physical explanations are given for the unique behaviors associated with deep drilling including plasma interactions with the crater wall, complex intra-crater laser reflection, absorption of laser energy by plasma still within the crater, and accumulation of energy from the wings of the laser profile [9,71].

Numerical studies have been done to investigate the effects of intra-cavity reflection within deep craters. Bailey [6] looked at CW irradiation of metallic surfaces at a 45° incidence angle using ray tracing. Good agreement was found with experimental results in both crater shape and burn through time. Modeling without reflections was found to overestimate the burn through time by up to 30%. Modest [90] used ray tracing to determine the distribution of irradiance on the surface. In that case, a nanosecond laser was oriented normal to the surface and the slight non-specularity of the reflector (crater walls) was handled explicitly by using a Gaussian magnitude reflection cone rather than a simple ray. Although no direct comparison is offered, the resulting crater shows many of the characteristics of real craters from other works [9,71]. One critical exception is that the experimental craters tended to veer randomly near the bottom, while the numerically derived craters drill normal the surface (or at least symmetrically). Both used a significantly simpler ablation model than those investigating single pulses (i.e. a single temperature model with conduction only perpendicular to the target surface) and neither modeled either laser-plume or plume-wall interactions.

2.2.3 Laser reflection and attenuation

A fair amount of work has been done, both experimentally and theoretically, on the interactions of the laser with the plume [42,48,49,91]. Plume interactions are of importance for high picosecond and longer pulses; shorter pulses end before plasma has a chance to form. Schall [48] attempted to determine the earliest onset of laser absorption by the plume, and to follow the propagation of the absorption front from the surface. A particularly interesting result: attenuation of the laser pulse seemed to occur farther from the surface than the ejected material appeared to have reached (based on front imaging). Ihlemann [49] directly measured the amount of laser energy reflected and absorbed by the ablation plasma, and the resulting effect on ablation depth for high intensity femtosecond, picosecond, and nanosecond pulses. The ablation rate is minimum at 5 ps, which is explained by formation of a highly reflective plasma spanning the peak of the pulse. At 5 ps, about 15% of laser energy was reflected, the highest of any pulse width in the experiment. The amount of pulse energy lost to the ablation plume varied from none to as much as 75%.

Bulgakova [91] finds that up to 35% of the energy absorbed by the plume is re-emitted into the target, leading to deeper than expected target melting. The percent of total energy re-irradiated goes up approximately linearly with total fluence until about 25% at 15 J/cm^2.

According to Eremin [92] and Plaksin[93], very fast laser pulses may saturate the ability of the material to absorb laser energy, which could increase the effective skin depth.

2.2.4 Plume expansion

Quite a bit of research has been done on pressure dependence of plume effects [22,94-96]. Such effects are not critical for an on-orbit system since it will always operate in vacuum. The most notable result, demonstrated by Anju [22] & Watanabe [94], is the possibility of additional impulse due to confinement of the plasma by the background gas. The plume spends longer near, and exerts a higher pressure on, the surface[94]. Similar plasma plume confinement can be achievable under vacuum conditions, if desired, by application of a transverse magnetic field [26].

Studies of the angular distribution of ablation products show that the particle flux in a given direction follows an exponential cosine [24,97].

$$F = F_0 \cos^n(\theta) \tag{8}$$

Where F_0 is the centerline flux and the angle theta is measured from the normal to the surface. A larger value of n corresponds to a more tightly focused plume. Ali [97] suggests that n correlates with specific material properties.

Zeng [55] observes that, while a nanosecond ablation plume expands approximately spherically, with the same velocity in the normal and lateral directions, femtosecond plumes expand in an approximately 1-D fashion, normal to the surface. For the nanosecond case, the perpendicular expansion distance grows as $t^{2/5}$ while for femtosecond it grows at $t^{2/3}$.

Mahmood [52] considers two models, “snow plow” and “shock wave,” for the rate of plume expansion. The snow plow model, which assumes free expansion into vacuum with a constant velocity, is more successful than the shockwave model, but to match the actual expansion rate it still suggests an ablated mass double that observed.

2.2.5 Plume Composition

Several researchers have investigating details of plume composition. Hermann [98], investigating ablation of brass via spectroscopy, found that the plume is stoichiometrically identical to the original sample. Urech [20] looked at the chemical composition of a plume of ablated polymer, finding mostly ionized partial polymer molecules and some elementals as well. This suggests that all of the material components in the ablated region are represented in the plume, though they may not remain in the same chemical form as the original sample. Zhang [30] and Srivastava [1] both developed energy and mass-per-charge spectra for ablation of aluminum under 5-6 ns pulses from a 1064 nm wavelength laser. Zhang reported a spectrum for $2x10^{8}$ W/cm^2, finding only Al^{+1} and Al^{+2} (up to 70% Al^{+1}) with energies up to just over 200 eV. Srivastava reported Al^{+1} to Al^{+4}, including observations from -10° through +45° off the plume axis, using a laser intensity of roughly $1x10^{10}$ W/cm^2. As Srivastava is closest to the current work, it will be used to consider whether decreased laser pulse duration and increased irradiance provide the anticipated benefits.

Femtosecond plumes are known to contain nanoparticles. Some effort has also gone into increasing or reducing their nanoparticle content. Colombier [99] noted that applying slightly longer laser pulses (~15 ps instead of ~150 fs) creates more fast ions and fewer nanoparticles/droplets in the plume. Double pulse ablation, with specific pulse separation, has also been shown to reduce nanoparticle content [45]. Nanosecond plumes have, more recently, been shown to also contain nanoparticles with increasing content under higher irradiance [5,100,101]. In each case,

nanoparticles were accounted by measuring accumulation on a surface – their charge state and velocity have not been addressed.

2.3 Laser Ablation Propulsion

2.3.1 Laser Pulse-width Regimes for Propulsion

Most laser ablation research for on-orbit propulsion uses lasers in the short pulse (low nanosecond or high picosecond) regime [3,4,7,8,22, 24,25,27,29,47, 58,59,62,63,68,82,94,96,102-110]. However, some use lasers in the ultra-short pulse (low picosecond to femtosecond) or middle (high picoseconds) regime [23,29,68,111] and others use long pulses (microsecond or millisecond) [20,112-116].

Ablation in the ultra-short regime has many qualities that may make it more desirable for propulsion use than short pulse ablation [9,35,68]. The reduced duration of energy deposition and earlier phase change reduce conductive heat loss from the ablated region and reduce energy deposited in the expanding plasma (energy which is lost to material ablation). Heat left behind in the non-ablated region and energy re-emitted by the plasma can produce a layer of melt which, if expelled at low velocity by the back pressure of the expanding plume, effectively wastes propellant. The reduced energy input to the plasma may mean a lower expansion velocity, but also may reduce energy loss to ionization (by not forming plasma) and increase the energy fraction reaching the surface. Of course, a second pulse could be used to add energy to the expanding plume if that were desired. Each of these effects also lowers the threshold fluence, relative to nanosecond ablation.

Current short pulse (nanosecond) lasers are less expensive and more powerful (both in pulse energy and average power) than current ultra-short pulse (femtosecond)

lasers. The lower peak power also reduces the damage threshold requirement on support components such as fiber-optic wires and focusing optics. The best operating regime will vary depending on the propellant, thruster design, and performance requirements.

2.3.2 Propulsion Characterization - Experiment

Most laser ablation propulsion research measures specific impulse (I_{sp}), propulsive efficiency, and/or momentum coupling (C_m). The primary variables are total laser fluence per pulse, laser pulse width, and the pulse repeat pattern. Phipps [117] provides an overview of much of the propulsion related ablation research as of 2010.

The most common propulsion study uses an impulse pendulum (or occasionally a force sensor) to evaluate the applied impulse to the target from laser pulses (1 pulse or short pulse train) and weighs the target before and after some number of repeated ablation events. The total applied impulse and mass loss together are converted into I_{sp}, C_m, and/or efficiency [3]. Occasionally ([24,62,109]), the actual plume flow velocity and/or lateral expansion rate are measured by flow visualization or ion time-of-flight. Specific impulse measurements that don't involve weighing the target (flow visualization and ion time-of-flight) are not ideal because ablation typically involves three separate plume components – fast ions; the bulk plume including slow ions; and high mass, low velocity particles or droplets, some of which these measurements can miss.

The threshold fluence [35,66] and maximum C_m (vs. fluence) [118] are roughly proportional to square root of laser pulse width for short pulses (nanosecond

and longer) and constant [23,67] for ultra-short pulses (picoseconds and shorter). Compiling results from several sources, Phipps [118] found that the ideal laser fluence (to maximize C_m) could be approximated for many materials (given generous bounds) from the pulse width alone. Adding a dataset [23] in the low femtosecond regime suggested that the proportional relationship breaks down below a few nanoseconds, at which point the ideal fluence remains approximately constant. The logarithmic ablation law, combined with idealized plume dynamics, suggests that the fluence to maximize C_m is proportional to the threshold fluence, as demonstrated by Sinko [4].

Much research is aimed at thrusters wherein the fuel material is freely chosen [3]. Polymers are the most studied material because of their light weight, relatively low reflectivity, and low ablation threshold. Impurities are often added to alter the properties of polymer fuels in desirable ways [20,85]. Reactive fuels are another key area of research [117]. Reactive fuels combine some of the benefits of chemical fuels in that, upon irradiation, they undergo an exothermal reaction, releasing energy beyond that supplied by the laser pulse. Such thrusters are often listed as having efficiency greater than 100% (taken relative to input laser power) [117].

Several researchers [7,28,29,68,110] have found that multiple pulses on the same spot produce a higher C_m, I_{sp}, and/or propulsive efficiency than a single pulse. In particular, Suzuki [7] found that the first 10 pulses (50 Hz repetition rate) showed a growing C_m with increasing pulse number, but that the growth trailed off for higher pulse numbers. There was still observable growth, but not to the same extent as for the first 10. A maximum of 110 pulses was used for that work, but with a wide beam

and moderate fluence, the crater was still shallow. They suggest nozzle effect as the cause; however, given the shallow crater, other effects, such as additional material removal, residual heat, or reduced nanoparticle content in the plume, may have played a significant part. An alternative sort of multi-pulse investigation was carried out by Mori (in atmosphere) [28]. Similar to the work of Cristoforetti [89,119] in the materials field, two pulses were applied per ablation event – the first to prepare the surface for the second. Two types of pre-pulses are considered. In the first case the surface is pre-heated by a lower power beam, which resulted in an improved C_m (over the pair used separately) but only for pre-heated surface temperatures up to about double the starting temperature. In the second case the initial pulse is used to produce a dense vapor cloud (via ablation) above the surface. The second shot creates a laser supported detonation wave in the vapor, providing several times the impulse of the two shots separately. The degree of improvement varies with material and fades at higher fluences (>10 J/cm^2).

2.3.3 Propulsion Characterization - Modeling

It is quite common for propulsion researchers to use the simplified log model of laser ablation, particularly alongside experimental results. Nanoparticles, ions, and incubation effects are not included. Sinko [3,4] uses the log ablation depth and assumes that energy is evenly distributed into kinetic energy of the ablated mass. He makes excellent use of this model to derive estimates of the material properties (Φ_{th}, z_0, & transmissivity) in those equations by comparing to measured specific impulse, ablated mass, momentum coupling, and efficiency.

Sakai [82] produced models that successfully recreate the averaged temporal profile of impulse generation under nanosecond ablation. The model used logarithmic laser energy deposition below the material surface with an axially symmetric laser profile and 1-D (only normal to surface) heat conduction. Hertz-Knudsen, Clasius-Clapeyron, and the liquid surface temperature were used to set the vapor velocity, pressure, and temperature respectively. The plume expansion model assumed axial symmetry and chemical equilibrium, making no special allowance for plasma effects or laser-plume interactions. A fixed reflectivity between 0% and 20% is used, with the higher reflectivity showing better agreement with lower fluence pulses. The authors note (as have others) that the chosen reflectivity value makes a significant difference in results.

Sakai [47] used numerical schemes (the same as in [82]) to estimate the final disposition of laser energy – how much goes to propulsion, material heating, reflection, etc. Target reflectivity of 50% is chosen so that the calculated C_m values agree as much as possible with experimental results. Unfortunately, the calculated I_{sp} values do not match experimental results. Specific values of C_m and I_{sp} were not addressed in [82].

2.3.4 Thruster Designs

Several systems have been designed for liquid propellants. Liquid propellants are desirable because they are easily stored and transported to the thruster, lose no input energy to melting, and because there are no surface defects left over from earlier pulses. Confinement is critical – if the entire free surface is not evenly irradiated there will be a variable surface pressure which will cause some propellant

to be expelled as a low velocity liquid, greatly reducing overall specific impulse. Low specific impulse due to splashing has been one of the largest hurdles to liquid propellants [117].

Luke [114] proposed, built, and tested a laser ablation thruster using a "fuel tape" to deliver fuel to the thruster. In this design, the target material (typically PVC, etc.) is coated on one side of an optically thin tape (typically kapton). Two laser/tape arrangements are considered. In the first, called reflection mode, the laser falls directly on the propellant side of the fuel tape, causing the surface of the material to ablate. If the material is sufficiently thin then the full depth is ablated, though the kapton backing remains. In the second arrangement, called transmission mode, the laser passed through the tape side of the fuel tape and irradiates the rear of the propellant. If the layer is sufficiently thin, the vaporized subsurface propellant escapes, driving out any non-vaporized portion as well. The transmission mode has the added benefit of keeping the backing tape between the ablation plume and the laser optics, preventing any potential contamination. This design has high potential for unusable propellant mass (space between individual craters).

Koizumi [113] uses a cylinder with individual pre-defined ablation sites. Each site (or a group of sites) can contain a different propellant, offering a great range of operating characteristics.

Horisawa [14] proposed hybrid laser-EM thrusters. Generally, these are standard electro-magnetic propulsion systems except that they use laser ablation as a plasma source. This can be seen as a means of improving laser ablation, by increasing specific impulse or focusing the plume. Alternately, it can be seen as an

improvement of existing electro-magnetic propulsion schemes. It imparts an initial velocity where the prior scheme began with stationary plasma and, more significantly, allows nearly any solid or liquid as propellant.

Sinko [8] and Thompson [112] have studied the effects of adding nozzles to help focus the ablation plume. Significant improvement in propulsive efficiency can result from adding nozzles. Using a numerical magnetohydrodynamic plasma model known as MACH2, Thompson [112] considered expansion ratios up to 10.5 and observes improvement up to 36% for C_m and 50% for I_{sp} with no significant additional mass removal, following a similar pattern to typical chemical rockets. Sinko [8] experimented with polymer targets under various fluences and using conical nozzles with expansion ratios up to 16. Both C_m and I_{sp} were observed to improve (depending on the case) by more than a factor of 10 while the total ablated mass and the shape of C_m and I_{sp} curves vs. fluence both remained approximately unchanged.

Unfortunately, the crater walls resulting from laser ablation are unlikely to be perfectly smooth. For such small nozzles, surface roughness and the resulting increase in boundary layer thickness can reduce the effectiveness of the nozzle. One source [120] observes that surface roughness perpendicular to the flow direction can reduce the effectiveness of a micronozzle by 12-20%. Fortunately, patterns parallel to the flow direction are observed to have little effect on performance and a micronozzle created for the paper using laser ablation showed variations primarily in the flow direction.

Nozzle effects may result from crater development, particularly for deep drilling. Intra-cavity reflections and heating of the plume while within the crater may also affect impulse generation. Although crater shape development and its effects on ablation rate per pulse have been studied, no study has been done to demonstrate the degree to which deep craters affect applied impulse. Some incubation effect studies have been performed, but using too few pulses for a sufficiently deep crater to form. This subject is particularly relevant if trying to maximize propellant usage.

In a variation of the nozzle theme, Rubin [21] and Zaidi [121] have shown that magnetic fields parallel to plume expansion can act as nozzles, providing focusing and redirection of the plume. Rubin [21] showed that the plume (at least the glowing portion) can be redirected more than 70° off surface normal by a 4T magnetic nozzle. Transverse magnetic fields have also been studied [26,122]. These can operate similarly to a background gas, keeping the ablation plume close to the target surface for longer, thus leading to a greater momentum transfer from plume to target.

2.4 Missions

Many missions have been proposed using laser ablation. The most relevant missions are debris removal and asteroid deflection.

Proposed debris removal missions use a ground- or space-based laser which fires at passing debris [68,106-108,123-128]. The target is small debris (1-10 cm) in LEO orbits. The smaller pieces are entirely vaporized, while larger pieces are propelled into lower orbits by reaction against the ablation plume. There are many issues with this mission type. The most critical issues are 1) targeting debris without

hitting/damaging active objects and 2) an inability to handle the larger objects responsible for the long-term threat. A variation of this mission deflects larger objects to avoid potential collisions involving uncontrolled objects [125].

Park[129] considered an asteroid deflection mission, sending a dedicated satellite to the target body and ablating material off the asteroid to provide deflecting propulsion. This is similar in principle to the laser ablation tug proposal for removal of large orbital debris [2].

There has also been significant research into laser-based launch systems [117,130-132]. Some of these operate by rapidly heating air within a nozzle-like geometry of the launch vehicle (referred to as "lightcraft"). This creates a laser supported detonation wave - the rapid heating generates a shock wave in the ambient gas which is focused by the vehicle geometry and propels the craft. Such systems have little to no ablation and would not operate in vacuum but, as noted elsewhere, some double pulse ablation schemes attempt to recreate this mode of operation by using the initial pulse to seed the near-surface region with a "background" gas – the vapor plume – in which the second pulse can create a laser supported detonation wave [28].

Chapter 3: Experiment

3.1 Overview

3.1.1 Laser Ablation Setup

The laser ablation plasma was produced by a 1064 nm laser with a pulse full width at half maximum (FWHM) of 0.72 ns and repetition rate of 40 kHz. The laser was fired in alternating 1 and 5 pulse bursts or as a continuous stream. The typical pulse energy at the target was 700 μJ. The laser was incident on an aluminum target (alloy 6061) at an angle of 45°, for a peak fluence of 130 J/cm^2 and a peak intensity of 170 GW/cm^2. Fig. 2 shows the relative location of the laser head (A), laser optics enclosure (B), and vacuum chamber (C). The vacuum chamber was maintained around 5x10^{-6} Torr during observations, making the total spectrometer flight length about 1/20th the mean free path. Ablation events and operation of the stages were monitored via a webcam (D) mounted above the mass spectrometer enclosure (E). The arrangement of optical components is shown in Fig. 3.

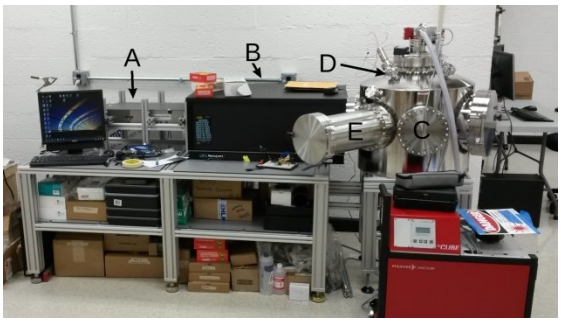

Fig. 2 Laser, Optics, & Chamber layout

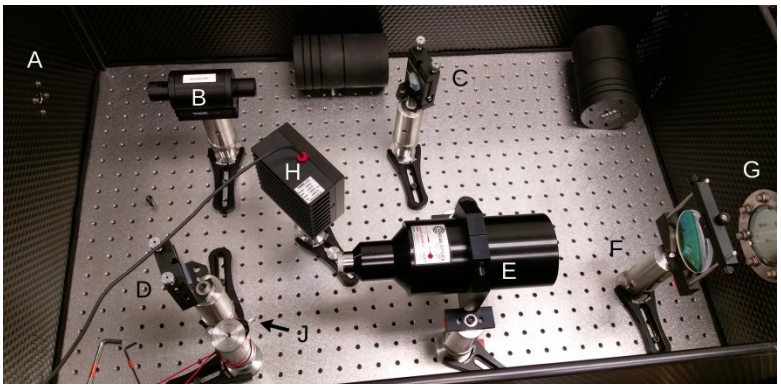

Fig. 3 Laser beam-line layout

The laser beam enters from the left (A). The beam first passes through an optical isolator (B), which protects the laser from back-propagating reflections. Second, the laser is reflected off of two flat mirrors (C and D), which both provide an adjustable length over which to expand the beam and allow proper alignment of the beam to the remaining optical elements and the target in the chamber without moving the laser head. Next the beam passes through a 20x beam expander (E), a lens with 0.5 meter focal length (F), and the window into the vacuum chamber (G). The laser is about 2mm in diameter when it reaches the expander. The lens is placed such that the focal spot of the laser is near the center of the vacuum chamber. The window of the vacuum chamber has two segments. The first supports the vacuum. The second is removable and protects the load-bearing window from contamination by the ablation plume. In Fig. 3 a power meter (H) has been placed between the mirrors. During operation, the power meter is removed and the power level is monitored by a fast photodiode (J). The photodiode measures light reflected off the beam expander entry and was calibrated against the power meter.

The ablation target is a 10.2 cm x 10.2 cm x 3.18 mm aluminum (6061) square mounted on a 3-axis translation stage. It was cleaned with water, acetone, and

isopropyl alcohol prior to use. It is assumed that any remaining surface contamination will be removed within the first few laser pulses. Two of the three translation axes expose new target areas to the laser, while the third allows adjustment of the laser focus and thus the fluence. Ablation sites were separated by approximately 1 mm. Fig. 4 shows the target prior to ablation and Fig. 5 the target after data collection. A number of imperfections are visible on the surface; however the collected data shows no significant impact. Precautions were taken to avoid issues related to surface imperfections, visible or not. The spacing of ablation sites was such that no single defect could impact more than one energy level in a given energy sweep and that the same defect also could not affect that same energy level when the sweep is repeated. Given the variability of the ablation plume, even between subsequent pulses on the same location, it is unlikely any interference would be apparent even without precautions. Note that the interesting features of the plume variation plots, Fig. 61 (across the top) and Fig. 62 (down the left side) from the 4.13 Spectrometer Signal Variability section (pg. 107), do not correspond to any visible issues on the target surface.

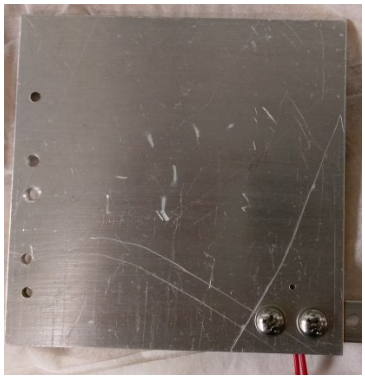

Fig. 4 Target prior to ablation

Fig. 5 Target after ablation

Fig. 6 shows the inside of the vacuum chamber, including the translation stages (A), the laser entry window (B), and the spectrometer enclosure (C). The target (D) is connected to the stages by a Macor plate (E), which provides thermal and electrical isolation from the translation stages. An LED shown through a hole in the target (F) simplifies alignment of the spectrometer. In this image, the LED is approximately at the laser focal point. The RPA (G) used in this work is visible, with its enclosure removed, between the ablation site and the spectrometer enclosure entry aperture (H).

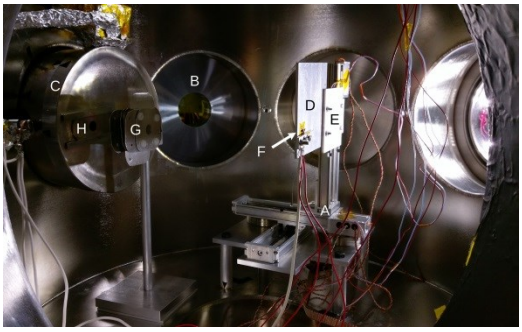

Fig. 6 Target and translation stages

3.1.2 Ion Source

An ionic liquid particle source (shown schematically in Fig. 7) was provided by the MIT Space Propulsion Laboratory, where the output was previously characterized [133,134]. The liquid is stored in a small cylindrical hole through a metallic block. A specially prepared needle mounted beneath that metal block protrudes through the hole. A bias of 1-1.5 kV is applied to the needle through the plate and ionic liquid. Suspended just above the top of the needle is another plate with a small hole in it just above the needle. This extractor plate is grounded. The bias applied to the needle creates a strong electric field between it and the extractor, causing emission of an ion beam, with polarity and output intensity controlled by the needle bias.

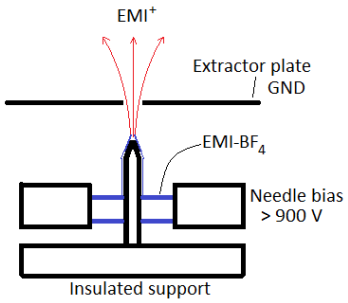

Fig. 7 Ion Source Operation

The beam has a parabolic profile, going to zero intensity at a half angle of about 16° [134]. The beam centerline can deviate significantly from normal to the extractor plate. Most of the beam is composed of three main species: monomers (a single molecular ion, e.g. EMI^+), dimers (a molecular ion combined with a pair of ionically bonded molecules, e.g. $[EMI\text{-}BF_4]\text{-}EMI^+$), and broken dimers (a molecular ion separated from a dimer after emission, e.g. EMI^+ separated from $[EMI\text{-}BF_4]\text{-}EMI^+$). Monomers and dimers are emitted from the needle and accelerated to the

same energy, approximately matching the needle bias. Nearly all dimers are expected to break up in flight. $[EMI\text{-}BF_4]\text{-}EMI^+$, for example, has a mean lifetime on the order of 1 μs compared to a flight time around 10 μs [135]. Broken dimers have the velocity of the dimer but the mass of the monomer, forming a distinct peak in the energy spectrum.

The initial masses of each monomer and dimer species, and the post-breakup monomer masses are in Table 1. The ratio of post-breakup to pre-breakup energy is the same as the ratio of post-breakup to pre-breakup masses. The liquids used were $EMI\text{-}BF_4$ (1-ethyl-3-methylimidazolium tetrafluoroborate), EMI-Im (1-ethyl-3-methylimidazolium bis(trifluoromethylsulfonyl)imide), and $EMI\text{-}GaCl_4$ (1-ethyl-3-methylimidazolium tetrachlorogallate).

Table 1 Ionic Liquid Species Mass and Energy

Species	Initial Mass [amu]	Monomer Mass [amu]	Ratio (Post/Initial)
$C_6H_{11}N_2^+$ (EMI)	111.2	111.2	1.0
BF_4^-	87	87	1.0
$C_2F_6N_1O_4S_2^-$ (Im)	280.2	280.2	1.0
$GaCl_4^-$	211.3	211.3	1.0
$[EMI\text{-}BF_4]\text{-}EMI^+$	309.4	111.2	0.36
$[EMI\text{-}BF_4]\text{-}BF_4^-$	285.2	87	0.305
$[EMI\text{-}Im]\text{-}EMI^+$	502.6	111.2	0.22
$[EMI\text{-}Im]\text{-}Im^-$	671.6	280.2	0.42
$[EMI\text{-}GaCl_4]\text{-}EMI^+$	433.7	111.2	0.26
$[EMI\text{-}GaCl_4]\text{-}GaCl_4^-$	533.8	211.3	0.40

The ionic liquid source serves to calibrate the energy gate pass band, verify the expected scaling of secondary emission, and demonstrate that single particle impacts can be observed via both secondary electrons and secondary ions for particles of similar size to small Al clusters. The ionic liquid source cannot be directly pulsed, so additional effort would have been required to attempt TOF measurements. The

effort was deemed unnecessary because sufficient calibration data and demonstrations would be available without TOF information, given the addition of aluminum ablation data.

The location of the peaks in the energy spectrum allows correlation of energy gate pass band to the applied gate voltage. Following changes in the peaks with movement of the source location shows how the pass band changes with beam entry angle, θ, (if the beam is not perfectly aligned to the spectrometer longitudinal axis). The former test can be performed with any dataset collected, while the latter was only performed using EMI+ (from EMI-BF_4).

3.2 Time-of-Flight Spectrometer Design

3.2.1 Design Summary

The system for this test consists of the following components: laser ablation plasma source, pre-spectrometer flight region, energy gate, accelerator, particle detector, scintillator, and photomultiplier (PMT). Fig. 8 shows the various elements and the primary and secondary particle paths. Primary ions fly from the ablation spot to the energy gate. Particles of the correct energy (U) are deflected to pass through the energy gate (from A to E in Fig. 8), accelerated (from E to G), and finally collide with the rear of the detector (G). The impact of each primary ion produces a shower of secondary ions and electrons, which are accelerated into the scintillator (H), generating photons that are detected by the PMT (K). Fig. 9 shows the completed spectrometer, including the 3-D printed support structure (C) and grounded aluminum struts (D). The spectrometer entry plate (A) and first gate deflection plate (B) are also labeled. The energy-per-charge required to pass through the energy gates depends on

the angle at which the beam enters the spectrometer. The entry angle is divided into one component along the same axis as the beam is deflected by the gate, θ_y, and one perpendicular to that, θ_z, with both perpendicular to the spectrometer's longitudinal axis. A positive entry angle along the deflection axis would point the undeflected beam closer to the center aperture (up in Fig. 8). A positive the entry angle along the non-deflection axis points the beam more towards the spectrometer support beams (into the page in Fig. 9).

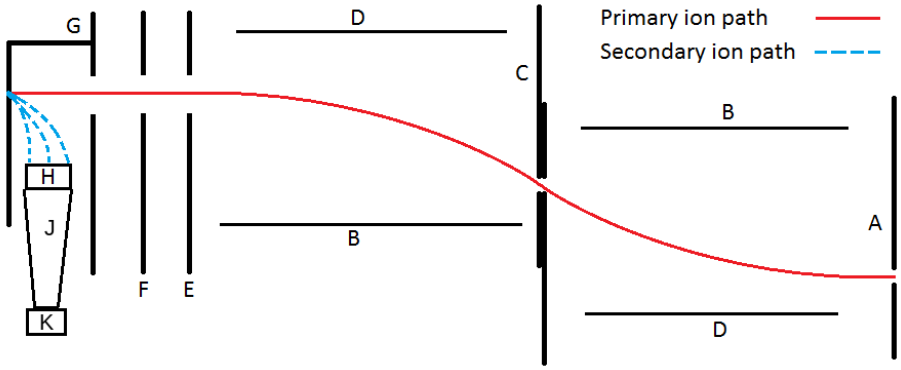

Fig. 8 Spectrometer Diagram showing primary and secondary particle paths

A: entry aperture plate, grounded
B: deflection plates, $V_{gate} = 3.2U$
C: center aperture plate V_{gate}
D: grounded plates, grounded
E: exit aperture plate, grounded
F: acceleration plate, $V_{accel} = 8.7*U$ or ±5 kV
G: detector box, $V_{det} = \pm 5$ kV
H: scintillator, $V_{scin} = V_{det} \pm 5$ kV
J: light guide, floating
K: photomultiplier, -1 kV

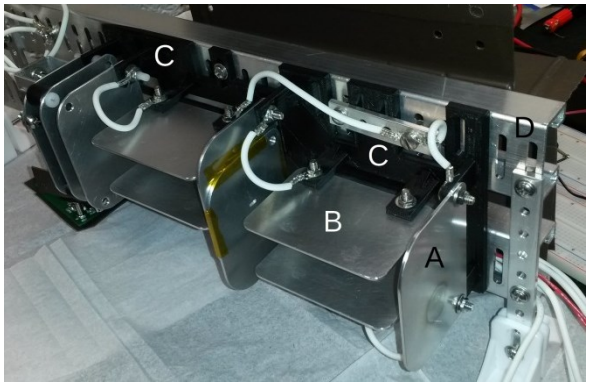

Fig. 9 Assembled Prototype

All spectrometer elements (energy gate through photomultiplier) are contained within a cylinder of mu-metal (C in Fig. 6), which reduces the external magnetic field to < 10 μT. The measurement was limited by magnetometer noise (Freescale Semiconductor, MAG3110). This is necessary to prevent Earth's magnetic field from interfering with low energy particle trajectories in the energy gates. The exit aperture plate was extended to the enclosing cylinder to prevent the accelerator and detector fields from interfering with the energy gates. Fig. 10 shows the exit aperture plate extension (E) and the interior of the detector box. The detector entry plate (G), scintillator support structure (A), light guide support and enclosure (B), and PMT (C) are all visible. The scintillator bias was applied by a wire mesh (D) covering the scintillator surface.

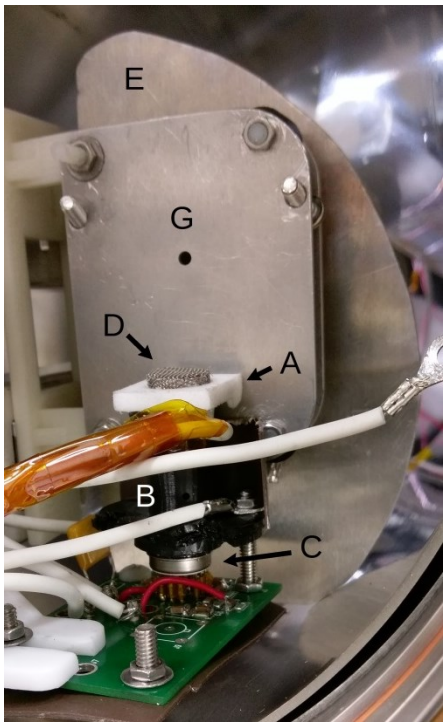

Fig. 10 Detector Interior

After a 0.24 m field-free flight, the ablation plume enters the mu-metal cylinder through a 1.27 cm diameter aperture, then enters the energy gates through a slit in the entry aperture plate (A in Fig. 8). The current hitting the entry aperture plate, hereafter the aperture current, is measured across a 2.497 kΩ resistor. The typical noise on the aperture current was about 20 mV, with frequent brief spikes up to 50-60 mV. The aperture current collection area is about 46 times the entry aperture area. The middle aperture has the same dimensions as the entry aperture. Assuming a point source, the middle aperture limits the effective entry aperture area to $1/250^{th}$ of the aperture current collection area.

An electron rejection bias was required prior to the entry aperture to obtain consistent aperture current measurements. For this work, a bias of +30V was applied

to a plate about 2.5 cm before the mu-metal cylinder entry. The plate (A) and mu-metal cylinder (spectrometer enclosure) entry aperture (H) are shown in Fig. 11.

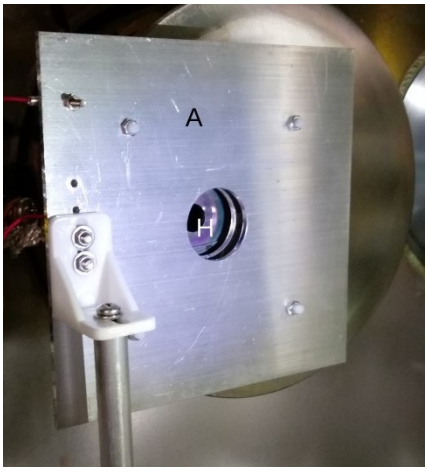

Fig. 11 Electron rejection bias plate

Electrons were deflected away from the mu-metal entry aperture as the beam passed through a 3.0 cm diameter hole in the plate. Fig. 12 shows a clean entry aperture current (across 2.5 kΩ) from an ablation event, using a +30V electron rejection bias. Fig. 13 shows the same scenario but using a +10V bias, which was always insufficient. The +30V bias was itself insufficient in a number of cases, particularly when the laser was maximally focused. Increasing the bias was not worth the disruption it would have on the incoming beam.

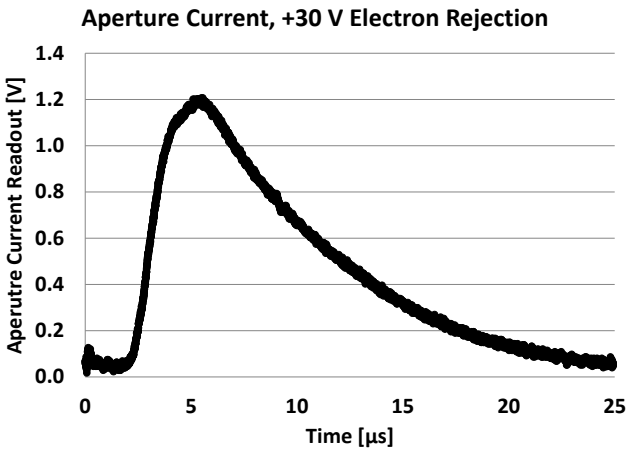

Fig. 12 Abl. Aper. Current (across 2.5 kΩ), Sufficient Electron Rejection Bias

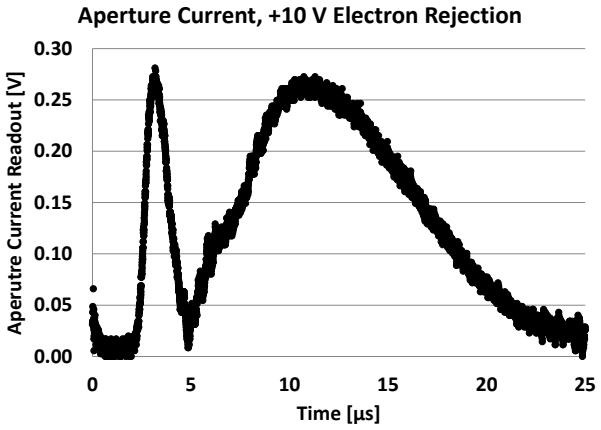

Fig. 13 Abl. Aper. Current (across 2.5 kΩ), Insufficient Electron Rejection Bias

The entry aperture permits a thin beam to enter the energy gates. Referring to Fig. 8, each gate is 100 mm long (A to C) with 30 mm between the bias plates (B to D) and 17 mm between the apertures. The entry and center apertures are 0.9 mm wide in the deflection direction and 3 mm wide in the other direction. All other apertures are 3mm in diameter to accommodate uncertainties in the realized instrument.

The energy gate entry aperture plate (plate A), and the energy gate ground plates (plates D) are grounded. The energy gate deflection plates (plates B), and the energy gate center aperture plate (plate C) are biased to V_{gate}. The field within the

gates is shown in Fig. 14. It is approximated by a uniform field for non-numerical uncertainty analysis, discussed later. The first gate deflects plume components of a particular energy (along the spectrometer axis) and polarity such that they pass through the center aperture and are straightened out by the second gate. All other particles are captured by the various gate plates.

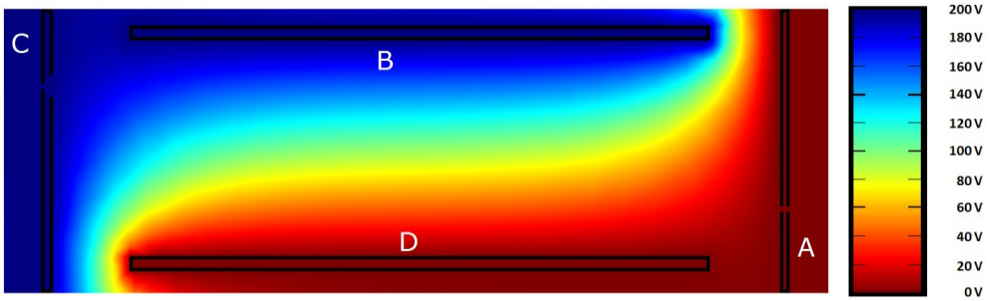

Fig. 14 Electric field within the energy gate (particles enter at lower right)

The gate dimensions, combined with uncertainty of the entry angle, are the primary drivers of uncertainty in the pass energy. 3-D printing the support structure ensured accurate and repeatable spacing of all the components. The center aperture is made as thin as possible to avoid particles catching within the aperture. The entry and center aperture widths perpendicular to the deflection direction and the (circular) exit aperture diameter do not affect the energy uncertainty and so are wider (3 mm) to improve signal strength and loosen alignment tolerances. If necessary, the pass energy can be varied to account for poor alignment in the deflection direction. The spectrometer is aligned by placing a light source at the ablation spot. The light source illuminates, through the entry aperture, a guide mark on the center aperture plate. The estimated entry angles are -0.1° in the deflection direction, θ_y, and 0° in the other direction, θ_z. The estimated accuracy of alignment is ± 0.1°.

The gate bias for this prototype will range from -7.5 kV to +7.5 kV. For voltages below 1 kV, the bias is supplied by a sourcemeter (Keithley 2410). For voltages above 1 kV, the bias is supplied by a single polarity high voltage supply (Acopian P/N010HA6) whose control voltage is supplied by the sourcemeter. The wiring of biases for the lower and higher voltage cases are shown in Fig. 15 and Fig. 16.

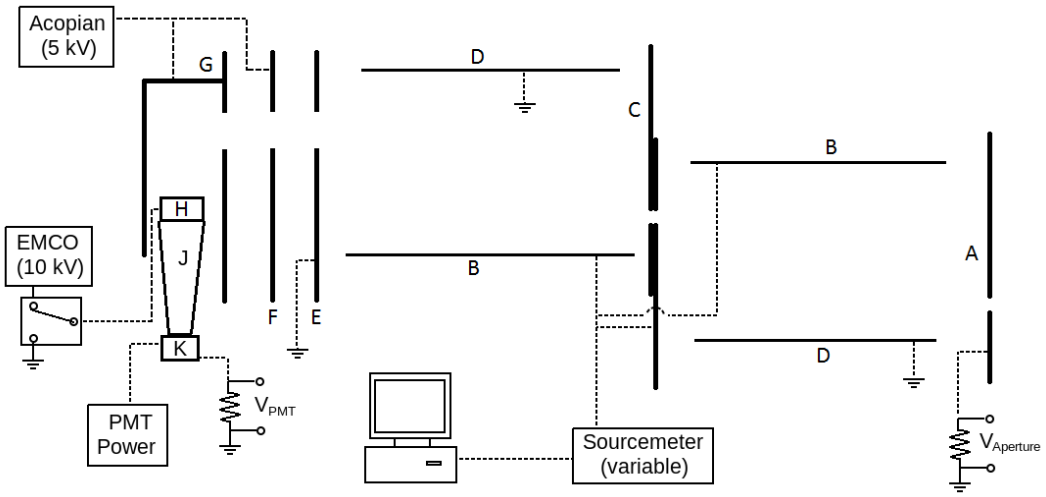

Fig. 15 Spectrometer bias wiring for lower voltages

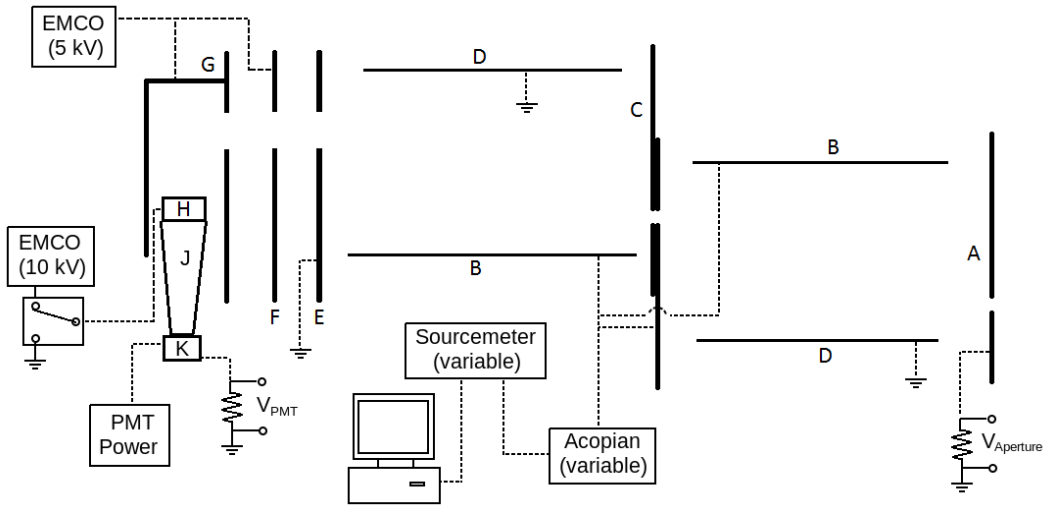

Fig. 16 Spectrometer bias wiring for higher voltages

The primary particles exiting the energy gate are accelerated through a 3-plate electrostatic lens (the accelerator: plates E, F, and G in Fig. 8). The plates are separated from each other by 10 mm and each has a 3 mm diameter aperture. The accelerator ensures the primary particles have sufficient energy to generate secondary particles within the detector. The first plate of the lens (E) is grounded and serves as the exit aperture of the energy gate. The third lens plate (G) is at the same bias as the detector (the detector bias) and serves as the entry aperture for the particle detector. The middle lens plate (F) provides an interim bias (the accelerator bias) which can be set to prevent lower energy ions from being defocused by the accelerator. Simulations performed using the COMSOL Multiphysics software indicate that the middle and final lens plates may be kept at the same bias, if the defocusing is accounted.

The detector design here-in is based on the Daly ion detector [136], which has previously been used to detect aluminum cluster-ions via secondary electron emission [137]. It consists of a rectangular aluminum box (G in Fig. 8) with an entry aperture facing the rear wall just below one end and a biasable scintillator (H) near the other end, about 1.5 cm below the entry aperture. The detector box is 2.4 cm across. Primary ions cross the top of the detector box at high energy and with little deflection, impacting the rear wall and generating secondary particles. Depending on the scintillator's bias relative to the detector, either secondary ions or secondary electrons will be accelerated into the scintillator, generating a flash of light. Having the scintillator within the detector box focuses the secondary particles onto the scintillator. As will be discussed in the next section, secondary electrons have a higher yield while secondary ions are expected to maintain a mass dependent yield

for heavier particles. Secondary electrons also produce a stronger signal within the scintillator [138]. The detector bias (G in Fig. 15) was chosen to be ±5 kV and the scintillator (H) to be ±5 kV relative to that (so either 0 or ±10 kV). Because of electrical shorting, the maximum bias of the scintillator was limited to ±8 kV, with the detector bias occasionally reduced to increase the scintillator yield at the expense of the secondary particle yield. The detector and accelerator biases are supplied by the same high voltage power supply (Acopian P/N010HA6 or EMCO F50). The scintillator was biased (when not grounded) by a separate high voltage supply (EMCO F101). The Acopian supplies were regulated with a slow response time while the EMCO supplies were unregulated. Both were monitored and observed to be stable.

The accelerator and detector are small compared to the flight region, so they add minimally to the flight time. The extra time can be accounted when determining the mass-to-charge ratio. The flight time of secondary electrons is negligible, but for secondary ions it must be estimated (by simulation) or measured (by comparison to secondary electron mode).

The scintillator (H in Fig. 8) is a cylinder, 12.7 mm in diameter and 6.35 mm thick, with a flat side facing the top of the detector box. The material is a plastic, EJ-212, with a nominal light yield of 10,000 photons per 1 MeV electron [139]. The expected photon yield was calculated using Birks' formula, Eq. (9), with coefficients for a similar material (BC-408) from [140] (A=12.6 photons/keV, $kB = 6.2\text{x}10^{-3}$ cm/MeV) and specific energy loss for the plastic matrix (polyvinyltoluene) [141], which is well approximated by Eq. (10) in the relevant range, 3 to 5 keV. The

integration was started at 3 keV instead of 0 because the specific energy loss is poorly behaved for low values. The calculation was confirmed against another similar scintillator at 10 keV, NE102, from [142]. The expected yield is 20 photons at 5 keV.

$$Y = \int_0^E \frac{A}{1 + kB\frac{dE}{dx}} dE \tag{9}$$

$$\frac{dE}{dx} = 0.8566E^{-0.721} \tag{10}$$

Light from the scintillator passes down a light guide (J in Fig. 8) made of Poly(methyl methacrylate) (PMMA) into the PMT (K). The scintillator and light guide are joined with optical grease between and epoxy around the side. The light guide is joined to the PMT by a 3-D printed part, which blocks stray light from entering either (Fig. 10). Even with this, LED lights inside the chamber needed to be disabled, else they would produce a small but noticeable signal from the PMT (about 270 nA). The light guide is a truncated cone, 2.5 cm long with the scintillator face 1.27 cm in diameter and the PMT face 0.8 cm in diameter. The index of refraction is 1.58, therefor total internal reflection is reasonably assumed. The scintillator does not include a reflective coating, as that could interfere with secondary ion detection, so approximately 25% of the generated photons are expected to enter the light guide (the light guide interface covers 25% of the scintillator's surface area) and all of those are assumed to reach the PMT.

The photomultiplier (K in Fig. 8) is a R9880-210 from Hamamatsu, with a detection efficiency of about 36% at the scintillator's output wavelength of 423 nm, and operated with a gain of approximately $2x10^6$. The PMT output is read by a fast oscilloscope (picoscope 5444A) across a 2.505 kΩ resistor. Fig. 17 shows an example

of the data captured by the oscilloscope: the laser photodiode output, the entry aperture current, and the PMT output. The resistor was selected to balance signal-to-noise ratio against RC distortion. A parasitic capacitance of about 125 pF was observed on the PMT output signal. The PMT readout background noise (peak) was generally < 40 mV. The PMT produced false hits, typically 50-100 mV height, with a mean time between occurrences of about 10 seconds. These false hits are unlikely to disturb measurements because the measurement spans are typically much less than 1 ms. Any individual impactor observations must be sufficiently repeatable to make it improbable that they are false hits.

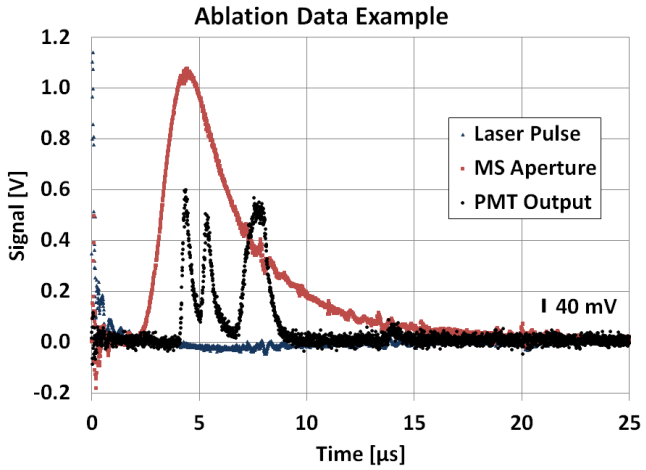

Fig. 17 Example of Ablation Data

Preliminary testing showed that the continuous part of the plume signal completed reliably within the first 25 µs after the laser pulse, allowing use of a continuous stream of laser pulses (repetition rate 40 kHz). Any unexpected content outside of the 25 µs window would still be apparent, but not readily traceable to a particular laser pulse. Data were also collected for individual and short bursts of laser pulses, recording the signal for between 20 and 100 ms. Although all the continuous data ends by 25 µs, there might still be individual particle hits from clusters and

nanoparticles. The extra delay between pulses also gives time for any slow plume components to clear the system before the next pulse. The first 100 μs were always recorded. To reduce collection time, processing time, and storage requirements, data after the first 100 μs were only kept in the neighborhood of any excursion above 0.1V. The threshold was selected to avoid frequent triggering by noise. The data captured, whether within the first 100 μs or triggered by a 0.1V excursion, do not suggest anything meaningful was missed due to the threshold.

The signal from the ionic liquid source was too weak for the oscilloscope to readily pick up, so a picoammeter (Keithly 6485) was used in place of the resistor and oscilloscope. This was possible for the ionic liquid source because, unlike the ablation source, its output is continuous. The typical picoammeter noise was the larger of 5% to 7.5% or 0.5 nA. The resistor and oscilloscope combination was used with the ionic liquid source for the cases where individual impacts were observed, but with a 9.84 kΩ resistor.

3.2.2 Time-of-Flight & Energy Uncertainty

The mass spectrometer portion of this system, including free flight from the particle source, passage through the energy gates, and a time of arrival from the detector, is used to calculate the energy and mass-to-charge ratio of plume components. A photodiode in the laser optics enclosure detects the laser pulse, which corresponds to the time-of-flight (TOF) start time. Together with the detector output signal, this determines the time-of-flight. By stepping the voltage on the energy gate and repeating the input plume, the full spectrum of incoming particles may be observed. The current arriving at the gate entry aperture is measured as a reference, to

establish consistency of the input plume as the individual energy bands are observed and to account for expansion of the plume within the spectrometer driven by inter-particle forces. The aperture current is also useful for establishing whether the entire plume has been accounted.

Uncertainties due to variation in energy gate geometry and bias voltages between cases where assessed by modeling the first half of the energy gate as a uniform field between two parallel plates. The equation of motion for a particle passing through the field is given by Eq. (11), where U is the pass energy, V_{gate} is the gate bias, L_{gate} is the length of the gates (along the spectrometer's longitudinal axis), d is the plate separation, and h is the separation of the entry and exit apertures (parallel to the field). The particle is assumed to enter with a velocity entirely along the spectrometer axis (entry angle of 0°).

$$U = \frac{V_{gate} L_{gate}^{\ 2}}{4dh} \tag{11}$$

Errors due to biases in each of these parameters are resolved by calibrating against a known particle source. Uncertainties due to variation of these parameters between cases were low enough to be neglected. The actual flight length and its uncertainty will be estimated based on TOF measurements.

The flight time calculation is given in Eq. (12), where L is the length of each region, η is the ratio of primary ion center pass energy, U, to gate voltage, V_{gate}. V_{det} is the detector voltage, m is the primary ion mass, and z is the primary ion charge state. The relevant values of L are provided in Table 2. The flight is divided into three stages: field-free & energy gate, acceleration, and detector. Their lengths are L_{free}, L_{accel}, and L_{det}, respectively. L_{free} includes L_{gate} from Eq. (11) and the distance from

target to spectrometer. Each particle's velocity (along the spectrometer's longitudinal axis) is assumed constant through the field-free, energy gate, and detector regions. The free-flight length includes the energy gates, which produce minimal acceleration along the spectrometer axis. Within the accelerator the particle is assumed to accelerate through a uniform field. In this work the accelerator used a single stage. If the acceleration is performed over two stages with different fields (as required for very low energy beams) then the acceleration region's equation will need to be updated (ηV_{gate} represents the particle energy at the start of the stage and V_{det} represents the energy added by the stage). The flight time of the secondary particles within the detector must also be considered, but does not vary with primary species.

$$t_{free} = \frac{L_{free}}{\sqrt{\eta V_{gate}}} \sqrt{\frac{m}{2z|e^-|}}$$

$$t_{accel} = \frac{2L_{accel}\sqrt{\eta V_{gate}}}{V_{\det}} \sqrt{\frac{m}{2z|e^-|}} \left(1 - \sqrt{1 - \frac{V_{\det}}{\eta V_{gate}}}\right) \tag{12}$$

$$t_{\det} = \frac{L_{\det}}{\sqrt{\eta V_{gate} + V_{\det}}} \sqrt{\frac{m}{2z|e^-|}}$$

Table 2 Spectrometer TOF segment lengths

Parameter	Length [m]
field-free / energy gate	0.475
accelerator	0.012
detector	0.035

The ratio of the energy-per-charge required for a primary ion to pass through the energy gates to the electric bias applied to the gates (the energy-to-gate-bias ratio, η) and the effect of a non-zero entry angle on that ratio were simulated via COMSOL and verified by observing ionic liquid ion source beam (whose energy is known) (see

pg. 79). The COMSOL simulation did not include space charge effects. An additional simulation was performed to assess and account for the effects of space charge within the spectrometer (see pg. 118).

The COMSOL model predicted an energy-to-gate-bias ratio of 3.5. The measured ratio was 3.2 (see pg. 79). In both cases the ratio changed 11% per degree for small entry angles along the deflection axis, θ_y, and negligibly for entry angles along the non-deflection axis, θ_z. Any error in the energy-to-gate bias ratio will be absorbed into the flight length, as the two appear together in t_{free} (Eq. (12)), which makes up the bulk of the primary ion flight time. The ion source value for energy-to-gate bias ratio was confirmed by comparing the flight length for Al^{+1}, Al^{+2}, and Al^{+3} estimated from the TOF signal against a direct (though less precise) measurement of the flight length (see pg. 98).

The mass-to-charge ratio and energy-per-charge uncertainties were determined experimentally using ionic liquid data and ablation data for Al^{+3} (see pg. 79 and pg. 98). The signals for Al^{+3} were the sharpest and most consistent among the available species in the ablation data (see Fig. 49 & Fig. 55), thus they most accurately reflect the underlying uncertainties of the spectrometer rather than characteristics of the particle source. The velocity uncertainty was estimated from those for mass-to-charge ratio and energy-per-charge (pg. 98). The resulting energy, velocity, and mass-to-charge ratio uncertainties (1-sigma) are in Table 3.

Table 3 Derived Uncertainties

Parameter	Uncertainty
Velocity	1.9%
Energy-per-charge	3.4%
Mass-to-charge ratio	1.6%

3.3 Particle Detection and Sizing via Secondary Emission

The detector component of this system makes use of secondary emission to identify the arrival time of particles and, based on the secondary particle yield, to estimate the mass of arriving particles. The timing function will be discussed further in the next section. This section will discuss two issues arising from the statistical nature of secondary emission – the minimum yield required to ensure detection of a particle and the minimum yield required to distinguish particles of different sizes but equivalent mass-to-charge ratio.

3.3.1 Single Ion Detection Limit

When a primary ion impacts the rear wall of the detector, secondary ions and electrons are emitted and accelerated onto a scintillator generating photons. Those photons are converted to electrons and amplified by the photomultiplier. The statistical behavior of the output is a combination of sequential Poisson and Binomial distributions. The Poisson distribution is generally applicable for processes with a small or moderate number of successes from a large number of trials - in this case, the interactions of an incident particle with the atoms of the target material, some of which will cause the phenomenon of interest (ion, electron, or photon emission). It is applied for secondary emission of ions and electrons [18,143-145], generation of photons within the scintillator, and generation of secondary electrons in each stage of the photomultiplier. The Binomial distribution is applicable to multiple trials with a fixed probability of any one succeeding. This covers the odds a photon generated in the scintillator will reach the PMT, whether such a photon will generate a photoelectron, and whether that photoelectron will reach the first multiplication stage

in the PMT. The output of each step determines the parameters of the statistical distribution of the next stage, so the combined distribution warranted simulation (pg. 133). Despite the complexity of the overall process, the mean output is the product of the means of each stage and thus proportional to the secondary particle yield.

A scintillator bias of 5 kV, will ensure all secondary particles reach the scintillator and, assuming the predicted yield, produce an average of 20 photons per secondary electron. About 5 of the generated photons will exit the rear face of the scintillator (because it is 25% of the scintillator's surface area) to enter the light guide leading to the photomultiplier. The light guide's transmission rate is about 87% over its 25 mm length [146]. Applying the photomultiplier's quantum efficiency of 38%, and estimating its collection efficiency at 95%, a mean of 1.6 photoelectrons will be counted. The PMT gain is about $2x10^6$ across 10 stages, so each stage has a multiplication factor of about 4.25. The mean signal height per photoelectron, seen over the 125 pF parasitic capacitance, is 2.2 mV.

The results (Fig. 18) indicated that, for a scintillator voltage of 5kV a mean secondary electron yield of 5 would be required for a 97.5% chance of producing output. The 2.5 percentile signal height is 1.1 mV while the mean is 19 mV. The uncertainty of the oscilloscope, including noise, is about ±20 mV. To have the 2.5 percentile signal height reach 20 mV requires a mean secondary electron yield of 14, at which point the mean signal height is 54 mV.

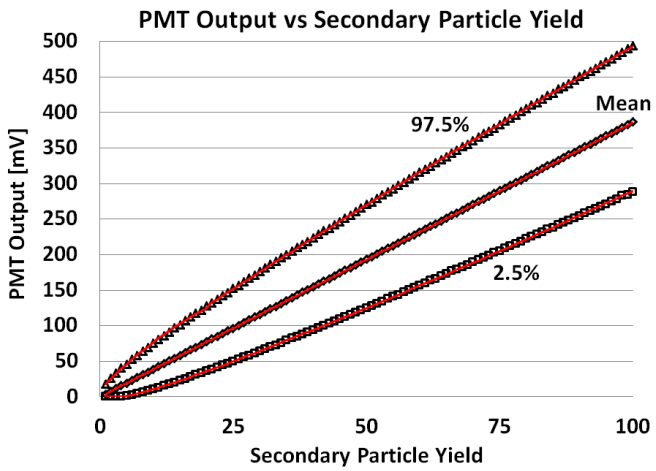

Fig. 18 PMT Output Probability

The ability of plastic scintillators to detect the impact of singly charged ions below 5 keV has previously been demonstrated [138]. The authors evaluated Ar^+ and Xe^+, noting that the response was linear above 3 keV and 8 keV respectively. The yield for this scintillator and secondary particle combination will be measured by redirecting the primary particles into the scintillator.

3.3.2 Mass determination

Studies of sputter and secondary ion yields from impacts of multi-atomic ions have indicated that the yield is proportional to the kinetic energy of the primary particle, once a material-dependent size and velocity threshold is reached [15,16,18]. The proposed design measures particle kinetic energy-per-charge and velocity as they existed prior to electrostatic acceleration and collision with the detector. Because the secondary particle yield depends on velocity and mass, with little or no charge dependence, the yield can be combined with the per-charge quantities to derive the impactor mass.

The secondary electron yield is also primarily a function of mass and velocity, however a "sweeping-out" effect has been observed, whereby larger impactors expel all easily available electrons and thus have a lower overall output than would be expected when comparing to smaller impacts for which additional easily available electrons remain undisturbed [144,147]. The "sweeping-out" effect should not interfere with particle detection, since it requires many secondary electrons to be generated, but may interfere with sizing. It is for that reason that secondary ion based particle sizing is required. Secondary electron yield based sizing may be possible for smaller clusters, which don't generate appreciable quantities of secondary ions. Given a good estimate of yield for the particular materials and energy range involved, the mass of any single primary ion impacting the detector may be estimated. Ions that are small enough to be identified by mass-to-charge ratio but large enough to reach the regime of linear yield vs kinetic energy (KE) could, if present, be used to develop the necessary estimate. If the particle sizes are too large to identify, but are consistent, a scaling law may be developed between impact velocity and yield and used to determine relative masses – all available literature suggests approximate proportionality to mass, even if not to the square of velocity. Without such estimates, scaling laws for the closest available impactor/target combination may, where available, be taken from literature. For the best result, particles of known size and charge state may be generated to calibrate the size measurement for any particular impactor/target combination, for example by MALDI [148].

To best determine the secondary particle yield and thus the mass of a primary particle, all impacts should be individually observable. This requires either a

sufficiently low flux of primaries or a sufficiently fast measurement system. The electronics readout resistor and parasitic capacitance are the limiting factors, giving an impulse signal (i.e. a single particle impact) decay time constant of approximately 300 ns, so the flux must be well below $3x10^6$ hits per second (0.5 pA for singly charged particles). Individual hits may also be visible for large primaries within a continuous background of small primaries, provided the readout's resolution is sufficient to observe a small blip on top of a larger continuous signal. When there are too many particles to distinguish, or the yield per particle is too low, size information may still be gleaned from the average yield, measured by the total yield or by monitoring those hits that happen to generate secondary particles.

This system is particularly useful for determining charge states in cases where inter-particle spacing is too large for convenient TOF measurements – where the extraction period must be unacceptably long. The energy gate fixes the pre-acceleration energy so differences in the impact kinetic energy are only a function of the charge and the detector bias. If, as expected, the secondary yield is proportional to kinetic energy, the charge state can be determined by correlating the size of the yield to an integer multiple of the measured energy-per-charge.

Any two charge states are clearly distinguishable for single impacts if the 97.5% probability level of the lower yield impact is below the 2.5% probability level of the higher yield impact – the impact of one is unlikely to generate a signal size within the likely range of the other. Assumption that the secondary electron yield is proportional to primary ion kinetic energy, a mean yield of 41 secondary electrons per primary ion charge (0.16 V across 125 pF, after scintillator and PMT) would be

required to reliably distinguish between singly and doubly charged ions (see Fig. 88). The contribution of the oscilloscope to sizing uncertainty is much less than that inherent in secondary emission. The inherent uncertainty in output height, σ_Y, is related to the mean output height, Y, by Eq. (13) where β is a constant of 7.08 mV.

$$\frac{\sigma_Y}{Y} = \sqrt{\frac{\beta}{Y}} \tag{13}$$

For mass determination, a moderate percent uncertainty in yield is sufficient. Since charge is discrete, the ability to distinguish specific charge states at the low end makes up for the poor percent uncertainty in the overall yield. The uncertainty may be improved by increasing the detector and/or scintillator biases. For this prototype, the detector bias is limited to ±5 kV and the scintillator to ±8 kV.

3.4 Retarding Potential Analyzer (RPA)

In addition to the mass spectrometer, the plume was evaluated with an RPA. The RPA consists of five aluminum plates (Fig. 19), the first four of which have a 12 mm diameter aperture in the center. Each aperture is covered with a mesh of 35 AWG wire having 0.46 mm square openings. Each combined mesh and plate is 1.7 mm thick, with a 3.5 mm separation from the next plate. An effective transparency of 13.7% was estimated by comparing the total current against the spectrometer aperture current. The RPA plates were enclosed in a grounded box and placed in front of the spectrometer entry (Fig. 20). The un-enclosed RPA is visible in Fig. 6. The RPA time-of-flight length was estimated by comparing the start time of the spectrometer aperture and RPA signals, giving 70% of the spectrometer aperture distance.

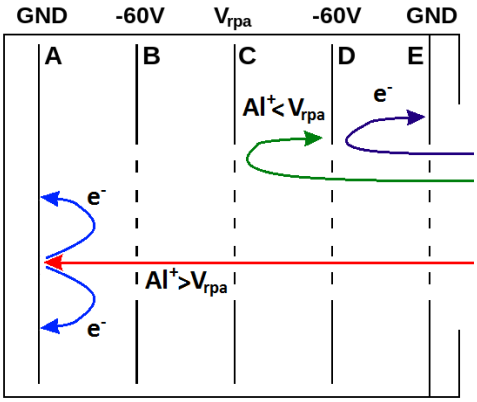

Fig. 19 RPA Diagram

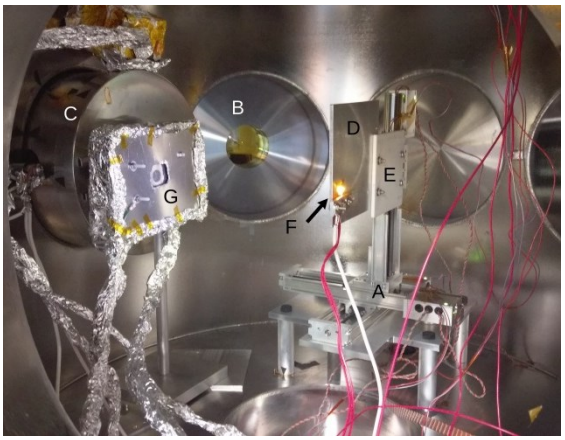

Fig. 20 RPA in chamber

The first RPA plate (E in Fig. 19) was grounded, to protect the incoming plume from the biases on the other plates. The RPA enclosure was also grounded, to protect the RPA interior from external particles and external particles from the internal RPA fields. A bias of -60 V was applied to the second plate (D) to block electrons. The retarding potential was applied to the third plate (C). The fifth plate acts as the charge collector (A), observed across a 2.5 kΩ resistor. The fourth plate (B) bias was -60 V, this time to push any secondary electrons back into the collector plate. Fig. 21 shows an example of data collected by the RPA.

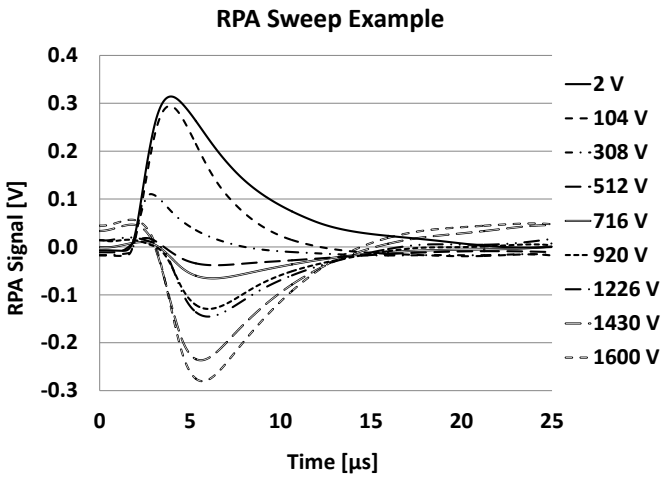

Fig. 21 RPA signal over full sweep

Unlike the spectrometer, the RPA is unable to identify the charge state of individual species. The calculation would use the difference in signal height over time between the RPA signals at neighboring energy levels. This requires both a very consistent signal between cases and a high signal to noise ratio (so the change between energy levels is sufficiently greater than the noise). As the spectrometer results will show, neither condition is met in this work. The RPA is less affected than the spectrometer by inter-particle forces as a result of its short length and large apertures. As the retarding potential increases, plume electrons will eventually be pulled through the electron rejection mesh. This limits the RPA's ability to handle the high energy portion of the ablation plume. The RPA must also use a higher bias for a given particle energy, though electron infiltration was observed before reaching a high voltage limitation. Given these limitations, the RPA was used only to provide a high-energy-only version of the aperture current for spectrometer calibration and to estimate propulsion performance metrics for any part of the plume below the spectrometer's observation range.

Chapter 4: Data Processing & Calibration

4.1 Laser Power Calibration

A fast photodiode was used to monitor the energy of each laser pulse (J in Fig. 3). The photodiode provides a fast rising signal when the laser fires that will be used as the start time for time-of-flight observations and a measure of the laser power. The photodiode has a very fast rise relative to the oscilloscope used to measure it, so the observed peak does not reliably reflect the actual peak. This issue is bypassed by using the integral of the laser signal rather than the peak as a measure of laser power.

The photodiode was calibrated against a thermal laser power meter (ThorLabs model S350C & PM100USB, H in Fig. 3). The power meter was placed just inside the laser entry window into the vacuum chamber. The highest observable laser power setting was limited by the damage threshold of the power meter. For calibration, the laser was operated at 40 kHz repetition rate at power settings of 5% and 10%.

The power meter indicated an average pulse energy of 4.1 kJ per Volt-second of laser photodiode integral. The calibration uncertainty is about ±5.3% (1-sigma), driven by uncertainty in the power meter calibration. There was a 3% variability in the integral of the photodiode output between different test pulses. The laser manufacturer indicates that the laser's output consistency is significantly reduced at low operating powers. In line with that expectation, the percent variability of the photodiode integral and the power meter dropped by almost half between 5% and 10% laser power. The decrease in laser variability with increasing power and averaging of the laser power over numerous pulses leave the power meter as the main contributor to laser pulse energy uncertainty.

4.2 Laser Focusing

The three-axis translation stages were assembled one on top of the other so that the bottom stage moves the middle stage, which moves the top stage, each along a mutually orthogonal axis. The top stage provides vertical motion. The middle and bottom stages are oriented so that only the middle stage will alter the distance between the laser and the target surface. The stage settings required to place the surface at the laser's focal spot were determined by setting a range of middle stage positions and adjusting the laser power setting to find the minimum that produces ablation. It was possible to get ablation down to the lowest laser setting over a roughly 0.5 mm range of middle stage motion. The middle of that range was selected. The same process was carried out at a few locations around the target. The results were sufficiently similar that no middle stage adjustments were required to keep the laser focused when moving the bottom or top stages.

The laser fluence at the best achievable focus was estimated based on SEM imaging of the crater generated by a single laser pulse at the selected middle stage position. Based on analysis from [149], focusing a laser beam with a Gaussian profile will produce a profile on a surface (at normal incidence) whose maxima and minima are given in Table 4. In Table 4, λ is the laser wavelength, f is the focal length of the focusing lens, a is the radius of the laser beam at the lens, and E is the laser pulse energy. Fig. 22 shows the crater resulting from a single laser pulse (at 45° incidence) with a visible intensity minimum of 50.4 μm diameter (stretched in one direction due to the angle). The formula from Table 4 for the radius of the first minimum may be used to estimate the peak intensity from the observed radius as in Eq. (14).

Table 4 Ablation Site Maxima/Minima

	1st max	1st min	2nd max	Units
radius	0	1.43	1.79	$\left[\frac{\lambda f}{2a}\right]$
intensity at r	0.924	0	0.0044	$\left[\frac{E\pi a^2}{\lambda^2 f^2}\right]$
power within r	95.5	96.2	97.3	% of total

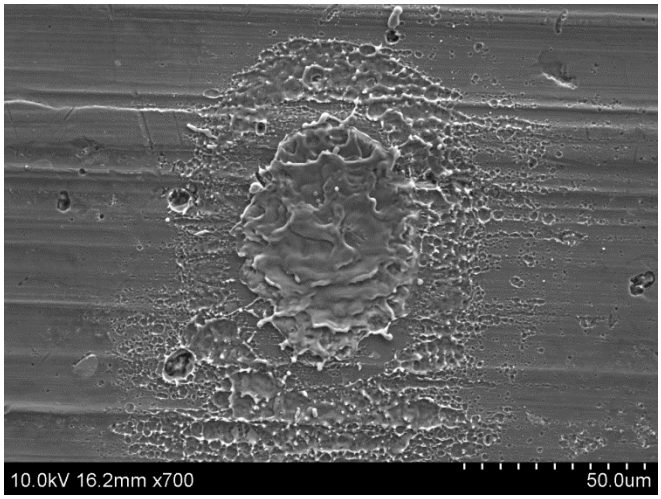

Fig. 22 Ablation Crater

$$I(0) = 0.924 E\pi \left(\frac{1.43}{50.4\mu m}\right)^2 \tag{14}$$

The laser should produce 827 μJ per pulse at 40 kHz, with a pulse FWHM of 0.72 ns. Based on the photodiode measurement the total energy per pulse reaching the target was 0.58 to 0.92 mJ (depending on which pulse in a group). Applying Eq. (14) and accounting for the angle of incidence, the peak fluence was most often between 100 and 130 J/cm^2 and the peak intensity between 130 and 170 GW/cm^2.

The fluence away from the focal point may be calculated based on the following laser beam propagation equations. The beam has a Gaussian temporal and spatial profile, Eq. (15), where *t* is time, *r* is radius perpendicular to the beam

propagation direction, z is distance along the propagation direction, w is the e^{-2} beam radius (see Eq. (17)), *FWHM* is the full width at half maximum (by time) of the pulse, and λ is the wavelength. The relationship between peak intensity and pulse energy is given by Eq. (16). The average pulse energy is just the average power divided by the pulse repetition rate.

$$I(r,z,t) = I_0\left(\frac{w_0}{w}\right)^2 \exp\left(\frac{-2r^2}{w^2}\right)\exp\left(\frac{-4\ln(2)t^2}{FWHM^2}\right) \tag{15}$$

$$E = I_0\left(\frac{w_0}{w}\right)^2\left(\frac{\pi w^2}{2}\right)\left(\frac{FWHM}{2}\sqrt{\frac{\pi}{\ln(2)}}\right) \tag{16}$$

$$w = w_0\sqrt{1+\left(\frac{z}{z_R}\right)^2} \qquad z_R = \frac{\pi {w_0}^2}{\lambda} \tag{17}$$

To calculate the laser intensity at a new location requires estimating the minimum beam radius, w_0, which can also be done using the formula from Table 4 for the radius of the first minimum. Given the focal length of 0.5 meters, the estimated beam radius at the lens, a, was 15 mm. Plugging into Eq. (17) indicates an estimated focal spot beam width of 11.3 μm. The nominal beam radius at the lens was 20 mm, giving a predicted focal width of 8.4 μm and airy disk first minimum diameter of 38 μm.

Some of this work uses a lower focus condition, with the middle stage shifted 0.80 mm, putting the target 0.56 mm from the focal spot (closer to the laser). Plugging the 0.56 mm offset, z, and the 11.3 μm minimum beam radius, w_0, into Eq. (17) gives a beam radius of about 20 μm at the low focus position. Plugging into Eq.

(16), and accounting for the incidence angle, the peak fluence and intensity were most often between 32 and 41 J/cm^2 and 42 and 54 GW/cm^2, 32% of the maximum focus.

The uncertainty in fluence as a function of stage position is based on Eq. (17), and given by

$$\frac{\sigma_{\Phi_0}}{\Phi_0} = \frac{-2z^2}{z_R{}^2 + z^2}\left(\frac{\sigma_z}{z}\right) \tag{18}$$

For the maximum focus, z is nominally 0, giving an uncertainty of 0, which is unrealistic. Based on experience locating the focal spot, the uncertainty is on the order of z_R, about 0.2 (predicted) - 0.4 (estimated) mm. The uncertainty then is 100% and, unsurprisingly, the peak power estimates are only good for order-of-magnitude. Repeatability is a higher concern. The translation stage specifications indicate repeatability of 6 μm, for an uncertainty of about 3.0%. This is small enough to be overwhelmed by natural variability in the ablation plume.

For the lower fluence case, assume the higher fluence case is at the focal spot, so z is 0.56 mm. Then the uncertainty in the relative fluence may be estimated using Eq. (18). The accuracy of the translation stages is approximately 40 μm, giving a relative fluence uncertainty of about 11%, or about 8% of the peak fluence. As for the high focus, the repeatability will be significantly better and likely swamped by natural variability in the plume.

4.3 Spectrometer Simulation

A simulation was created using the COMSOL Multiphysics software package to calculate the ratio of particle energy-per-charge to gate bias, η, required to pass the energy gates, the variation of that pass-energy-to-gate-bias ratio with the angle (along

the axis of beam deflection with the energy gates) at which the beam enters the spectrometer, $\eta(\theta_y)$, and the span of energies, $\Delta\eta$, and entry angles, $\Delta\theta$, around the nominal value that will reach the detector. The same simulation was used to estimate the flight time of secondary particles between generation in the detector and capture by the scintillator and to estimate the fraction of primary ions lost to defocusing if the accelerator bias is not set correctly. Fig. 23 shows the model used for the simulation, including the spectrometer (A), the spectrometer support structure (B), and the spectrometer enclosure including its aperture (C). The path of primary and secondary ions through the spectrometer was illustrated in Fig. 8. The electric field within the first energy gate was shown in Fig. 14. The field within the second gate is the same, but flipped vertically. The spectrometer enclosure and structure were grounded. All of the spectrometer plate biases (V_{gate}, V_{det}, V_{accel}) and the scintillator bias (V_{scin}) were modeled. The photomultiplier, light guide, and 3D printed structure were not included. The simulation also did not include space charge effects or time-varying electric fields, as might result from ions being captured by the spectrometer plates or from variations of in power supply output voltages. The ion species was not varied because the modeled system is electrostatic; therefore a particle's path is fully determined by its energy-per-charge. Space charge was modeled in another simulation (pg. 118) while variations in plate biases were evaluated analytically and determined to be insignificant compared to other sources of uncertainty (pg. 54).

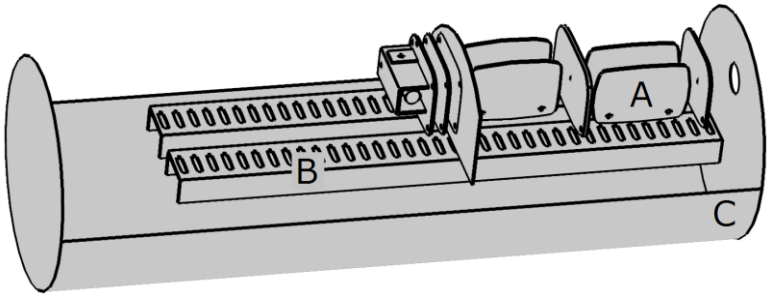

Fig. 23 Spectrometer COMSOL Model

4.3.1 Gate Passband

To determine the pass energy-to-gate-bias ratio, η, and its dependence on the entry angle along the deflection axis, $\eta(\theta_y)$, the electric field within the spectrometer was solved using an energy gate bias of 200 V, a detector bias of 5000 V, and a scintillator bias of 0V. Individual singly ions were released at the approximate location of the particle source, directed at the center of the spectrometer entry aperture with a specified energy. The location of the particle source was varied in along the deflection axis to change the entry angle, θ_y. To get the pass energy for each particle source location, $\eta(\theta_y)$, the ion's energy was changed until it passed through the center of the aperture between the first and second energy gates. With an entry angle of 0°, the pass energy-to-gate-bias ratio, η, was 3.45. Fig. 24 shows the variation of pass energy-to-gate-bias ratio with entry angle along the deflection direction as determined from the simulation. The fit, Eq. (19), is restricted to ±1° to most closely fit the expected uncertainty in spectrometer alignment. The slope is -11% for entry angles in the neighborhood of 0°. The pass energy-to-gate-bias ratio and its variation with entry angle also be evaluated experimentally (pg. 79).

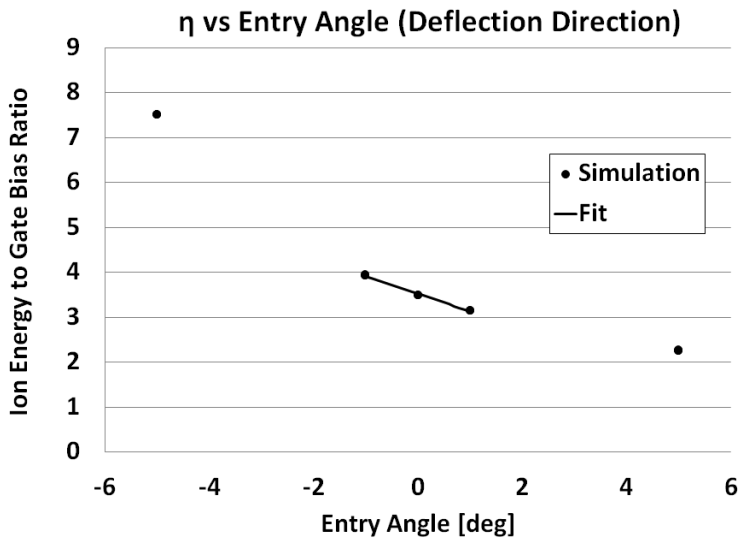

Fig. 24 Simulated Pass Energy vs Entry Angle

$$\eta = -0.392\,\theta_y + 3.52 \tag{19}$$

The passband width in energy and angle were estimated by placing the simulated particle source at the expected distance from the spectrometer, 0.300 m, and a nominal entry angle of 0°. The particle energy and entry angle were varied ($\Delta\eta$ and $\Delta\theta$) both positively and negatively until no ions reached the detector. Fig. 25 shows the range of particle energies reaching the detector ($\Delta\eta$), including a Gaussian fit with a mean of 3.46 and a standard deviation of 2.5%.

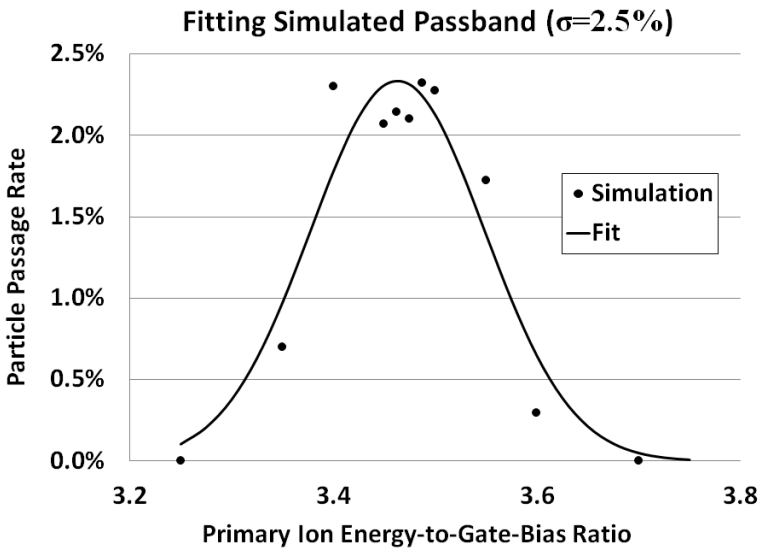

Fig. 25 Simulated Energy Passband Width

Fig. 26 shows the entry angle range along the deflection axis, $\Delta\theta_y$, that was able to pass the spectrometer as a function of the ion's energy-to-gate-bias ratio, given a nominal entry angle of 0°. The fit of the average angle is given by Eq. (20). The average difference between the highest and lowest angle at each energy-to-gate-bias ratio, excluding the outer most points, is 0.057°.

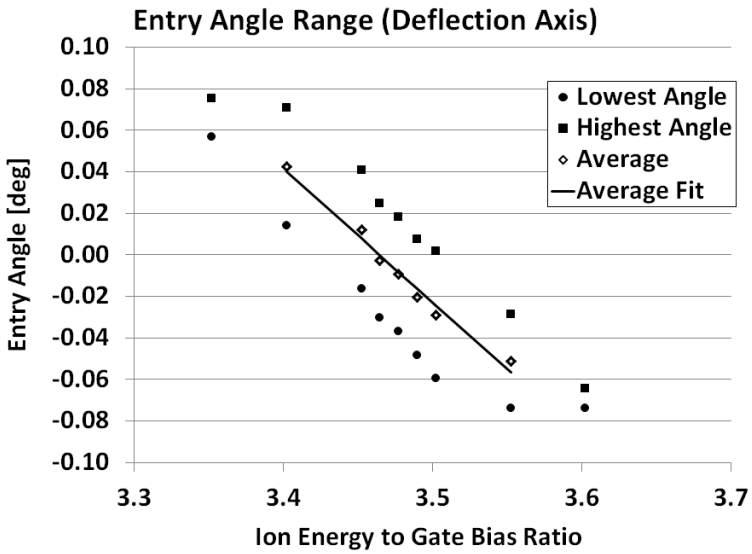

Fig. 26 Simulated Entry Angle (Deflection Axis) Passband

$$\Delta\theta_y = -0.6454\,\eta + 2.236 \tag{20}$$

Fig. 27 shows the entry angle range along the non-deflection axis, $\Delta\theta_z$, that was able to pass the spectrometer as a function of the ion's energy-to-gate-bias ratio, given a nominal entry angle of 0°. The fit of the average angle is given by Eq. (21). The average difference between the highest and lowest angle at each energy-to-gate-bias ratio, excluding the outer most points, is 0.41°. The cause of the 0.1° offset in Fig. 27 was not investigated because the offset reflects an error of less than 0.2% in ion energy-per-charge (by not observing the component perpendicular to the spectrometer's longitudinal axis) and because the total pass range is close to the expectation of 0.34° (3 mm exit diameter after approximately 500 mm of flight), with no dependence on ion energy.

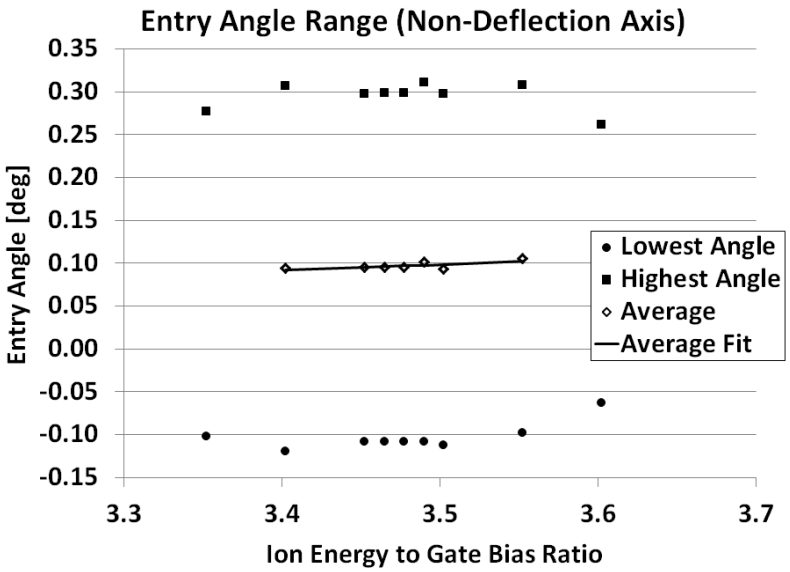

Fig. 27 Simulated Entry Angle (Non-Deflection Axis) Passband

$$\Delta\theta_z = 0.0682\,\eta - 0.1402 \tag{21}$$

4.3.2 Accelerator Focusing

Primary ions are accelerated prior to impacting the rear wall of the detector. This enhances their secondary particle yield, particularly for low energy ions. Low energy ions, however, may also be defocused by the accelerator if accelerated too quickly. To avoid defocusing, the accelerator plate provides an intermediate bias, V_{scin}, between ground at the energy gate exit and the detector bias, V_{det}. The ideal accelerator bias was found using geometric ion optics for parallel plates with circular apertures and assuming a low off-axis velocity exiting the gates [150]. The path of an ion was projected through the accelerator to determine what bias would be required to pass ions of any given initial energy-per-charge. The best result was achieved by setting the middle plate bias to 8.7x the primary ion energy (8.7 kV per 1 keV/C), with the accelerator bias never being set above the detector bias.

Passage of ions through the accelerator was also evaluated using the same COMSOL simulation as used for the energy and entry angle passbands. Both the detector and accelerator biases were set to 5 kV, and the primary ion energy varied while tracking the fraction of particles that passed the accelerator into the detector. The gate bias was adjusted along with the primary ion energy so the ions would correctly pass the energy gate. The simulation indicated that the middle and final lens plates may be kept at the same bias, if the defocusing is accounted.

Fig. 28 shows the effect of defocusing in the accelerator region on the number of primary particles that reach the detector, and that it has no effect for particles with greater than 350 eV/e^- energy. The fit line is given by Eq. (22), where R is the relative pass count and U is the ion energy in eV/e^-. For this work, the accelerator plate was

kept at the same bias as the detector, so a correction will be applied for any species below 350 eV/e^- using Eq. (22).

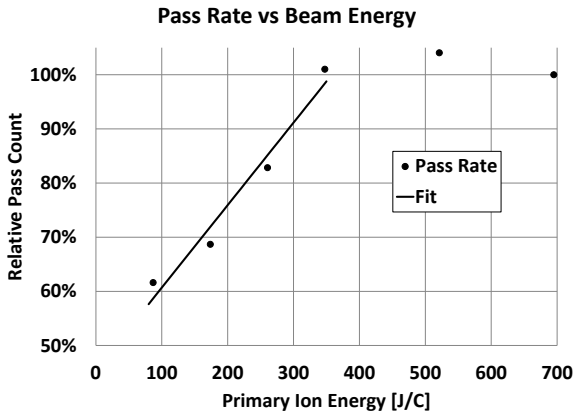

Fig. 28 Defocusing with accelerator at 5 kV

$$R = \frac{U}{\left(658\frac{eV}{e^-}\right)} + 0.454 \text{ for } U < 350\frac{eV}{e^-} \tag{22}$$

4.3.3 Secondary Particle Flight Time

The same COMSOL simulation was also used to assess the impact of secondary particle energy and release angle on measurements of arrival time. A single primary ion of the correct energy and 0° entry angle was run through the spectrometer to identify where primary ions would impact the rear wall of the detector. Singly charged Al ions of 0.5, 1.0, 5.0, and 10.0 eV and electrons of 0.05 and 1 eV were then generated at the identified location with velocity vectors filling a 60° half-angle cone around the surface normal. Fig. 29 shows a single primary ion (red) and secondary electron (blue) trajectory from this simulation. The accelerator plate (F), detector box (G), and scintillator (H) can all be seen.

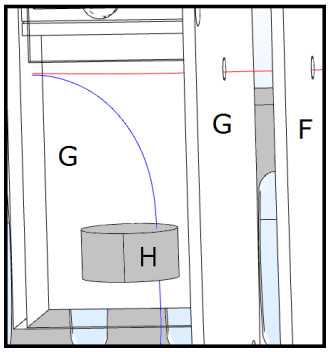

Fig. 29 Secondary Ion Timing Simulation

The simulation was run with the detector at 5 kV and the scintillator grounded and again with the detector at 4 kV and the scintillator at 8 kV. Secondary electrons arrived at the scintillator within about 5 ns with a range of up to 2 ns, providing no significant addition to the time-of-flight. Secondary ions took 0.7 to 1.3 us to arrive, depending more on particle energy than detector-to-scintillator voltage. Fig. 30 shows the minimum and maximum simulated flight times for secondary ions. The secondary ion timing was not evaluated further because no time-of-flight data were collected using secondary ions.

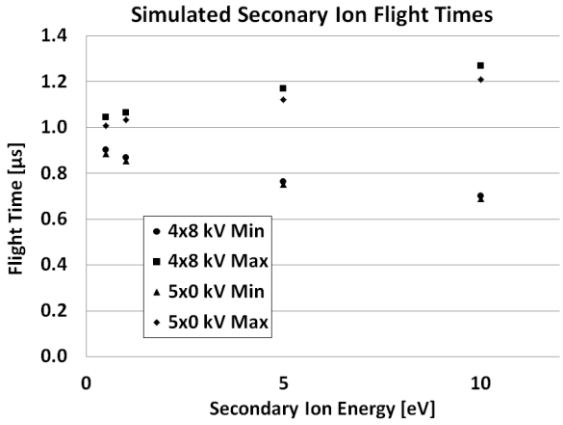

Fig. 30 Secondary Ion Timing Simulation

4.4 Gate Pass Energy Measurement

4.4.1 Primary Ion Energy-per-charge to Gate Bias Ratio

The energy-per-charge to gate bias ratio was measured using the ionic liquid particle source, whose ion beam is approximately monoenergetic and equal to the applied needle voltage. Fig. 31 shows an example energy sweep with the typical large main peak at a beam energy to needle bias ratio close to 1 (indicating an appropriate choice of η). A number of energy sweeps were performed with each of the three ionic liquids Fig. 32 shows the distribution of the ratio the ionic liquid source's needle voltage to the energy gate voltage at which the main peak was observed. From this, the ratio of the energy-per-charge of particles that pass through the gate divided by the gate bias, η, is taken to be 3.2.

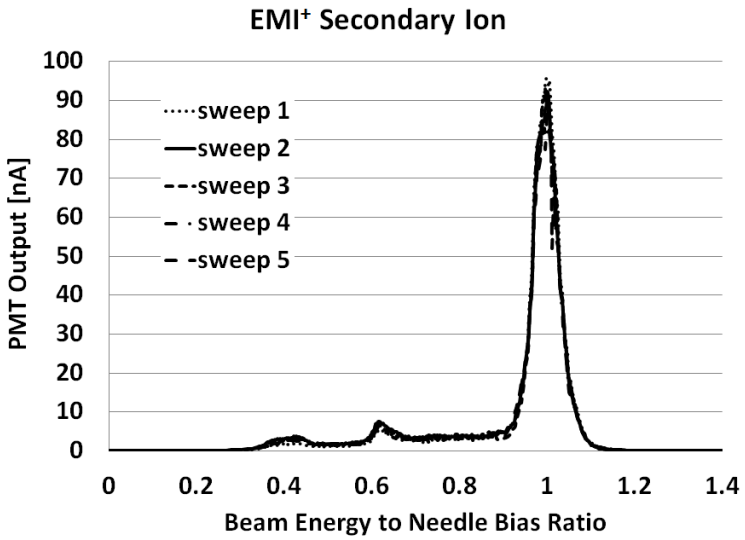

Fig. 31 Example Ionic Liquid Ion Source Energy Sweep

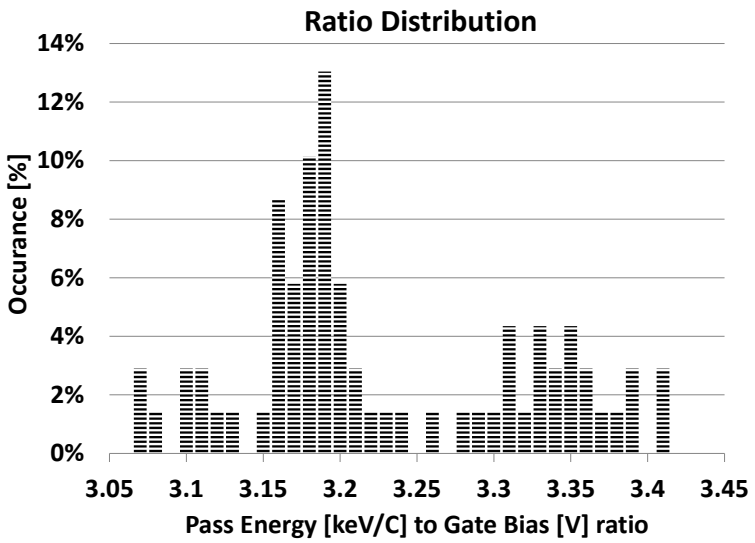

Fig. 32 Distribution of beam energy to gate voltage ratio

The ratio varied with species (see Fig. 33) possibly due to physically interacting with the stages when refreshing or changing ionic liquids (which would change the entry angle, thus the pass energy). In that case the earliest data should be the best because the spectrometer was most recently aligned to the stage position. It is unlikely to be an issue of consistency in identifying peaks because the beginning and end of each peak were also examined and showed the same trend. The difference is small, about 5%, and any error will be canceled by a corresponding error in the flight length estimate, so the correct species will still be identified. This is because the flight time (Eq. (12)) is dominated by t_{free}, where η and L_{free} appear together, and the value of L_{free} is estimated based on observations of Al^{+3} using the selected value of η (see pg. 98). Because the different values of η are suspected to be a result of changes in beam alignment, the mean of each group (circled in Fig. 33) was used to calculate its contribution to the standard deviation of the set. This gives an uncertainty of 0.9% for

η. If the mean across all the points is used instead, the standard deviation would be 2.9%.

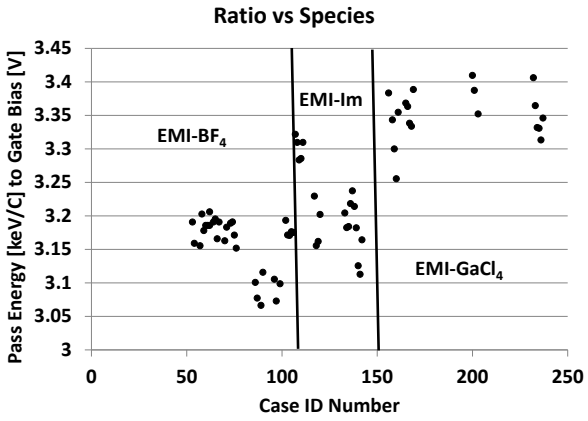

Fig. 33 Gate pass ratio vs. species

4.4.2 Variation of the Ratio with Entry Angle

The variation of η with entry angle was determined by moving the ionic liquid ion source and re-measuring the location of the main peak of the energy spectrum. Fig. 34 shows the ratio of pass energy to gate bias as a function of beam entry angle into the energy gates along the deflection axis. The fit is given by Eq. (23) where η is the ratio of pass energy to get bias and θ_y is the entry into the spectrometer angle in degrees. The percent change matches the results from the COMSOL simulation: about -11% per degree when the entry angle is near 0°. Since the fit is centered at 3.25 rather than 3.2, only the percent change should be used.

$$\eta = 0.04695\,\theta_y^{\,2} - 0.3653\,\theta_y + 3.250 \tag{23}$$

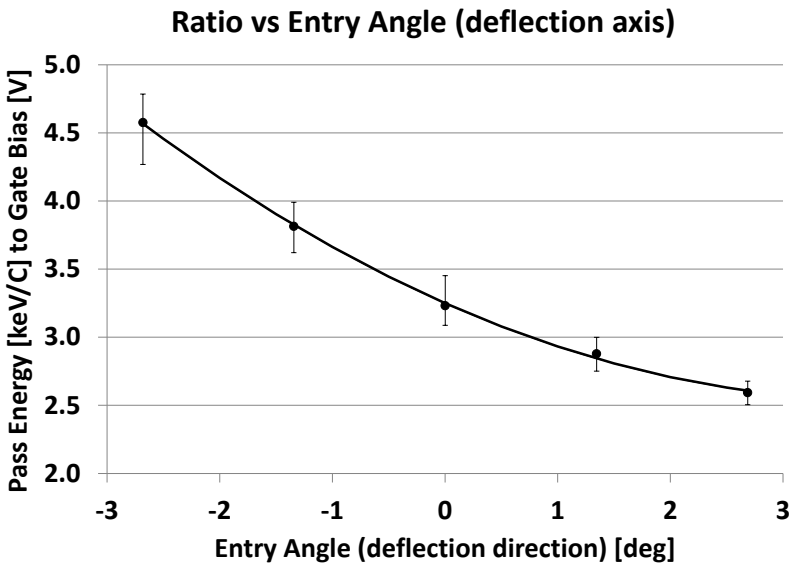

Fig. 34 Gate pass ratio vs. entry angle (parallel to deflection)

Fig. 35 shows the ratio of beam energy to gate voltage as a function of beam entry angle into the energy gates along the non-deflection axis. As expected, there is no effect on the gate pass ratio from an entry angle perpendicular to the deflection direction. Although the gate pass ratio is unaffected, the amount of material passing may still be affected.

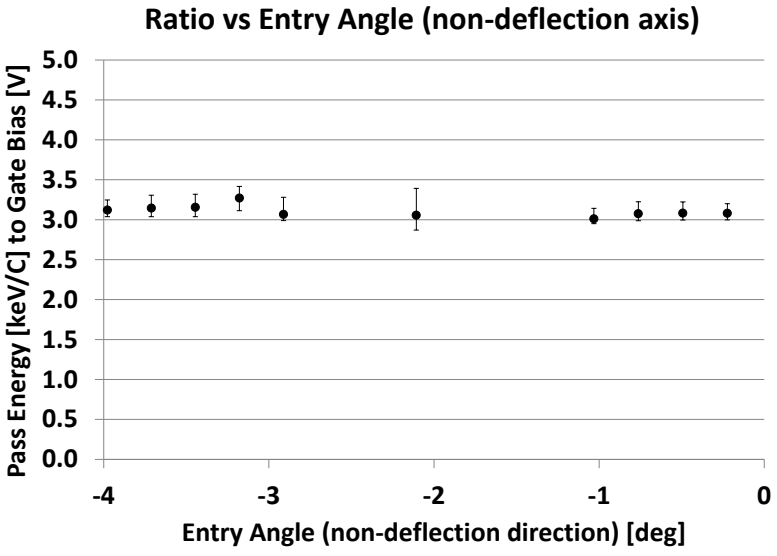

Fig. 35 Gate pass ratio vs. entry angle (perpendicular to deflection)

4.4.3 Variation of the Ratio with Flight Length

The ionic liquid ion source was also moved along the spectrometer's longitudinal axis to observe any change in η from flight length variation. Fig. 36 shows the ratio of beam energy to gate voltage as a function of flight length. Peak height would be an appropriate parameter to quantify space charge effects; however, the beam produced by the ionic liquid is often emitted at an angle relative to the needle. Because of that, moving the ion source relative to the spectrometer aperture will change the current hitting the aperture in a way that is not possible to account. It is, therefore, not meaningful to compare the relative signal heights at different ion source locations.

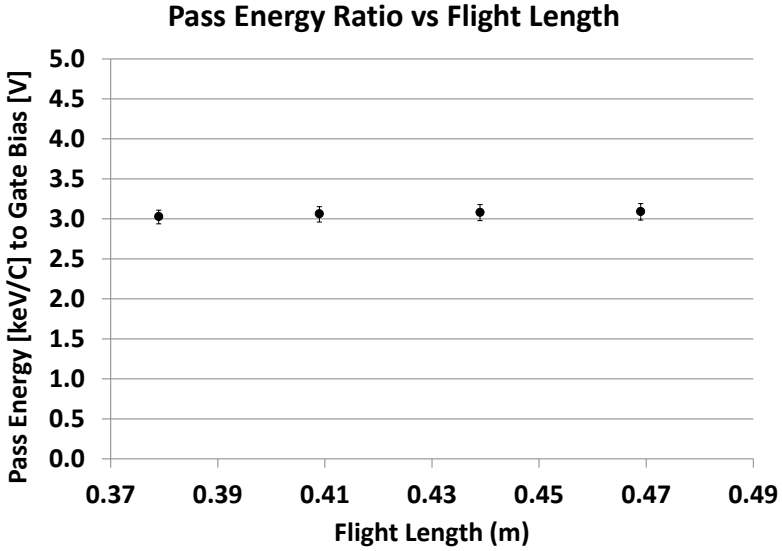

Fig. 36 Gate pass ratio vs. flight length

4.4.4 Energy Passband Width

The finite width of the energy gate apertures allows a small range of primary ion energies, the energy passband, to pass the energy gates for a give gate bias. Because the ionic liquid ion source beam is approximately monoenergetic, the width of the main peak in its energy spectrum (Fig. 31) provides an estimate of the width of

the energy gate passband. A Gaussian distribution was fitted to the main peaks of two ionic liquid energy spectra, giving passband widths of 3.0% (Fig. 37) and 3.3% (Fig. 38).

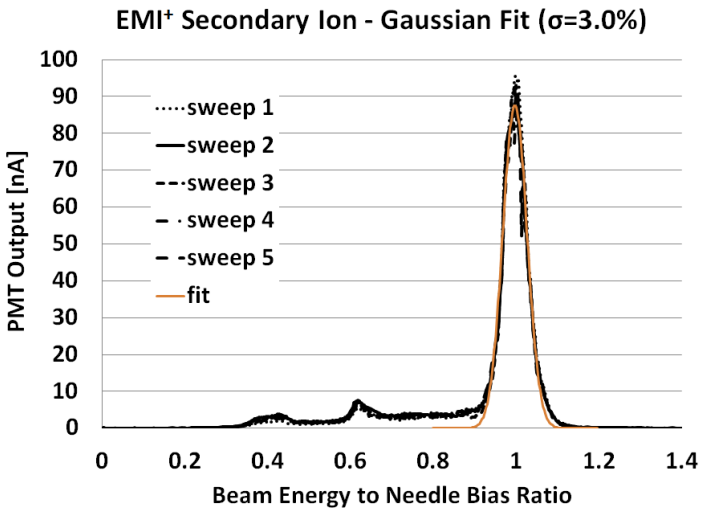

Fig. 37 Gaussian Fit to Energy Sweep Main Peak 1

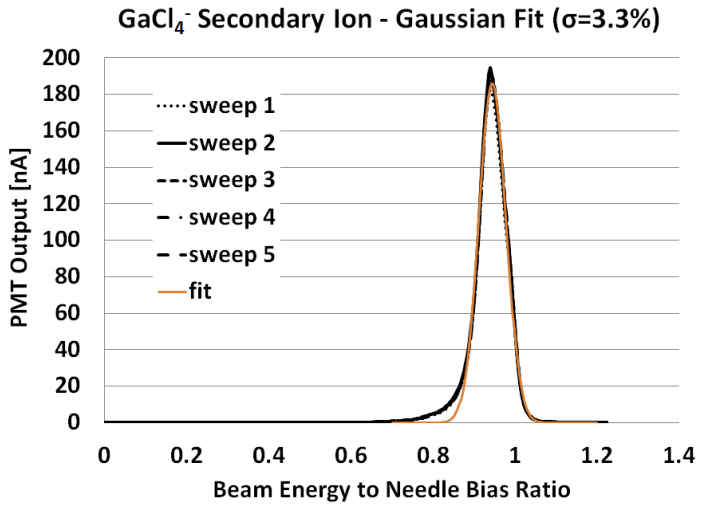

Fig. 38 Gaussian Fit to Energy Sweep Main Peak 2

For ablation data, the energy passband translates to a minimum width of the time-of-flight signal. As with estimating the flight length, only Al^{+3} data is used because the time-of-flight signal was more consistent and more often well fit by a

single Gaussian pulse (Eq. (26)) than the signal for Al^{+1} or Al^{+2}. Fig. 39 shows the distribution of the standard deviations of Al^{+3} time-of-flight data fit by single Gaussian pulses using Eq. (28). The chart is zoomed onto the peak of the distribution and so covers 87% of the processed cases. From Fig. 39 it is apparent that the energy passband results in a time-of-flight spread of 1.65%. Applying the t_{free} equation from Eq. (12), it is clear that a differential change in energy is twice that for time-of-flight, so then energy passband width is 3.3%. Combining the energy passband width and the 0.9% uncertainty of the mean pass energy (the uncertainty in η), the overall energy-per-charge uncertainty is 3.4%.

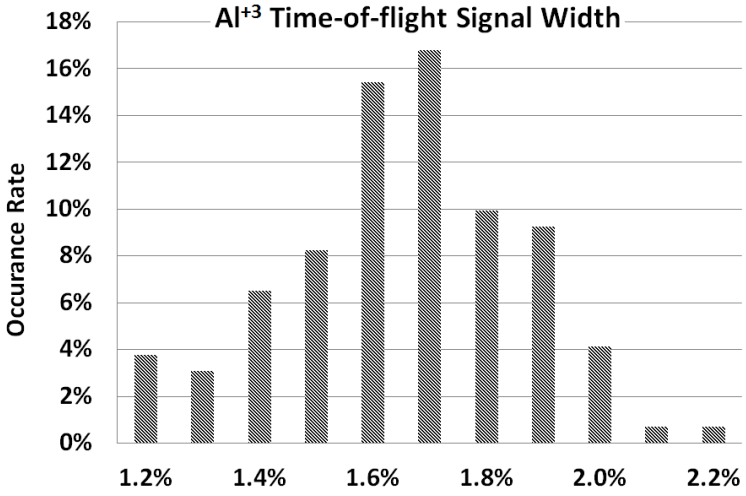

Fig. 39 Preliminary species occurrence rate

4.5 PMT Output Parasitic Capacitance

The signal strength resulting from a single or group of primary ions is a function of the readout resistor and parasitic capacitance. The selected readout resistor was measured to be 2.505 kΩ, which is enough to swamp any parasitic resistance. The readout resistor is useful for increasing the signal height when

observing continuous signals. For single ion impacts, the readout resistor slows the decay of the signal pulse allowing it to be more easily separated from noise. Particularly for single particle hits, the parasitic capacitance dictates the readout voltage. The capacitance was estimated using moderately sized shot noise observations from the PMT and confirmed using ablation data and individual particle hits from the ionic liquid source. This section focuses on processing the shot noise signals. Ablation data and ionic liquid source processing are discussed elsewhere. Fig. 40 shows one of the cleaner shot noise signals.

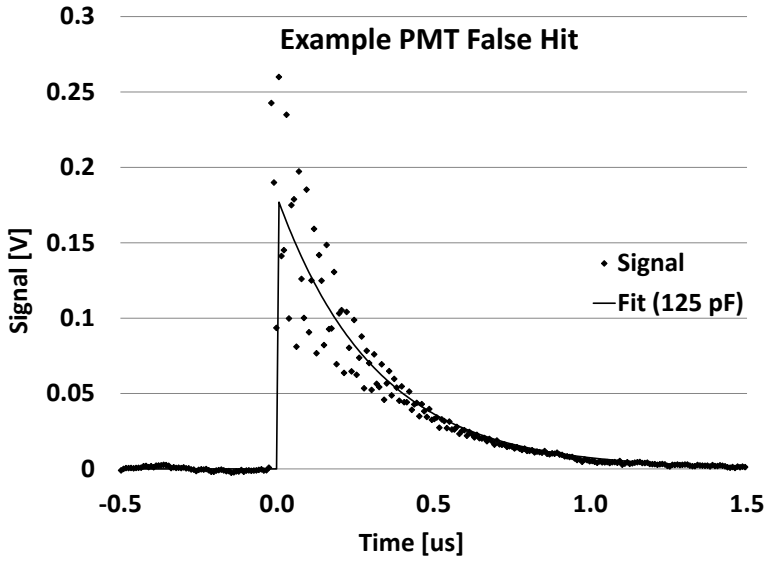

Fig. 40 PMT false hit example

A least squares fit was applied individually to 40 shot noise observations to determine the decay constant of each. The fits were plotted and visually assessed to determine if the resulting exponential decay appropriately fit the data. This was necessary because noise would occasionally distort the fit, but smoothing to avoid the noise would distort the impulse response. Out of 40 fits, 31 were deemed successful. The exponential decay constant was divided by the read-out resistance to yield a

capacitance. The distribution of capacitances (rounded to nearest 0.05 pF) is plotted in Fig. 41, suggesting a parasitic capacitance of 125 pF.

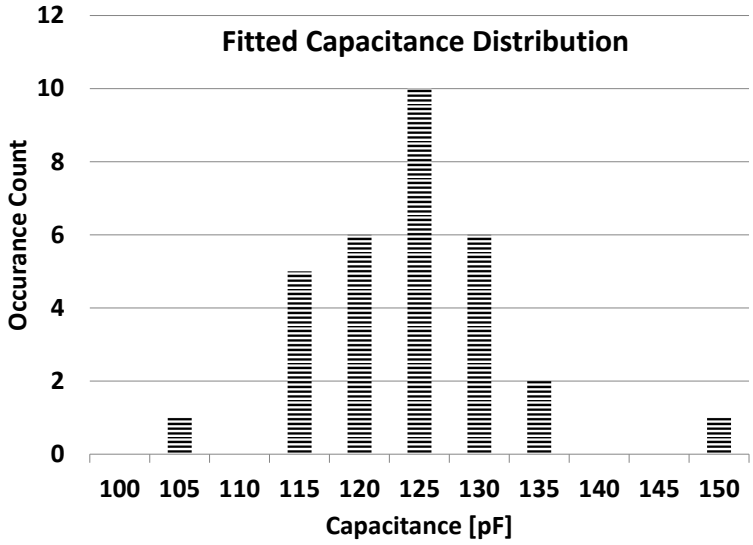

Fig. 41 Readout capacitance distribution

An exponential decay using the selected value (125 pF) was plotted and visually assessed against all 40 observations. Of those cases, 31 were successful, 5 were unsuccessful, and 4 were questionable, confirming that 125 pF is a reasonable value.

With the parasitic capacitance and readout resistance known, the RC distortion may be removed to reveal the input signal using Eq. (24), where R is the readout resistance and C is the readout parasitic capacitance. Significant noise reduction is required because removal of the RC distortion amplifies any noise present.

$$I_{in} = \frac{V_{RC}}{R} + C\frac{dV_{RC}}{dt} \tag{24}$$

4.6 PMT Readout Resistor Selection

The PMT output is read across a 2.505 kΩ resistor. The resistor was selected to balance signal-to-noise ratio against RC distortion. Fig. 42, Fig. 43, and Fig. 44 show sample data collected with different resistor values. While too much RC distortion makes it impossible to distinguish the arrival of different species, the characteristic signal decay from a small amount of RC distortion makes it easier to distinguish small impulses in the signal from background noise.

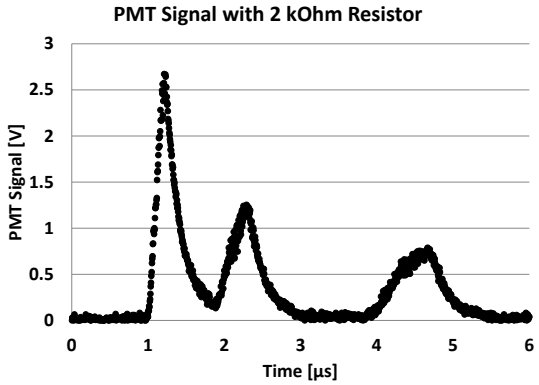

Fig. 42 PMT readout across 2 kΩ

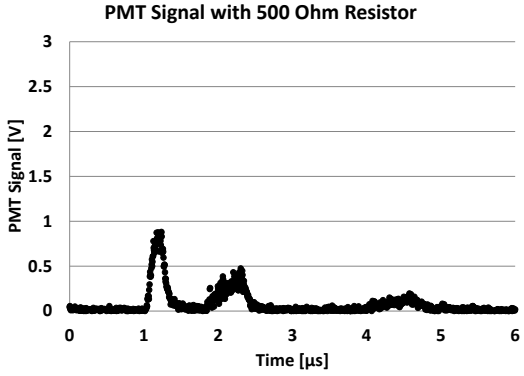

Fig. 43 PMT readout across 500 Ω

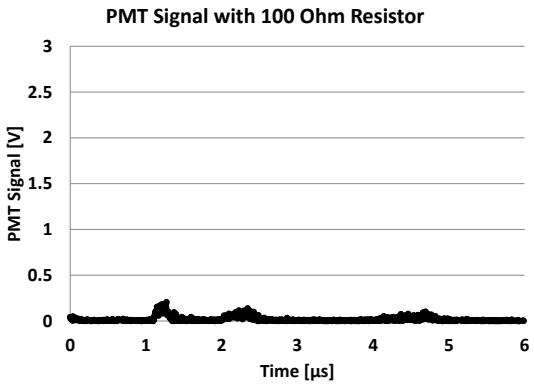

Fig. 44 PMT readout across 100 V

4.7 Aperture Current and RPA Signal Fitting (ablation only)

The current arriving at the mass spectrometer entry aperture was monitored for both the laser ablation and the ionic liquid particle sources. For the ionic liquid source, the aperture current was continuous, measured with a transimpedance amplifier. For ablation, the aperture current was short lived and so recorded by the same oscilloscope as the PMT output. A typical aperture current signal from ablation is shown in Fig. 45 with the fit in red.

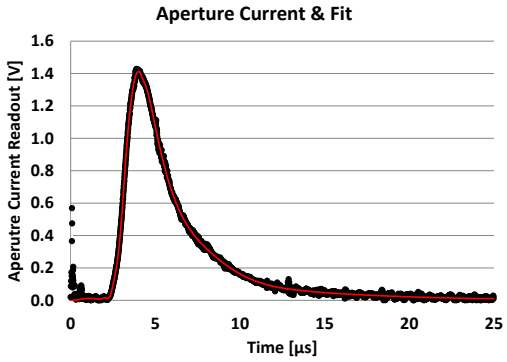

Fig. 45 Aperture Current Signal

The aperture current signal was fit by a piece-wise function of fourth degree polynomials (Eq. (25)). The boundary times, t_i, between polynomials were manually

selected. The constant, first, and second derivatives were constrained to match starting and ending polynomials at each boundary time.

$$\begin{aligned} & a_i(t-t_i)^4 + b_i(t-t_i)^3 + c_i(t-t_i)^2 + d_i(t-t_i) + e_i \\ e_i &= a_{i-1}(t_i - t_{i-1})^4 + b_{i-1}(t_i - t_{i-1})^3 + c_{i-1}(t_i - t_{i-1})^2 + d_{i-1}(t_i - t_{i-1}) + e_{i-1} \\ d_i &= 4a_{i-1}(t_i - t_{i-1})^3 + 3b_{i-1}(t_i - t_{i-1})^2 + 2c_{i-1}(t_i - t_{i-1}) + d_{i-1} \\ c_i &= 12a_{i-1}(t_i - t_{i-1})^2 + 6b_{i-1}(t_i - t_{i-1}) + 2c_{i-1} \end{aligned} \tag{25}$$

Once a fit of the original signal has been obtained, the RC distortion may be removed to reveal the input signal using Eq. (24). Fitting the raw data in this way serves to remove almost all noise from the signal without sacrificing the fast components of the signal.

4.8 Aperture Current and RPA Parasitic Capacitance (ablation only)

The current arriving at the mass spectrometer entry aperture was monitored for both the laser ablation and the ionic liquid particle sources. For the ionic liquid source, the aperture current was continuous, so the following section is only relevant to the ablation source. The parasitic capacitance of the aperture current and RPA current readouts were determined by the same technique and so are reported here together.

The current signals were distorted by the parasitic RC properties of their readout circuits. The nominal readout resistance was 2.497 kΩ for the aperture current and 2.505 kΩ for the RPA. There are no impulse signals available from the aperture or RPA currents, as there were for the photomultiplier output. Instead, the capacitance may be deduced by deconvolving the signals as observed with different

resistors – only when the correct capacitance is selected will the deconvolved signals line up. Deconvolution is performed by fitting polynomials (Eq. (25)) to smooth the data then applying Eq. (24). Fig. 46 shows the aperture current observed with various resistors under the assumption of no parasitic capacitance and with the best fitting capacitance, 130 pF. Fig. 47 shows the same thing for the RPA with two resistors. The best capacitance was 180 pF, which produced an acceptable match of shape but did not exactly match the height.

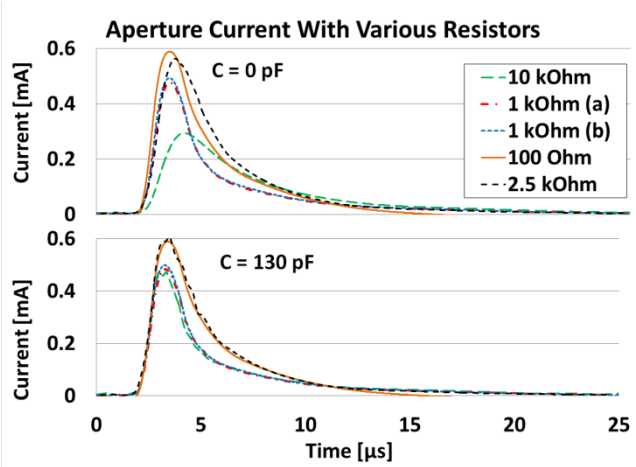

Fig. 46 Deconvolved Aperture Current with Various Resistors

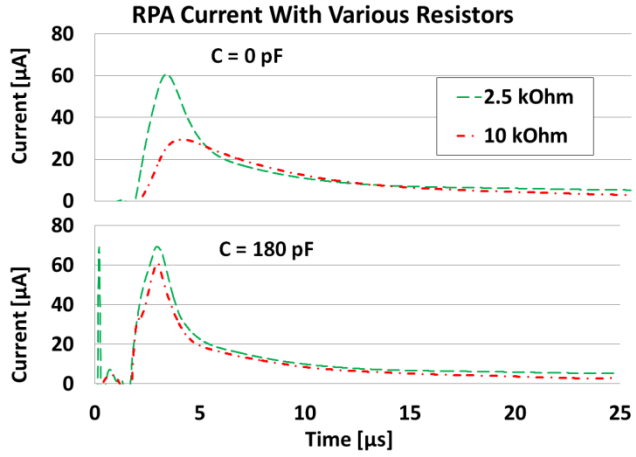

Fig. 47 Deconvolved RPA Current with Two Resistors

4.9 Ablation Data Processing

When the PMT output signal is continuous, as is generally the case when using the ablation particle source, the input signal is distorted by the RC circuit formed from the readout resistor (R) and parasitic capacitance (C). Because the pass band of the spectrometer is Gaussian, the input to the RC circuit (undistorted output of the PMT) was modeled as a sum of N Gaussian pulses, Eq. (26), where a, b, and c are to be fit. A combination of fast rise times and noise in the raw PMT signal made it impractical to simply smooth the raw signal, as sufficient smoothing to remove all noise would hide the fast rise times and any noise would be amplified by the process of removing the RC distortion. Rather than smooth and deconvolve the noisy output data, an RC circuit model was applied to produce a direct model of the output, the differential Eq. (27), whose solution is Eq. (28).

$$I_{in} = \sum_{i=1}^{N} a_i \exp\left(-\frac{(t-b_i)^2}{2c_i^{\,2}}\right) \tag{26}$$

$$\frac{\partial Q(t)}{\partial t} = -\frac{Q(t)}{RC} + \sum_{i=1}^{N} a_i \exp\left(-\frac{(t-b_i)^2}{2c_i^{\,2}}\right) \tag{27}$$

$$\begin{aligned} V(t) &= V_0 \exp\left(-\frac{(t-t_0)}{RC}\right) + \\ &\exp\left(-\frac{t}{RC}\right)\sum_{i=1}^{N}\sqrt{\frac{\pi}{2}}\frac{a_i c_i}{C}\exp\left(\frac{2RCb_i + c_i^{\,2}}{2R^2C^2}\right)\left[\operatorname{erf}\left(\frac{RC(b_i - t_0) + c_i^{\,2}}{\sqrt{2}c_i RC}\right) - \operatorname{erf}\left(\frac{RC(b_i - t) + c_i^{\,2}}{\sqrt{2}c_i RC}\right)\right] \end{aligned} \tag{28}$$

The parameters a, b, and c for N pulses, plus a constant background, were adjusted to fit the model to the actual output. Because the gate system is electrostatic, the standard-deviation for all the pulses should be the same fraction of their center arrival time. A second fitting option used the same model, but derived c for each

pulse from *b* for that pulse using a solved-for proportionality constant shared among all pulses. The second option was most useful where outliers would cause a poor fit while the first option was best when pulses significantly overlapped. Fig. 48 shows an example of fitting with *c* proportional to *b*, collected at 750 eV/e^-.

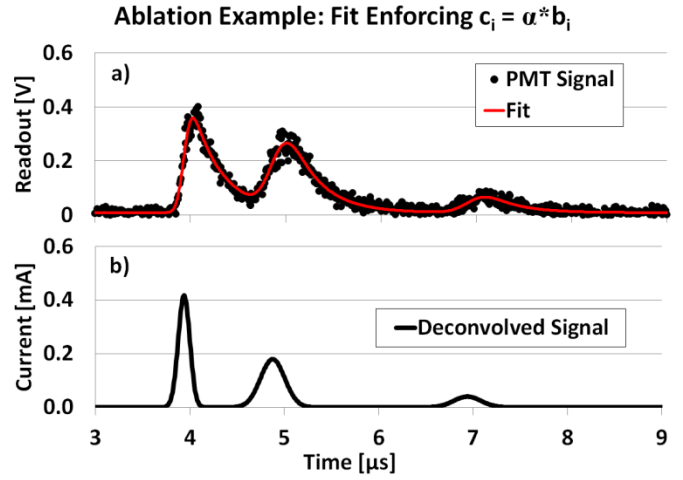

Fig. 48 Example of Signal Fitting (a) and Deconvolution (b)

Multiple Gaussian pulses of varying widths were sometimes needed to correctly fit the PMT signal shape even through the individual charge states are still clearly visible, as illustrated in Fig. 49.

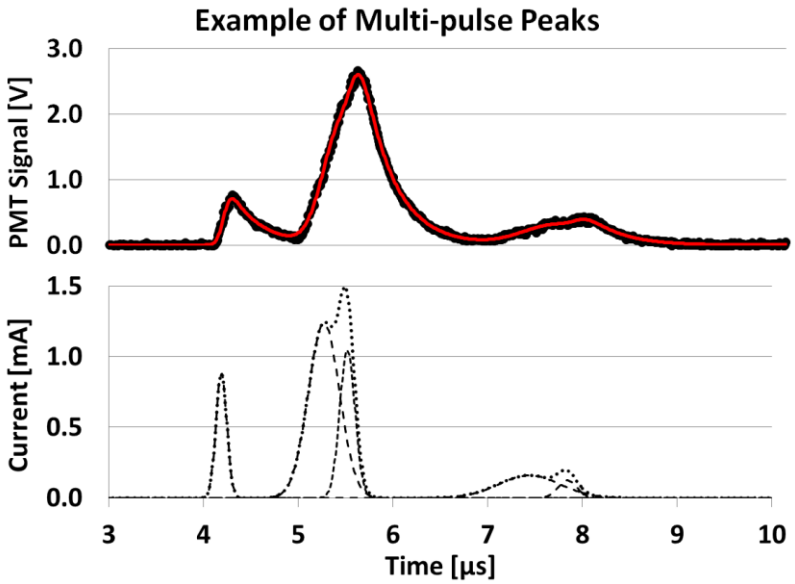

Fig. 49 A fit showing individual Gaussian pulses

Extra pulses were often required for Al^{+1} and Al^{+2}, but almost never for Al^{+3}. The Al^{+3} pulse, and the Al^{+1} and Al^{+2} pulses (when only one Gaussian is needed to fit the signal), have a width in line with the passband estimated via COMSOL. Based on their location, shape, and repeatability, it is believed that the extra pulses mostly reflect a non-ideal but consistent distribution of aluminum in the ablation plume rather than the significant presence of another species or readout noise. The distribution could result from a sufficiently lengthy ablation event, emitting the lower charge states over a longer time. Fig. 50 shows a case (captured at 720 eV/e^-) where there are two Al^{+1} peaks, at nominal masses of 25 (-7%) and 29 (+8%) amu.

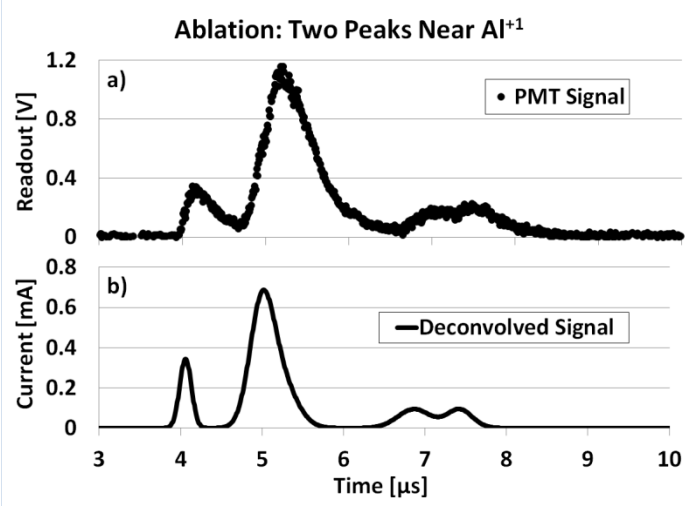

Fig. 50 Ablation w/ Double "Al^{+1}" Peak

At lower energies, the signals get closer together and arrive earlier than expected. This distortion first becomes noticeable around 400 V. Fig. 51 shows an example of this (captured at 320 eV/e^-). The individual peaks are visible in the deconvolved data, corresponding to aluminum with 1 to 5 charges. The significant width of the Al^{+1} (10 µs) peak is likely due to being only slightly above the background – because the peak is low, the fitting Gaussian can spread out to make a net subtraction from the background without taking a hit for missing the peak.

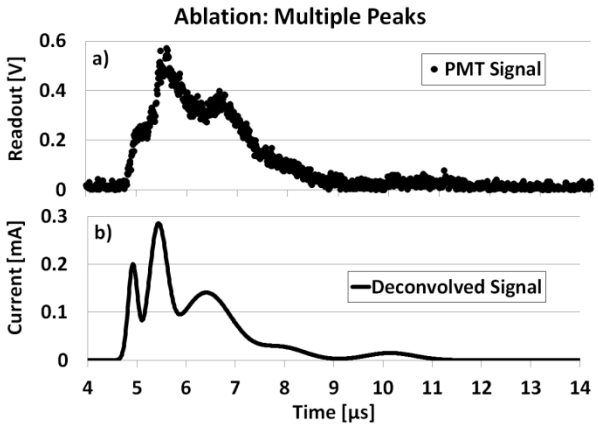

Fig. 51 Ablation w/ Multiple Overlapping Peaks

In a plot of the processed PMT signal across a range of energies (for example: Fig. 52), one can follow the low charge states' signal peaks as they get earlier at lower energies, eventually arriving at times expected of higher charge states. The highest reliably-identifiable charge state is Al^{+4}. The lowest energy with no apparent shift was 480 eV/e^-. The charge states must be identified in order to calculate the impact kinetic energy at the detector, and therefore the actual quantities present. Since the signals get close together, an average charge state will have to suffice. The original energy of these particles is less important, as they make up a small portion of the total plume and, with their low energy, don't add appreciably to the thrust.

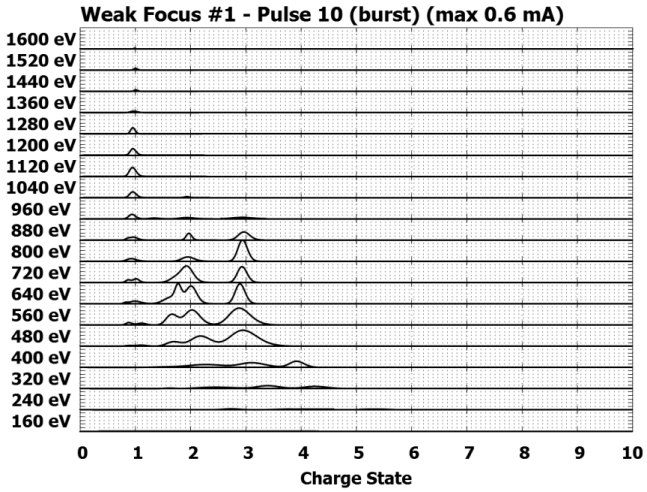

Fig. 52 Sweep summary plot example

Finally, Fig. 53 shows an example of cluster ion impacts (captured at 640 eV/e^-). The Al_3^{+1} peak is sharp enough that it could be a single impact, but that is unlikely to be the case given that Al_2^{+1} is also visible and, despite being at a higher velocity, produces a smooth and significantly smaller peak. It could be a false hit from the PMT, but the presence of other clusters (unlike most other cases), the precise timing, and the lack of comparable false hits in any other results suggest otherwise.

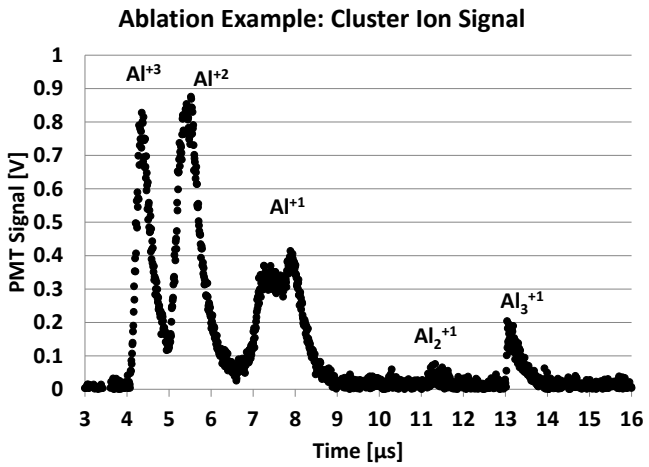

Fig. 53 Example of Cluster Ion Signal

4.10 Single Particle Impact Processing

Individual particle impacts ideally appear as an instantaneous step in the PMT signal, which then exponentially decays through the readout RC circuit. Data were scanned for single particle impacts by taking the cross-correlation of the PMT output signal with the exponential decay of an RC circuit, normalized so that the peak of the signal corresponds to the height of the PMT output, Eq. (29). All the available data were scanned for instances when the correlation exceeded 30 mV, flagging such cases for manual review.

$$corr(\tau) = \int_{\tau}^{+\infty} \left[\left(\frac{2}{RC} \exp\left(\frac{-(t-\tau)}{RC} \right) \right) signal\,(t) \right] dt$$

$$signal(t) = noise\,(t) + \sum_{i} \left[A_i \exp\left(\frac{-(t-t_i)}{RC} \right) Heavyside\,(t-t_i) \right] \tag{29}$$

Hits are distinguishable from noise by the sharp peaks produced in the correlation output. If the correct RC constant is used, the cross-correlation of real impact signals will be symmetric about the peak. Fig. 54 shows a typical single

particle impact, captured near the peak energy of the negative beam component of ionic liquid EMI-$GaCl_4$.

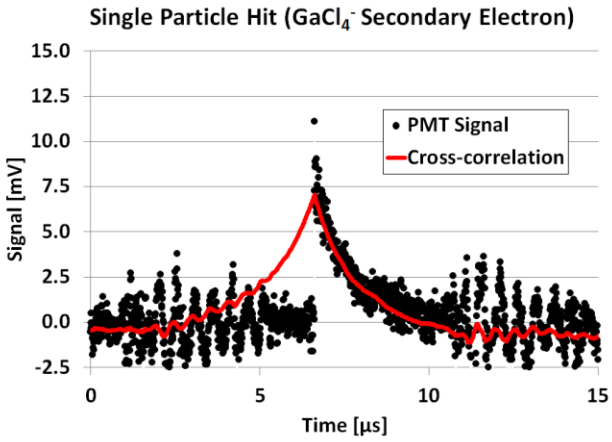

Fig. 54 Example ablation single particle hit

4.11 Time-of-flight Length

The flight length is divided into 4 regions whose lengths must be determined. The energy gate (L_{gate}), accelerator (L_{accel}), and detector (L_{det}) lengths were designed and controlled by the 3-D printed structure on which the spectrometer is assembled. Their uncertainty is negligible compared to the remaining segment. The length of the pre-spectrometer region from the ablation site to the spectrometer entry (L_{pre}) was measured directly (with measuring tape and caliper) as 0.282 m with an uncertainty on the order of a centimeter. The uncertainty was mostly due to the measurement being physically awkward. The pre-spectrometer and energy gate lengths are combined into L_{free} and reported along with L_{accel} and L_{det} in Table 2.

Fitting of the ablation signals and removal of the RC distortion do not require knowledge of the flight length, so the arrival times of all observed signal peaks were determined before the flight length was confirmed. Given the ratio of pass energy-

per-charge to gate voltage determined via the ionic liquid source and the assumption of single, double, and triple charged aluminum in the ablation plume, the field-free length measurement may be confirmed based on the relative timing of the peaks in the deconvolved signal.

The species were identified by the product of gate bias and pulse time squared ($V_g t^2$), which is a constant for each species across all gate biases. This is a trivial rearrangement of Eq. (12) under the assumption that almost all of the time-of-flight is spent in the field-free or energy gate regions. Once a large portion of the ablation cases were processed, that quantity was calculated for each signal peak and the frequency of occurrence plotted, Fig. 55. Three peaks are clearly visible and at the correct ratios for Al^{+1}, Al^{+2}, and Al^{+3}. Possible reasons for the relatively few peaks away from the expected species are discussed in the ablation data processing section.

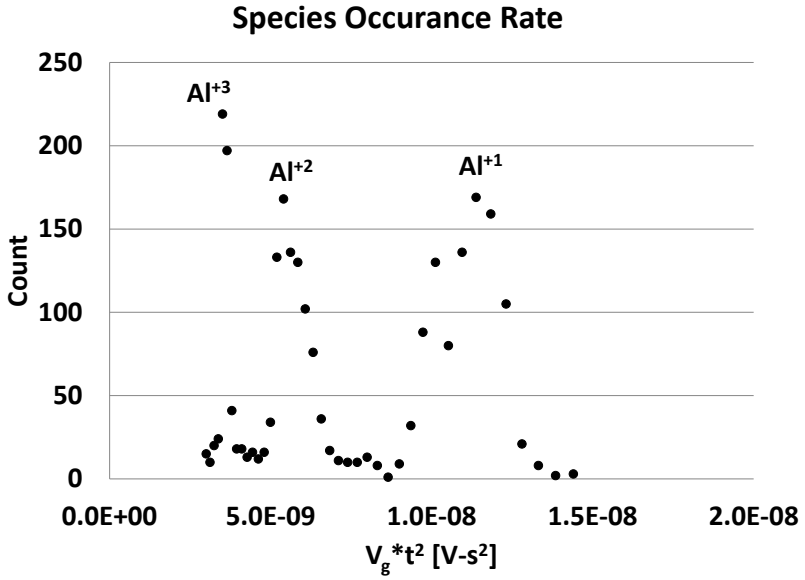

Fig. 55 Preliminary species occurrence rate

To determine the flight length, all Al^{+3} data taken with a gate bias of 200V, a detector bias of 5000V, and the scintillator grounded was used with Eq. (12) to solve

for the field-free length that best matches the known mass-to-charge-ratio of Al^{+3}. These bias settings were selected because they were by far the most common among the collected data. Al^{+3} was used exclusively because it was the cleanest peak in the PMT signal, while Al^{+2} and Al^{+1} were frequently split into smaller, neighboring peaks (e.g. Fig. 50), as the widths of the three peaks in Fig. 55 suggest. The resulting flight length of 0.269 m is slightly lower than the measured value of 0.282 m, but not unreasonably so given the difficulty of measurement and possible influence of error in η. The discrepancy in the overall pre-acceleration flight length, L_{free}, is -2.7%. The distribution of times-of-flight errors based on the fitted flight length are shown in Fig. 56 for all 3 species and for just Al^{+3}, using the same bias settings as the flight length calculation. Based on the standard deviation of the residuals from fitting the Al^{+3} flight times, the uncertainty in flight length is 0.8%. Since the flight length was fit to actual data for a known mass-to-charge ratio and used the chosen value of the pass energy-to-gate-bias ratio, the flight length uncertainty is also a measure of the uncertainty in mass-to-charge ratio. Based on the t_{free} term from Eq. (12), the mass-to-charge uncertainty is twice the length uncertainty: 1.6%. When the primary ions have discrete mass-to-charge ratios, the uncertainty in mass-to-charge ratio is effectively zero. Because the flight length was chosen to give the correct mass-to-charge ratio, the velocity uncertainty is based on Eq. (12) given the mass-to-charge ratio uncertainty, 1.6%, and the energy-per-charge uncertainty (pg. 83). The velocity uncertainty is estimated to be 1.9%.

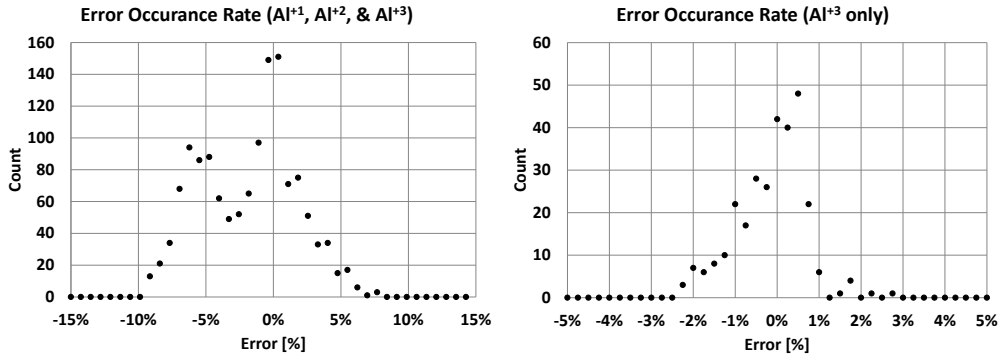

Fig. 56 Time-of-flight errors using solved flight length

4.12 Signal vs System Biases

There are three critical settings within the particle detecting component of the mass spectrometer which affect the strength of the output signal: the detector bias, the scintillator bias, and the photomultiplier gain. The detector bias and scintillator bias were recorded directly for every case, while the photomultiplier gain is determined for each case based on a control voltage provided to its power supply and the conversion in its documentation. Since each parameter is manually dialed in at least every time the system is powered up, it is necessary to assess the impact of minor differences in settings and correct for sufficiently large differences if present. The detector bias determines the primary particles' impact energy in combination with their inherent energy, as measured/selected by the spectrometer's energy gate. A change in detector bias has the same effect on secondary particle yield in the detector as does a difference in primary particle pre-acceleration energy, so the variation of the signal with detector bias also enables comparison across different primary particle energies. If the effect of potential energy is ignored, this is also sufficient to compare across different charge states.

No significant secondary ion signal nor any negative beam signal were visible for any laser ablation case, therefore no scaling of the secondary ion signal or

negative beam signal vs system biases will be required. Similar data were collected for the ionic liquid particle source. However, as discussed in the ionic liquid section, the output was sufficiently inconsistent to make the data unsuitable for this use.

For the high laser focus data collection the detector bias was set to -4.86 kV. For all other cases, except those specifically involving a detector bias change, the detector bias was set to -5.00 kV. The case to case variation of the biases was negligible. For all cases with clear signal, the scintillator bias was grounded so the secondary particle energy is dictated by the detector bias. The photomultiplier gain setting was consistent within 0.2%, corresponding to a gain change of 3%.

4.12.1 Detector Bias

Fig. 57 shows the change in photomultiplier signal with changing primary particle energy (changing the detector bias), with an energy gate bias of -200V. The data were collected on two separate days, represented by "grp1" and "grp2" in the legend, for laser pulse #10 through pulse #15. Each species each day was normalized by the mean of the highest energy case for that species for that day. The full dataset for Al^{+1} is reasonably well fit by Eq. (30), where x is kinetic energy in keV. Al^{+2} and Al^{+3}, on the other hand, appear roughly constant across most of the energies observed. Based on the rough similarity between all three species in the ranges they overlap, it is expected that the Al^{+1} will also be constant, starting right about the highest energies at which it was observed, which is where Al^{+2} and Al^{+3} also reach 1.

$$\frac{S_{Al^{+1}}}{S_{Al^{+1}@5keV}} = 0.4122\ln(x) + 0.2499 \tag{30}$$

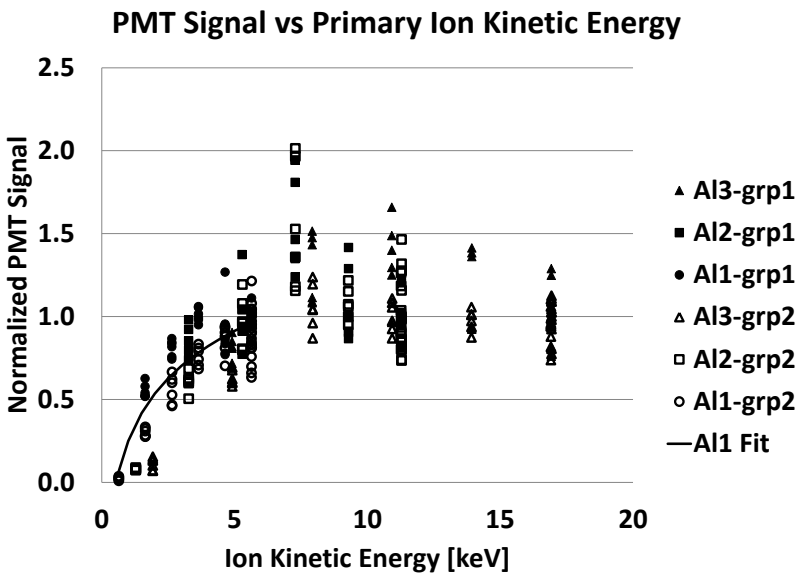

Fig. 57 Signal vs Primary Particle Energy

Fig. 58 shows the percent change in signal vs kinetic energy based on the mean value of laser pulses 10-15 for each kinetic energy. All three species together are reasonably well fit by Eq. (31), where x is the kinetic energy in keV and S is the signal.

$$\frac{\Delta S}{S\Delta x} = 2.1636x^{-1.5209} - 0.0803 \tag{31}$$

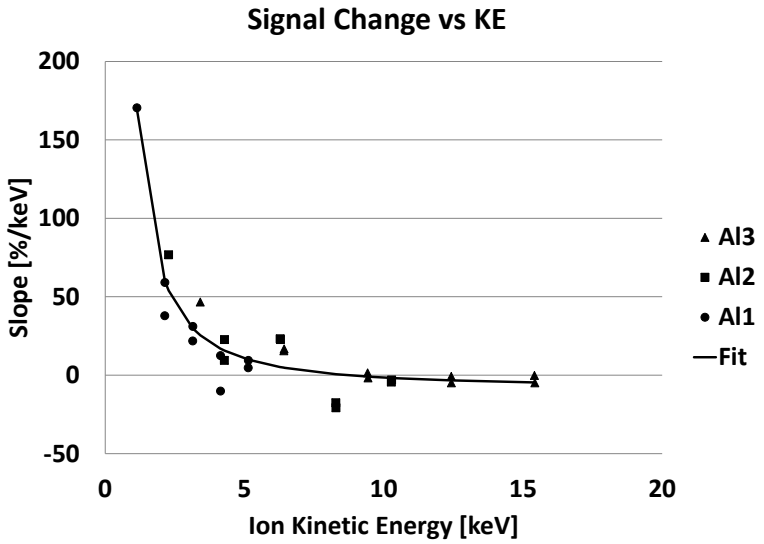

Fig. 58 Signal Change vs. Kinetic Energy with Fit

The signal is approximately constant starting shortly above 5 keV, based on Fig. 57, so no corrections should be applied for Al^{+2} or Al^{+3}. A correction will be applied for Al^{+1} and clusters using the reciprocal of Eq. (30), with *x* being the kinetic energy of a single A^{+1} atom at the same velocity as the cluster and limiting the correction to a minimum of 1.0. As the next section will show, typical variation of the signal is on the order of 20%, so corrections close to 5.6 keV become negligible.

The closest comparison in literature is [151], which reported an average yield of 2.5 electrons/ion for a combination of Al^{+1}, Al^{+2}, and Al^{+3} at 5kV acceleration, with a slow increase up to almost 5 electrons/ion at 55 kV acceleration. [151] also indicates the yield was correlated to ion kinetic energy with little influence by charge state, except to determine the impact energy from accelerating voltage. Combining all three species makes the result suitable only as an order of magnitude for a plume of different composition. Still, the slow climb vs acceleration bias is, at least in character, in line with the leveling of Fig. 57 and the assumption of a constant yield vs. impact energy in the energy range of ions observed in this work.

A similar energy range was available from [152] for Ar^{+1} impacting on aluminum between 1.5 and 3 keV. The data for 1.5-3 keV from [152] and for 1.6 to 3.6 from this work were normalized by the signal at 2.5 keV and fitted to compare slopes. The slope from [152] was 0.175 while the slope from this work was 0.338, about double.

4.12.2 Scintillator Bias

Fig. 59 shows the signal variation with the magnitude of the scintillator bias relative to the detector (in kV) or, equivalently, secondary electron impact energy (in keV) onto the scintillator. The results are well approximated by Eq. (32), where x is the relative bias in kV. Using this, a correction factor of 1.07 will be applied to all high focus data where the scintillator bias was 4.86kV compared to 5.00 kV for all other cases. All of the other cases would need a correction of less than 1%, so none will be applied. The variation of scintillator output with secondary electron energy is nominally linear above a material dependent threshold [140]. Although the relative scale here does not indicate a specific photon yield per secondary electron impact, that the relationship is quadratic indicates the yield will be lower than that predicted by the high energy proportionality factor given in the datasheet, less than 10,000 ph/MeV.

$$\frac{S}{S_{5kV}} = 0.0586x^2 - 0.0857x - 0.0368 \tag{32}$$

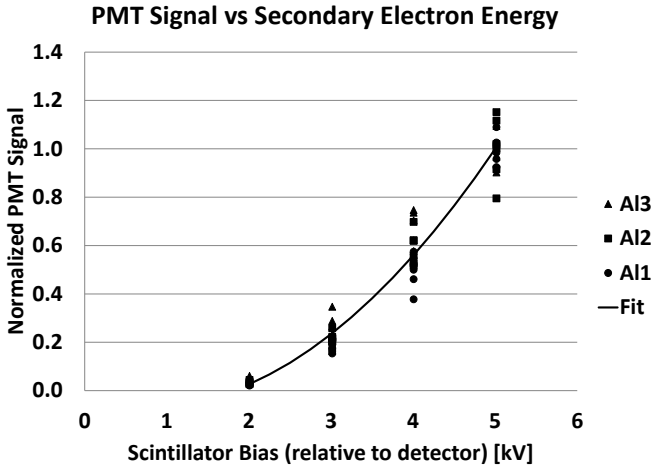

Fig. 59 Signal vs Secondary Electron Energy

4.12.3 Photomultiplier Gain

Fig. 60 shows the effect of photomultiplier gain setting on its output, normalized for Al^{+1} and Al^{+3} by their signal at maximum gain (about $2x10^6$). The Al^{+2} data were normalized to match the second highest gain case with the Al^{+1} and Al^{+3} data. This caused the two lower gain Al^{+2} cases to also line up. The data (excluding Al^{+2} at maximum gain) are well fit by Eq. (33) where x is the gain and S is the signal.

$$\frac{S}{S_{2x10^6}} = 0.426 * \ln(x) - 5.15 \tag{33}$$

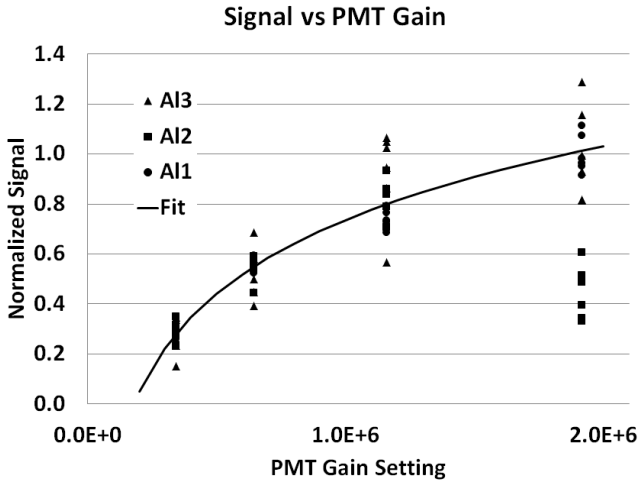

Fig. 60 Signal vs Photomultiplier Gain

The PMT gain is calculated from a control voltage based on the photomultiplier and power supply datasheets. A control voltage setting of 4 V nominally gives a gain of $2x10^6$. The signal should be linear vs gain, but clearly is not. Fortunately, the signal is linear vs the control voltage (though it should not be), following Eq. (34) where x is the control voltage in volts and S is the signal.

$$\frac{S}{S_{2x10^6}} = 1.01x - 2.98 \tag{34}$$

The PMT control voltage setting varies by about 0.8% over all case (except those varying it specifically). According to the datasheets this should produce an error of ±6%. Based on the results here, the expected error is ±0.4%.

An independent estimate of the PMT gain was performed based on the individual impacts observed using the ionic liquid particle source, at which time the PMT control voltage was set to 3.983 V, which is also the setting to which all the data in Fig. 60 is normalized. Given the low number of impacts observed relative to the expected rate, it was assumed that each observed hit represents a single photoelectron. The distribution of photomultiplier pulses was calculated in the same way as for the detector design, but beginning with a single photoelectron rather than a fixed secondary particle yield. The distribution was rescaled to remove any signals below 1 mV, the smallest hit detected and likely the lowest that could reasonably be detected. A readout parasitic capacitance of 125 pF was used to convert electron yields to readout voltage, the same as for all other data processing. Mean gains from 2.48×10^6 to 2.54×10^6 were able to fit the observed cumulative distribution. In both cases, the lowest signals (up to about 2.5 mV) were overrepresented in the simulated distribution, presumably because smaller signals are harder to identify. Based on these, the nominal gain at 3.98 V is estimated to be 2.51×10^6.

4.13 Spectrometer Signal Variability

From the plots in the previous section (signal vs system biases) it is clear that the magnitude of the photomultiplier output signal has significant variability for all ablation cases. Four sweeps in two pairs were run to assess this variability and consider any remediation, tracking the content of Al^{+1}, Al^{+2}, and Al^{+3} in each case.

The first pair repeated the same spectrometer configuration, a gate bias of -200 V, at many locations across the top and side of the target. These sweeps would show an error in target alignment as a systematic change in the signal from one end to the other. With any such systematic drift removed, the remainder represents the general variation in output of the ablation event. Fig. 61 shows signal vs. bottom stage position and Fig. 62 shows the signal vs the top stage position. Each plot also shows the stage position on its axis at which the other's sweep was performed. In order to compare the two plots, the signal magnitudes in both figures are normalized by the same quantities, the median value across both sweeps for each species (three total normalizing factors). At each stage position 190 laser pulses were applied. Pulses 10-15 are plotted here, and are the reason for multiple points for each species at each stage location.

In all cases except the second sweep of this pair, the ablation spot is moved (by moving the target) across the bottom stage in 1 mm steps then, upon reaching the end, the top stage increments 1 mm and the bottom stage begins 1mm steps again, now in the opposite direction.

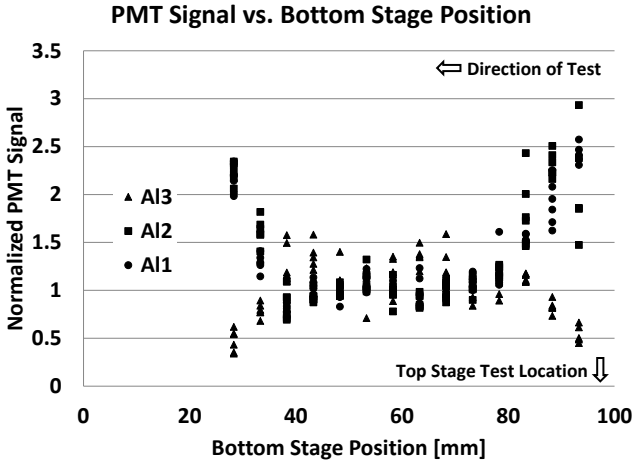

Fig. 61 PMT Signal vs Bottom (Horizontal) Stage Position

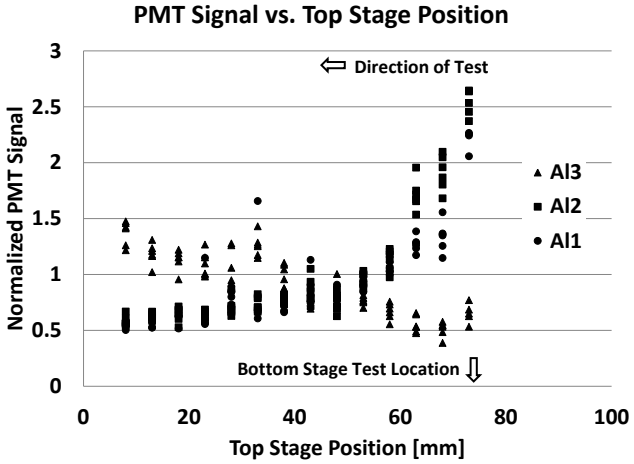

Fig. 62 PMT Signal vs Top (Vertical) Stage Position

Clearly both sweeps show a pattern, but are the patterns useful for applying corrections to other datasets? The bottom stage sweep was performed at a top stage position of 74 mm. The top stage plot suggests, therefore, that Al^{+1} and Al^{+2} should have a higher value than Al^{+3}. Although that is initially the case, the signals fall back to parity almost exactly as in the top stage sweep. Since the top stage sweep was performed at a bottom stage setting of 97 mm, the exact same discrepancy applies. The data for variation of the signal with primary kinetic energy from the previous section (Fig. 57) was taken from this region as well. Group 1 was taken at a top stage of 73 mm and bottom stage from 80-92 mm. Group 2 was taken at a top stage of 67 mm, with bottom stage from 57-66 mm. Both the top and bottom stage sweeps suggest that group 1 data should show relatively more Al^{+1} and Al^{+2} and less Al^{+3} compared to group 2. Fig. 57 demonstrates this is not the case, which suggests in turn that the patterns in Fig. 61 and Fig. 62 are not useful for rescaling data to account for stage position. The possibility of variations between ablation sites was anticipated and

is accounted for by repeating each sweep twice at two different (though generally close) locations. Although the direction of stage motion should make no difference, as the stages are stationary during the laser firing, the bottom stage alternates direction of motion. Any significant direction dependence should be visible by comparing appropriate gate bias cases between the repeated sweeps.

Fig. 61 and Fig. 62 both show the same pattern at the beginning of their sweeps. The variation vs kinetic energy data were collected in individual cases, separated by several seconds to a few minutes between laser firings, while the variation vs stage position data were collected in two sweeps, with just a couple seconds between laser firings. Both of these could suggest the variation is due to some build-up phenomenon which is able to dissipate only if cases are at least 10's of seconds apart. The aperture current recorded in both cases seems to suggest so as well. Fig. 63 shows the aperture current recorded for each of the first 25 pulses. The same pattern holds for all of the cases in the previous section (Fig. 57, Fig. 59, and Fig. 60) and for only the first laser firing in each of the two sweeps so far in this section (Fig. 61 and Fig. 62). Note that the 2^{nd} pulse produces the largest aperture current and that the 3^{rd} through 25^{th} are very consistent and smaller than both the 1^{st} and 2^{nd}. In the laser firing mode used for all these cases, it happens that the same is true of the laser pulses: the 2^{nd} is largest and the 3^{rd} through 25^{th} are very consistent and smaller than the 1^{st} and 2^{nd}.

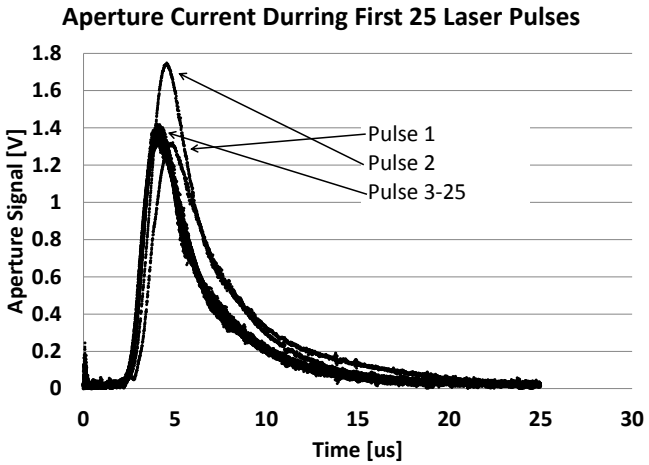

Fig. 63 Aperture Current For 1st 25 Laser Pulses

Fig. 64 shows the aperture current for every 5th laser firing from the full bottom stage sweep, the same cases that appear in Fig. 61. Note that, although the content of the ablation plume at the end of the sweep approximately matches the start of the sweep, the aperture current in both cases does not match. Most of the aperture current cases are reasonably consistent even as the spectrometer signal varies, suggesting the two phenomena have independent causes.

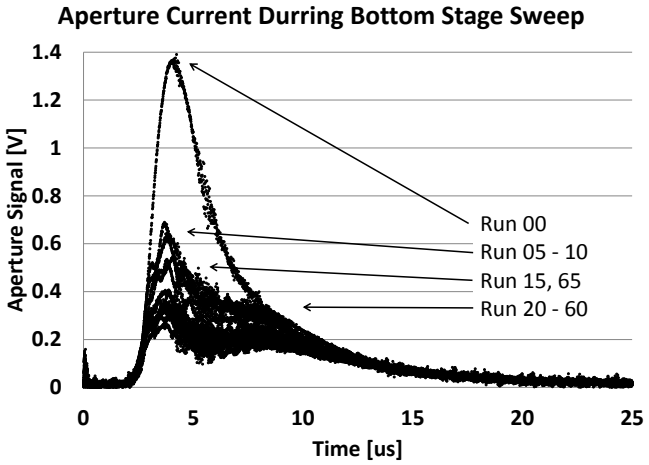

Fig. 64 Aperture Current During the Bottom Stage Sweep

The second pair of sweeps in this section tests whether the spectrometer signal has some dependence on the duration of a sweep. The first sweep of the pair ran from a gate bias of -50V to -350 V (forward, 141 laser firings). The second sweep started from the next ablation site (1 mm from the end of the previous sweep) at a gate bias of -350 V and ran to -50 V (reverse, 71 laser firings). Enough time elapsed between the two sweeps that the aperture current at the start of the second sweep matched that from the first sweep. The relative signals for Al^{+1}, Al^{+2}, and Al^{+3} were compared (Fig. 65) between the two sweeps at two gate biases, -325 V and -200 V, for laser pulses 1, 5, 10, 15, 20, and 25. The high magnitude end was used over the low magnitude end because the higher magnitude gate biases are easier and more reliable to process and the two cases used neighboring ablation sites, limiting location dependence. A gate bias of -200 V was chosen because it is close to the middle of the sweeps and generally has a clean signal. The sweeps are different lengths, so -200 V occurs after a different number of pulses, but a steady state, if one exists, should have been reached in each case.

The reverse case shows a slightly higher Al^{+1} content than the forward case at -350 V, though much less than Fig. 61 and Fig. 62 would predict if their structure were based on duration and the Al^{+2} signal is identical for most of the pulses. At -200 V, the Al^{+1} content matches, Al^{+2} is a bit different, and Al^{+3} is quite different.

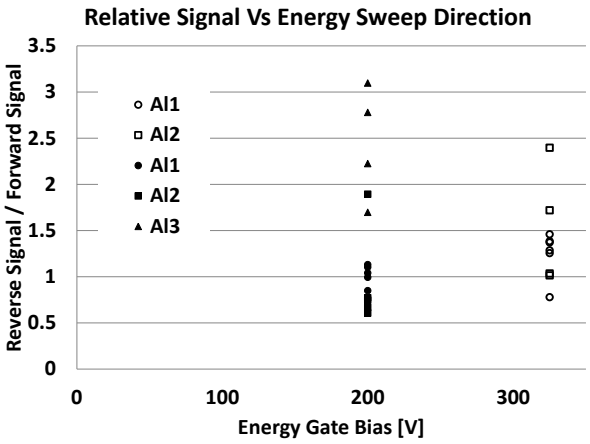

Fig. 65 Comparison of Energy Sweep Direction (effect of run duration)

Taking all four sweeps into account, there seems to be no actionable dependence of the spectrometer signal on target location or duration of sweep. The observations in Fig. 61 and Fig. 62 will be used to estimate the expected variance in all sweeps. The inconsistency may be due to minor variations in the target surface, slight alignment errors, or simply the nature of the ablation phenomenon. In either case, the issues are all likely to be unavoidable for a real laser ablation tug. Additionally, while any given observation of a specific energy level from a specific laser pulse may vary (as repetition is intended to reveal, if not correct), calculations of the overall plume composition add up over multiple observations, and thrust and specific impulse estimates represent sums over all the cases, reducing the effect of case-by-case variations.

Fig. 66, Fig. 67, and Fig. 68 show the content of each species over the course the top and bottom stage sweeps at a gate voltage of -200 V. The content for each species is normalized by the value of the most populated bin for that species. The standard deviation for each species is presented in Table 5 for these three and the next three distribution plots. Table 5 also includes a FWHM for the primary peak from

each plot. Al^{+1} and Al^{+2} have significant outlier populations, so the FWHM represents a more typical variation. For a normal distribution, FWHM is about 2.35x the standard deviation.

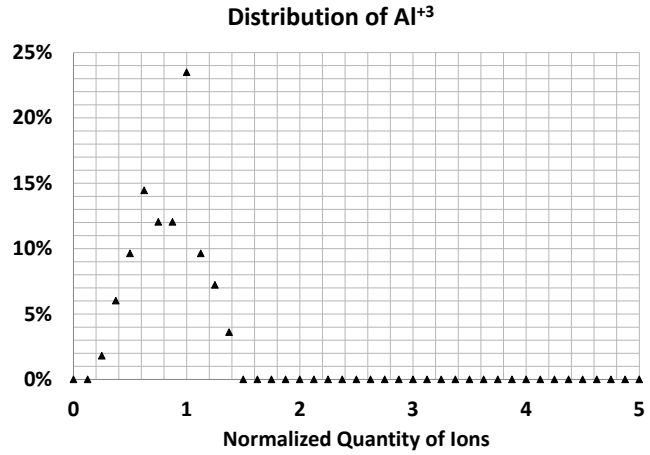

Fig. 66 Overall Distribution of Al^{+3}

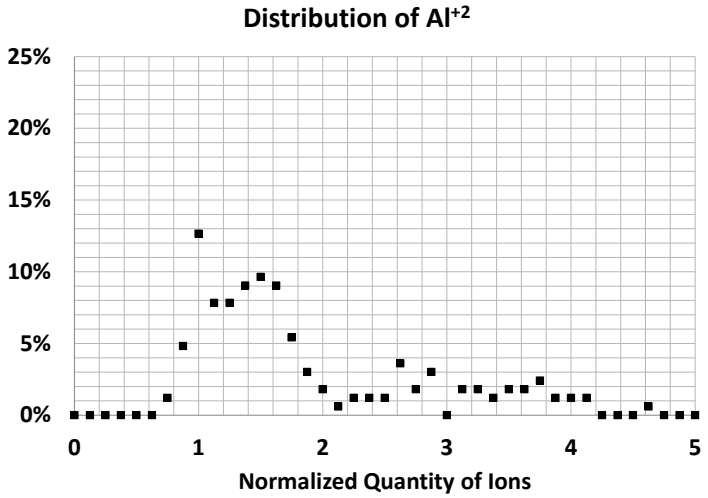

Fig. 67 Overall Distribution of Al^{+2}

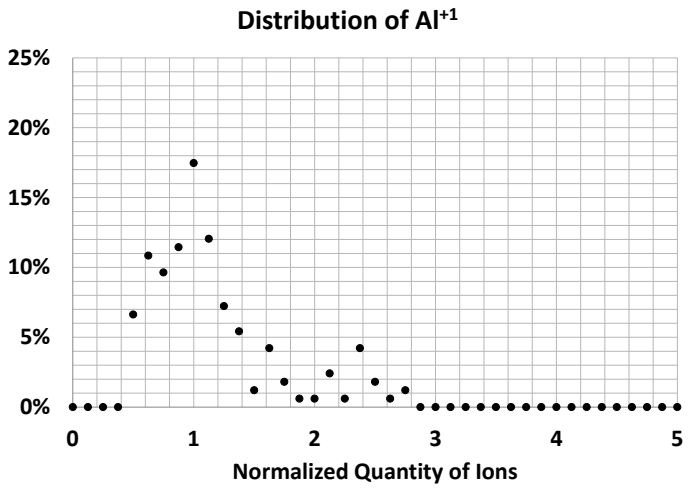

Fig. 68 Overall Distribution of Al^{+1}

When comparing laser pulses applied to the same ablation spot, the variation will be different. The stages have not moved, so cannot be a source of variation. The crater shape, laser power, and aperture current may have changed, but testing of each suggests they are all relatively constant between pulses 10 and 15. The remaining driver of variation is the actual ablation event. Fig. 69, Fig. 70, and Fig. 71 present the same content as the previous three figures (note the different scales), but with the species content of each laser pulse normalized by pulse number 10 from the same ablation spot. Notice that the outliers have mostly disappeared and the main peak is thinner, but still has noticeable width. Fig. 72 shows the same normalization, but with all points plotted vs pulse number to show there is no overall correlation with pulse number (e.g. 11^{th} pulse is consistently 90% of the 10^{th} while the 12^{th} pulse is reliably 115% of the 10^{th}). The variability in content of each species is about 20% when comparing pulse-to-pulse and up to about a factor of 2 overall. The Al^{+3} signal is significantly more consistent that Al^{+1} or Al^{+2} between laser firings, with approximately 30% variability.

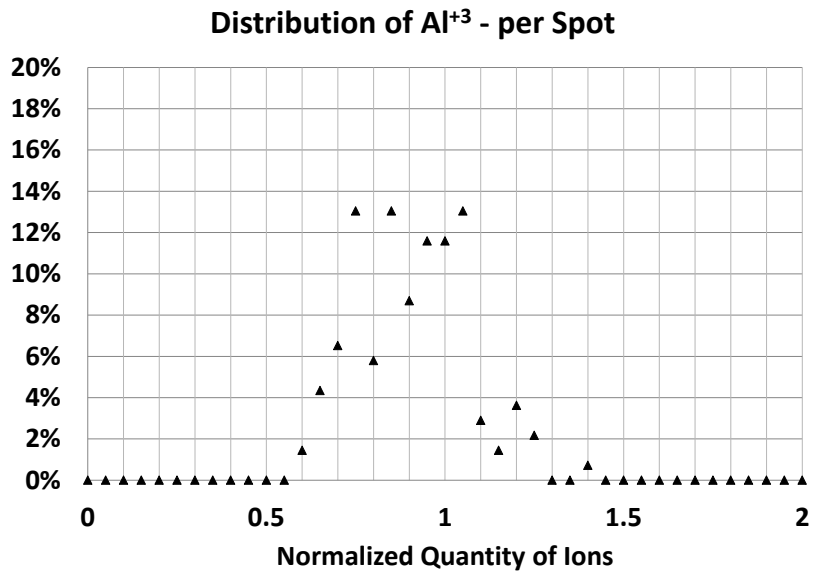

Fig. 69 Overall Distribution of Al^{+3}, Normalized per Ablation Spot

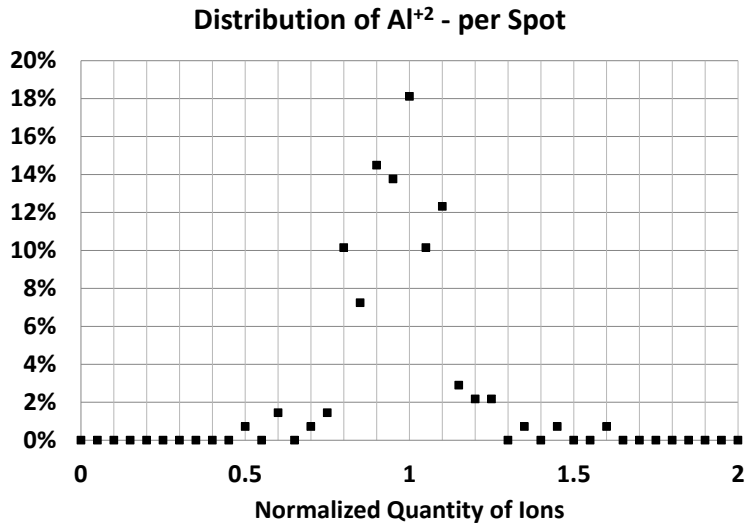

Fig. 70 Overall Distribution of Al^{+2}, Normalized per Ablation Spot

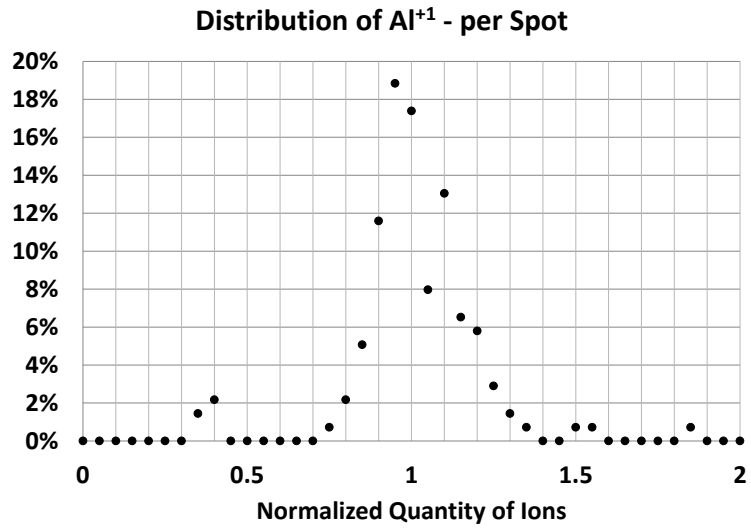

Fig. 71 Overall Distribution of Al^{+1}, Normalized per Ablation Spot

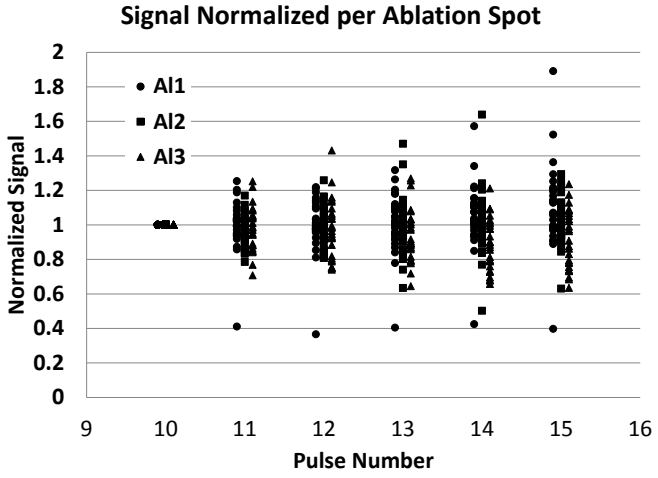

Fig. 72 Signal vs Pulse Number, Normalized per Ablation Spot

Table 5 Summary of Ablation Signal Variability

Species	Standard Deviation (overall)	FWHM (overall)	Standard Deviation (by spot)	FWHM (by spot)
Al^{+1}	54%	75%	19%	30%
Al^{+2}	92%	85%	15%	35%
Al^{+3}	27%	60%	16%	40%

4.14 Beam Expansion Simulation

The spectrometer will almost immediately strip away electrons from the plume upon entry into the energy gates. Without electrons to balance the positively charged ions, the beam will expand. This expansion due to inter-particle forces must be assessed, at least so far as it is different for different species and at different velocities. Beam expansion prior to the spectrometer will be accounted using a typical ablation plume expansion profile (Eq. (48)) from other work and will be discussed in the results chapter.

Because of the growth of the beam, particles over a wider energy range will be able to pass the mid-point of the energy gates – particles that, for example, would have fallen below the gate aperture will, because of beam expansion, now pass through the aperture. Beam expansion is significantly reduced within the second energy gate because so much of the plume has been blocked, so particles that have passed the first gate due to space charge will not have the correct energy, nor the assistance of neighbors, required to pass the second half of the energy gate. Therefore, the pass energy-per-charge for a given gate bias is not expected to change as a result of space charge.

An approximate model for expansion of a uniform, circular beam [153] was used to evaluate the relative influence of current density vs energy-per-charge on beam expansion. Eq. (35) was solved for R_B, the ratio of the beam outer radius (at a distance z from the position of the minimum beam radius) to the minimum outer beam radius, r_m. J is the beam current, U is the beam energy-per-charge, m is the mass of the ions in the beam, and the remainders are standard constants. Eq. (35) was

solved using the geometry of the first energy gate, beam energy-per-charge from 100 to 2000 eV/e^-, and charge density from 3.33×10^{-6} to 3.33×10^{-4} C/m^3. The second energy gate is neglected because the ion density will have dropped significantly due to the action of the first energy gate. The relative expansion in beam area is well approximated (±6%) by Eq. (36), demonstrating the area is a function of the ratio of current density, σ, to energy-per-charge, U, in the region of interest to this work. A_0 is the beam area at the entry aperture and A is the beam area at the exit of the first energy gate. The constant in Eq. (36) was chosen to give a reasonable answer near zero, but the multiplier and exponent were solved. For Eq. (36), current density, σ, is in C/m^3 and energy-per-charge, U, is in eV/e^-. Eq. (36) will not be quite correct because the spectrometer entry angle is a slit rather than a circle and the ablation plume has multiple ion species with a range of energy-per-charge. Nonetheless it suggests that σ and U will appear together and have an exponent in the neighborhood of 1.25.

$$\int_1^{R_B} \frac{dR_B}{\sqrt{\ln(R_B)}} = \frac{z}{r_m}\left(\frac{1}{2^{1.5}\pi\varepsilon_0}\frac{J}{U^{1.5}}\sqrt{\frac{m}{e^-}}\right)^{\frac{1}{2}} \tag{35}$$

$$\frac{A}{A_0} = 4.54 \times 10^{10}\left(\frac{\sigma}{U}\right)^{1.256} + 1 \tag{36}$$

A simulation of particles passing through the first energy gate of the spectrometer was used to estimate the effect of the non-ideal ion beam. The electric field from the energy gate was extracted from the COMSOL simulation of the spectrometer and trilinear interpolation used to find the value at each required location. The field was linearly scaled to match the desired gate bias. The beam was

represented by evenly spaced super-particles covering the aperture in five steps along the deflection axis and fifteen steps along the non-deflection direction (recall the aperture area is about 1 mm x 3 mm). The electrostatic force between all super-particles was updated every 0.1 ns, including only the particles currently within the energy gate. Particle spacing along the spectrometer longitudinal axis was controlled by particle velocity. The velocity range, around a chosen center velocity, was divided into five values selected to produce the same longitudinal as lateral inter-particle spacing at the aperture. This velocity span, limited by run time, was smaller than that of the real ablation plume. Comparing the nominal five step run to a run with twenty velocity steps (effectively lengthening the simulated plume) showed no significant difference in results.

The total beam current was divided evenly among the three simulated species: Al^{+1}, Al^{+2}, and Al^{+3}. The same velocity values were used for all three species so they would be close enough to interact with each other upon reaching the spectrometer. The species then also represent different values of energy-per-charge. Ions were removed from the simulation immediately upon encountering any of the spectrometer plates.

The main simulation runs used a center velocity corresponding to 1055 eV (three energies-per-charge because of the three species) and five current densities from 1.25×10^{-5} C/m^3 to 2×10^{-4} C/m^3. Fig. 73 shows a case where the gate bias was appropriate to pass Al^{+3}. Al^{+1}, Al^{+2}, and Al^{+3} can all be seen with and without inter-particle forces modeled (the former making the larger ellipses).

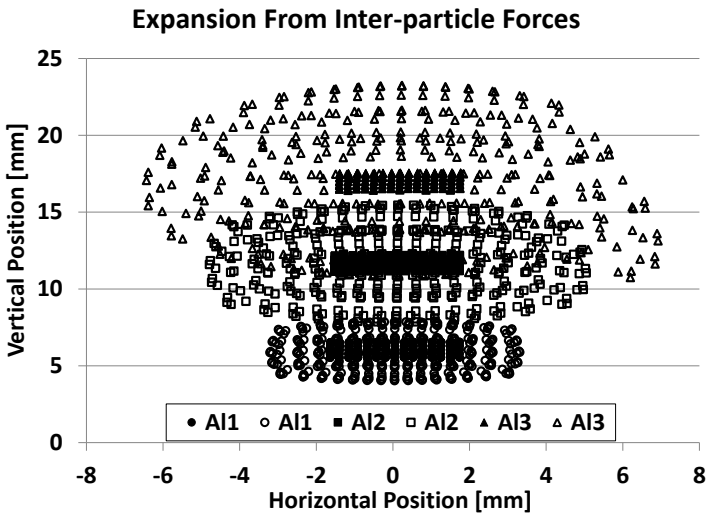

Fig. 73 Beam Expansion Within Energy Gates

For all species, it was observed that the path of the center of the beam was minimally affected by the expansion and passed the spectrometer at the same gate voltage as without inter-particle forces. This can be seen in Fig. 73, where the distributions of each species with inter-particle forces modeled are approximately concentric with the distributions neglecting inter-particle forces. It was also observed that beam expansion was minimally affected by changing the gate bias. Because of its minimal impact, the gate bias was set to zero to simplify analysis of the effect of charge density and energy-per-charge.

Ratios of the beam area at the exit with and without inter-particle forces, from the simulation, are shown in Fig. 74 along with the best fit (Eq. (37)). The current density, σ, is in C/m^3 and energy-per-charge, U, is in eV/e$^-$. As with the previous fit, the constant was fixed and the multiplier and exponent solved to minimize the maximum percent error. Notice that the exponent is 1.07 compared to 1.26 from fitting the solution to Eq. (35). Using the same the exponent as Eq. (36) gives a maximum error over the evaluated span of -30% compared to ±4% for Eq. (37).

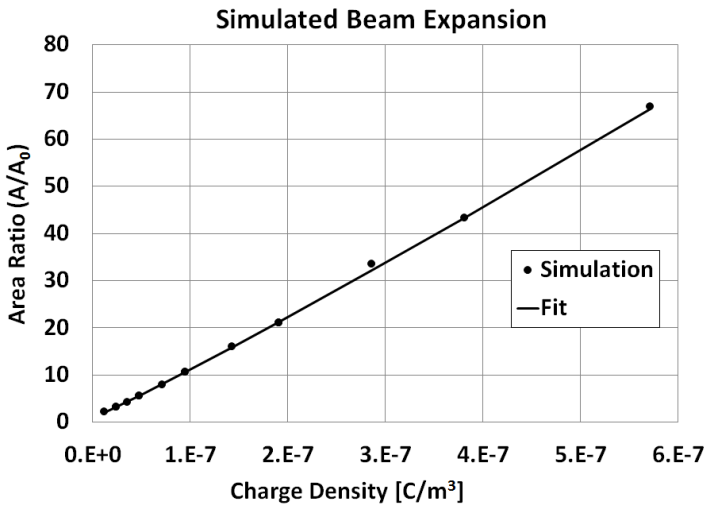

Fig. 74 Beam Expansion Simulation Results

$$\frac{A}{A_0} = 3.13\times10^{8}\left(\frac{\sigma}{U}\right)^{1.070} + 1 \tag{37}$$

The spectrometer signal will be multiplied by the area ratio from Eq. (37) to correct for beam expansion due to space charge. The charge density will be pulled from the aperture current at the time the ion passed the entry aperture (calculated via its time-of-flight). Ideally, the aperture current measurement from each individual pulse should be used to determine the time-dependent charge density at the entry aperture. The aperture current measurement was unreliable (Fig. 64), but observations, when clean, tended to be consistent over most of the first 25 pulses (Fig. 63). So, a single typical clean aperture current case (Fig. 75) was selected for use with Eq. (37). The energy-per-charge will be determined from the gate bias. The correction is not useful once the signal to noise ratio is below the detection threshold.

Inter-particle forces also drive the early parts of the plume to higher velocity and the trailing elements to lower velocity. The change in overall flight time, from the

simulation, was ±1-2%, insufficient to interfere with species identification or significantly change the energy spectrum. A longer plume might produce a larger shift at the ends; however, more than half the flight time will already be accumulated by the time the particles arrive at the spectrometer and any particles that pass the first gate due to a velocity change within the gate will be rejected by the second gate. The observed current from the ion source was insufficient to noticeably expand the beam or change the particle velocities within the spectrometer.

4.15 Estimating Plume Content

To this point, the results of spectrometer measurements have only been relative to other measurements by the spectrometer. This is sufficient for comparisons across different laser focus and pulse combinations, but not for estimating propulsion parameters like thrust and specific impulse. To make those estimates will require a translation from spectrometer measurements, specifically the secondary electron yield of each species, the yield of the scintillator in response to secondary electrons, the gain of the photomultiplier, and the effective capture rates of the output of each multiplication stage by the input of the next. The photomultiplier and scintillator gains are specified in datasheets, however the non-linearity of the signal vs. gain in Fig. 59 and Fig. 60 suggest both are not behaving quite in line with the documentation. For the scintillator, this is not unexpected and an approximate correction may be possible. Recall that, for the PMT, the single hits observed using the ionic liquid source suggest a full gain roughly in line with expectation.

For the purposes of this work, all of these factors may be combined into a single multiplier, for an impact energy-per-charge of 5.64 kV. (Recall that the PMT

output of each species was corrected to an equivalent yield at 5.64 kV.) The multiplier is determined by using the measured spectra from the spectrometer for energies above 300 eV/e^- to estimate the RPA signal for the same energy range. The multiplier was assumed to be the same for all species. This is in line with the minimal change vs kinetic energy observed in Fig. 57 and [151] in the relevant kinetic energy range. The contribution of secondary electron yield to the aperture current was neglected. Fig. 57 shows the secondary particle yield without acceleration (as would occur at the aperture) relative to that with 5 kV acceleration. Assuming a secondary electron yield at 5 kV on the order 1-2 (in line with [151]) the yield at the aperture should be sufficiently below the current from the primary ions.

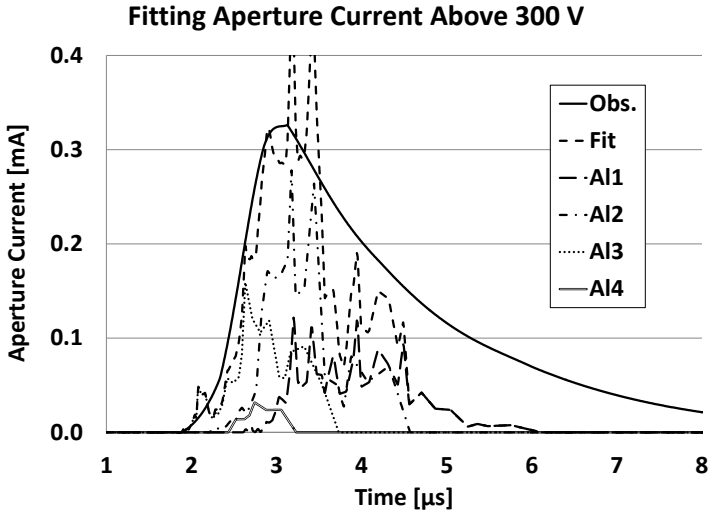

Fig. 75 Estimated Aperture Current from Observed Spectrum

The fit (Fig. 75) is rough, but sufficient for an estimate of the scaling factor from PMT output to actual plume content. The resulting scale factor is $7x10^3$. Using the PMT gain estimated above, $2.5x10^6$, the combination of secondary electron and scintillator photon yields is approximately $2.8x10^{-3}$. Assuming a secondary electron yield of order 1 [151,152], the scintillator yield is about 570x lower than the

anticipated (pg. 58). Some of this is likely explained by simplifying assumptions like a single photon wavelength out of the scintillator or perfect optical coupling of the scintillator, light guide, and photomultiplier. At the far end of the scintillator output spectrum, the detection efficiency of the photomultiplier drops by about 30% [139,154]. The scintillator and light guide were glued together at the edges, but the light guide and photomultiplier were held loosely in contact. All three components were connected with optical grease to minimize changes in refractive index at the interfaces. The interfaces or optical grease could have shifted, blocking some light. The simulation run to evaluate secondary particle flight times (4.3.3 Secondary Particle Flight Time, 77) also suggested that the secondary electrons, at least, wouldn't have a high tendency to hit the wire mesh used to bias the scintillator. The most likely cause is that the secondary particles are at a very low energy for scintillation type detectors. The typical calculation (Eq. (9)) for electrons passing through the bulk of a material may be insufficient. One of the input sources used for inputs to that calculation, [141], indicates an anticipated error in the supplied data on the order of 10%, another small contribution. The other source, [140], generated electrons within the scintillator bulk, avoiding any issues that might occur with shallow penetration of electrons into the scintillator.

4.16 Nanoparticle Imaging

The presence of nanoparticles was verified and their quantity and size distribution estimated based on SEM imaging (Hitachi SU-70). A total of 39,105 laser pulses were applied to a small aluminum target at the laser focal point, with between 1 and 252 pulses per site on the target. The ablation sites were imaged by an SEM to

observe crater development as a function of pulse number, which is discussed in the next section. A smooth copper sample (Fig. 76) was placed in the path of the ablation plume near the spectrometer axis (0.21 m) so that any nanoparticles present in the plume would be collected on the surface (Fig. 77).

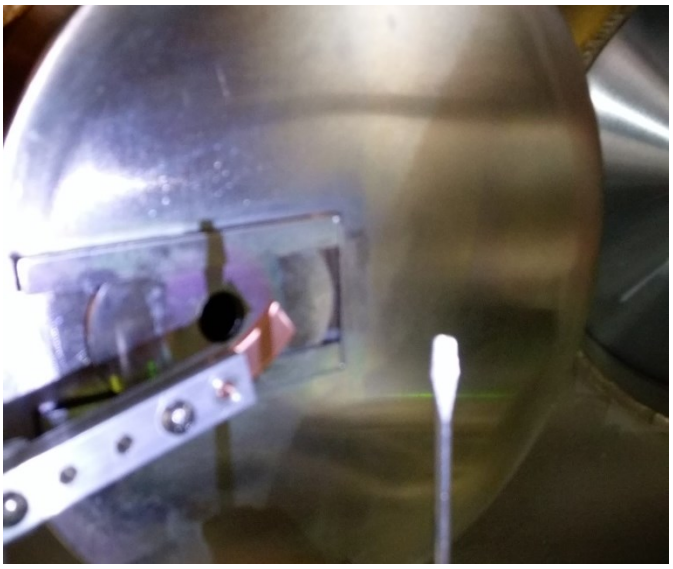

Fig. 76 Copper target in place (light from an LED at the ablation site)

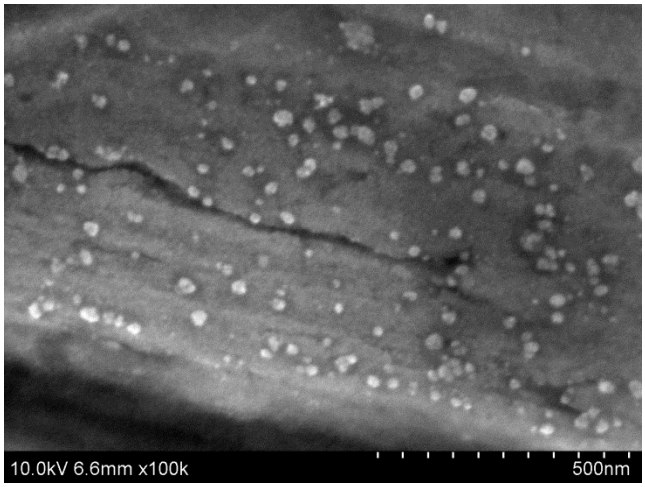

Fig. 77 SEM image showing collected nanoparticles

The large number of pulses was necessary to ensure sufficient nanoparticle content to get a viable sample size within the SEM viewing window at sufficient resolution for particle sizing. Particle diameter was measured horizontally and

vertically in the picture for all particles whose center fell in a 500 nm by 500 nm box in the middle of the image ($5.0x10^{-12}$ sr). Within the box, 52 individual particles were identified for an average flux of $2.7x10^{8}$ particles per steradian per laser pulse. The size distribution is given in Fig. 78. Particles under a few nanometers could be undercounted based on the SEM image resolution. Given the spectrometer entry aperture size, 2,400 nanoparticles per laser pulse is a reasonable order of magnitude estimate of the fluence entering the spectrometer, assuming no significant dependence on pulse number. It was not feasible to collect and process enough SEM samples to count nanoparticles as a function of laser pulse number.

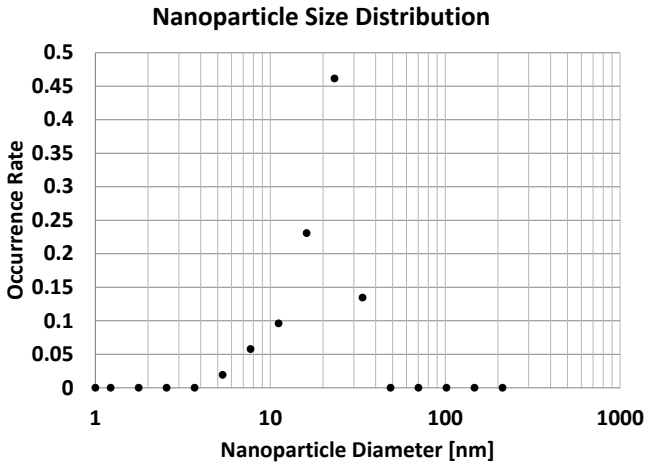

Fig. 78 Nanoparticle Size Distribution

The spectrometer made no clear observations of nanoparticles. It is possible that the spectrometer was unable to observe nanoparticles because of a low secondary particle yield, because they occurred outside the spectrometers energy-per-charge range, or because they are more common at higher laser pulse numbers. The former two options could not be addressed due to electrical shorting that limited the biases used in the spectrometer. It is likely the latter option is at least partially responsible,

given the mass of SEM observed nanoparticles exceeds the SEM observed mass removal over the first 24 laser pulses. The average nanoparticle mass, calculated from the observed diameters, is 1.66×10^{-20} kg for a total of about 4.4 ng per steradian per laser pulse. Looking ahead to the mass removal rate (for the first 24 laser pulses) in Table 6, this is about triple the complete mass removal rate if the plume occupies 1 sr. Nanoparticles could be generated by accumulated surface damage rather than condensing within the plume or given a significant lateral velocity as a result of the expanding plume. In the second case they would be ejected more towards the spectrometer (and SEM target) as the crater turns back towards the laser.

4.17 Crater Imaging

A series of craters were ablated onto an aluminum target and imaged with an SEM (Hitachi SU-70) to observe development of the ablation crater. The goal was to identify any limitation on the number of repeated laser pulses on the same location and the amount of material ablated. The ablated volume will be used for a second specific impulse estimate to complement that from the plume composition analysis. Laser pulses were applied to an aluminum target in alternating groups of 1 and 5 pulses up to a specified number, the same pattern used for plume composition measurements. Fig. 79 shows a wide view of several craters from this test. Fig. 80 to Fig. 87 show sampling of the individual crater images.

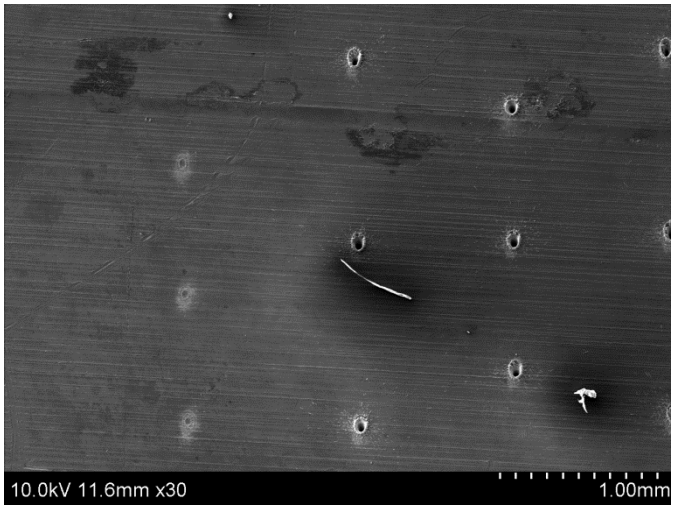

Fig. 79 Wide view of ablation craters

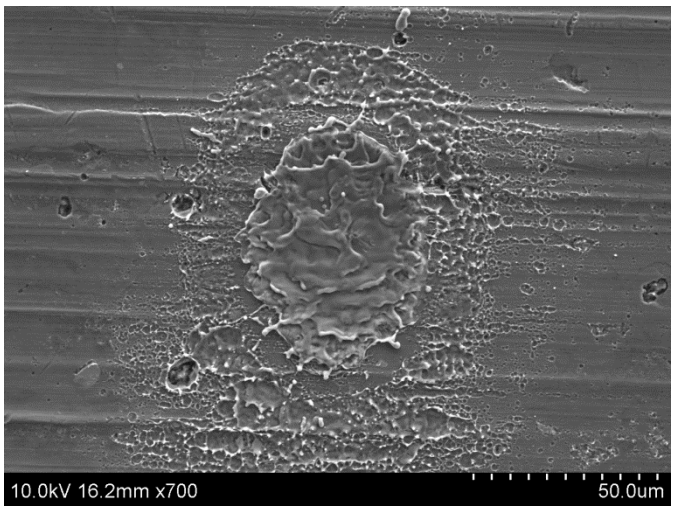

Fig. 80 Ablation Crater – 1 pulse

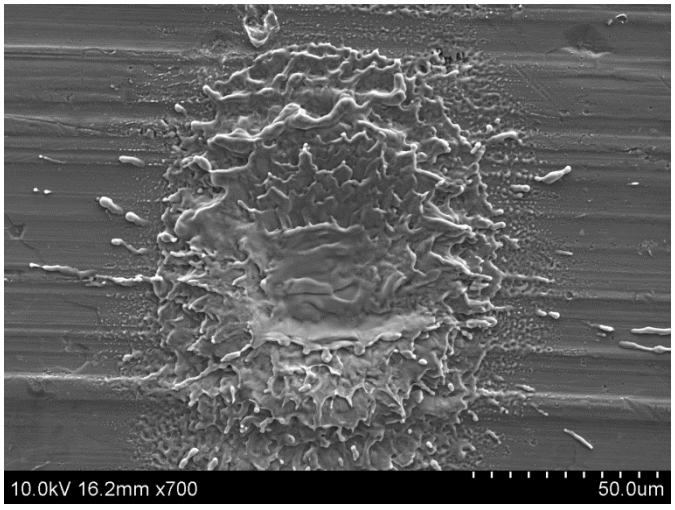

Fig. 81 Ablation Crater – 6 pulses

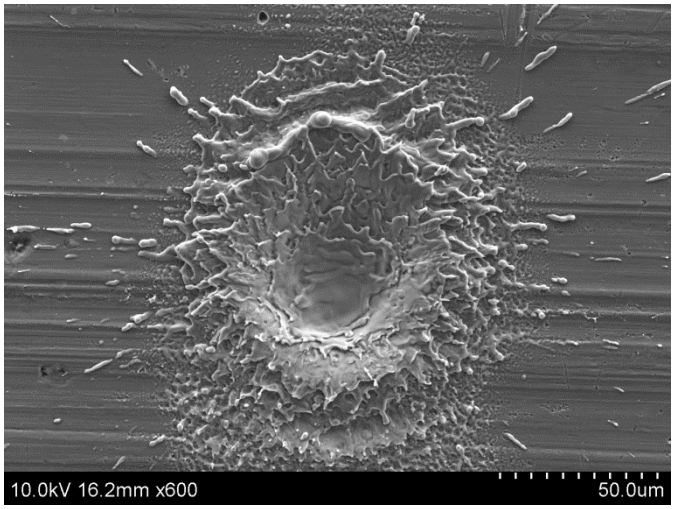

Fig. 82 Ablation Crater – 13 pulses

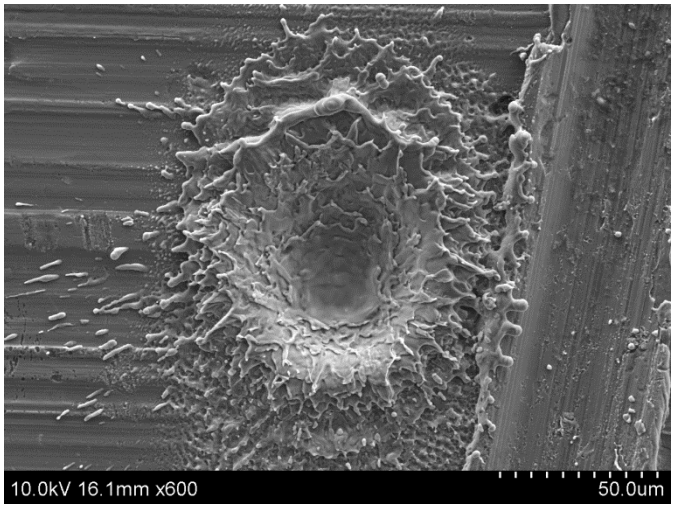

Fig. 83 Ablation Crater – 19 pulses

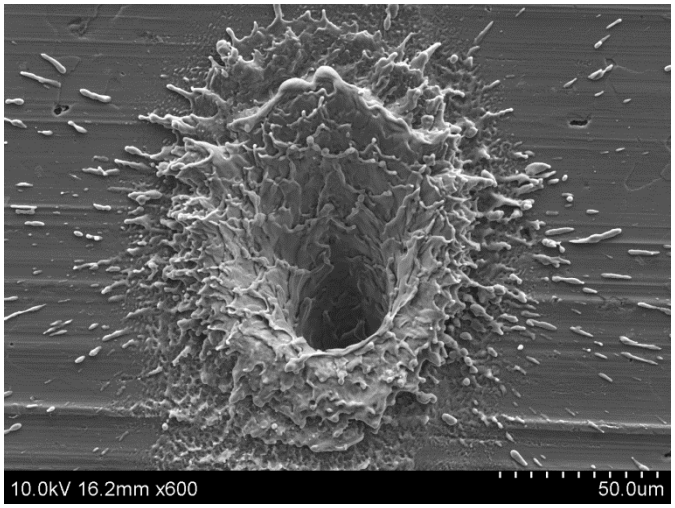

Fig. 84 Ablation Crater – 25 pulses

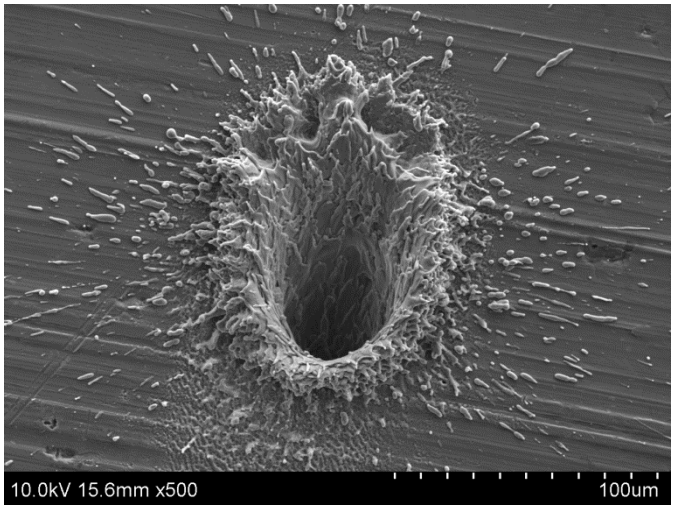

Fig. 85 Ablation Crater – 42 pulses

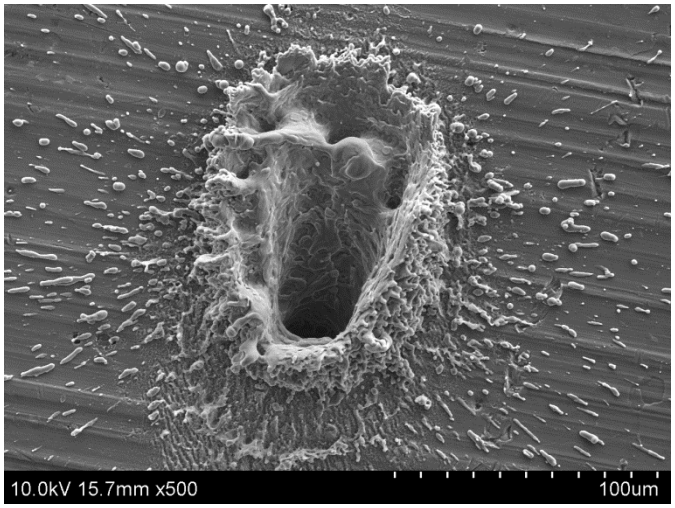

Fig. 86 Ablation Crater – 96 pulses

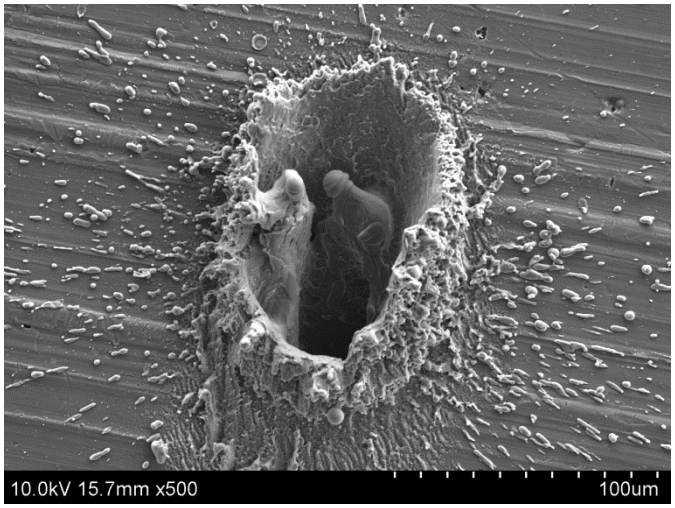

Fig. 87 Ablation Crater – 204 pulses

To estimate the removed volume, the craters were imaged at 15° and 30°. The image processing software MeX generated a 3-D profile for craters representing up to 25 pulses. By the 25th pulse the craters were too deep to process in this way. The 3-D profiles were cleaned up using the Gwyddion software package, which also calculated the average height of the crater and a matching region of undisturbed area next to the crater. The difference in average height corresponds to the average volume removed. The volume removed is not the same as the crater volume, but rather accounts for material redeposited around the edges of the crater. Mass removed is calculated from the volume removed and target density. The average height was measured at the bottom of the crater, which compared with the average height of the undisturbed area represents the crater depth. The crater depth and mass removed are listed for each crater in Table 6. Since all the values are reasonably close, 1.5 ng/pulse will be used as a typical mass removal rate for all cases.

Table 6 Crater Depth and Removed Mass

Pulse	Depth [µm]	Removed Mass [ng]	Mass Uncertainty	Mass per Pulse [ng]
1	1.3	1.1	10.1%	1.1
6[a]	5.6	7.9	5.3%	1.3
7	6.8	10.2	2.8%	1.4
12[a]	11.1	18.4	1.4%	1.5
13	11.9	19.8	1.9%	1.5
18[a]	15.6	27.1	1.6%	1.5
19	16.4	35.6	1.4%	1.9
24[a]	22.1	41.8	0.9%	1.7

a) Last of a 5 pulse burst

By the 25th pulse, the crater has begun to undermine the neighboring region of the target, which would almost certainly interfere with any attempt to ablate that region, reducing the usable area of the target. Under continuous ablation the plume can be seen to travel back along the path of the incoming laser. The crater profiles

and spectrometer signals suggests that the initial plume is normal to the target surface, as expected, and that the plume deflection begins around the 25th pulse. Both the interference to neighboring areas of the target and the redirection of the plume suggest a maximum limit of 25 pulses per target site.

4.18 Detector Statistics Calculation

This section describes calculation of the distribution of photomultiplier output as a function of the mean yield of secondary particles. The calculation applies for both secondary ions and secondary electrons. The only difference between the two is the mean yield of photons within the scintillator in response to a secondary particle impact. The distribution as a function of secondary particle yield is summarized by the mean signal, the 2.5% probability level, and the 97.5% probability level, all of which are plotted in Fig. 88. Fits to the three curves (red) are reported in Eqs. (38), (39), and (40). The 2.5% and 97.5% fits are piecewise to keep the error below 2.3%. Either the plot or the fit equations can be used to determine when two ions are reliably distinguishable – the 97.5% level of the lower yielding ion should be less than the 2.5% level of the higher yielding ion.

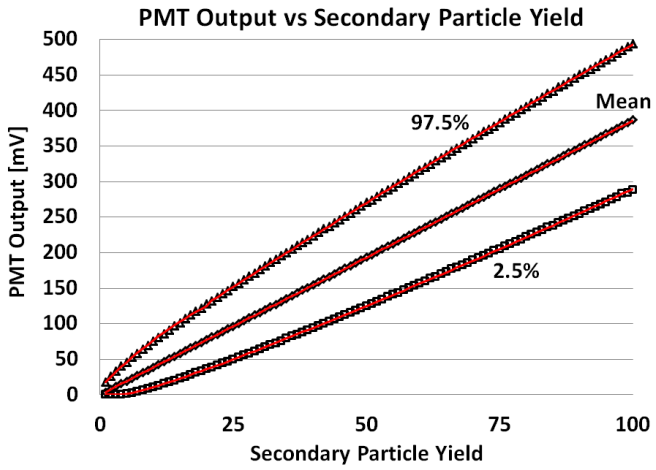

Fig. 88 PMT Output Distributions

$$V_{mean} = 3.86 Y_{se} \tag{38}$$

$$V_{2.5\%} = \begin{cases} 4.02\times10^{-2} Y_{se}^{\ 2} + 1.363 Y_{se} - 6.768 & 5 \le Y_{se} \le 20 \\ 3.85\times10^{-3} Y_{se}^{\ 2} + 2.715 Y_{se} - 20.41 & Y_{se} > 20 \end{cases} \tag{39}$$

$$V_{97.5\%} = \begin{cases} -8.85\times10^{-2} Y_{se}^{\ 2} + 7.456 Y_{se} + 10.91 & 0 \le Y_{se} \le 20 \\ -3.54\times10^{-3} Y_{se}^{\ 2} + 4.990 Y_{se} + 29.31 & Y_{se} > 20 \end{cases} \tag{40}$$

The yield of secondary particles, Y_{se}, resulting from the impact of a primary ion on the rear wall of the detector follows a Poisson distribution with mean yield λ_{se}. The number of photons emitted the scintillator in response to the impact of a secondary particle, Y_{sc}, also follows a Poisson distribution, with mean yield per secondary particle of λ_{sc}. The probabilities that an emitted photon will reach the photomultiplier and that it will generate a photoelectron that reaches the first dynode of the photomultiplier both follow Binomial distributions. The probabilities are designated p_{lg} for reaching the photomultiplier and p_{pe} for activating the first dynode. The number of photoelectrons reaching the first dynode is designated Y_0. At the i^{th} dynode within the photomultiplier, incoming electrons spawn secondary electrons, Y_i,

following a Poisson distribution with mean yield per incoming electron of λ_{dy}. The number of dynodes is designated N.

The photomultiplier output distribution for a given secondary particle yield is calculated by repeatedly simulating this sequence of events, drawing a particle yield (for Poisson distributed processes) or a fraction of the particles from the previous event that reach the next event (for Binomial distributed processes) to determine the input of the next event. (Simulation is required because having a Poisson distributed variable as the parameter of a Poisson distribution produces a compound Poisson distribution, which has no closed form representation.) The output of the final photomultiplier dynode is divided by the parasitic capacitance, C, of the readout to get the peak output voltage V_{out}. The output from the photomultiplier for a single particle is fast enough that the readout resistance can be neglected when calculating the peak readout voltage. The sequence of steps for a single yield simulation is laid out in Eq. (41), where Y=Pois(λ) represents randomly drawing a specific yield, Y, from a Poisson distribution with mean λ. The Binomial distributions are incorporated into the next Poisson distribution. A sequence of Binomial distributions yields a Binomial distribution whose probability is the product of the probabilities of the constituent distributions. A Binomial distribution followed by a Poisson distribution yields another Poisson distribution whose mean is the product of the Binomial's probability and the initial Poisson's mean.

$$
\begin{aligned}
Y_{se} &= Pois\left(\lambda_{se}\right) \\
Y_0 &= Pois\left(Y_{se}\lambda_{sc}p_{\mathrm{lg}}p_{pe}\right) \\
\text{for i} = 1:\mathrm{N} \quad &\left\{ Y_i = Pois\left(Y_{i-1}\lambda_{dy}\right) \right\} \\
\mathrm{V_{out}} &= Y_N \frac{e^-}{C}
\end{aligned}
\tag{41}
$$

The photomultiplier has 10 dynodes (N=10) with a total gain of $2\text{x}10^6$, giving each dynode a mean gain, λ_{dy}, of 4.25. The light guide covers 25% of the scintillator's surface area and its documentation [146] indicates that approximately 13% will be absorbed within its 25.4 mm length. The combined probability of a photon entering and passing through the light guide, p_{lg}, is therefore 21.8%. The photomultiplier datasheet [154] states a quantum efficiency of 38% for the peak output wavelength of the scintillator and the manufacture indicates that 95% of photoelectrons reach the first dynode [155], so p_{pe} is 36.1%. The scintillator yield per secondary electron, λ_{sc}, was estimated to be 20 using Eq. (9).

Chapter 5: Results

5.1 Ionic Liquid Ion Source Results

The energy spectrum of the ionic liquid ion source was evaluated for positive and negative beams with three different liquids: EMI-BF_4, EMI-Im, and EMI-$GaCl_4$. Since the particle source is continuous, time-of-flight information was not collected. Energy sweep plots for all of the liquid-beam polarity-secondary particle combinations are presented in Appendix A. The positive beam/secondary electron and negative beam/secondary ion cases used a ±5 kV detector bias with the scintillator at ground. Due to short circuiting, the positive beam/secondary ion and negative beam/secondary electron cases used a detector bias of ±3 kV and a scintillator bias of ±5 kV. For each case, five consecutive energy sweeps were run, lasting about 20 minutes per set. Fig. 89 shows a set of sweeps and the variation that was common within a single, well behaved set. In many cases 3 or more sweeps approximately matched, in which case the matching sweeps are used for analysis.

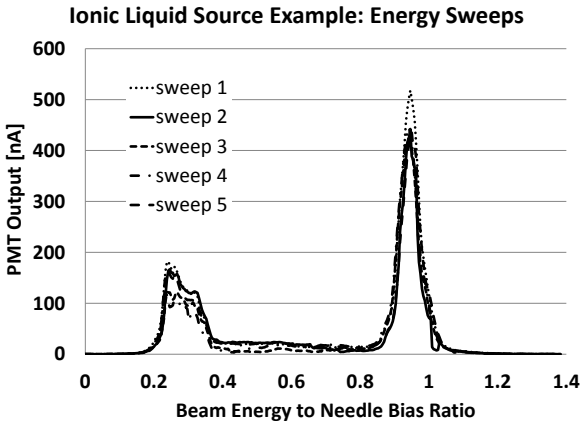

Fig. 89 Five energy sweeps (EMI-GaCl4, positive beam, secondary electron)

The broken-dimer peak is clear in the secondary electron mode energy sweeps, located in line with the expectation in Table 1. With sufficient zoom, the

broken-dimer peak does appear to exist in the secondary ion mode sweeps, but it is disproportionately suppressed, 5-10x, relative to the main peak. The main peak was, itself, 5-10x lower using secondary ion mode compared to secondary electron mode.

The variation of each case's signal with detector bias (ion impact energy) and scintillator bias was observed. Only cases with reasonably consistent results over multiple energy sweeps were used. Liquid-beam polarity-secondary particle combinations with three or more good cases are plotted in Fig. 90, Fig. 91, Fig. 92, and Fig. 93. Characteristic fits are also plotted, and given by Eqs. (42), (43), (44), and (45), respectively. There was no apparent dependence on particle mass in either the secondary electron or the secondary ion detector modes.

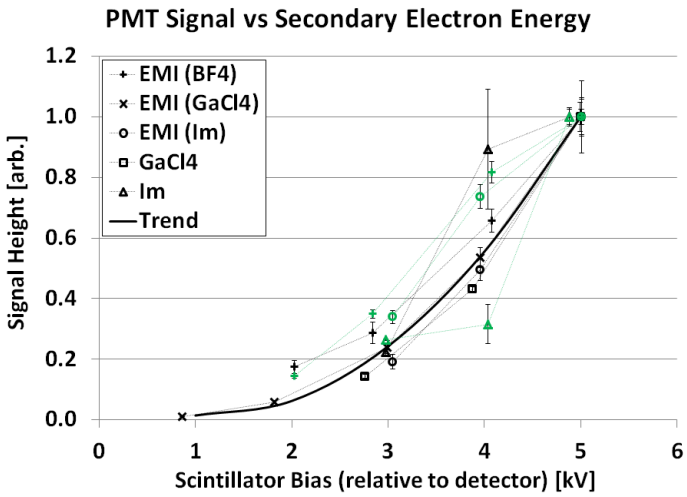

Fig. 90 Scintillator Output Vs Secondary Electron Energy

$$y = 6.612\times10^{-2}x^{2} - 1.502\times10^{-1}x + 9.858\times10^{-2} \tag{42}$$

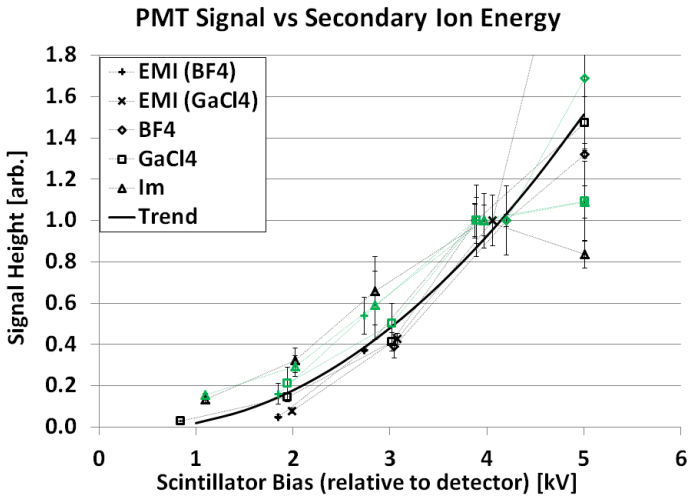

Fig. 91 Scintillator Output Vs Secondary Ion Energy

$$y = 7.172\times10^{-2}x^2 - 5.675\times10^{-2}x + 4.720\times10^{-3} \tag{43}$$

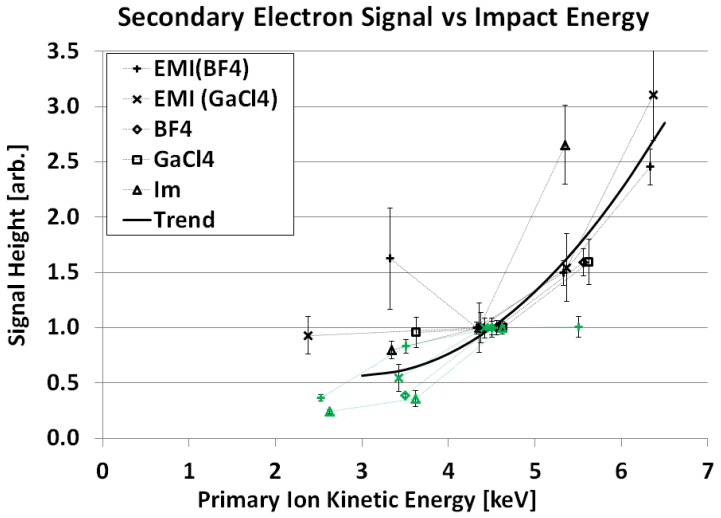

Fig. 92 Secondary Electron Emission vs Primary Impact Energy

$$y = 1.820\times10^{-1}x^2 - 1.076x + 2.158 \tag{44}$$

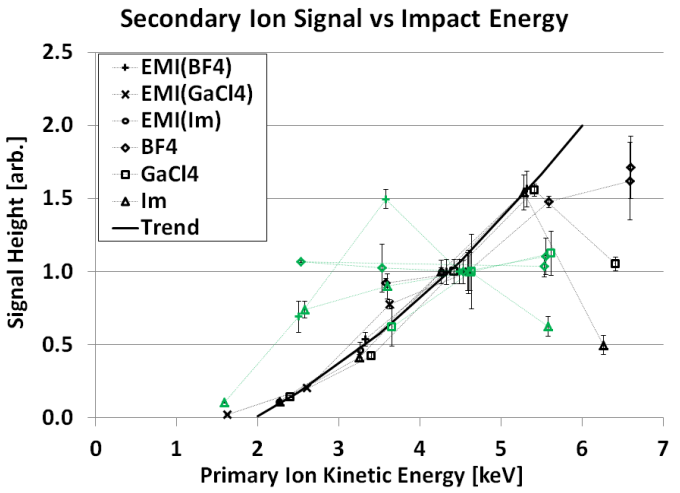

Fig. 93 Secondary Ion Emission vs Primary Impact Energy

$$y = 4.917 \times 10^{-2} x^2 + 0.1040x - 0.3940 \tag{45}$$

The fit of scintillator yield variation with secondary electron energy from the ion source, Eq. (42), agrees with that from the ablation source, Eq. (32), within 4% from 3 to 9 keV. Recall that the ablation source measurement started at 2 keV and that both are set to unity by definition at 5 keV. Accounting for the relative collection areas, the typical PMT output with a 4.5 keV impact energy and 5 keV secondary particle energy was about 3000x the aperture current using secondary electron mode and about 750x using secondary ion mode for the main peak. For the broken-dimer peak with the same primary impact and secondary particle energy, it was about 750x the aperture current in secondary electron mode and 75x in secondary ion mode. At 4.5 keV, EMI has the same impact velocity as Al^{+1} at 1.1 keV. Adjusting the 3000x magnification according to Eq. (30) at 1.1 keV gives a magnification of $1x10^4$ for comparison to $7x10^3$ from ablation. The difference could easily be due to different secondary electron yields between the two ions. Still, both suggest a significant under performance of the scintillator (350x to 570x).

The liquid EMI-$GaCl_4$ was used to demonstrate detection of single positive and negative ions via secondary electrons and secondary ions. The impacts were distinguishable from background noise by observing an increase in frequency near the peak of the energy spectrum and a lack of impacts sufficiently far from the peak. Individual hits were cataloged within a 1 ms window at an energy far enough from the peak to make overlapping impacts unlikely. Fig. 94, Fig. 95, Fig. 96, and Fig. 97 show energy sweeps using ionic liquid EMI-$GaCl_4$ using all four combinations of beam polarity and secondary particle. The detector biases for each case are provided in Table 7. The vertical line indicates the location at which single impact observations were tallied. Table 8 summarizes the single particle impact results, adjusted by Eqs. (42), (43), (44), and (45) to a primary ion impact energy of 6.45 keV and a secondary particle energy of 5 keV. The detection rate is based on a nominal aperture current of 12 nA and scaled according to the energy spectrum height at the measurement energy relative to that at the peak energy.

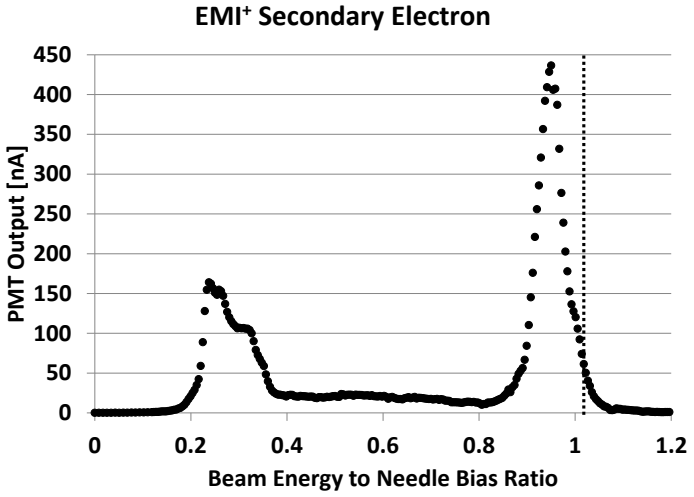

Fig. 94 EMI-$GaCl_4$, Positive Beam, Secondary Electron

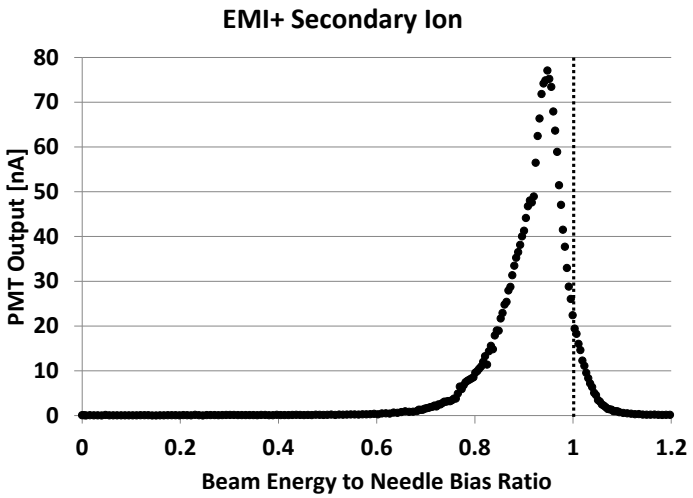

Fig. 95 EMI-$GaCl_4$, Positive Beam, Secondary Ion

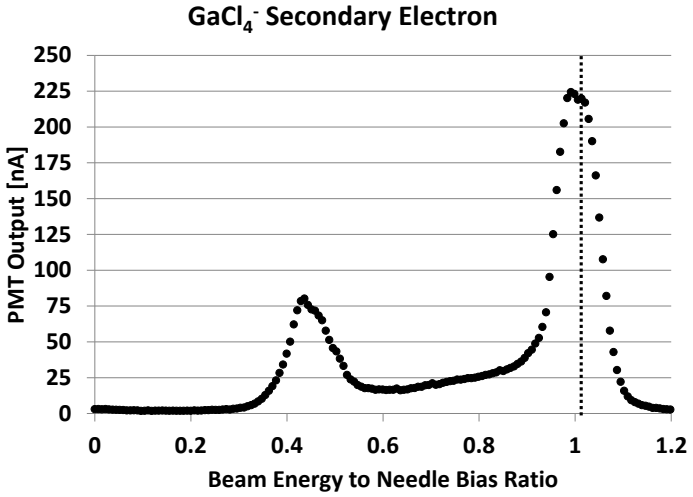

Fig. 96 EMI-$GaCl_4$, Negative Beam, Secondary Electron

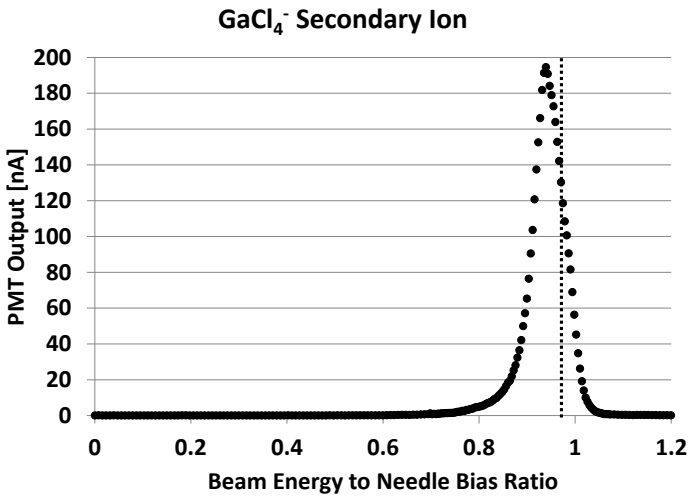

Fig. 97 EMI-$GaCl_4$, Negative Beam, Secondary Ion

Table 7 Detector and Scintillator Biases

Case	V_{det} [kV]	V_{scin}-V_{det} [kV]
EMI^+ Secondary Electron	-5	+5
EMI^+ Secondary Ion	-3	-5
$GaCl_4^-$ Secondary Electron	+3	+5
$GaCl_4^-$ Secondary Ion	+5	-5

Table 8 EMI-$GaCl_4$ Single Impact Summary

Case	Hit Rate [kHz]	Mean Size [mV]	Detection Rate[a]
EMI^+ Secondary Electron	73	3.4	1.8×10^{-3}
EMI^+ Secondary Ion	41	3.5	7.9×10^{-4}
$GaCl_4^-$ Secondary Electron	77	4.0	5.7×10^{-4}
$GaCl_4^-$ Secondary Ion	52	2.9	2.7×10^{-4}

a) Adjusted to 6.45 keV primary energy, 5 keV secondary energy

The mean hit size, 3.5 mV, is compatible with single photoelectrons, accounting for the fact that hits producing no output cannot be counted and considering that hits smaller than 2 mV are significantly more difficult to identify. Single secondary particles, considered under the same assumptions, would be expected to produce an observed mean of 11 mV. This suggests the low detection rates are due to very low scintillator output (mostly single photoelectrons) as opposed to very low secondary particle output (mostly single secondary particles). The signal

heights were insufficient to distinguish ions of different mass based on comparing single impacts.

5.2 Ablation Plume Composition

5.2.1 Spectrometer Case Summary

Six energy sweeps were performed under different laser conditions, with the spectrometer's energy gates varied from 160 or lower through 500 or higher J/C. Several laser pulses were recorded at each setting. Based on rotation of the crater, most cases don't go past 25 pulses. Plots for all of the cases are presented in Appendix A. The cases are named according to the laser focusing condition, either weak or strong. Recall the weak condition is about 30% the intensity of the strong condition. The particulars and purpose of each case are presented here. In addition to comparisons across cases, each allows comparison vs pulse number. Fig. 98 and Fig. 99 show an example of the data collected for a single case, first the raw PMT signal, then the derived spectrum. The sweep data plot (pg. 147) and spectrum plot (pg. 151) layouts are discussed in more detail shortly.

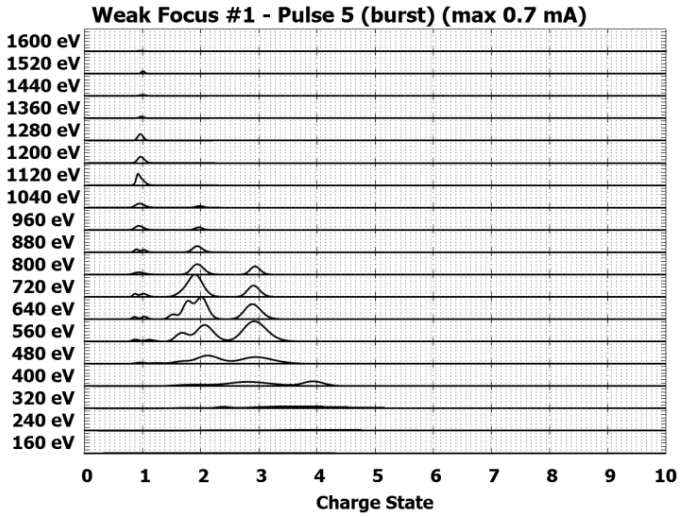

Fig. 98 Energy Sweep Data Example: PMT Signal

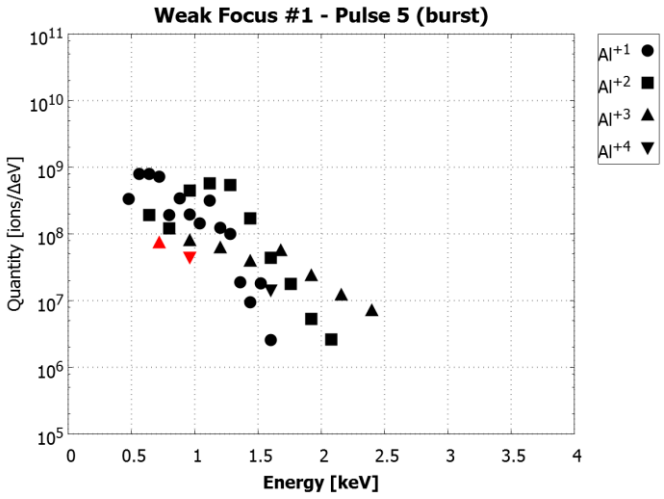

Fig. 99 Energy Sweep Data Example: Energy Spectrum

Weak Focus #1 & Weak Focus #2

Both of these cases were collected under identical conditions to those used for the Data Processing section. Weak Focus #1 was used to complete the calibration by fitting the aperture current. The laser was fired approximately 190 times with 25 µs between pulses, more than any other case. Because the pulses are close together, it was possible that the plume from one pulse may arrive after the next. This does not appear to have happened to any significant degree. The 1st and 2nd pulses were stronger than the remainder by 40% (~5.64x10^{10} W/cm^2) and 60% (~6.35x10^{10} W/cm^2) respectively. The remaining pulses had 75-95% the energy of their single and short burst counterparts (~4.02x10^{10} W/cm^2). These cases were run from 0 to 1600 J/C for a positive beam.

Strong Focus #1 & #2

These cases were run under identical conditions. For both of these cases the laser was fired with alternating single pulses and bursts. The burst pattern consisted of

1 pulse followed by a 75 μs gap, then 4 additional pulses with a 25 μs gap between each. The 1st pulse at each energy level was consistently ~1.68×10^{11} W/cm^2 while the remainder varied between that and ~1.33×10^{11} W/cm^2. Positive and negative beams were investigated from 0 to 23.5 kJ/C. Comparing against the Weak Focus cases shows the impact of laser intensity. To see the effect of short bursts, compare each single pulse with the final pulse of the preceding burst (e.g. pulse 7 vs pulse 6, pulse 6 being the end of the burst that started with pulse 2).

5.2.2 RPA Case Summary

RPA data were collected to fill in the low energy range that the spectrometer had difficulty observing. The Weak Focus #1 & #2 cases, being the most promising, were observed 3 times with the RPA, producing cases RPA #1, RPA #2, and RPA #3. The pulse pattern was altered slightly to provide some comparison to the other burst options observed by the spectrometer - the 1st and 5th pulses have an extended gap (75 us instead of 25 us). The 5th pulses is most similar to the short burst mode, the 6th pulse is most like the single pulse mode, and the 10th through 25th pulses are the same as the long burst mode. The 1st pulse is equivalent across all weakly focused cases. As a consequence of the delay after the 5th pulse, the 6th pulse is 67% more intense than the others, though not as high intensity as the high focus cases.

The retarding potential was stepped from 2V to 1600 V in steps of 34 V. Fig. 100 shows the RPA signal from a subset of the observed energy levels from 1 of the 3 sweeps. After about 340 V, the signals begin to dip below 0, indicating electron infiltration. As for the spectrometer signals, RC distortion must be removed from the output signal. The 2V signal was not well behaved generally, particularly for the first

few pulses. For this reason, all processing begins at the 36V level. Fig. 100 shows a case where the 2V signal was good.

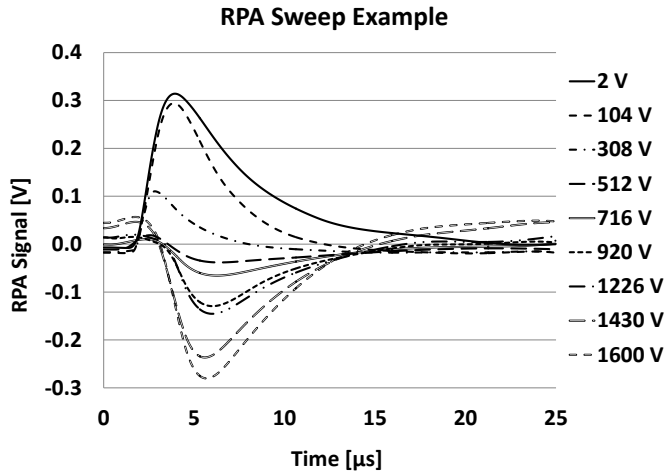

Fig. 100 RPA signal over full sweep

5.2.3 Spectrometer Sweep Plots

Fig. 101 shows a representative sweep plot, in this case the tenth pulse of case Weak Focus #1. The chart title identifies the case, the pulse number, whether this is a single pulse or part of a burst (the last pulse of the burst for the Strong Focus cases), and the maximum signal current displayed. The signal for each energy level is presented horizontally, with the energy level specified (in eV/e^-) along the left side. This is the signal as output by the photomultiplier (the output signal with RC distortion removed). Energy levels for which no signal was observed are not plotted. Those that appear empty here simply had that little compared to the maximum. The vertical axis of each segment is normalized by the signal current specified in the title. The horizontal axis identified the locations at which each aluminum charge state would be expected to be observed. None of the corrections discussed in the Data

Processing section, except removal of the RC distortion, have been applied to the results in the sweep summary plots.

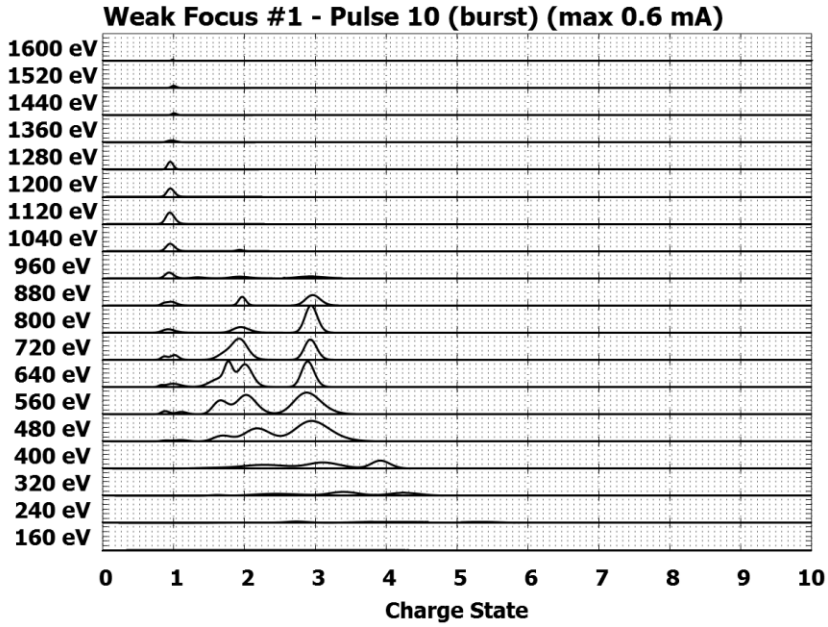

Fig. 101 Sweep Summary Plot Example

Note the progression of peaks in Fig. 101, which is common to all cases: above 400 J/C (400 eV/e^-) the peaks begin to shift towards higher charge states indicating an early arrival. The shift grows as the gate pass energy is lowered. The arrival is earlier than expected for the most likely species, but is still later than that same species at the prior energy level. In order for particles to appear to arrive early, they must have started at a higher energy and been slowed by interaction with other particles in the plume. The arrival time would be dictated by their average velocity while gate passage would depend on their later energy. Because the velocity has dropped, they would arrive sooner than their final energy would predict. The peak aperture current is behind the first particles showing this phenomenon, implying they should be accelerated rather than slowed. The extent of the shift also suggests inter-particle forces within the gate are insufficient to cause the observed shift in energy.

Following the top two peaks from 400 J/C to 240 J/C, Al^{+3} and Al^{+4} both arrive 13% early.

Simulation suggests the arrival time change due to inter-particle forces near 240 J/C is, at most, several percent, with an energy change of around 10%. Based on the arrival time, the particles would have started over 320 J/C. This is far enough that, should spreading due to inter-particle forces cause a particle to pass through the first gate, that particle would not have the correct energy to pass the second gate, even including deceleration due to inter-particle forces, in addition to entering at the wrong angle. Shifted peaks, as discussed here, are binned with the nearest whole charge state for calculating energy distributions and performance metrics. Since all the impacted species are single aluminum ions, this keeps their velocity as close as possible to that observed.

Comparing plots for the first pulse (Fig. 129, Fig. 137, Fig. 145, Fig. 154) shows a broadly similar composition, but with the stronger focus cases having a higher overall output and generating Al^{+1} at higher energies than the low focus cases. Comparing short bursts against single pulses (Fig. 145 - Fig. 162) shows the bursts increase the overall output and produce distinctly higher quantities of higher charge-state species, with them also extending to higher energies compared to single pulses. The long bursts (Fig. 129 - Fig. 144), which were carried out at low focus, produced a larger increase in high energy Al^{+1} than strong single pulses. There was far less output at low energy compared to all the other cases, but the same was true for the first pulse so it may not be due to the burst. The first pulse of the long bursts had

slightly more energy than the other cases, but the subsequent pulses had less energy, so pulse energy is also unlikely to be the cause.

Comparing the lower energy levels, it is clearly possible for the spectrometer to detect ions in those levels that sometimes appear empty (compare Weak Focus #1 & #2 against Strong Focus #1 & #2 between 150 and 300 eV). The aperture current suggests there is current there, even when the spectrometer sees nothing.

5.2.4 RPA Sweep Plots

Fig. 102 shows a subset of energy levels up to 512 V after deconvolution. To assess variability, the RPA signal was compared for pulses 11-15 across all three cases. The RPA signal varied 10-20%, the difference between neighboring levels, about 30%. The overall quantity of charge, based on integrating the RPA signal, has an uncertainty of 10-20%.

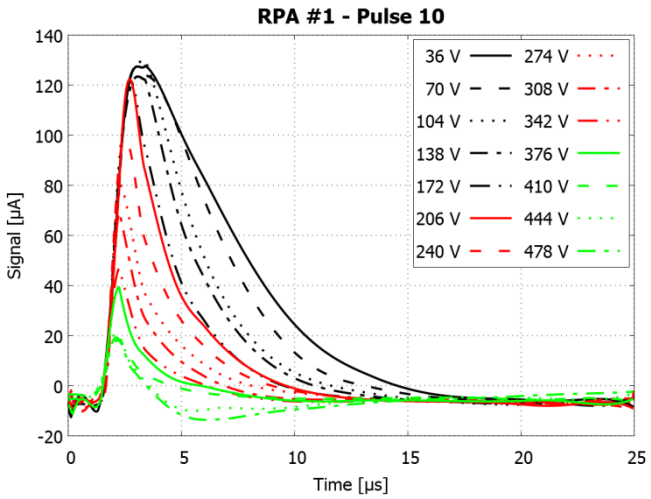

Fig. 102 Deconvolved RPA signal

The RPA's overall transparency and flight length were 13.7% and 0.187 m. The flight length was determined by shifting the signal so the start aligns with the

aperture current. The transparency was estimated by scaling full RPA signal to match the height of the aperture current, accounting for the different aperture areas.

5.2.5 Spectrometer Energy Distribution Plots

Fig. 103 shows a representative energy distribution plot. As in the previous section, it is the tenth pulse of case Weak Focus #1. The chart title identifies the case, the pulse number, and whether this is a single pulse or part of a burst (the last pulse of the burst for the Strong Focus cases). Each point represents the quantity of each species at that energy - the number of ions per differential step in energy. The quantity scale is logarithmic, so points with no observed content are not plotted. This data has been corrected using the calibrations discussed in the Data Processing section. Species higher than Al^{+4} should be considered suspect, moreso the higher the charge state. They only appear at low energies and may reflect a shift in particle energy during flight rather than actual charge states, as discussed in the previous section. Entries whose energy-per-charge is less than 310 eV/e^- use the same symbol, but in red. Such entries may be misidentified due to arriving early, as discussed in the prior section.

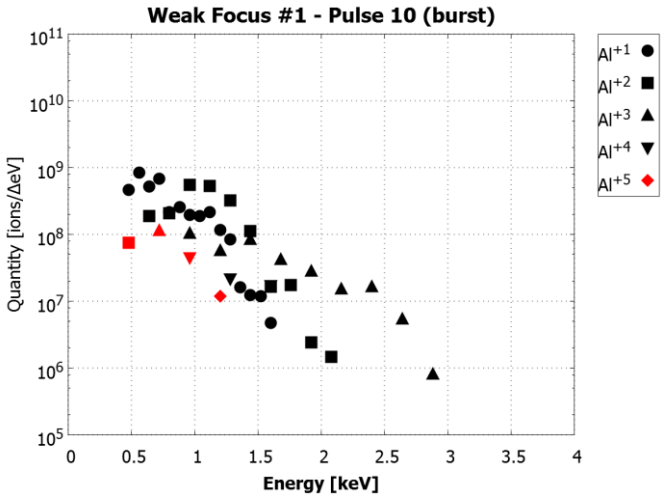

Fig. 103 Spectrometer Energy Distribution Plot Example

5.2.6 RPA Energy Distribution Plots

The spacing of RPA energy levels was too large, and the variability too significant to see clear peaks for each species. Instead, the most appropriate charge state for each species was determined by Eq. (46) and limited to Al^{+1} through Al^{+4}. ($TOF_{Al^{+1}}$ is the flight time for Al^{+1}, TOF is the observed flight time, and n is the resulting charge state.) This matched the borders between charge states for those cases where the borders were apparent. Having assigned a species, the ion count was extracted from the received current and the velocity derived from the flight time. Fig. 104 shows an example of the resulting energy distribution. Points with energy-per-charge greater than 310 eV/e^- are shown in red.

$$n = ceiling\left(\left[\frac{TOF_{Al^{+1}}}{TOF}\right]^2\right) \tag{46}$$

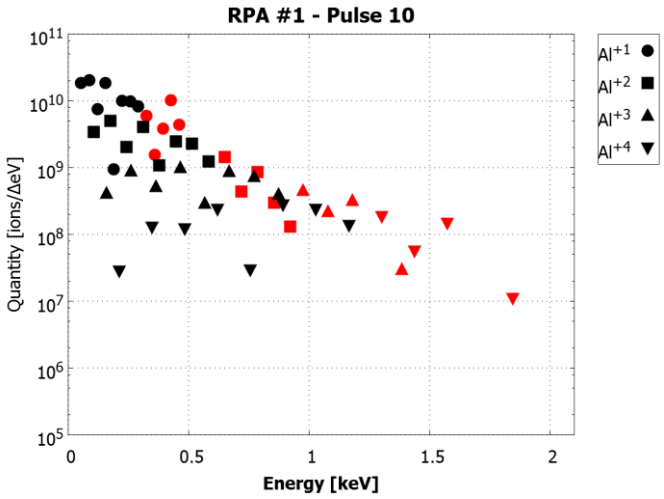

Fig. 104 RPA Energy Distribution Plot Example

The flight time for Al^{+1} used in Eq. (46) was determined by Eq. (47) where L_a is the flight length, L_b through L_e are the spacing between the five RPA plates, V_{e1} is the primary electron rejection bias (2nd plate), V_r is the retarding potential (3rd plate), V_{e2} is the secondary electron rejection bias (4th plate), and U, m, and n are the kinetic energy, mass, and charge state of the ion in question.

$$TOF = t_a + t_b + t_c + t_d + t_e$$

$$t_a = \frac{L_a}{\sqrt{U}}\sqrt{\frac{m}{2n|e^-|}}$$

$$t_b = \frac{L_b\sqrt{2}\sqrt{U}}{V_{e1}}\sqrt{\frac{m}{|e^-|}}\sqrt{\frac{1}{n}}\left(1-\sqrt{1-\frac{V_{e1}}{U}}\right)$$

$$t_c = \frac{L_c\sqrt{2}\sqrt{U-V_{e1}}}{V_r-V_{e1}}\sqrt{\frac{m}{|e^-|}}\sqrt{\frac{1}{n}}\left(1-\sqrt{1-\frac{V_r-V_{e1}}{U-V_{e1}}}\right) \quad (47)$$

$$t_d = \frac{L_d\sqrt{2}\sqrt{U-V_r}}{V_{e2}-V_r}\sqrt{\frac{m}{|e^-|}}\sqrt{\frac{1}{n}}\left(1-\sqrt{1-\frac{V_{e2}-V_r}{U-V_r}}\right)$$

$$t_e = \frac{L_e\sqrt{2}\sqrt{U - V_{e2}}}{-V_{e2}}\sqrt{\frac{m}{n|e^-|}}\sqrt{\frac{1}{n}}\left(1 - \sqrt{1 - \frac{-V_{e2}}{U - V_{e2}}}\right)$$

5.2.7 Combined Energy Distribution Plots

Cases RPA #1 and Weak Focus #1 were plotted together to show the full (ionized) plume energy distribution. Fig. 105 shows an example of an energy spectrum combining RPA data (black) below 310eV/e^- with spectrometer data (red) above.

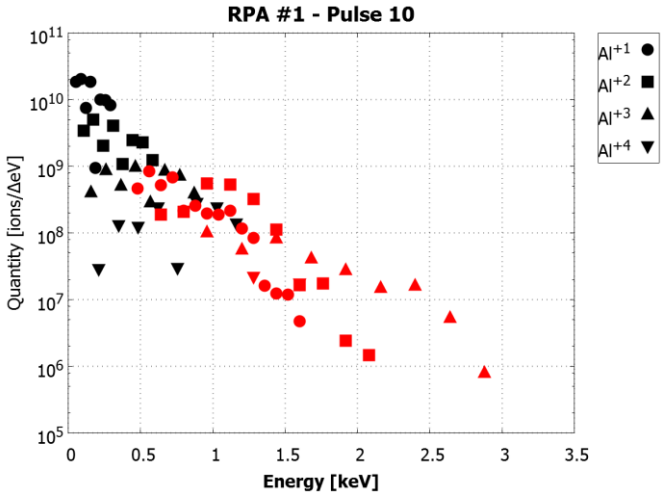

Fig. 105 RPA (black) & Spectrometer (red) Energy Distribution

5.3 Propulsion Metrics

The spectrometer energy distributions described previously were integrated to determine the average velocity, energy, and total mass of material per steradian in the ablation plume. The impulse, the momentum coupling coefficient (ratio of impulse to laser pulse energy), C_m, and the propulsive efficiency (ratio of plume kinetic energy to laser pulse energy) were derived from them. All these together represent a convenient set of metrics by which to compare all the cases. The metrics are presented separately for the spectrometer and RPA datasets, both because the laser

conditions were slightly different and to show what each instrument alone would miss. While the lower energy portion of the ablation plume (observed by the RPA) contains more than 85% of the mass, it accounts for only 70% of the impulse and half the plume energy. Propulsion metrics from both instruments combined, covering the full (ionized) plume, are presented in the conclusion, section 6.2.2.

Both instruments were only able to measure the plume content normal to the surface. This is sufficient to compare results between cases, but requires an estimate of the plume's angular distribution to complete the calculation. Ablation plume distributions are typically modeled by Eq. (48). F_0 is determined from the spectrometer for each case and an n of 6 is based on typical experimental values reported in literature for nanosecond ablation of aluminum [156-158]. Integrating this profile, and assuming the velocity is along the axis from the ablation site to plume edge ($v = v_0 \cos(\theta)$), the mass is 1.05x the per-steradian value and the average velocity is 0.90x the per-steradian value (thus energy 0.85x).

$$F(\theta) = F_0 \cos^n(\theta) \tag{48}$$

Fig. 106 through Fig. 117 show the propulsion metrics, first the spectrometer measurement (>310 eV/e^-) then the RPA measurement (<310 eV/e^-). Recall that Weak Focus #1 & #2 represent long bursts of laser pulses while Strong Focus #1 & #2 include both single pulses and short bursts (5 pulses). For the short bursts, only the final pulse is displayed, so the bursts' result appears immediately before the neighboring single pulse in all these plots. The strong focus cases, having used alternating bursts and single pulses on the same site, are best for comparing the two

pulse schemes. The RPA cases are most similar to Weak Focus #1 & #2, except the 6th pulse, which is in between the Weak and Strong Focus intensities.

Fig. 106 and Fig. 107 show the average velocity of the plume. The additional energy density expected in the strongly focused cases doesn't significantly increase the average velocity, nor does the increased intensity of the 6th RPA pulse. However, there is a clear, though small, gain across all cases from repeated ablation of the same site, mostly disappearing by 25th pulse.

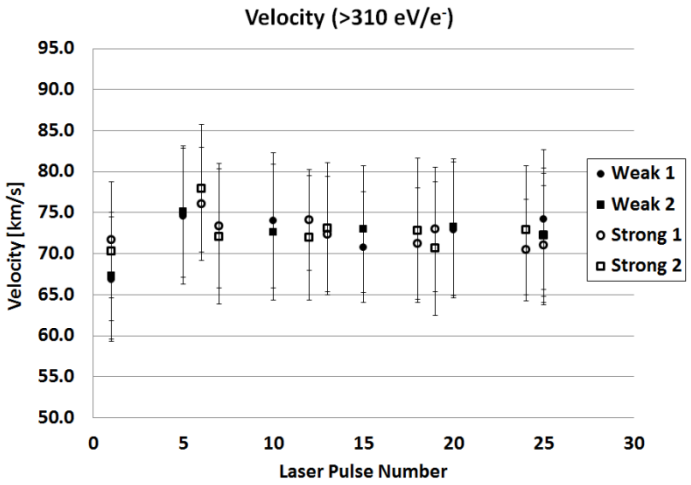

Fig. 106 Average Ion Velocity (spectrometer)

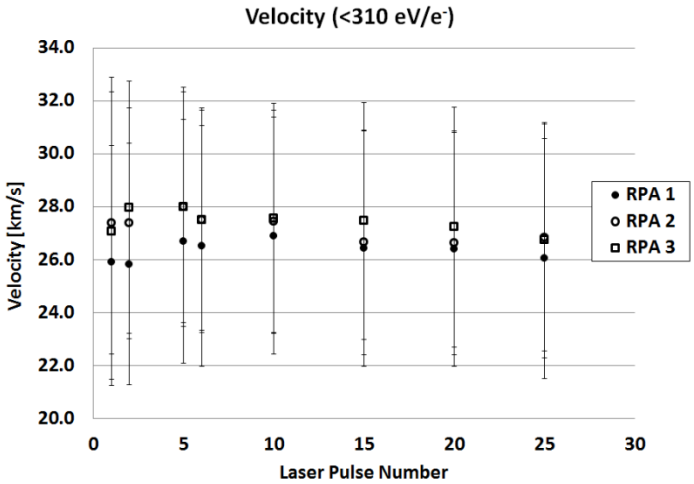

Fig. 107 Average Ion Velocity (RPA)

Calculation of the per-pulse uncertainties displayed in these figures is discussed in Appendix B. An alternative estimate of the measurement uncertainty may be made by taking the normalized standard deviation of all the points using the mean value for the source case. For this calculation the first pulse of each case is ignored and the burst and single pulses are separated, despite coming from the same case. The resulting uncertainty is 2.5% for the spectrometer and 1.7% for the RPA. This does not, by design, include variation between ablation sites, which was discussed in the Data Processing section and is included in the uncertainties from Appendix B. Although each energy level was captured at a different location, all the pulses for that level were captured together. The overall sweep result is, therefore, a sum of values whose variance reflects repeated pulses on the same site, even if the mean value varies more from site to site. Each set of conditions was repeated twice so the pairs provide some insight into overall variability to supplement the analysis in the Data Processing Section.

Fig. 108 and Fig. 109 show the mass removal rate; Fig. 110 and Fig. 111 the impulse per laser pulse. The mass removal is relatively more variable than the velocity between and within cases. Again, the per-pulse uncertainty calculation is in Appendix B. Using the same alternative technique as for velocity, the mass removal measurement uncertainty is 18% for the spectrometer data and 2.5% for the RPA. The variation in impulse is dominated by the variability of the mass removal.

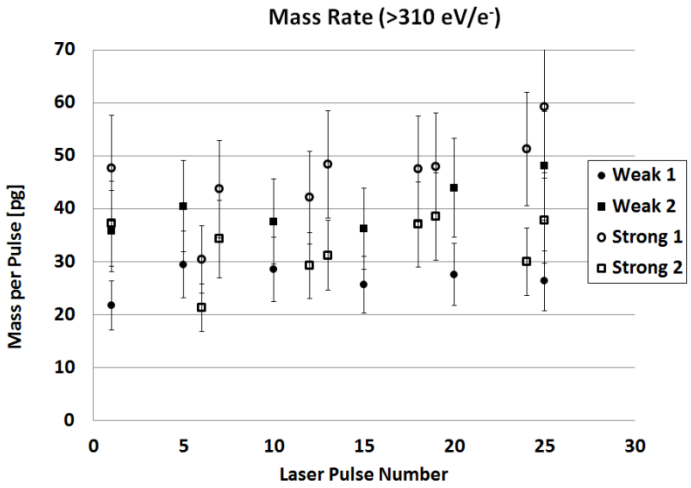

Fig. 108 Mass per Pulse (spectrometer)

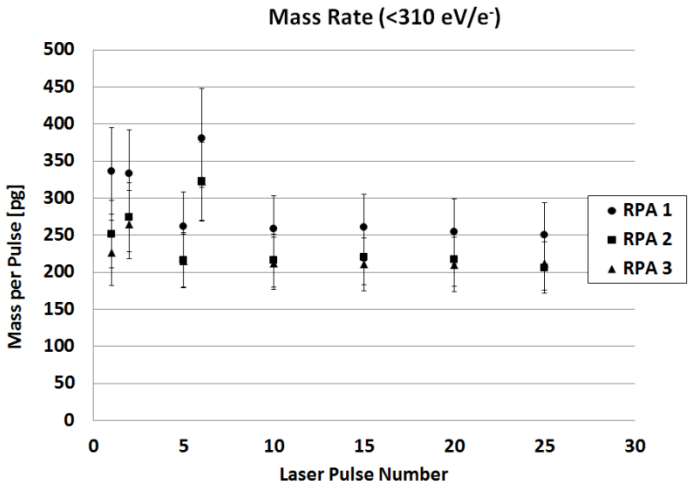

Fig. 109 Mass per Pulse (RPA)

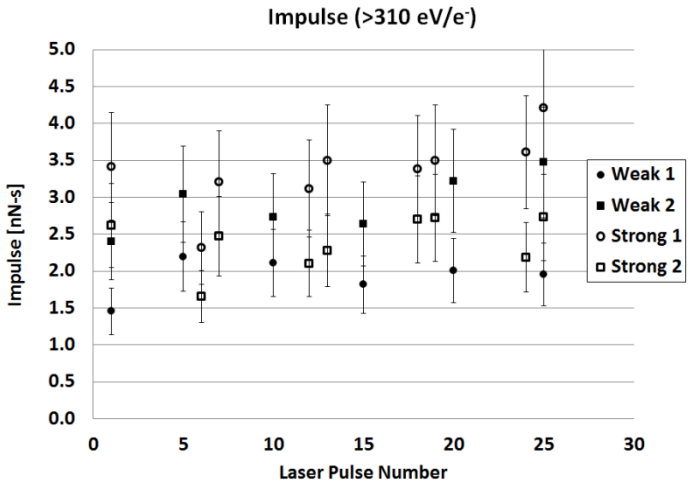

Fig. 110 Impulse (spectrometer)

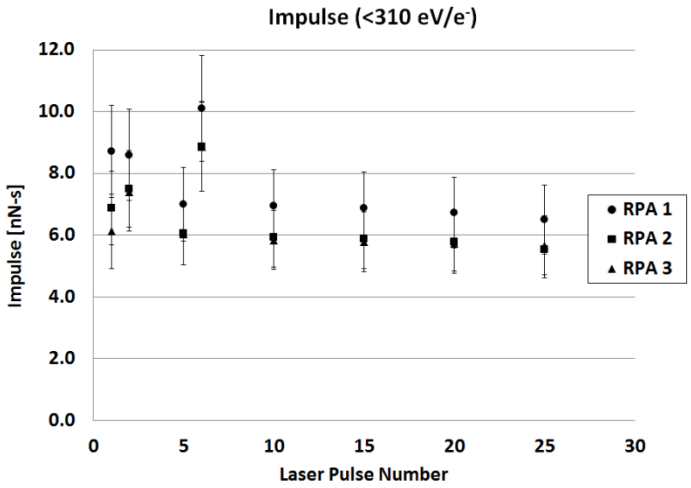

Fig. 111 Impulse (RPA)

The difference between the first and subsequent pulses and between the burst and single pulse modes is much more significant upon considering the pulse energy, Fig. 112 & Fig. 113. The laser pulse energy is an average of the observed pulse energies over all the energy sweep levels, with a typical standard deviation of 1-2%. The first pulse and single pulses have 30-40% more energy than the burst pulses (the 6th RPA pulse has 67% more), which goes to removing more mass at similar velocity. The impulse is increased, but mass efficiency is not improved.

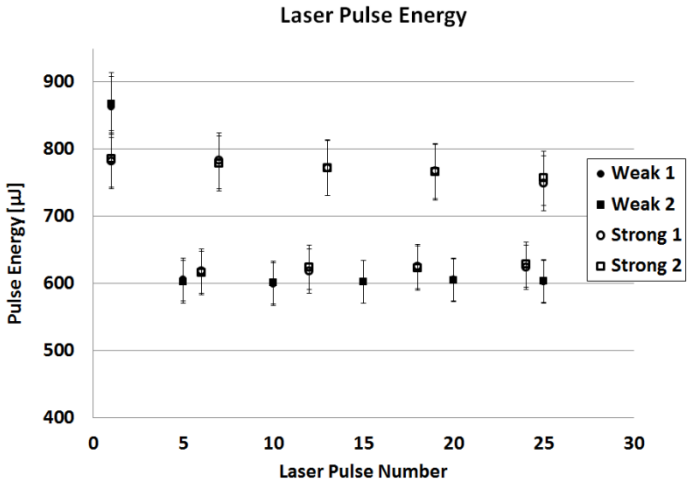

Fig. 112 Laser Pulse Energy (spectrometer)

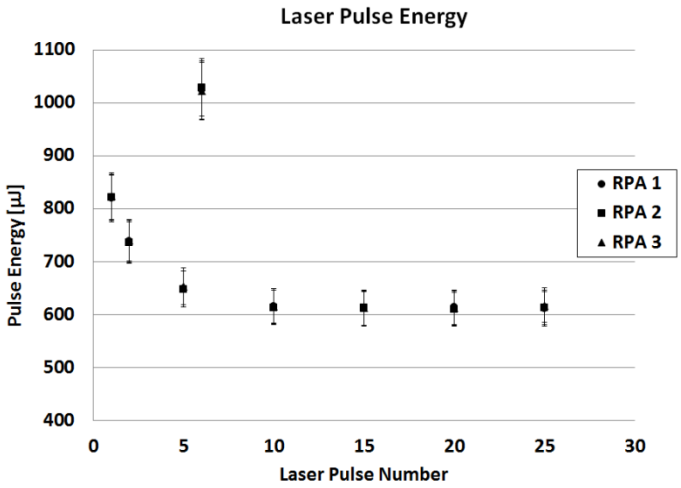

Fig. 113 Laser Pulse Energy (RPA)

Fig. 114 and Fig. 115 (momentum coupling coefficient, C_m) and Fig. 116 and Fig. 117 (propulsive efficiency) show that using bursts to ablate the same site repeatedly makes more efficient use of available power.

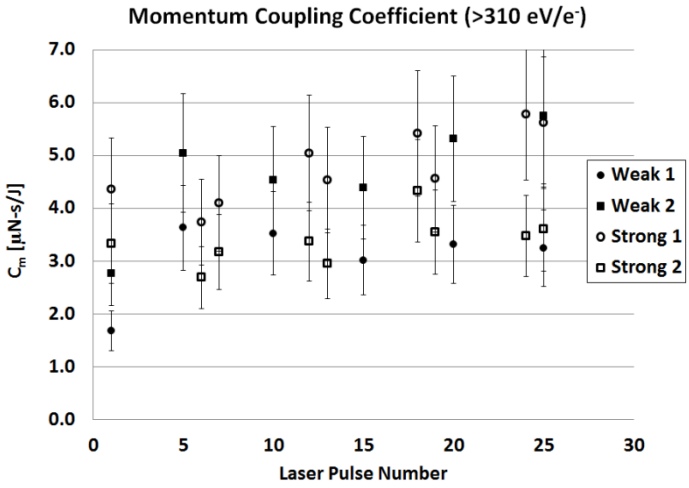

Fig. 114 Momentum Coupling Coefficient (spectrometer)

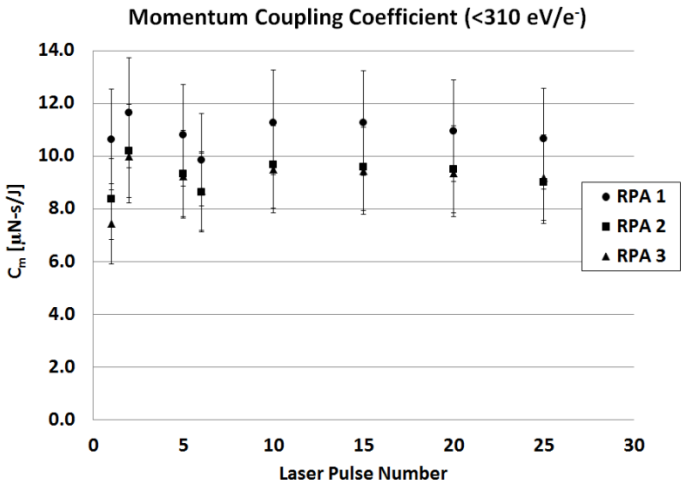

Fig. 115 Momentum Coupling Coefficient (RPA)

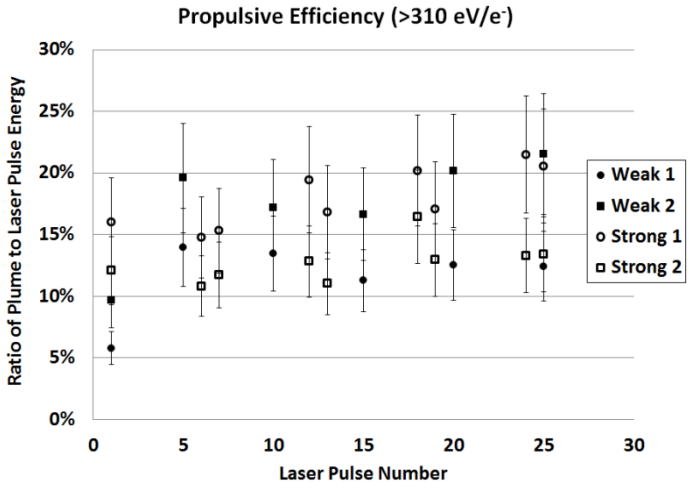

Fig. 116 Propulsive Efficiency (spectrometer)

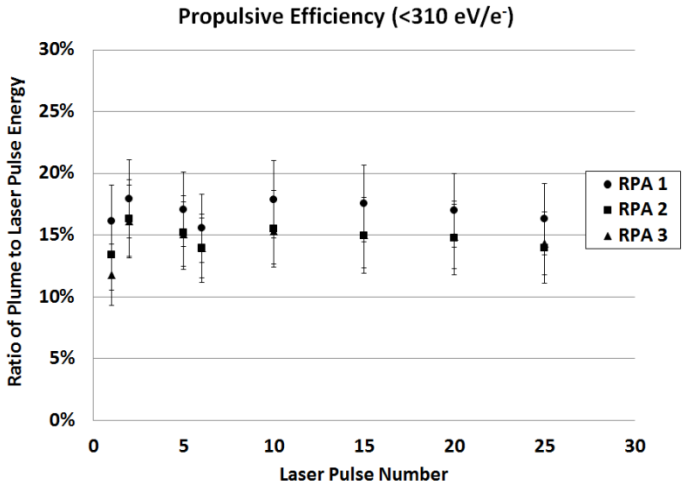

Fig. 117 Propulsive Efficiency (RPA)

Weak Focus #1 and Weak Focus #2 included data after 50 and 100 laser pulses. No other cases went out so far because SEM imaging strongly suggested using no more than 25 pulses per ablation site. Mass removal was widely different between the cases at pulse 50 while velocity was comparable to the other pulses. By pulse 100 both cases saw distinct drops in mass removal and average velocity relative to pulse 25.

These metrics provide the following insight for design of a laser ablation thruster propulsion system for a debris removal tug.

First, using bursts of laser pulses on the same site is preferable to single pulses with each on a fresh ablation site. Neither of these options is precisely achievable if a large portion of a target is to be ablated. The design could, however, approximate single pulses by moving approximately one laser site per pulse, only returning to the original site after everything around it has been ablated, making the surface as close to flat as possible. With a crater diameter of about 50 μm and pulse repetition rate of 40 kHz, the laser from this experiment would need to sweep about 2 m/s across the surface. The results herein show it would be better to have many pulses per site. Based on the steep wall of the crater in Fig. 84 (25 pulses on the same location), the angled drilling, which limits the pulse number per site, could probably be avoided by moving about 13 μm (about $1/4^{th}$ of a crater diameter) away from the steep wall per 25 pulses, 20 mm/s for this laser. The next section considers the lower translation speed limit more directly.

Second, exact laser focusing is desirable but not critical. The performance is similar between both the high and low focus cases (burst vs. single pulses has a

greater impact), indicating that positioning of the laser focus may be at least as far off as the spacing of these two cases (about ±0.5 mm) without noticeable detriment. This provides a tough but manageable positioning accuracy criterion, about 0.1% of the focal length for a similar lens.

Finally, nanoparticles made up significantly more of the removed mass than ions so will significantly lower the effective specific impulse. Looking at ablation craters reported in literature from nanosecond and femtosecond pulses, the latter produce much less damage to the surroundings. The raised features around nanosecond craters, clearly visible even in this work, suggest that higher intensity, shorter duration laser pulses would make more efficient use of a given target. However, nanoparticle content in known to increase with increasing irradiance [5] and the relative mass allocated to nanoparticles vs. ions in these results suggest that the benefit of cleaner future ablation sites may be overtaken by the detriment of significant nanoparticle content.

5.4 Plume with a moving ablation site

Operationally, the laser is likely to be swept across the surface. To gain some insight into the effects of moving the laser across the target surface, a series of videos were taken of the ablation plume with the target moving at different speeds. The target's motion was toward and away from the laser, constrained to the plane of the target surface, which was rotated 45° off the laser focal plane. This is the same orientation and primary motion direction as for the plume composition data collection, but now continuous instead of stepping between groups of pulses.

Fig. 118 shows continuous ablation with a stationary target. The ablation becomes distinctly stronger when the stage is kept moving. Fig. 119 shows the target sliding toward the laser at 10 mm/s, equivalent to the laser shifting toward the steep wall of the ablation crater in Fig. 84. With this direction of motion, the plume reached a stable maximum intensity at a speed of 7 mm/s, equivalent to about 75 pulses per 1/4th crater. For all the tested cases in this direction (up to 13 mm/s), the plume was visibly asymmetric, appearing tilted back toward the laser. Fig. 120 shows the target sliding away from the laser at 10 mm/s, moving the laser spot away from the steep wall of the crater. With this direction, the plume reached a stable maximum intensity at 4 mm/s, equivalent to about 130 pulses per 1/4th crater. This direction was also tested up to 13 mm/s and shows little change after reaching the maximum visible intensity. The plume appears to be normal to the target surface as long as the target remains in motion.

The plume is bright enough to make it impossible to properly identify the edges and the video is slow enough that each frame contains well over 1000 pulses. It is still apparent that, as expected, it is preferable to move the laser across the surface away from the steep side of the ablation crater. Combining with the crater imaging, the sweep rate should be somewhere between 4 and 20 mm/s (25-130 pulses per 1/4th crater).

Fig. 118 No stage motion

Fig. 119 Stage moving 10 mm/s left

Fig. 120 Stage moving 10 mm/s right

5.5 Other Observations

5.5.1 Nanoparticles and Clusters

The photomultiplier output from all of the single laser pulse and short burst cases was examined for any single particle impacts. Fig. 121 shows an example of such an impact. Cases were reduced to a manageable number by calculating the cross-correlation of the signal with an exponential decay, using the readout resistor and calculated parasitic capacitance, and examining all those cases that exceed 30 mV.

Recall that data beyond 100 μs was only captured if some point exceeded 100 mV, the threshold selected based on observed noise.

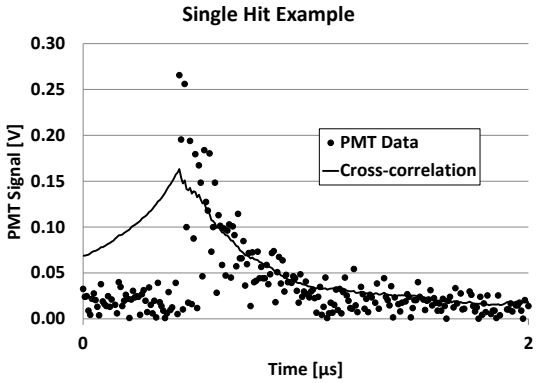

Fig. 121 Example Ablation Single Particle Impact

A total of 51 possible single particle impacts were found over the Strong Focus cases, representing 9 and 18 pulses per energy level, respectively. Of those cases, 14 exceeded the 5 V measurement limit. Given the number of pulses and the number of particles observed via SEM, discussed in the Data & Processing chapter, many more hits were expected. Fig. 122 shows the mass-to-charge ratio and energy-per-charge of the observed hits, where the mass-to-charge ratio is in multiples of Al^{+1}. The particle distribution from Fig. 78, based on SEM observations, shows no particles larger than 50 nm diameter, which corresponds to$10^{6.6}$ multiples of Al^{+1}. Fig. 122 shows significant content with a higher mass-to-charge ratio than the highest observed by SEM.

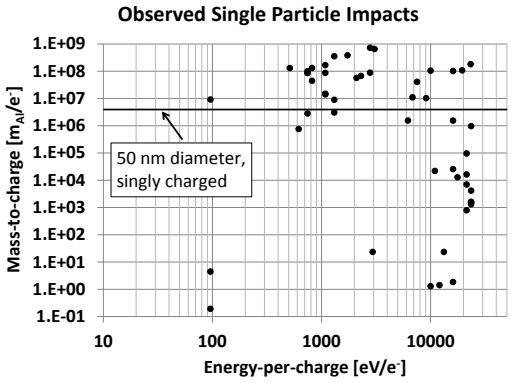

Fig. 122 Observed Single Particle Impacts

Fig. 123 and Fig. 124 show the signal heights (for those less than 5 V) vs velocity and energy-per-charge respectively. The size of the signal from each impact goes down with increasing velocity and doesn't change significantly with increasing energy. In both cases the change is in the opposite direction of expectation and significantly smaller than expected given the several order-of-magnitude range over which the observations occur. Combined with the unlikely high mass-to-charge ratios in Fig. 122 (> 50nm, singly charged) it is unlikely that most of these are real single particle hits. There were insufficient impacts of small to medium clusters to clearly establish a relationship between impactor size and signal height. Ideally the signal height vs. particle size would be determined by calibration against a known nanoparticle source and an anti-coincidence system added to the spectrometer, making it possible to assess small numbers of impacts.

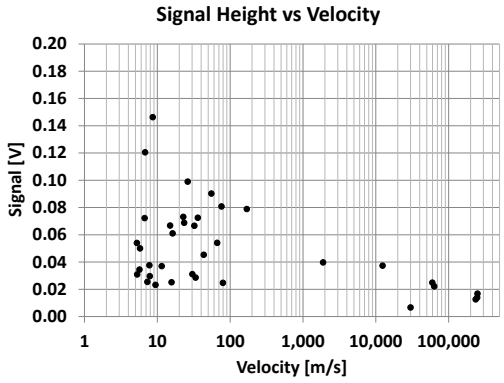

Fig. 123 Single Impact Signal vs Velocity

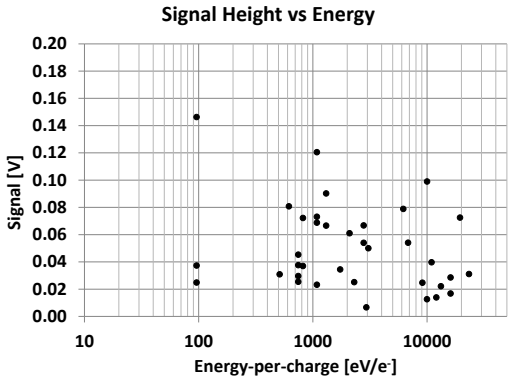

Fig. 124 Single Impact Signal vs Energy

There were a number of clear observations of small clusters (2-4 atoms), but they mostly appeared to represent multiple hits rather than individual impacts (the signal rise was not sufficiently sharp). Fig. 125 shows a rare example with three clusters of up to 8 atoms. Although not appearing nearly as frequently as single ions, the smallest clusters did appear in a number of cases, including some that showed more than one cluster size following a single laser pulse.

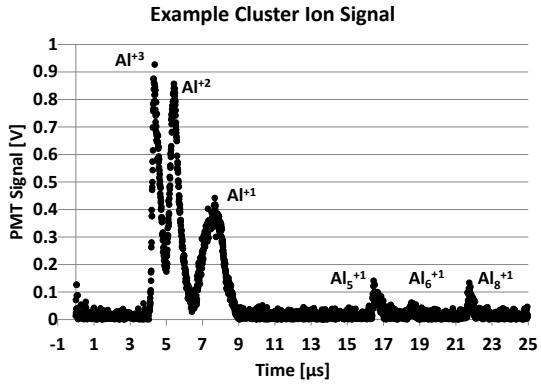

Fig. 125 Example of Observed Clusters

Observations with the ionic liquid particle source demonstrated the ability to observe, even with reduced scintillator bias, singly charged ions equivalent to a cluster of 19 Al atoms. The PMT current using the ionic liquid source was 14 nA. The PMT output signal for single ions in the ablation cases was routinely greater than 10 μA, almost 1000x higher than for the ionic liquid source. The lack of cluster observations is, therefore, due to absence as a significant plume component rather than inability to detect, at least up to about 20 atoms.

5.5.2 Anomalous PMT Signals

Some cases showed a long continuous signal, unlikely to be real. Fig. 126 and Fig. 127 show examples of such signals. This occurred in 30 cases, all of which had an 8 kV bias applied to the scintillator and 28 of which were from the same energy sweep. None of the cases showed a meaningful signal either at nearby energy levels or at the same level in another laser pulse or in the second energy sweep. One secondary ion and several negative beam cases showed a shorter and lower signal, but with the same time of occurrence across all energy gate biases. It is suspected that the signal in those cases is also caused by the high scintillator bias.

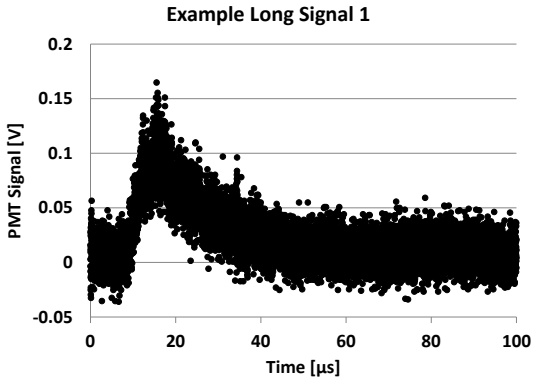

Fig. 126 Example of a Long Signal 1

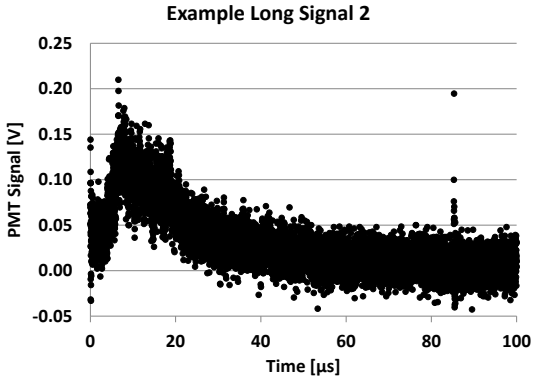

Fig. 127 Example of a Long Signal 2

Chapter 6: Conclusions, Limitation, & Future Work

6.1 Spectrometer Performance

Using the ionic liquid particle source, the spectrometer was demonstrated to be able to observe both positive and negative polarity beams using secondary electrons and secondary ions for particle detection. The ability of the scintillator to see secondary ions was demonstrated a second time by redirecting the ablation plume within the detector to hit the scintillator directly rather than impact the rear wall of the detector. Unsurprisingly, the yield was higher for higher charge states.

The ionic liquid data were sufficient to demonstrate that the secondary ion mode yield is proportional to the square of the particle velocity while the secondary electron mode requires a higher power of the velocity. There was no clear dependence on ion mass for either secondary particle yield over the 3x mass range evaluated. It is natural to assume the yield is proportional to mass. If that is the case, the yield would be proportional to ion kinetic energy. The impact energy in this work is determined solely by the charge state of the ion (for a given spectrometer bias configuration). The ionic liquid source produces singly charged ions, so it would be expected that all ions studied would produce indistinguishable yields. The secondary electron yield should still have shown some mass dependence (or equivalently some velocity dependence). The lack of mass dependence is clearly inconclusive due to the variability of the ionic liquid source's output. No signal was seen with the aluminum ablation source using secondary ions, despite a significantly higher impact velocity compared to the ionic liquid ions, so it is probable that there is a lower mass limit for secondary ion emission in the energy range used.

The main peaks for each ionic liquid ion showed the expected energy passband, despite being of a single polarity for roughly twice the length of the energy gates (wherein inter-particle forces are of concern). However, the energy-per-charge was sufficiently high and the overall beam current sufficiently low that simulation suggested no deviation of the passband due to inter-particle forces within the spectrometer. The ablation data showed several likely effects of inter-particle repulsion. At low energy-per-charge, particles were observed to arrive earlier than otherwise predicted, to have wider Gaussian pulse shapes, and to have slightly distorted pulse shapes. Al^{+2} was most impacted by slightly distorted pulse shapes, perhaps due to a high content within the plume. Al^{+1} had a double peak up to the highest energies, so that is likely a feature of the plume rather than an effect of the spectrometer. Below about 320 eV/e^- the combination of effects made it difficult to distinguish the pulses from individual species.

The spectrometer failed, in some cases, to see particles below 200 eV/e^-. This is presumably caused by beam expansion due to inter-particle forces, as predicted by simulation. Particle defocusing within the accelerator should also have caused a loss of some particles below about 350 eV/e^-, but not more than 40% by 100 eV/e^-, which is much less than expected from inter-particle forces. There were, however, cases that did show content below 200 eV/e^- energies, making for a more complicated picture.

Looking at four full energy sweeps performed with the weaker laser focusing condition, the first two saw a significant drop in particle content starting at 320 eV/e^-, with all content gone between 240 and 160 eV/e^- across all laser pulses (so not a single bad capture). The second two saw noteworthy content down to 160 eV/e^-,

though it might still have been underreported. The bulk of the particle content in the second two cases is 100-200 eV/e^- lower than for the first two cases, so it would not be unreasonable to conclude that the full beam has been observed. RPA data indicates that 85-90% of the plume is below 310 eV/e^-, with an average energy of 144 eV/e^-. While the RPA has issues with electron infiltration at high energies and the high variability of the ablation plume, this result is still sufficient to conclude that the spectrometer is, in fact, missing some of the plume. The spectrometer and RPA may be used cooperatively, as for parts of this work, or adjustments made to improve spectrometer performance at low energies. The easiest fix is to lower the charge density of the beam entering the spectrometer in a controlled fashion.

The spectrometer's output could not be sufficiently calibrated to completely recreate the aperture current, RPA data, or even just the RPA data above 310 eV/e^- (though the fit was better in that case). The spectrometer observed 6-7x less mass than the RPA and filled about half the area of the RPA signal above 310 eV/e^-. The cause is likely a combination of unmodeled inter-particle forces within the RPA, poor charge determination in the RPA data, unobserved plume components within the spectrometer, and inconsistency in the aperture current between cases (preventing capture-by-capture rescaling). Improved measurement of the aperture current for both instruments, in addition to the other improvements discussed for other issues, should help.

With the ionic liquid EMI-$GaCl_4$, the spectrometer demonstrated the ability to observe individual particle impacts using both beam polarities and both secondary particle options. The photomultiplier performed within expectation, and the system

was able to observe single photoelectrons, albeit with a difficulty in extraction from background noise. The scintillator yield, on the other hand, was significantly lower than anticipated, 570x based on ablation results, with comparable results from the ionic liquids. The low scintillator yield prevented single-impact particle sizing tests with ionic liquid data. It may also have hidden single particle impacts from the ablation particle source, where the background noise was higher. A number of apparent single-particle impacts were observed from the ablation source; however their distribution was highly improbable, suggesting shot noise. A lack of intermediate sized cluster ions (e.g. 5, 10, and 20 atoms with 1 charge) prevented any attempt to build a correlation between secondary particle yield and primary particle size, and further suggests the apparent impacts were not real.

Data processing proved more challenging than anticipated. Time-of-flight signals at high energy-per-charge showed that a Gaussian detector input pulse model is appropriate, as simulation of the energy gate passband suggested. Fitting the signal to that model was effective at removing noise and generating the clean derivatives required for deconvolution or the RC output circuit distortion. Noise and misshapen pulses (presumably due to inter-particle repulsion within the spectrometer) made automatic fitting unreliable.

The main difficulty was in determining where pulses should occur. The signal could not be relied upon to drop below any specific threshold between species, particularly at low energy (Fig. 51). Random noise or an occasional larger oscillation (several MHz, likely conducted from a power supply) would impede a slope-based peak detector while sufficient smoothing to remove them would also remove small

peaks in the signal. Fixed locations were not sufficient because the pulses would arrive earlier with lower energy-per-charge, and a pulse applied where there was no signal would occasionally fit the random noise. Having identified the main peaks, the Gaussian pulse assigned to fit a smaller peak might be drawn over to relatively small variations in a larger peak, fitting noise on the large peak while missing the real signal of the small peak. An applied pulse might also get drawn to fit oscillatory noise features in the signal. Most of these issues can be reduced by design improvements to the spectrometer, particularly including increasing the scintillator yield (thus signal-to-noise ratio). Regardless of spectrometer design improvements, they are likely solvable, perhaps requiring significant effort, through improvements to the fitting technique.

6.2 LAT Design Considerations

6.2.1 Laser Pulse Pattern and Focusing Requirements

Three laser burst patterns (single/5/many) and two focusing conditions (strong/weak) were considered, as well as variation with the number of repeated pulses on the same site. The plume was observed with the mass spectrometer and details reported for the material over 310 eV/e^-, the range the spectrometer was best able to observe. The character of the results did not change significantly when using the full range of mass spectrometer data. The results are assessed relative to the first pulse of each case. This avoids the undesired variability between cases. The variability is clear from the initial pulses, which should be the same for all cases with the same focusing condition.

SEM imaging of the ablation craters shows that, by the 25th pulse the angled laser beam has started to drill under the neighboring surface. Repeated ablation beyond 25 pulses on the same site should, therefore, be avoided.

The largest gain across all tests resulted from simply re-ablating the same site several times. The strong focus burst mode and both low focus pulse patterns saw a significant rise in mass removal and average velocity after the first pulse. The single pulse strong focus case, on the other hand, saw much more limited gains from repeated pulses.

The burst pulse modes generally performed better than the single pulse modes. The difference was much more apparent with the strong focus tests, where the burst mode was always better. Presumably this is because the strong focus testing alternated single pulses and 5 pulse bursts – using the same ablation site reduces variability. The strong focus, burst mode cases were slightly better than the low focus cases, but the difference was not sufficient to warrant significant effort maintaining the higher focusing condition.

In operation it is unlikely a laser ablation tug will make discrete steps across the target surface. It will most likely sweep continuously across the surface. Sweeping the laser across the target (actually, moving the target) was evaluated at difference speeds and directions by visual observation of the plume. Sweeping the laser towards the shallow end of the crater (back towards the laser source) produced a visibly better directed and more stable plume compared to the other direction of motion. A minimum speed across the surface of 4 mm/s (about 130 pulses per 1/4th crater) was required to produce the stable plume.

6.2.2 Overall Performance

In addition to the spectrometer data, an RPA was used to observe the weak focusing condition with a long burst of laser pulses. The RPA was able to assess the overall plume current, but was only able to estimate charge states and thus propulsion performance below about 310 eV/e^-. The spectrometer was able to observe reliably at least down to 310 eV/e^-, but started to lose reliability below, presumably due to inter-particle repulsion within the spectrometer. The RPA and spectrometer data sets were combined to produce an overall estimate of the charged components of the plume. Overall the spectrometer and RPA observations of Al^{+1} through Al^{+4} were able to account for 86% of the observed plume current. The performance metrics calculated for laser pulse 10 for the RPA, spectrometer, and overall plume are presented in Table 9, with all values accounting for the assumed plume profile, Eq. (48).

Table 9 Ablation Plume Summary

Case	RPA	Spectrometer	Total
Composition by Charge[a] [%]	96.5	58	86
Composition by Mass [%]	85	15	8[b] ± 15%
Ionized Mass [pg/sr]	220 ± 17%	32 ± 21%	250 ± 15%
Average Velocity [km/s]	30 ± 17%	81 ± 11%	33 ± 13%
Impulse [nNs/sr]	6.5 ± 17%	2.7 ± 22%	9.3 ± 13%
Kinetic Energy [μJ/sr]	120 ± 17%	110 ± 22%	230 ± 14%

a) vs charge below 300 eV/e^- measured by RPA

b) vs total mass observed by spectrometer and RPA

A mass removal rate of 1.5 ng per pulse was estimated from SEM imaging of the ablation crater. Using this, the observed ions represent 8% of the removed material and the effective specific impulse is at least 270 seconds. Dividing the remaining energy over the remaining mass, the maximum effective Isp would be 1,400 seconds (impulse 69 nNs/sr). The nanoparticle collection results suggest they represent a large portion of the mass. As discussed in the nanoparticle collection

section, the observed nanoparticle flux was 4.4 ng per steradian per pulse. Using the assumed plume profile, that is higher than the total mass removal observed per pulse, so it is not viable to estimate the ratio of nanoparticles to atomized mass. It is reasonable, however, to conclude that the Isp will be closer to 270 than to 1,400 seconds.

6.2.3 Alternate Laser

This work considered one particular laser pulse duration and intensity on the expectation that decreasing pulse duration and increasing intensity would improve the mass efficiency of the laser system. The results herein were compared with the plume composition from [1]. In that work, the laser pulse duration was 5 ns (vs 0.7 ns here), the intensity was 1.0×10^{10} W/cm^2 (vs 9.0×10^{10} W/cm^2 here), and the laser was not as strongly focused as in this work (0.3 mm^2 vs 1.3×10^{-3} mm^2 here). The observation in [1] was made 0.35 m from the ablation site compared to this work where the spectrometer started at 0.27 m (end at 0.37 m) and the RPA was placed at 0.19 m. The different laser pulse energies are accounted by presenting relevant parameters per joule of laser pulse energy. Table 10 shows the per-laser-energy values from [1] and this work.

Table 10 Ablation Plume Summary – per Laser Energy ([1])

Case	[1]	This Work
Composition by Mass [%]	3	8[b] ± 15%
Average Velocity [km/s]	39[a]	33 ± 13%
Avg Kinetic Energy [eV]	240	200 ± 20%
Ionized Mass [ng/J-sr]	290	260 ± 16%
Kinetic Energy [mJ/J-sr]	260	320 ± 15%
Impulse[a] [μNs/J-sr]	11.5	14 ± 14%
Specific Impulse (ionized plume) [sec]	120	270 ± 20%
Laser Energy [mJ/pulse]	125	0.60 ± 5%

a) Estimated from average kinetic energy
b) vs total mass removal from SEM images

The shorter, higher intensity pulses produced a higher ionization fraction, but with slightly lower energy ions. Accounting for the ionization fraction, the slower pulse ablated about 1.7x more mass than the shorter pulse. Both cases invest a significant faction of the laser's energy into the ionized portion of the plume. Given that, the neutral component of both plumes will have to be significantly slower on average than the ion portion. Dividing the remaining energy from [19] evenly over the remainder of the ablated mass yields an overall specific impulse of 1,000 seconds (momentum coupling 98 μNs/J). Just like the shorter pulse (1,400 seconds, 69 μNs/J), this high estimate is unlikely to be met. Still, it suggests the high intensity case will have lower thrust and higher mass efficiency after accounting for the neutrals.

6.3 Future Work

6.3.1 Spectrometer Design Updates

All of the issues observed with this spectrometer design are solvable (or at least significantly improvable). The most significant issue is the low scintillator yield. The easiest fix is to increase the scintillator bias. Data from both aluminum ablation and ionic liquids show a super-linear gain in signal for increasing scintillator bias in

at least the secondary electron cases. It was noted during testing that changes in scintillator bias had a significantly larger impact on signal strength than changes in the detector bias. The scintillator bias was not increased in this work because shorting was observed. The scintillator mounting structure, and possibly the rest of the detector's structure, will need to be redesigned to support a higher scintillator bias. Consideration should be given to applying a thin metal coating to the scintillator to reflect light that would otherwise leave away from the PMT. The coating may prove detrimental by impeding ions or lower energy electrons reaching the scintillator interior.

The aperture current may be improved by adding two or three mesh grids in front of the aperture and using an annular plate. The outer mesh would be grounded and the middle mesh biased to reject electrons, just as for an RPA. These protect the annular plate, which can then measure the arriving current free from electrons. If the mesh wire spacing is sufficiently close it will block some of the beam from entering the spectrometer aperture, ultimately reducing beam distortion within the spectrometer.

If the added aperture grid does not reduce particle flux sufficiently to ignore inter-particle repulsion, the current entering the spectrometer may be reduced by other means. Most beneficial is simply increasing the flight length – the beam will spread out more before reaching the spectrometer and the relative particle timing will be more precise. Alternatively, the beam may be intentionally defocused in a controlled fashion prior to entering the spectrometer.

Addition of an ionization stage to the spectrometer entry would allow observation of otherwise neutral particles. It would ideally be placed just prior to the spectrometer entrance, between the grounded mesh and the electron rejection mesh.

The impact of inter-particle forces might alternately be addressed by replacing the parallel plate-based energy gates with a cylindrical energy gate. The cylindrical gate's curved plates are significantly closer together, resulting in a stronger electric field and causing ions of incorrect energy to strike the plates and be removed much more quickly than in the current design. The parallel plate design was chosen to provide flexibility in arrangement and to be able to switch the gates on and off rapidly. The switching ultimately was not required because the laser's inter-pulse delay was long enough for all particles to reach the detector.

Cross-axis alignment features should be added to the 3-D printed part. The part provided excellent spacing of the various flat plates normal to their surface, the most important axis for each. The plates were bolted to the 3-D printed part. In order to insert the bolts, the holes in both the 3-D printed part and the plates had to be slightly larger than the screw, allowing slightly erroneous alignment in two axes. Slight horizontal and vertical steps should be added to the 3-D printed part to ensure precise and repeatable alignment along those axes as well. The lower edge of the plate would rest on the horizontal step, one side edge would be pressed against the vertical step, and the face would be pressed into the 3-D part as it currently is.

6.3.2 Development of a Dual Polarity Secondary Particle Detector

Results from the ionic liquid particle source demonstrated that the secondary ion energy yield is almost linear in ion energy-per-mass (Fig. 93) while the secondary

electron yield is more quadratic (Fig. 92). Other works (e.g. [144]) have noted the secondary electron yield per mass being proportional to velocity to a power greater than 2, thus super-linear in energy-per-mass. Given the different dependence on velocity and a common proportionality to mass, the two yields could be combined to yield the actual impact velocity (dividing electron yield by ion yield) and impact mass (via the calculated velocity and either yield). Addition of either a time-of-flight stage or an energy-per-charge measurement would allow calculation of the charge state as well. The combination of dual polarity secondary detector and energy gate is particularly useful when low particle flux or timing uncertainty make time-of-flight assessment infeasible or where mass-to-charge ratio alone is insufficient for full mass determination. The detector could be similar to that from this work, but with a second scintillator and photomultiplier above the primary particle impact site – a mirror image of the current scintillator, but with a bias for the opposite polarity secondary particle. To prevent the primary from being deflected, a low bias mesh (ΔV) would be required on each side of the primary particle path prior to the secondary particle acceleration region. This configuration is illustrated in Fig. 128. A range of different ions should be investigated to verify that the observed relationship between the yields holds and to develop calibrations for future measurements.

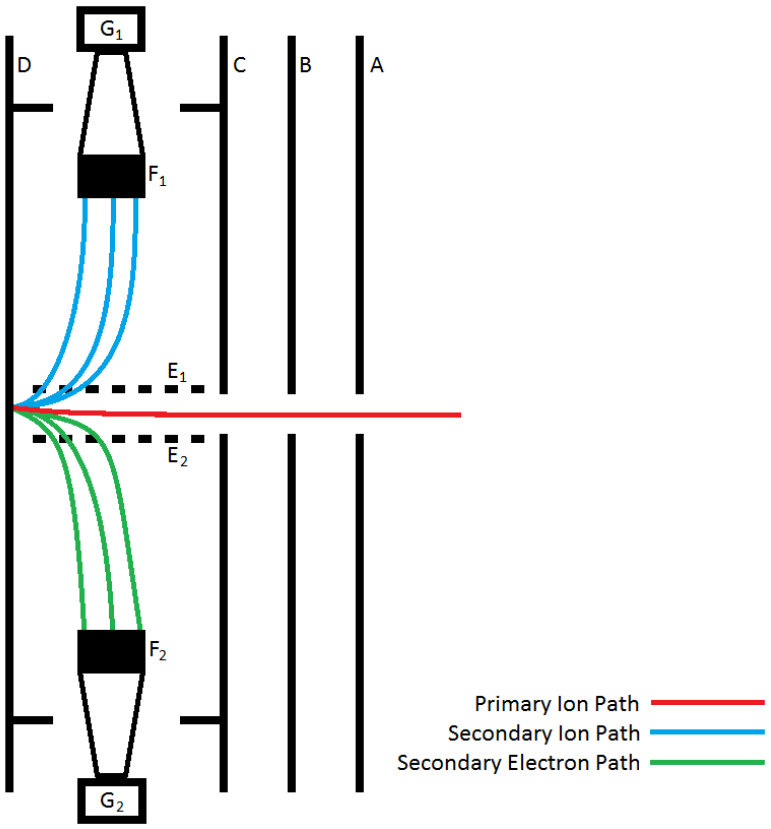

Fig. 128 Dual Polarity Detector

A: entry plate, grounded
B: accelerator plate, $V_{accel} = 8.7*U$ or V_{det}
C: detector entry plate, V_{det}
D: detector target plate, V_{det}
$E_{1/2}$: field reduction grids, $V_{det} \pm \Delta V$
$F_{1/2}$: scintillators, $\pm V_{scin}$
$G_{1/2}$: photomultipliers, V_{pmt} = -1 kV

6.3.3 Ionic Liquid Broken-dimer Peaks

Most ionic liquid data showed at least one lower peak in addition to the main peak. The energy of the lower peak relative to the main indicates the peak represents dimers that have broken up in flight prior to the mass spectrometer energy gate. Comparing the yield of the broken-dimer and main peak in secondary electron and secondary ion modes shows a significant drop in relative yield from secondary electron to secondary ion mode. The drop must be a detector phenomenon, since the

gate biases are identical for both secondary particle options. Biases within the detector cannot be the issue because the negative beam secondary electron mode uses a functionally identical configuration to the positive beam secondary ion mode, and both beam polarities show the same large relative drop in the broken-dimer peak. The broken-dimer energy-per-charge, prior to acceleration, is much lower than main peak.

Varying the detector bias, thus particle impact energy, showed that the observed drop is much larger than the difference in impact energy would explain. In addition, there was no apparent dependence on monomer to dimer mass ratio, which changes the relative energy of the broken-dimer peak. An issue of ionic liquid source setup can also be ruled out based on observing the same phenomenon even when the only change between secondary electron and secondary ion mode observations was turning up the scintillator bias power supply voltage. The data collected from the ion source cannot distinguish monomers and dimers, so dimers surviving to reach the detector, although not expected, cannot be eliminated as a possible cause. If dimers are the cause, their higher mass can be eliminated as the determining factor by comparing the main peak of the EMI-BF_4 positive beam (dimer mass 309 amu) against the broken dimer peak of the EMI-Im negative beam (monomer mass 280 amu). The broken dimer peak drops 60x while the main peak drops 5x between secondary electron and ion modes, even though the EMI-BF_4 main peak is barely larger than the Im^- broken-dimer peak. The relative drop in the broken-dimer peaks compared to the main peak, having eluded the most likely explanations, is a good candidate for further investigation.

6.3.4 Explicit Detector Calibration for Nanoparticles

In this work, the nanoparticle components of the beam were not well controlled. The upper mass detection limits of the detector design in this work (after the aforementioned improvements) should be evaluated using a more controllable nanoparticle source, ideally including control of the nanoparticle charge state. Matrix assisted laser desorption/ionization (MALDI) provides a viable mechanism for generating a beam of singly charged nanoparticles [148,159]. Nanoparticles of known size and composition are mixed into a material (the matrix, typically a plastic) with an ablation threshold much below that of the nanoparticles. Under irradiation just above the matrix's ablation threshold, the matrix is converted into an ionized plume. The nanoparticles imbedded in the matrix are expelled along with the matrix material and ionized by interaction with the plume of matrix material. The matrix material would be removed either by the energy gate of the mass spectrometer or the electron rejection grid prior to the spectrometer entry aperture. An extra ionization stage may be added either just before the spectrometer entry aperture or just after the energy gates to drive up the nanoparticle charge state, increasing the impact velocity for a given detector bias.

6.3.5 Applications of Collected Data

The data collected in this work, and any follow-on work using the improved spectrometer, should be used to predict the performance of laser-electric hybrid propulsion systems (e.g. [14]). Once the plume of a given laser has been characterized, a suite of laser-electric hybrid options can be considered on paper, saving effort for building and testing only the most promising options. A laser-

electric hybrid might be reasonable for a laser ablation tug to improve the mass efficiency of whatever laser is ultimately selected and/or to allow dialing of thrust (traded against mass efficiency) without requiring variable laser parameters.

The details of the ablation plume should also be used to estimate the effect of the plume upon the tug spacecraft. Although the design is far from complete, it is probable that a laser ablation tug would be at least partially within the ablation plume coming from the target satellite. As the tug will be exposed to the plume for an extended period, days to weeks at least, impingement may be a serious issue. The on-axis observations from this work provide a worst case scenario. Ideally, additional observations should be performed with the spectrometer closer to the laser's angle.

6.3.6 Maximize Laser Ablation Tug Target Usage

While this work would be profitably repeated for other laser parameters and using the spectrometer improvements discussed above, there is another significant area of investigation needed in support of the laser ablation tug concept. For consistency sake, this work used fresh ablation sites for each observation, with sufficient spacing to avoid the influence of damage from previous ablation events. A laser ablation tug would most likely have to ablate nearly all the outer surfaces of any satellite it deorbits.

As a first step, the plume from two immediately adjacent ablation sites should be assessed. For each observation, a number of pulses would be applied to a site and the plume observed as in this work (again with the improved spectrometer design). The ablation site would then be shifted by the nominal diameter of the ablation crater and the same observation case repeated. Pairs of observations would be made at all

desired energy levels to complete the plume. Assembling all the second sites and comparing to the first sites will show how the plume is affected by the damage. Assuming performance is reduced by damage from previous laser pulses, the next step is to assess mitigation techniques. For each technique, the resulting surface morphology should be examined by SEM and any promising options evaluated by the same tight spacing of ablation spots used for the baseline.

The final step is to attempt to drill completely through a target, measuring the applied impulse at intervals. To be meaningful, the area removed must be significantly larger than the laser beam width. A strong candidate for improving the ablation of neighboring sites and enabling complete target penetration is to use one or more very low fluence laser pulses to melt the smallest possible layer of the target surface, hopefully allowing surface tension to smooth out all the surface irregularities visible in SEM images of ablation sites (e.g. Fig. 81). The low fluence would be achieved using the nominal pulse energy with a less focused beam, allowing numerous ablation sites to be resurfaced simultaneously.

Appendix A: Results Plots

A.1 Spectrometer Sweep summary plots

None of the corrections discussed in the Data Processing section, except removal of the RC distortion, have been applied to the results in the sweep summary plots below. Energy levels for which no signal was observed are not included – those that appear empty do so because the signal is so much lower than the maximum. Extra energy levels were evaluated for Weak Focus #1 Pulse 15, so the presence of a level there does not indicate that other Weak Focus #1 pulses showed nothing at that level. Slightly different energy levels were evaluated for Weak Focus #1 & #2 compared to Strong Focus #1 & #2.

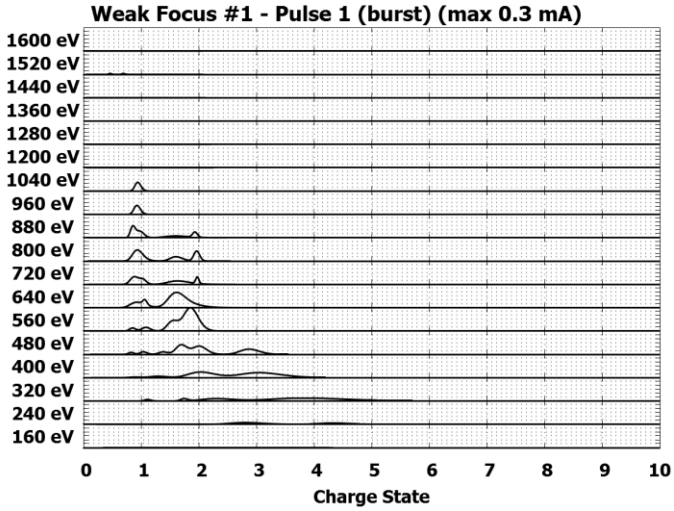

Fig. 129 Weak Focus #1 Pulse 1 Sweep Summary

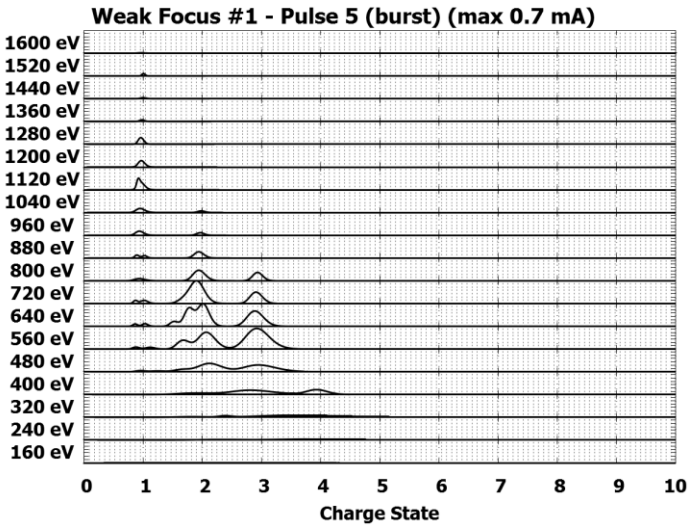

Fig. 130 Weak Focus #1 Pulse 5 Sweep Summary

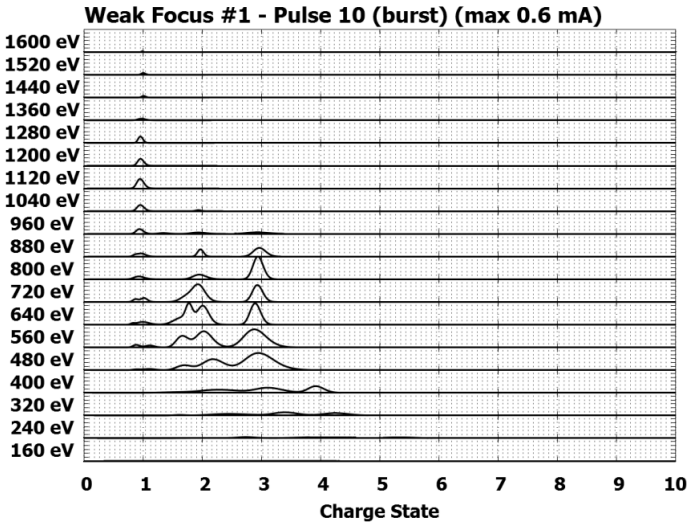

Fig. 131 Weak Focus #1 Pulse 10 Sweep Summary

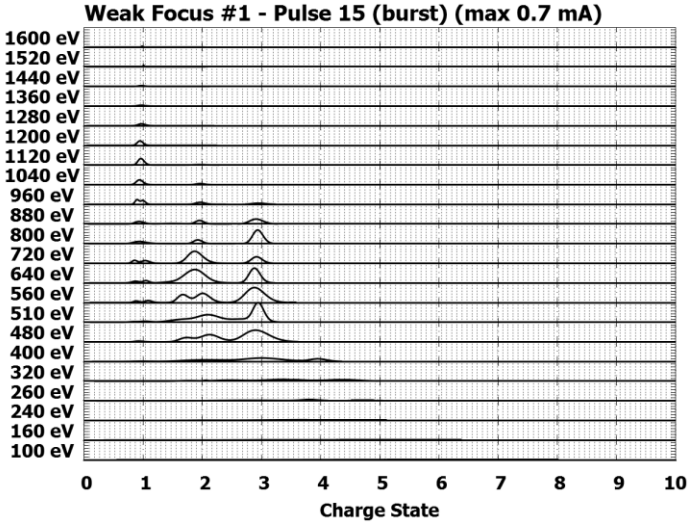

Fig. 132 Weak Focus #1 Pulse 15 Sweep Summary

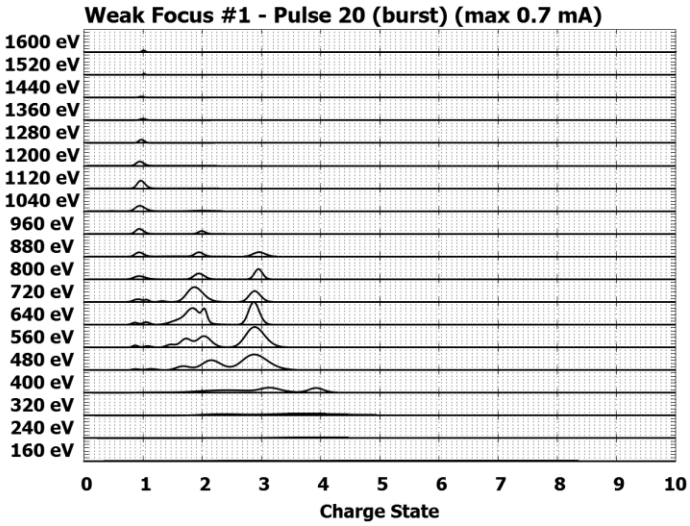

Fig. 133 Weak Focus #1 Pulse 20 Sweep Summary

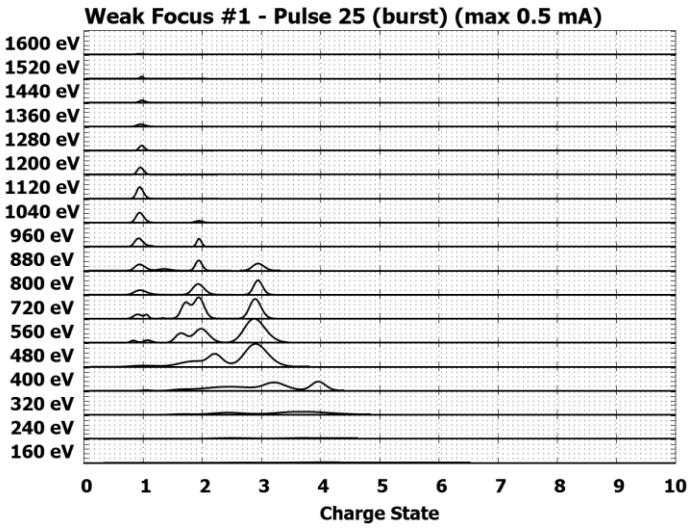

Fig. 134 Weak Focus #1 Pulse 25 Sweep Summary

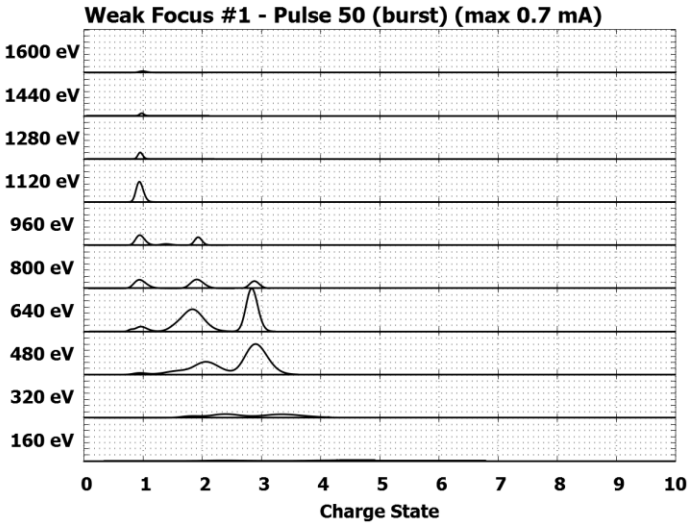

Fig. 135 Weak Focus #1 Pulse 50 Sweep Summary

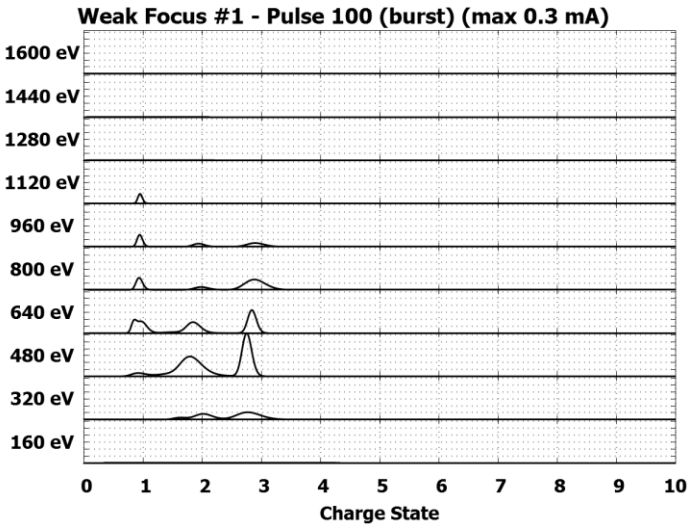

Fig. 136 Weak Focus #1 Pulse 100 Sweep Summary

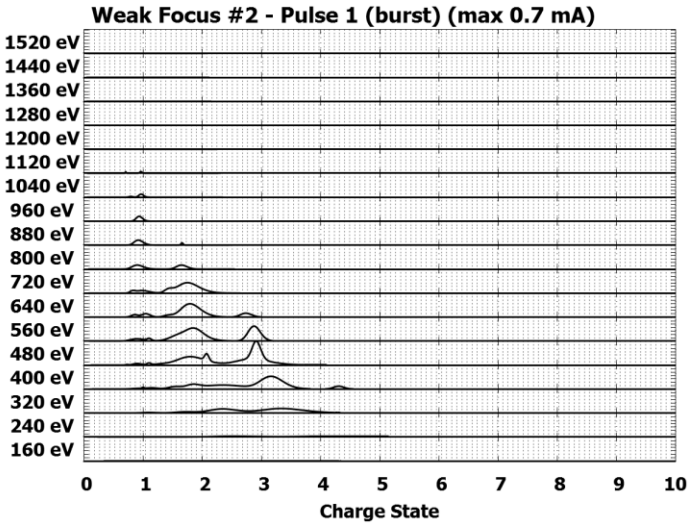

Fig. 137 Weak Focus #2 Pulse 1 Sweep Summary

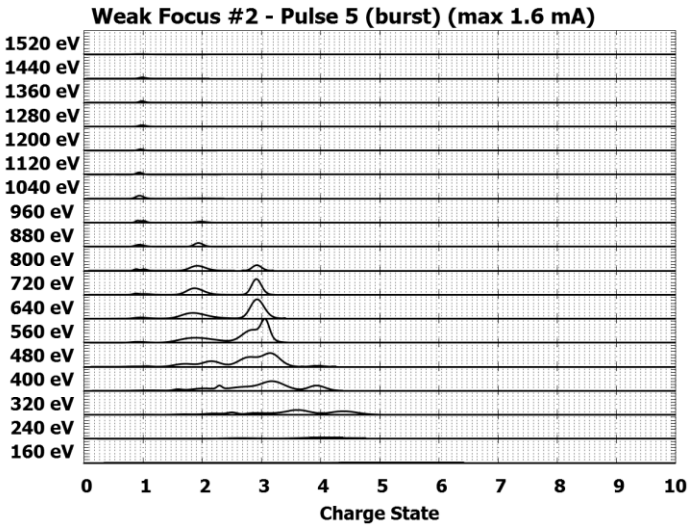

Fig. 138 Weak Focus #2 Pulse 5 Sweep Summary

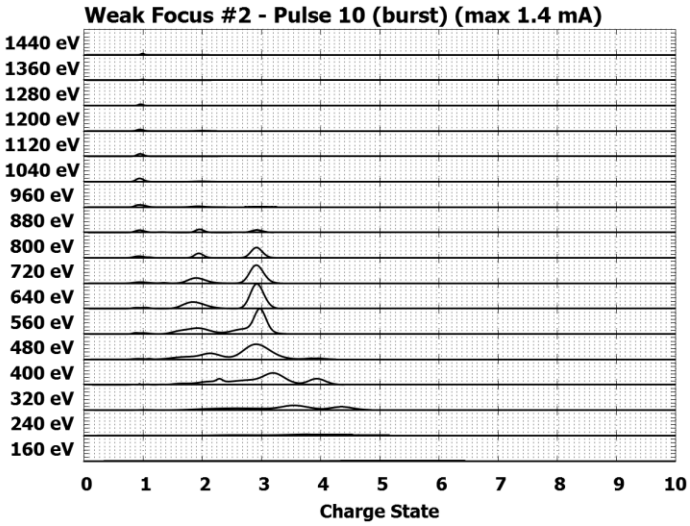

Fig. 139 Weak Focus #2 Pulse 10 Sweep Summary

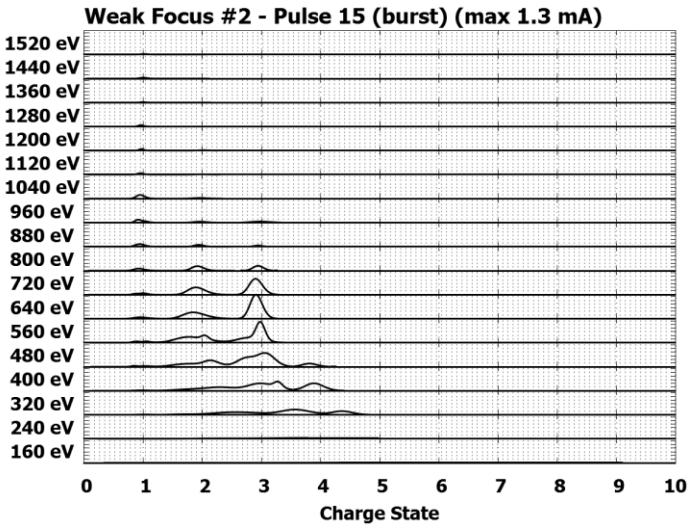

Fig. 140 Weak Focus #2 Pulse 15 Sweep Summary

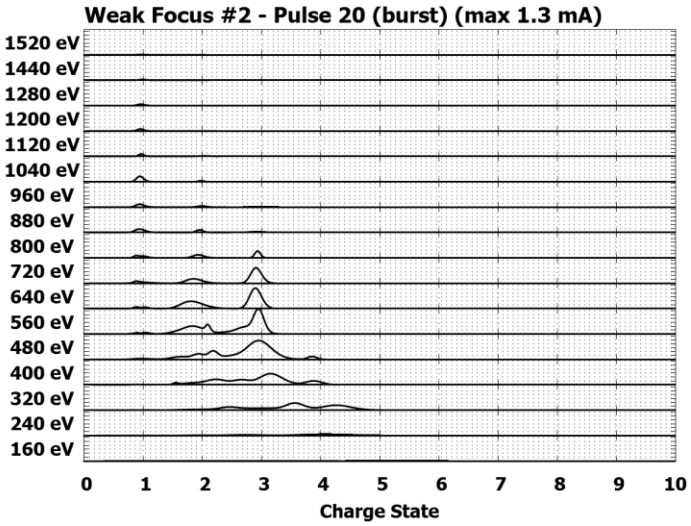

Fig. 141 Weak Focus #2 Pulse 20 Sweep Summary

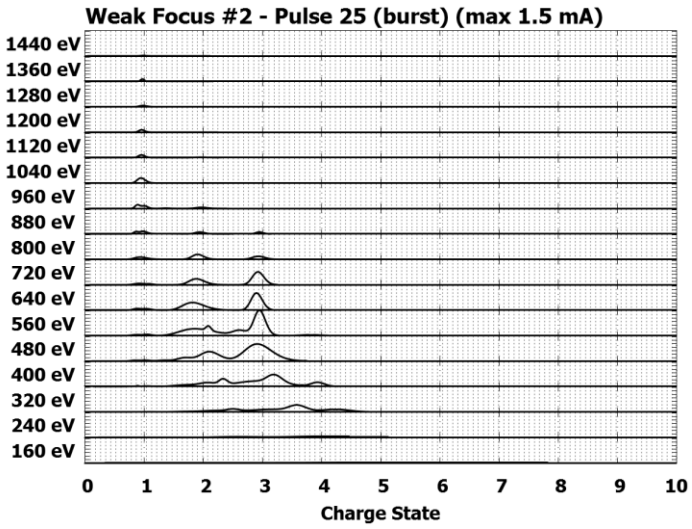

Fig. 142 Weak Focus #2 Pulse 25 Sweep Summary

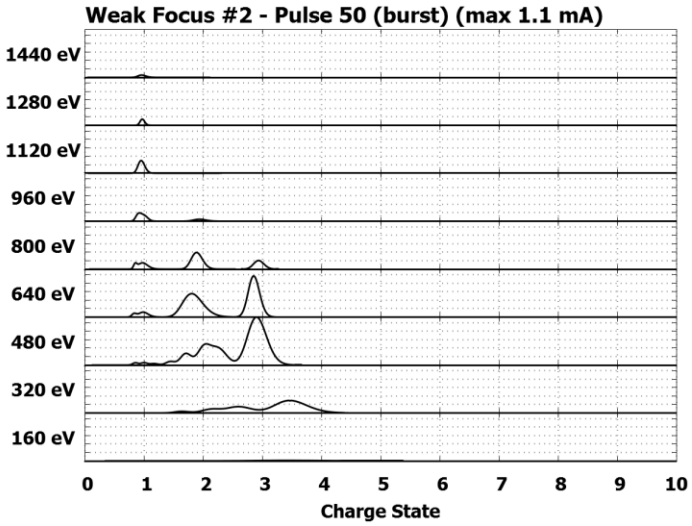

Fig. 143 Weak Focus #2 Pulse 50 Sweep Summary

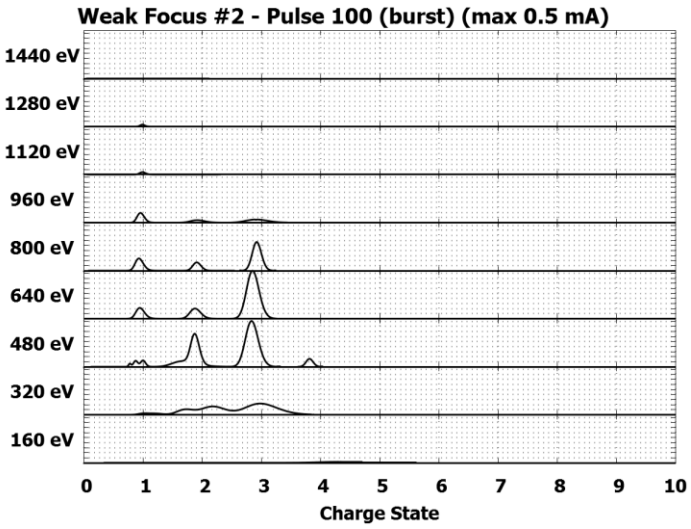

Fig. 144 Weak Focus #2 Pulse 100 Sweep Summary

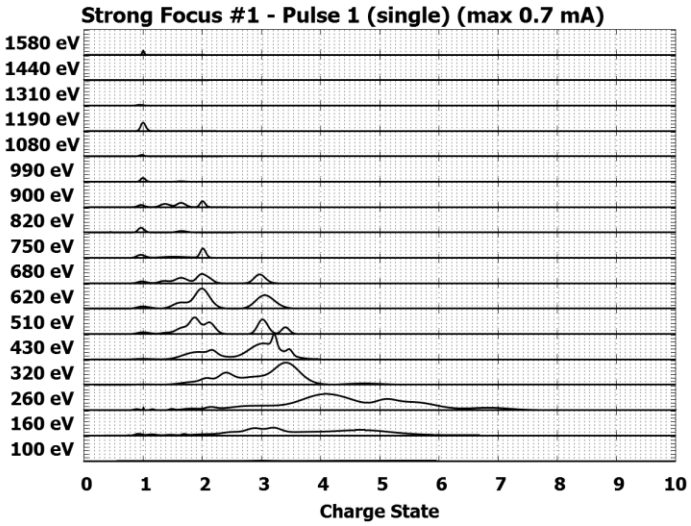

Fig. 145 Strong Focus #1 Pulse 1 Sweep Summary

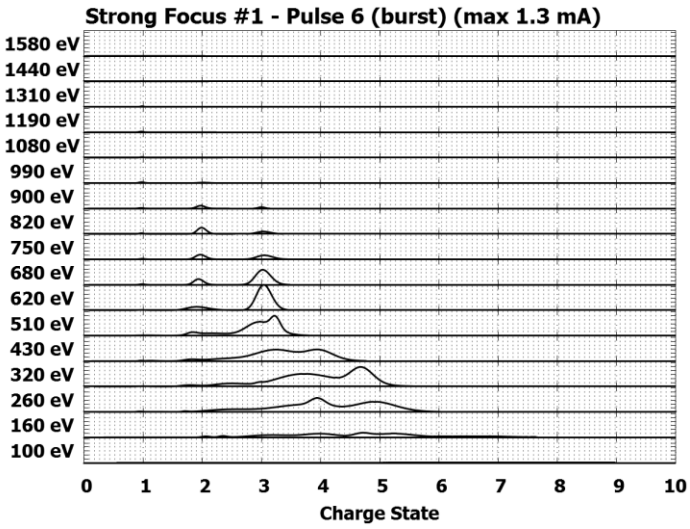

Fig. 146 Strong Focus #1 Pulse 6 Sweep Summary

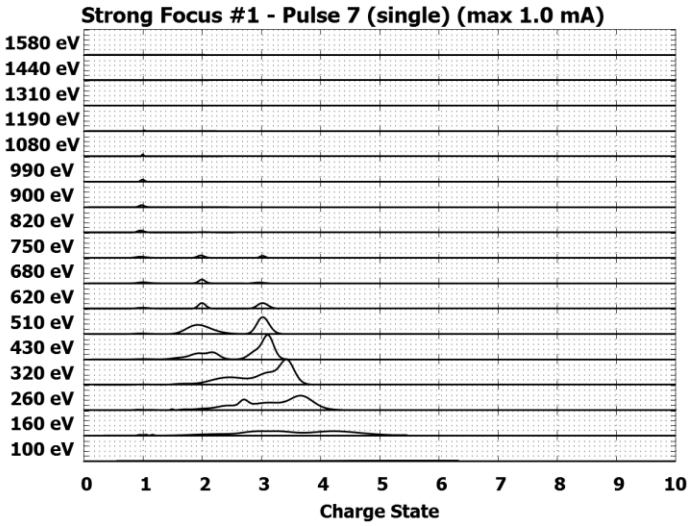

Fig. 147 Strong Focus #1 Pulse 7 Sweep Summary

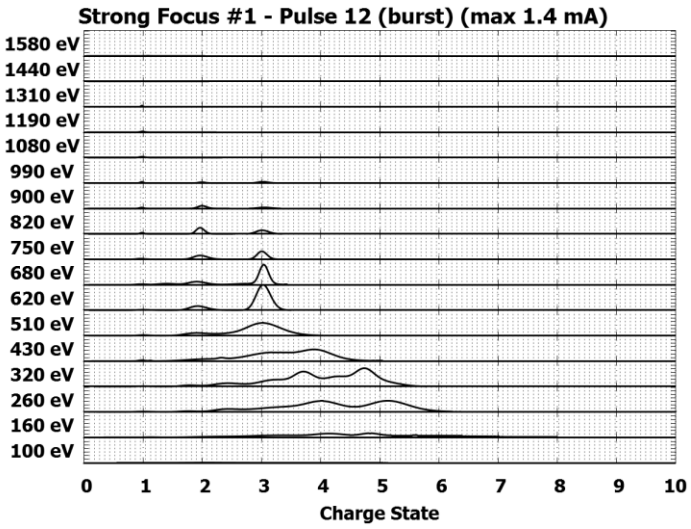

Fig. 148 Strong Focus #1 Pulse 12 Sweep Summary

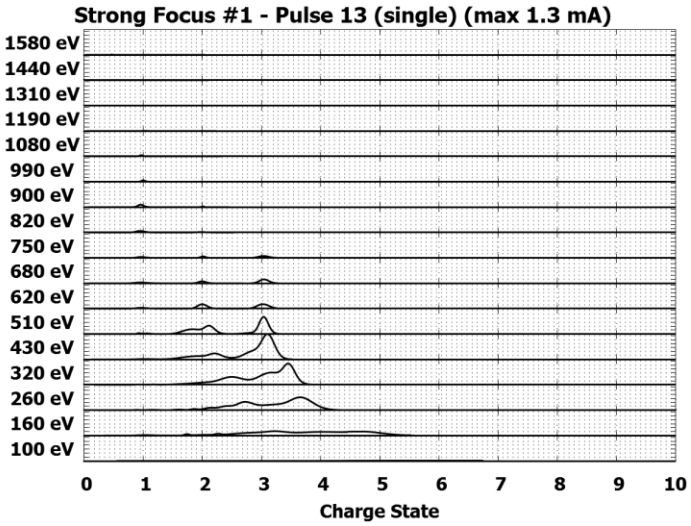

Fig. 149 Strong Focus #1 Pulse 13 Sweep Summary

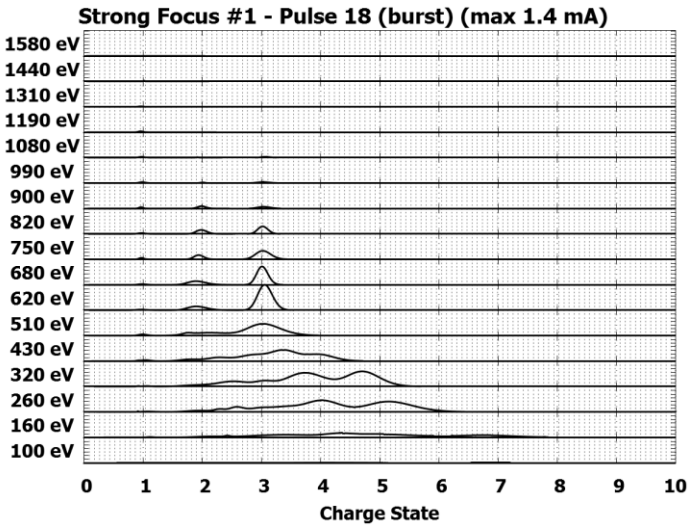

Fig. 150 Strong Focus #1 Pulse 18 Sweep Summary

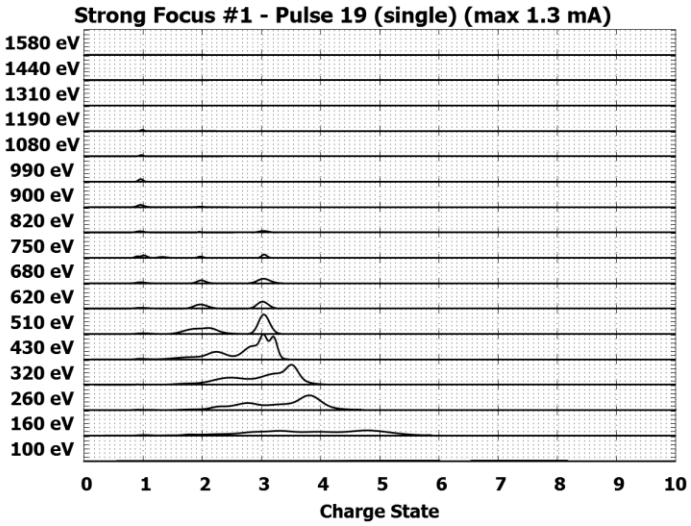

Fig. 151 Strong Focus #1 Pulse 19 Sweep Summary

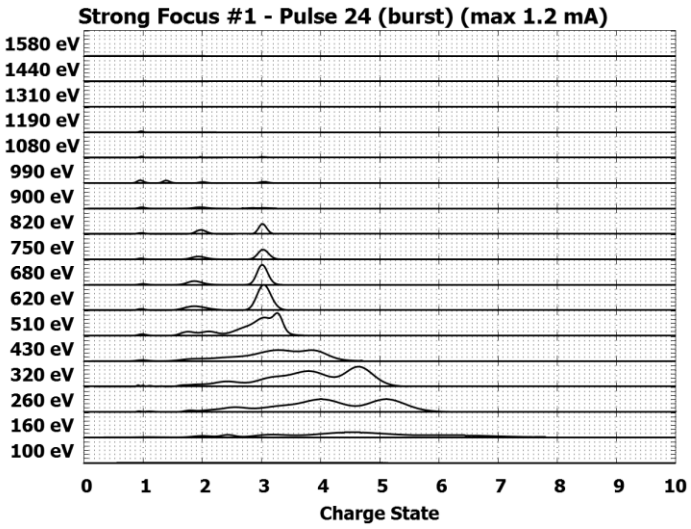

Fig. 152 Strong Focus #1 Pulse 24 Sweep Summary

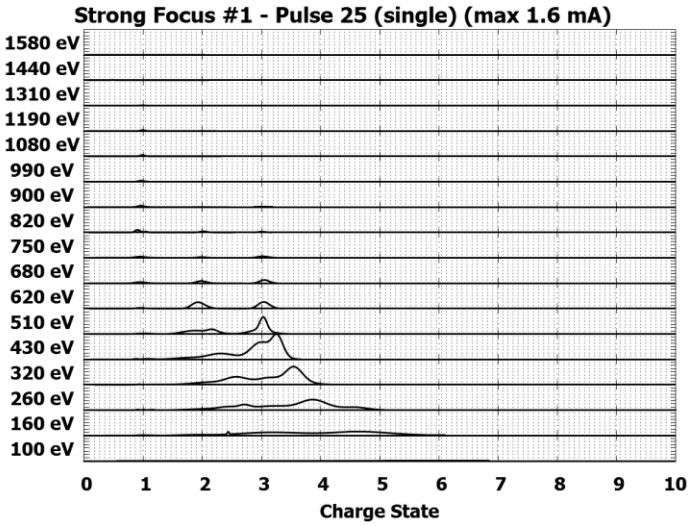

Fig. 153 Strong Focus #1 Pulse 25 Sweep Summary

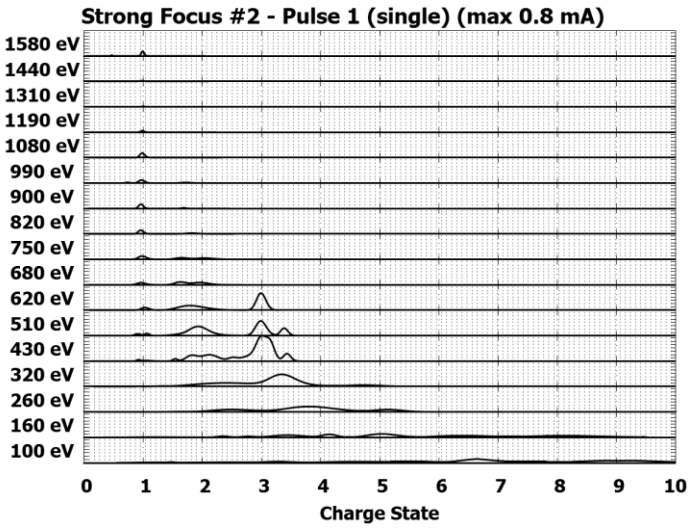

Fig. 154 Strong Focus #2 Pulse 1 Sweep Summary

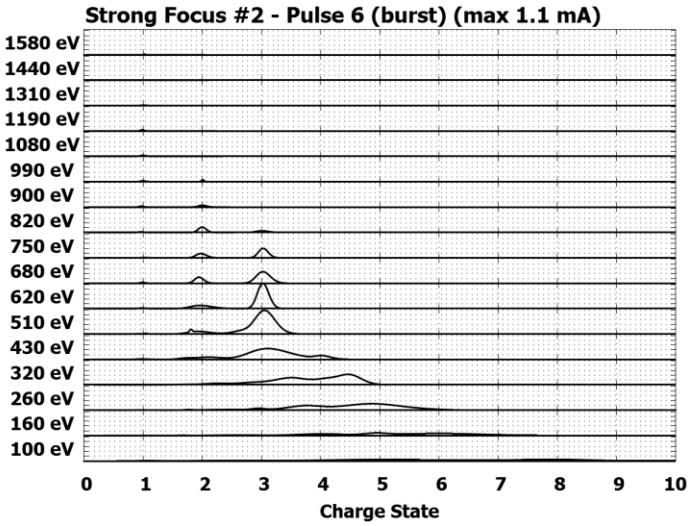

Fig. 155 Strong Focus #2 Pulse 6 Sweep Summary

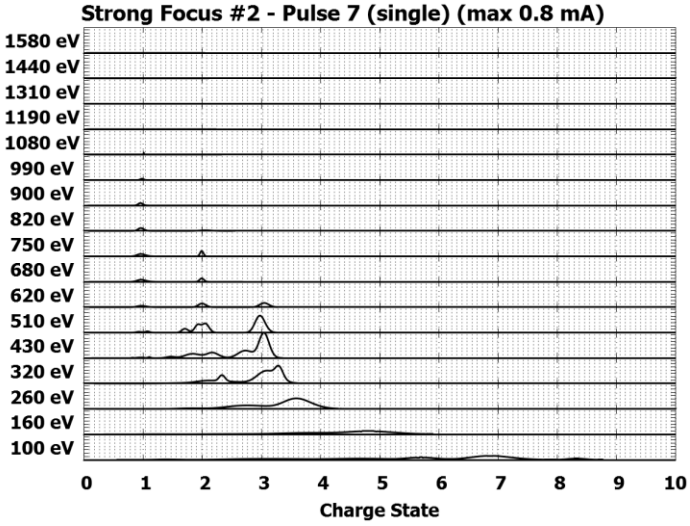

Fig. 156 Strong Focus #2 Pulse 7 Sweep Summary

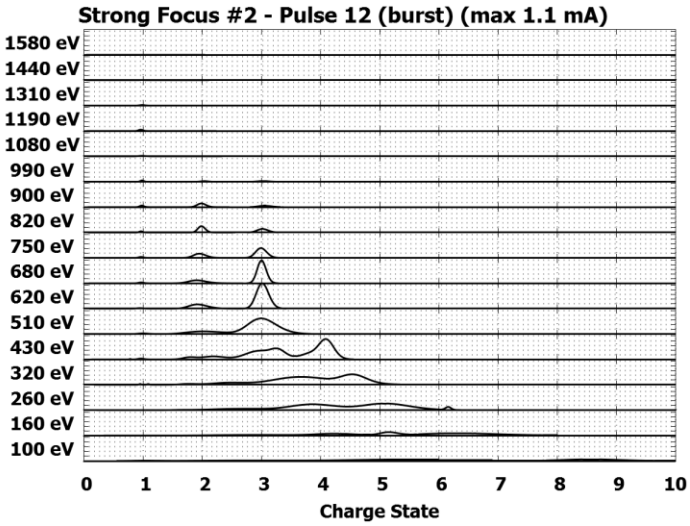

Fig. 157 Strong Focus #2 Pulse 12 Sweep Summary

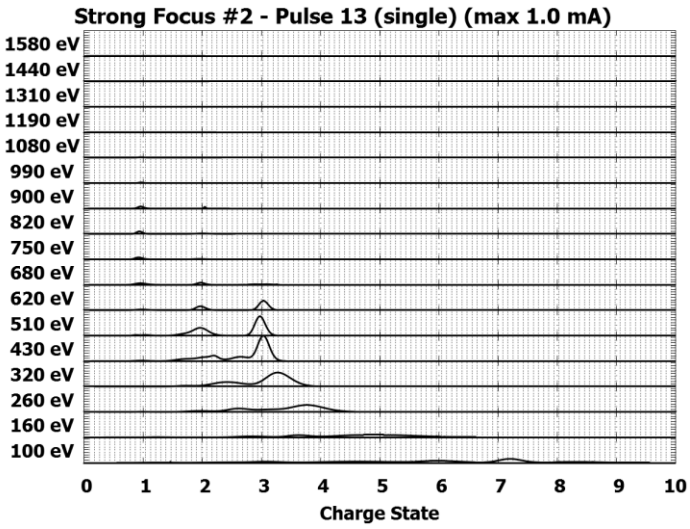

Fig. 158 Strong Focus #2 Pulse 13 Sweep Summary

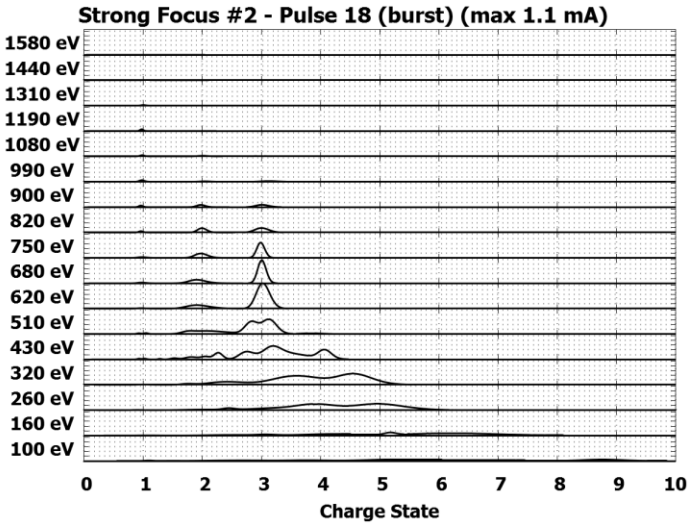

Fig. 159 Strong Focus #2 Pulse 18 Sweep Summary

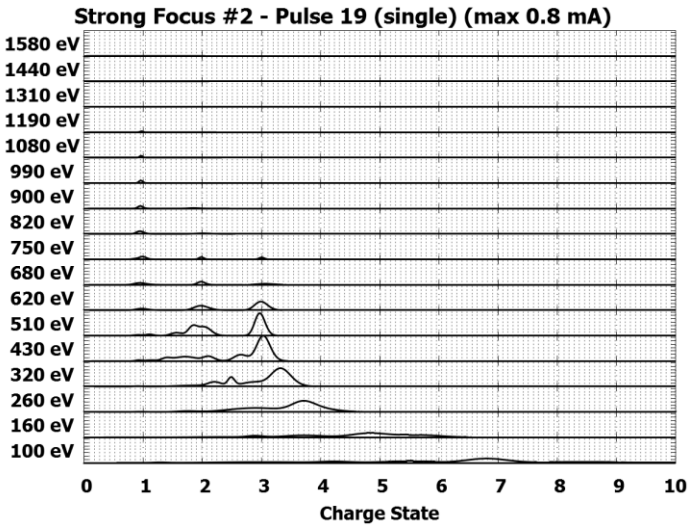

Fig. 160 Strong Focus #2 Pulse 19 Sweep Summary

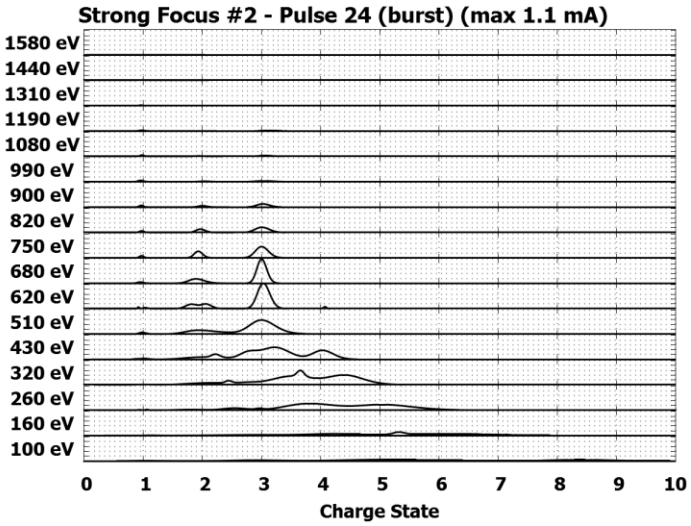

Fig. 161 Strong Focus #2 Pulse 24 Sweep Summary

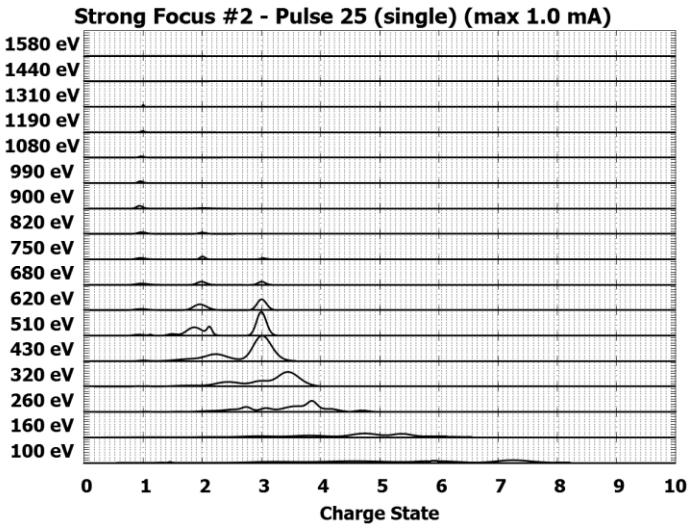

Fig. 162 Strong Focus #2 Pulse 25 Sweep Summary

A.2 Spectrometer Energy Distribution Plots

This data has been corrected using the calibrations discussed in the Data Processing section. Entries whose energy-per-charge is less than 310 eV/e^- use the same symbol, but in red. Species higher than Al^{+4} should be considered suspect, more so the higher the charge state. They only appear at low energies (per-charge) and may reflect a shift in particle energy during flight rather than actual charge states, as discussed in the Sweep Summary portion of the Results chapter.

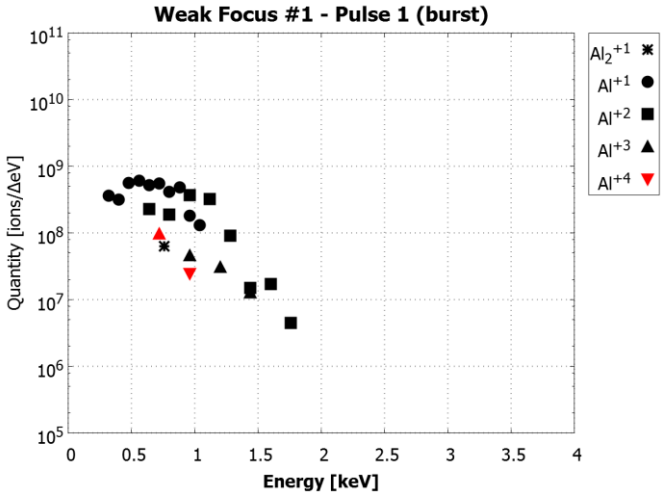

Fig. 163 Weak Focus #1 Pulse 1 Energy Spectrum

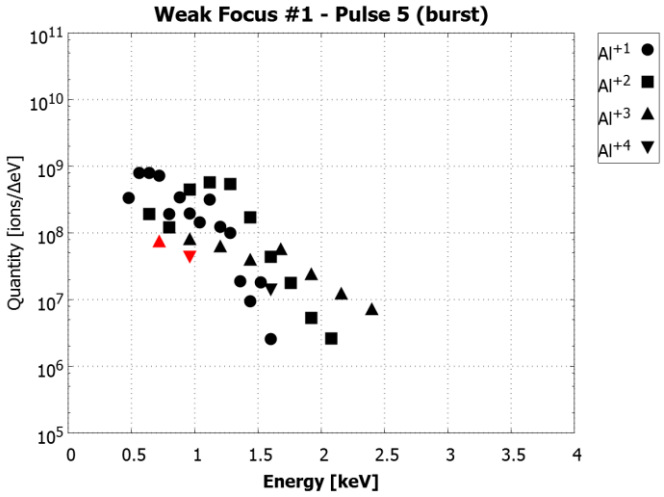

Fig. 164 Weak Focus #1 Pulse 5 Energy Spectrum

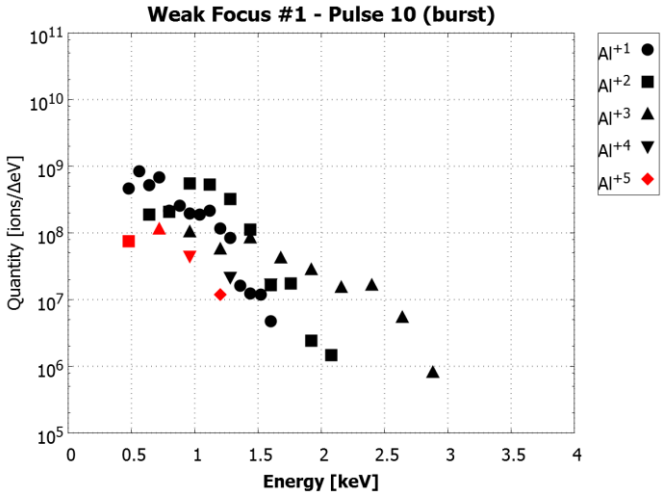

Fig. 165 Weak Focus #1 Pulse 10 Energy Spectrum

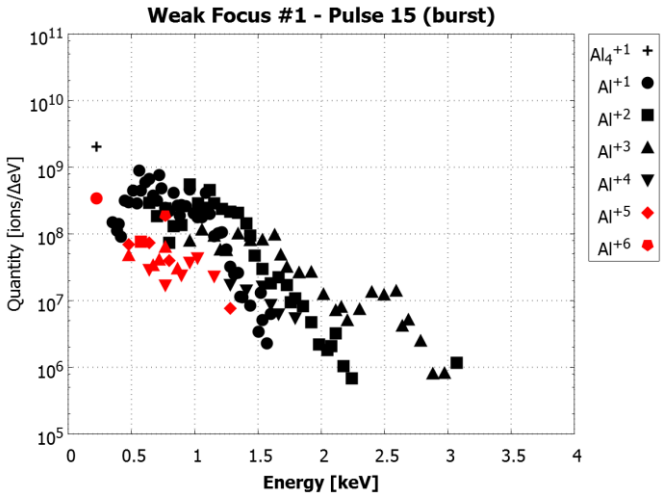

Fig. 166 Weak Focus #1 Pulse 15 Energy Spectrum

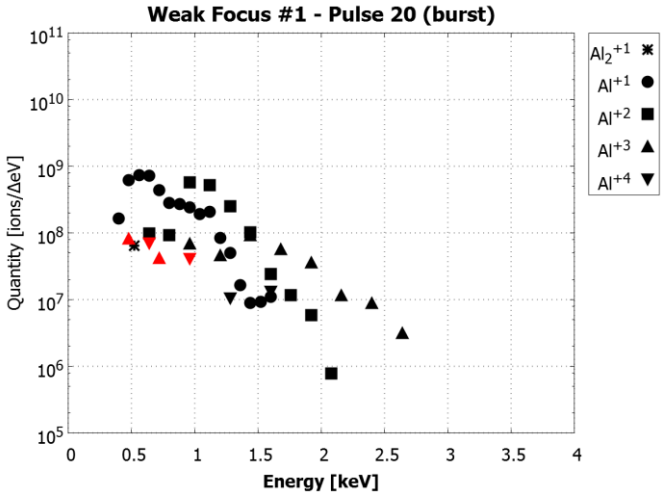

Fig. 167 Weak Focus #1 Pulse 20 Energy Spectrum

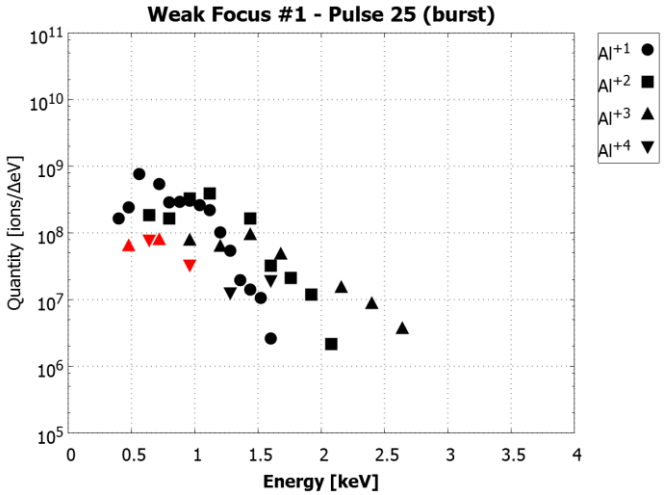

Fig. 168 Weak Focus #1 Pulse 25 Energy Spectrum

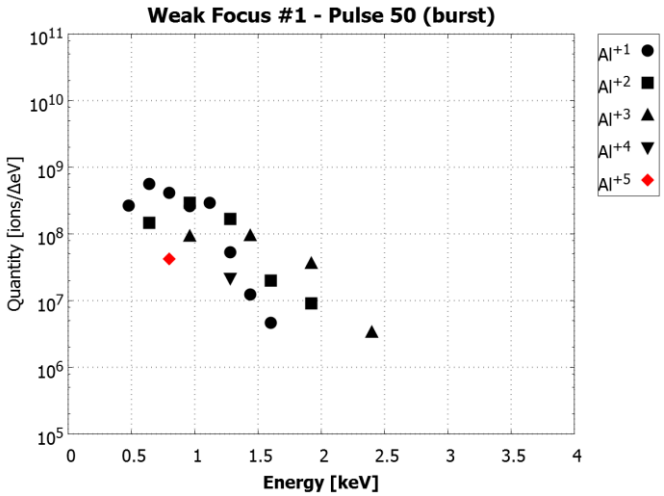

Fig. 169 Weak Focus #1 Pulse 50 Energy Spectrum

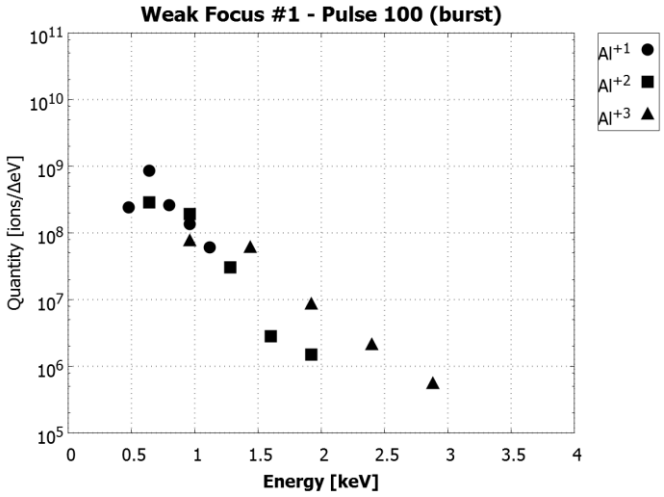

Fig. 170 Weak Focus #1 Pulse 100 Energy Spectrum

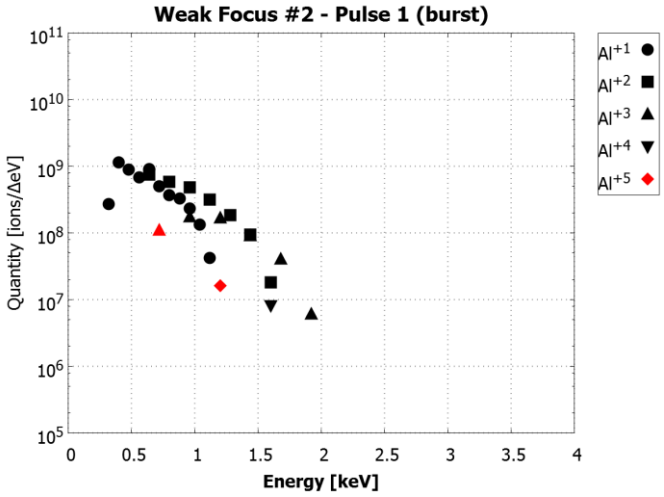

Fig. 171 Weak Focus #2 Pulse 1 Energy Spectrum

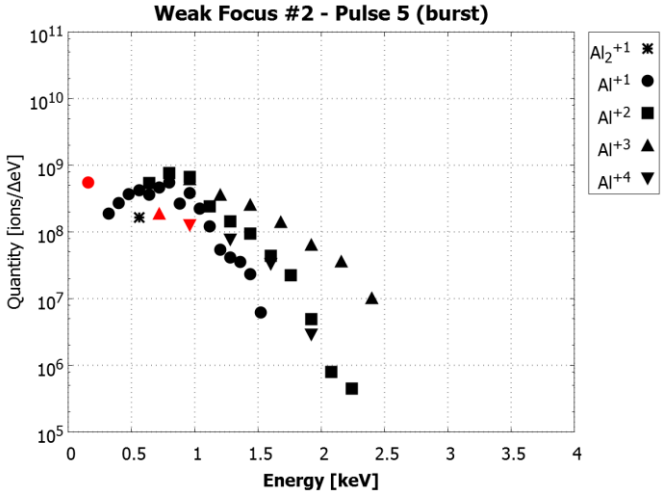

Fig. 172 Weak Focus #2 Pulse 5 Energy Spectrum

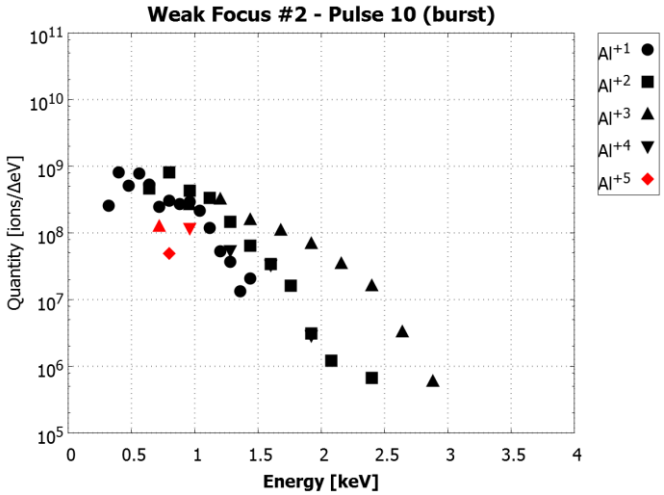

Fig. 173 Weak Focus #2 Pulse 10 Energy Spectrum

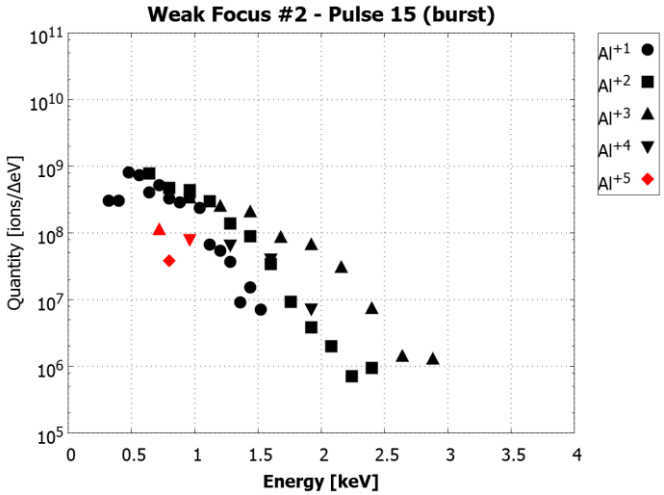

Fig. 174 Weak Focus #2 Pulse 15 Energy Spectrum

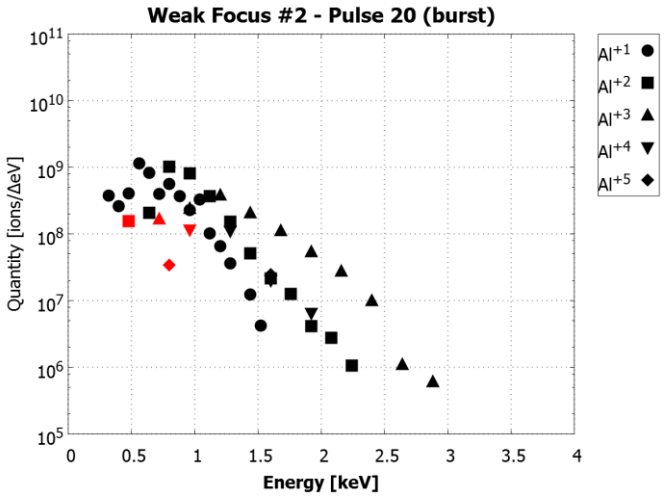

Fig. 175 Weak Focus #2 Pulse 20 Energy Spectrum

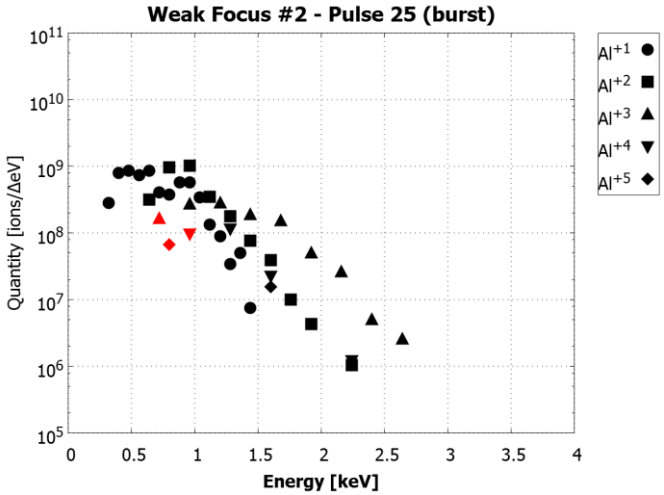

Fig. 176 Weak Focus #2 Pulse 25 Energy Spectrum

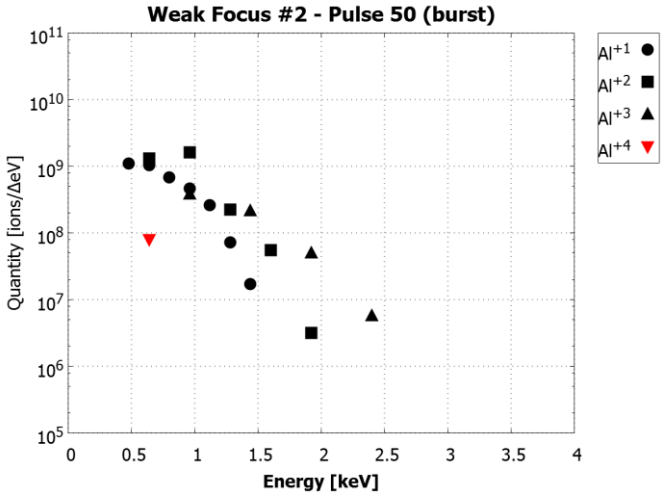

Fig. 177 Weak Focus #2 Pulse 50 Energy Spectrum

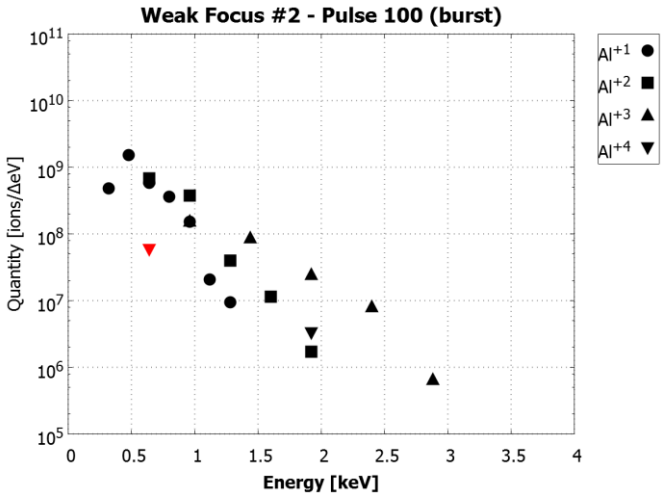

Fig. 178 Weak Focus #2 Pulse 100 Energy Spectrum

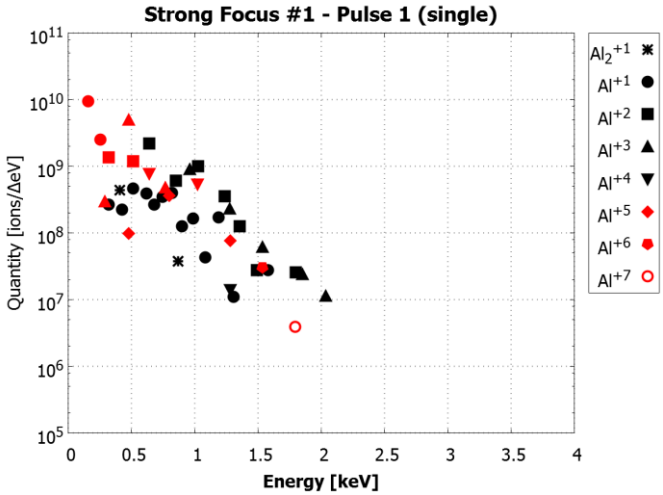

Fig. 179 Strong Focus #1 Pulse 1 Energy Spectrum

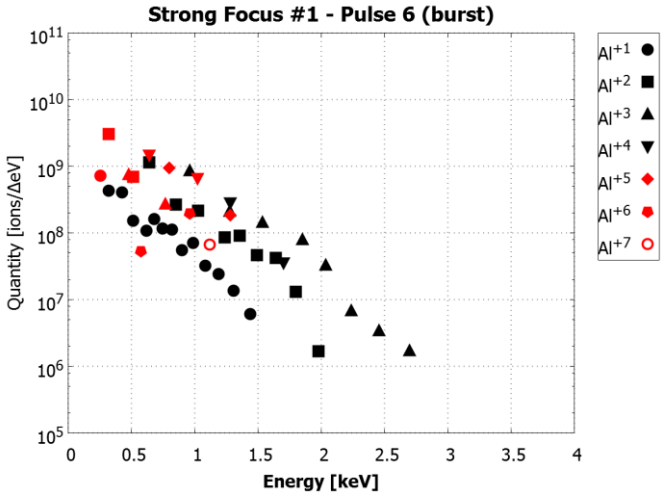

Fig. 180 Strong Focus #1 Pulse 6 Energy Spectrum

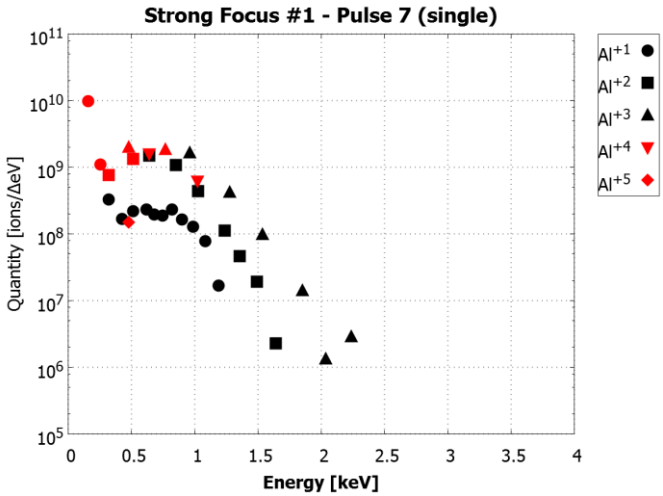

Fig. 181 Strong Focus #1 Pulse 7 Energy Spectrum

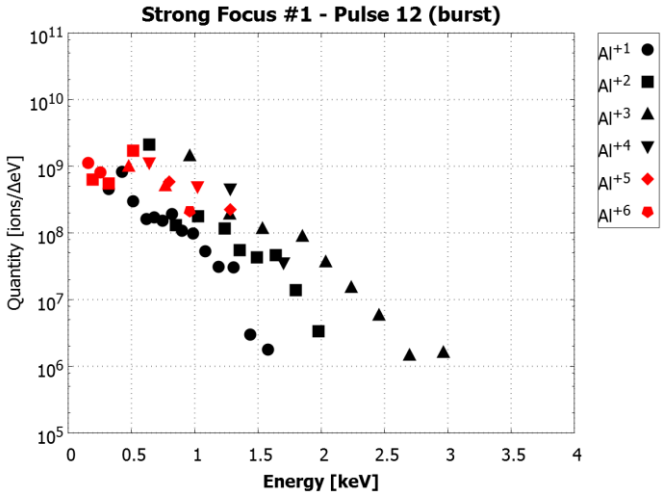

Fig. 182 Strong Focus #1 Pulse 12 Energy Spectrum

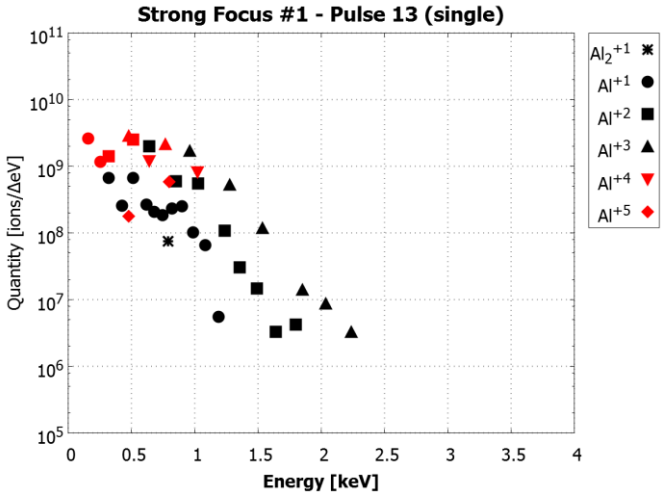

Fig. 183 Strong Focus #1 Pulse 13 Energy Spectrum

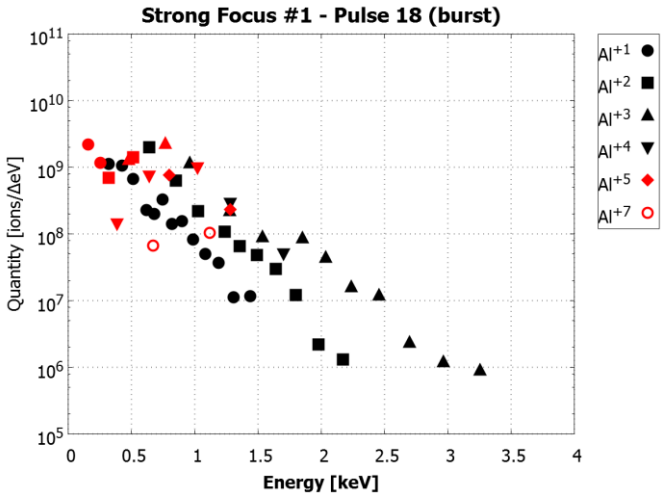

Fig. 184 Strong Focus #1 Pulse 18 Energy Spectrum

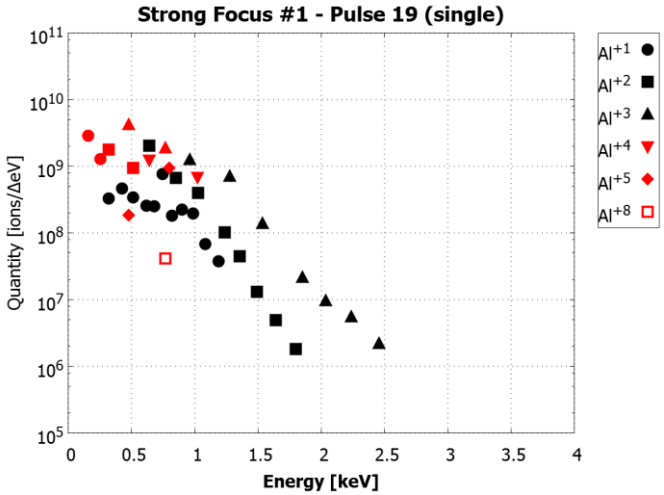

Fig. 185 Strong Focus #1 Pulse 19 Energy Spectrum

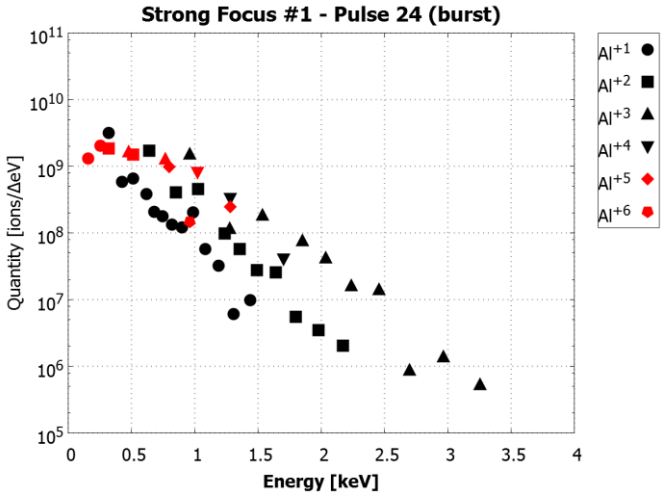

Fig. 186 Strong Focus #1 Pulse 24 Energy Spectrum

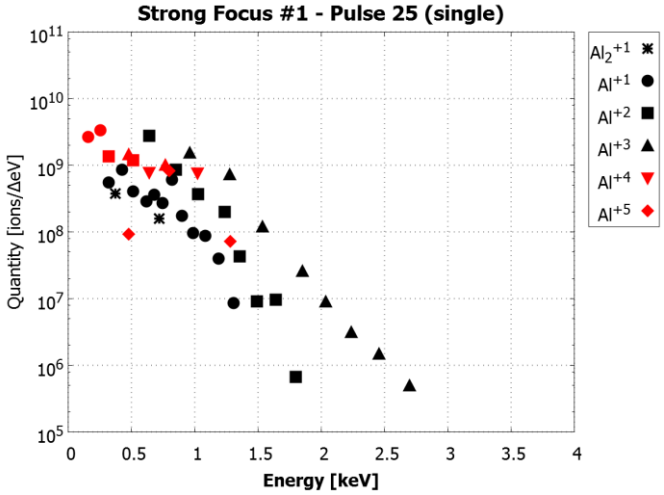

Fig. 187 Strong Focus #1 Pulse 25 Energy Spectrum

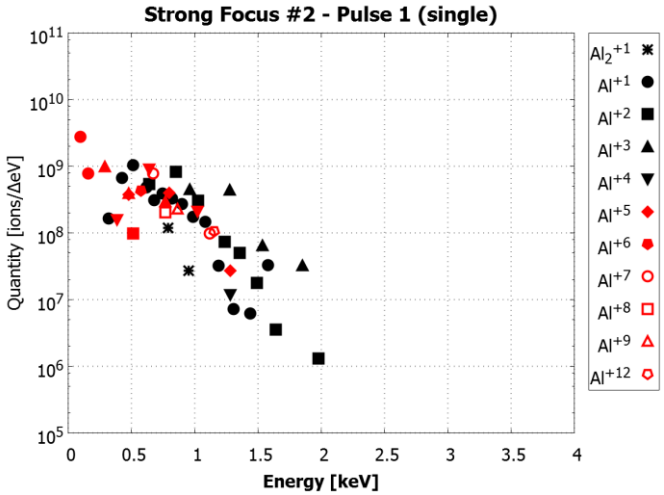

Fig. 188 Strong Focus #2 Pulse 1 Energy Spectrum

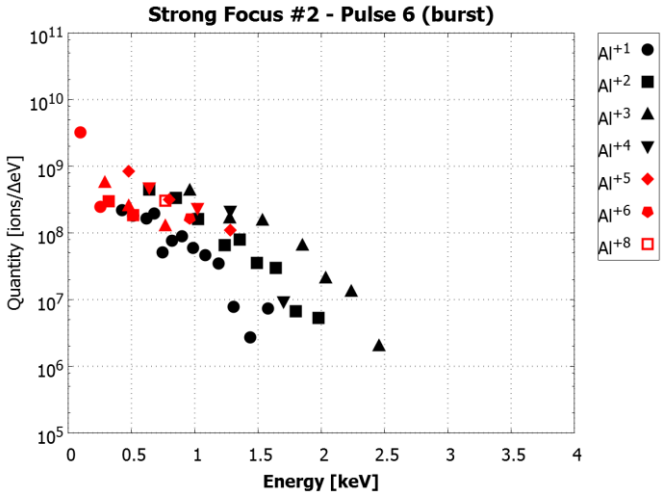

Fig. 189 Strong Focus #2 Pulse 6 Energy Spectrum

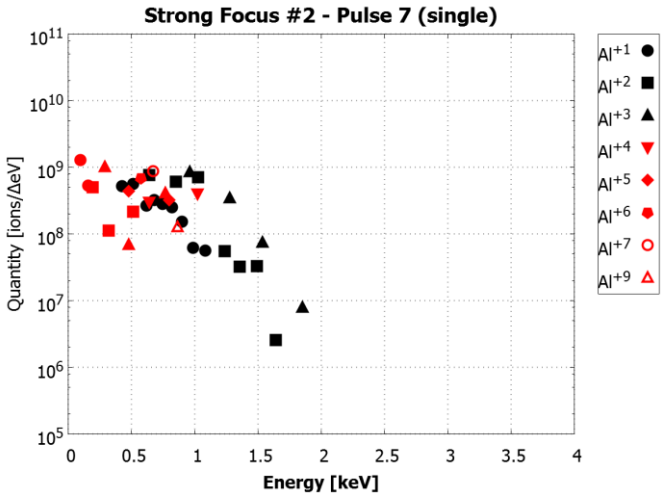

Fig. 190 Strong Focus #2 Pulse 7 Energy Spectrum

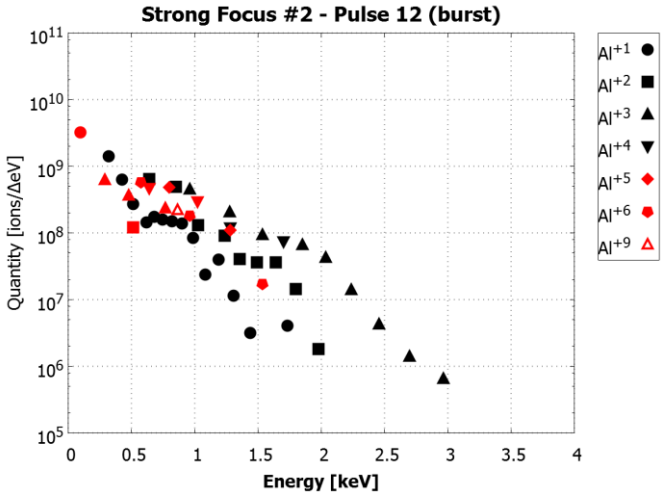

Fig. 191 Strong Focus #2 Pulse 12 Energy Spectrum

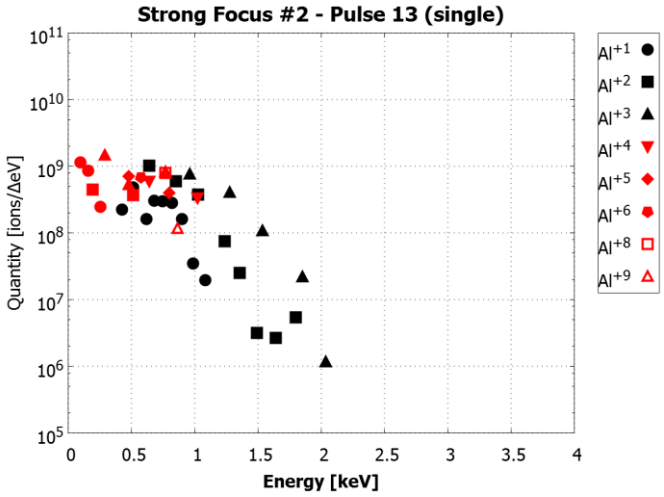

Fig. 192 Strong Focus #2 Pulse 13 Energy Spectrum

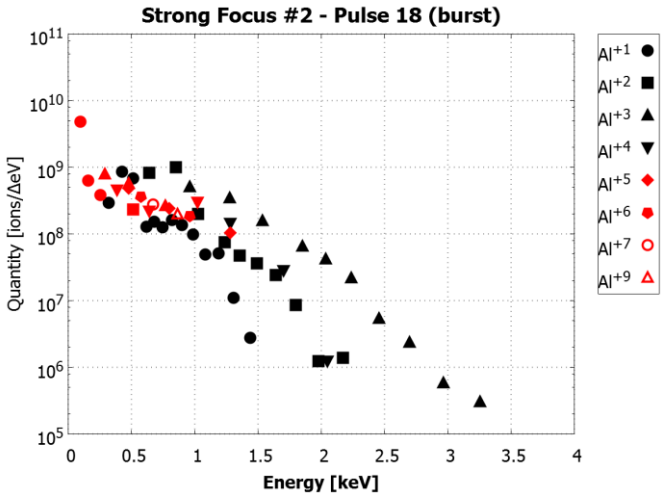

Fig. 193 Strong Focus #2 Pulse 18 Energy Spectrum

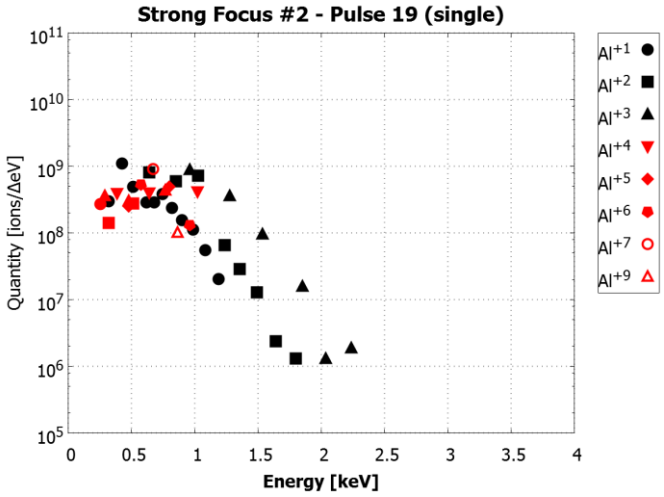

Fig. 194 Strong Focus #2 Pulse 19 Energy Spectrum

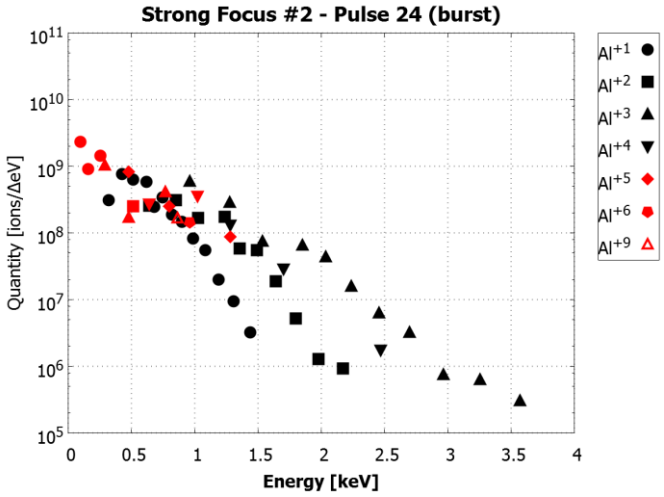

Fig. 195 Strong Focus #2 Pulse 24 Energy Spectrum

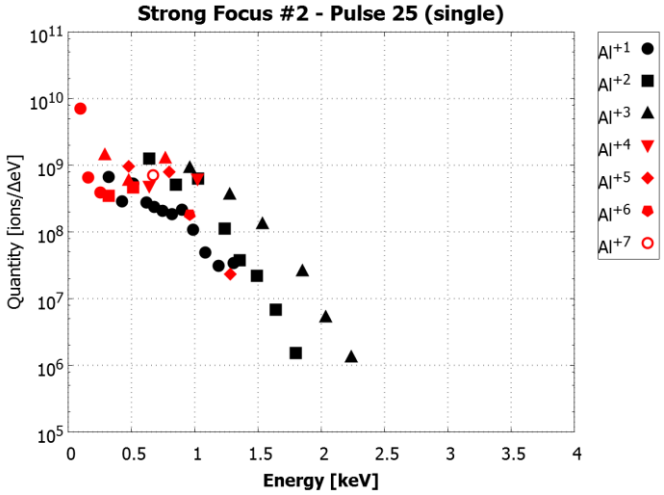

Fig. 196 Strong Focus #2 Pulse 25 Energy Spectrum

A.3 RPA Sweep summary plots

None of the corrections discussed in the Data Processing section, except removal of the RC distortion, have been applied to the results in the sweep summary plots below. All the RPA data were collected under the same configuration as the Weak Focus cases.

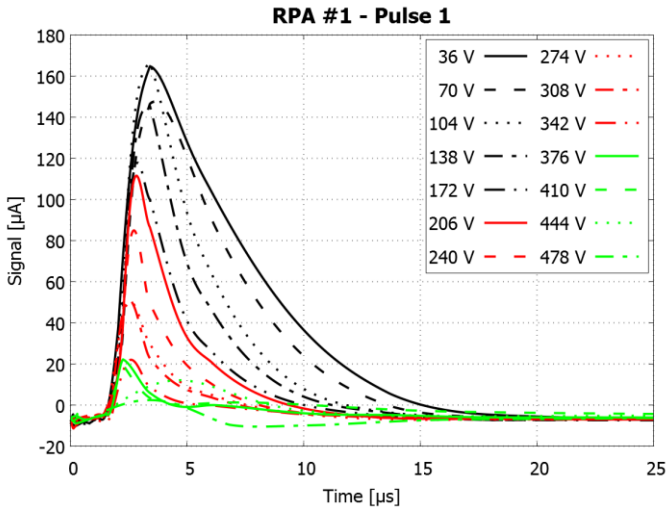

Fig. 197 RPA #1 Pulse 1 Sweep Summary

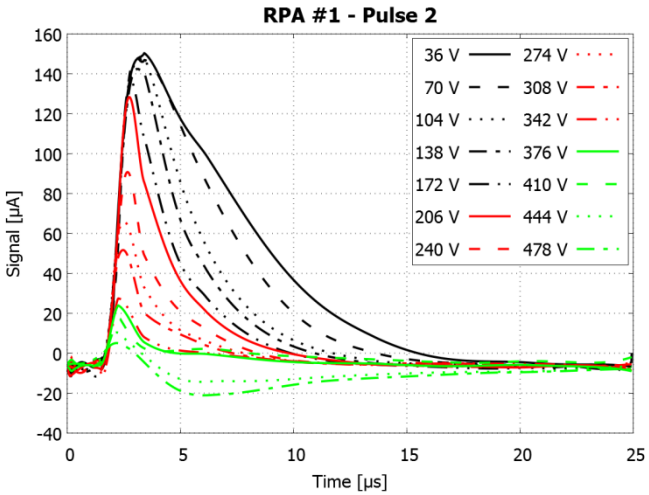

Fig. 198 RPA #1 Pulse 2 Sweep Summary

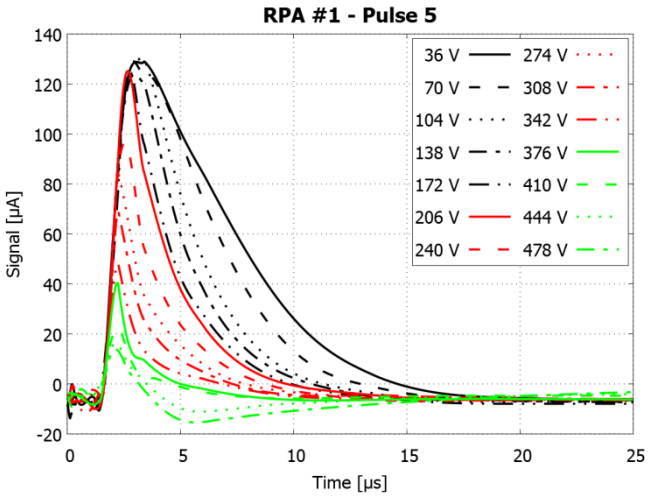

Fig. 199 RPA #1 Pulse 5 Sweep Summary

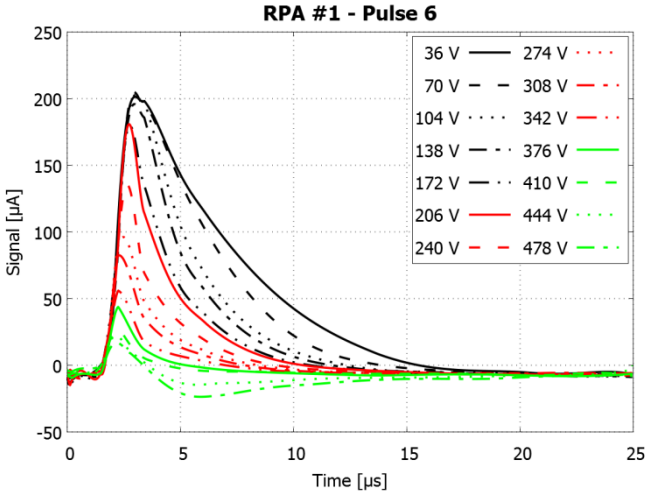

Fig. 200 RPA #1 Pulse 6 Sweep Summary

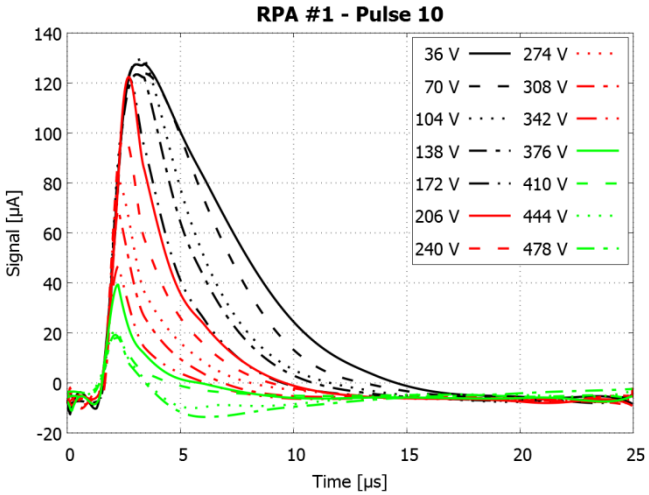

Fig. 201 RPA #1 Pulse 10 Sweep Summary

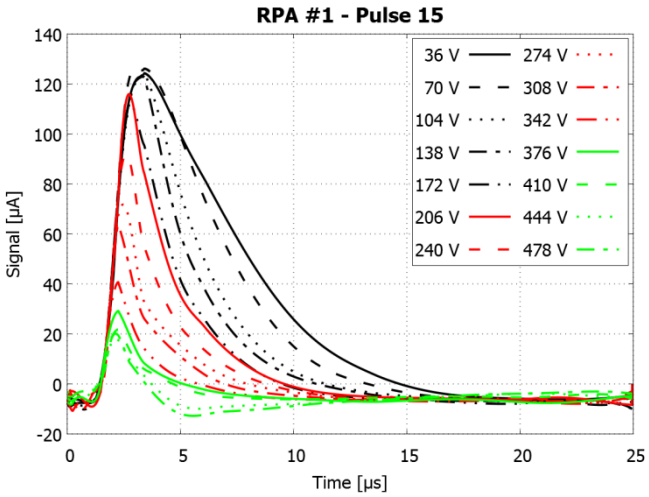

Fig. 202 RPA #1 Pulse 15 Sweep Summary

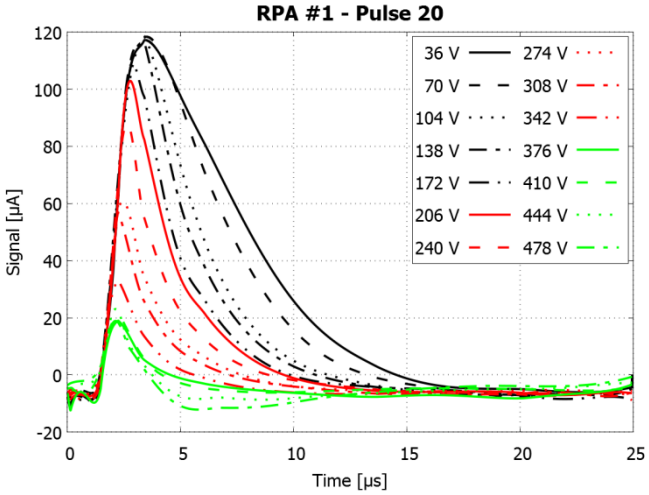

Fig. 203 RPA #1 Pulse 20 Sweep Summary

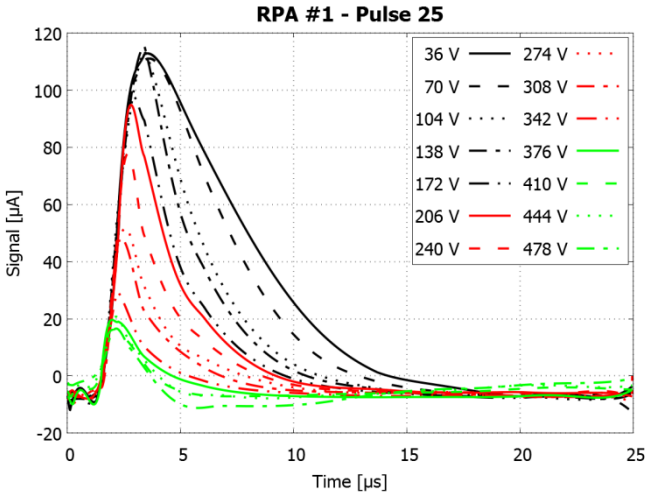

Fig. 204 RPA #1 Pulse 25 Sweep Summary

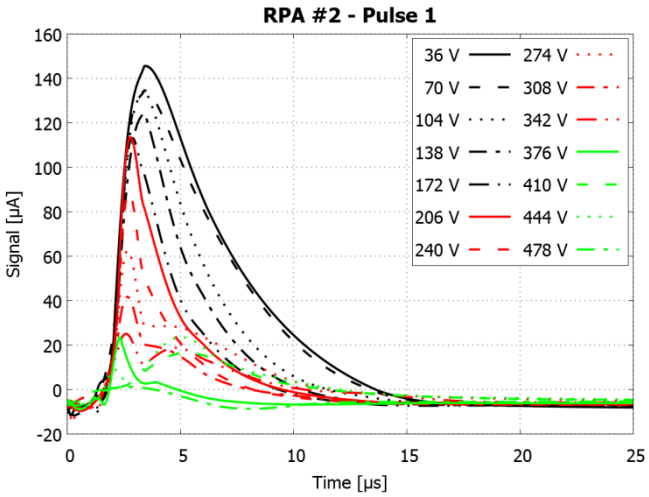

Fig. 205 RPA #2 Pulse 1 Sweep Summary

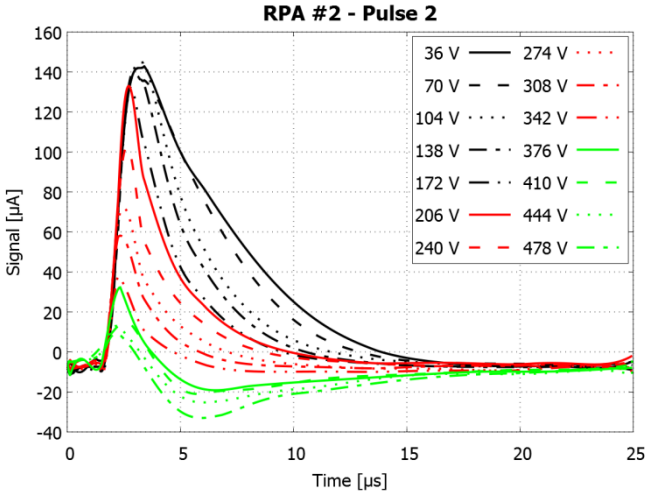

Fig. 206 RPA #2 Pulse 2 Sweep Summary

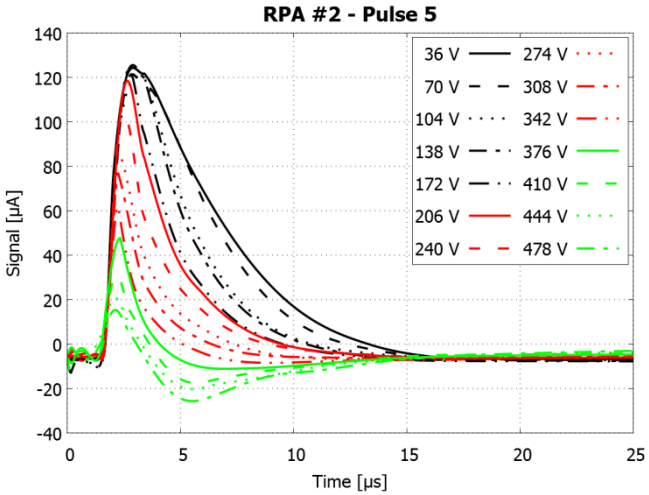

Fig. 207 RPA #2 Pulse 5 Sweep Summary

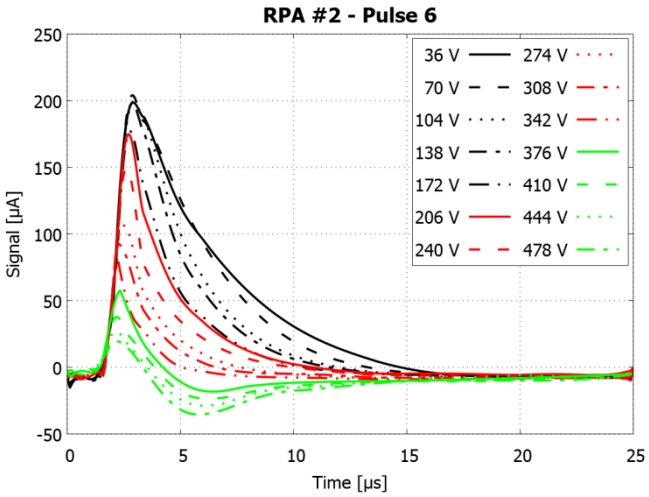

Fig. 208 RPA #2 Pulse 6 Sweep Summary

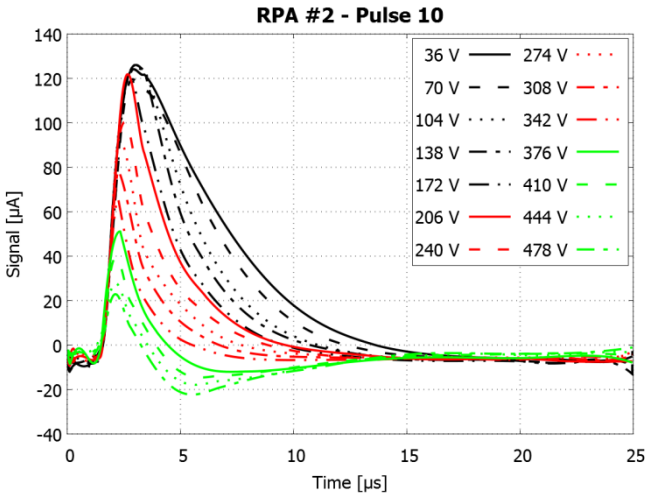

Fig. 209 RPA #2 Pulse 10 Sweep Summary

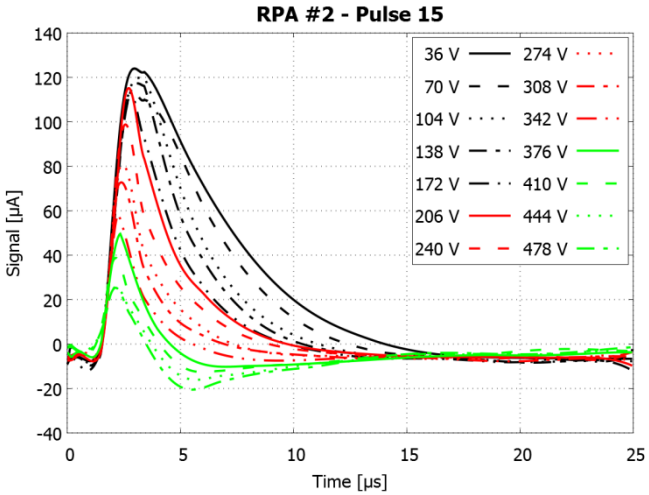

Fig. 210 RPA #2 Pulse 15 Sweep Summary

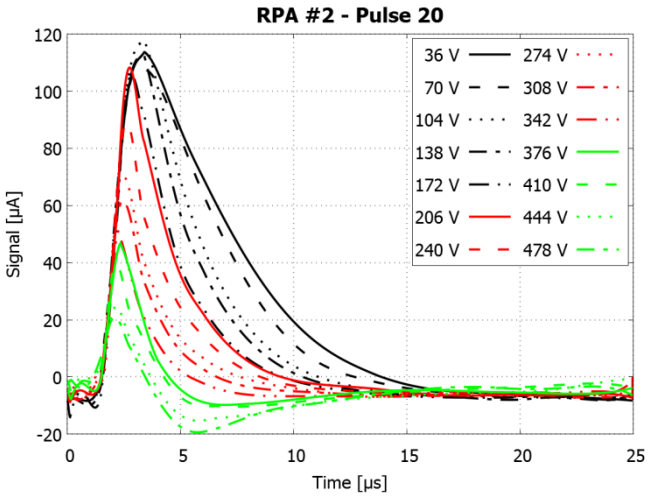

Fig. 211 RPA #2 Pulse 20 Sweep Summary

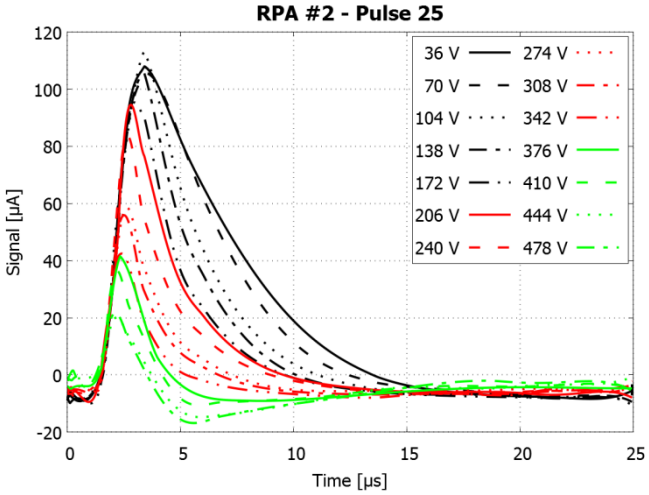

Fig. 212 RPA #2 Pulse 25 Sweep Summary

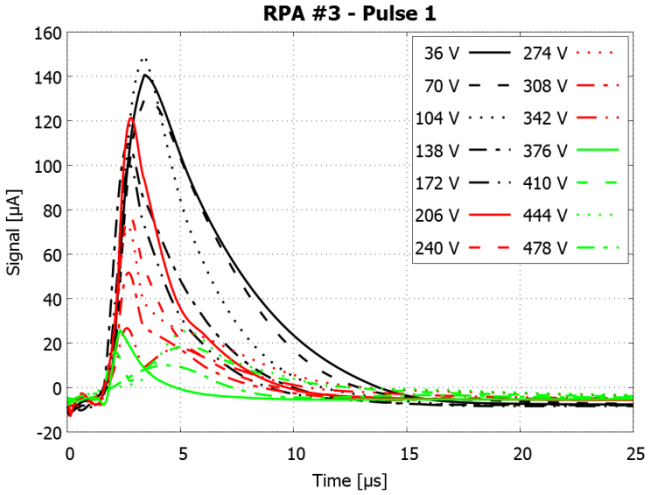

Fig. 213 RPA #3 Pulse 1 Sweep Summary

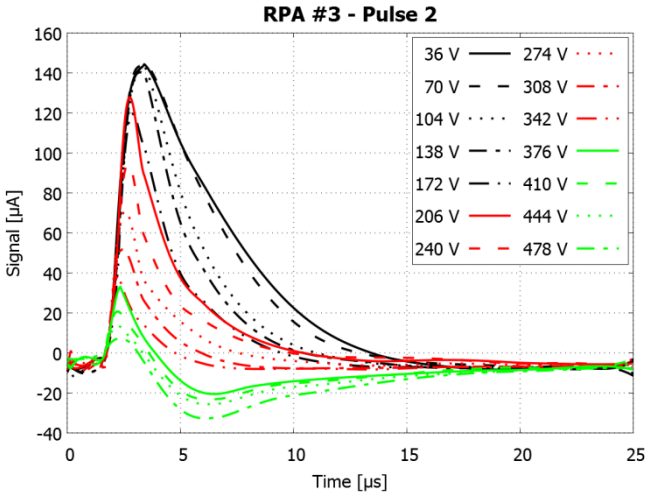

Fig. 214 RPA #3 Pulse 2 Sweep Summary

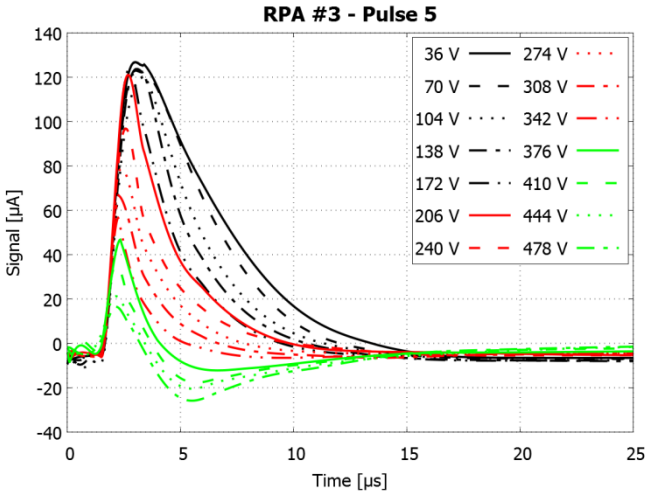

Fig. 215 RPA #3 Pulse 5 Sweep Summary

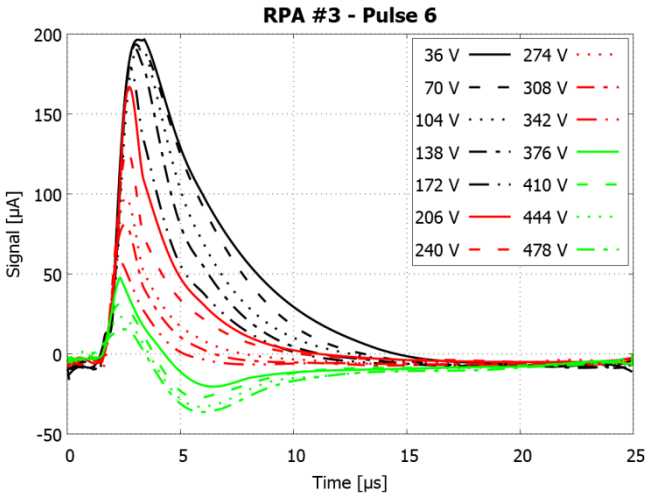

Fig. 216 RPA #3 Pulse 6 Sweep Summary

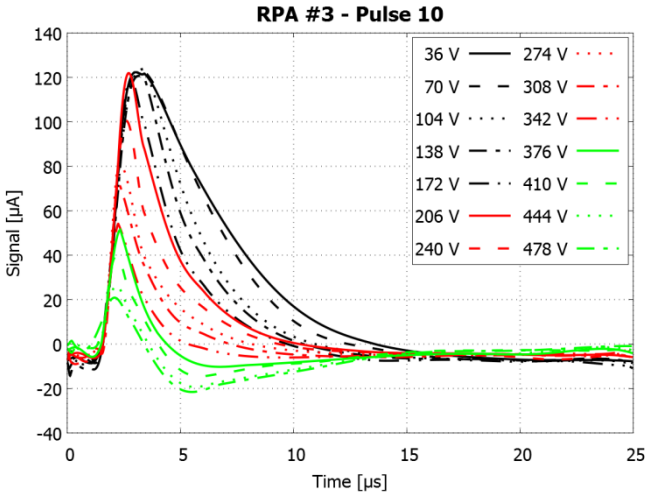

Fig. 217 RPA #3 Pulse 10 Sweep Summary

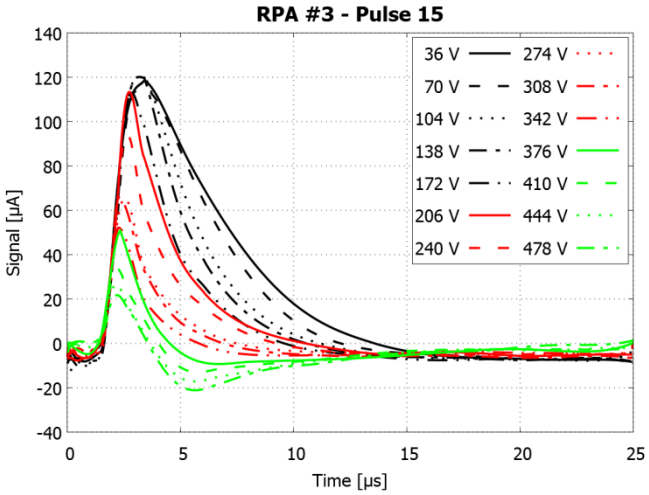

Fig. 218 RPA #3 Pulse 15 Sweep Summary

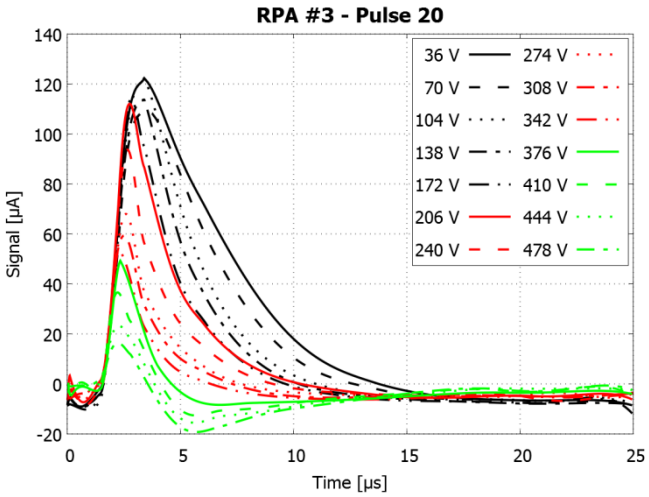

Fig. 219 RPA #3 Pulse 20 Sweep Summary

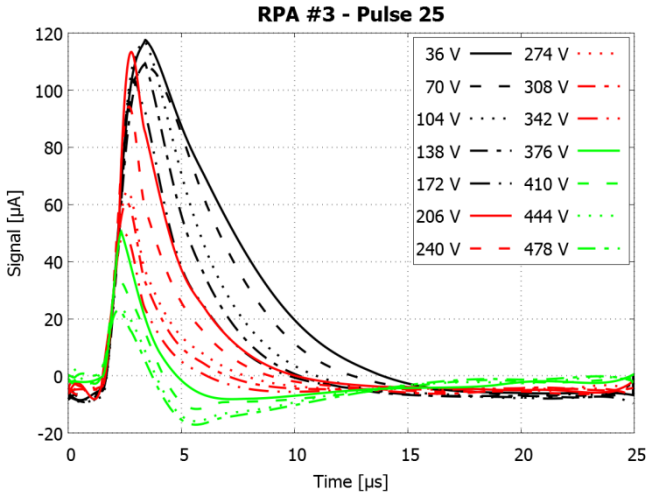

Fig. 220 RPA #3 Pulse 25 Sweep Summary

A.4 RPA Energy Distribution Plots

Entries whose energy-per-charge is greater than 310 eV/e^- use the same symbol, but in red.

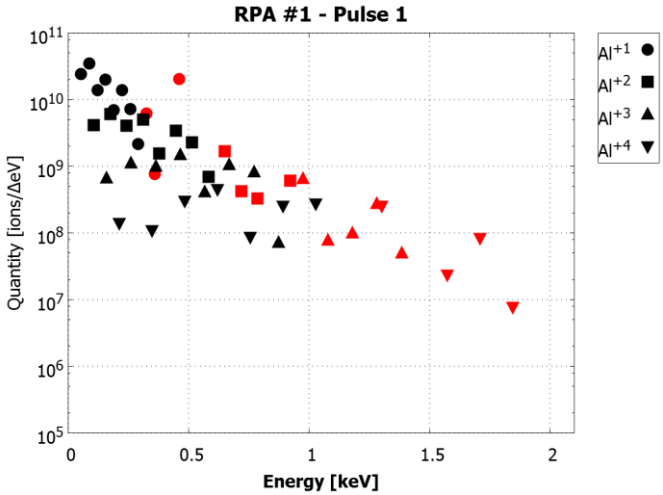

Fig. 221 RPA #1 Pulse 1 Energy Spectrum

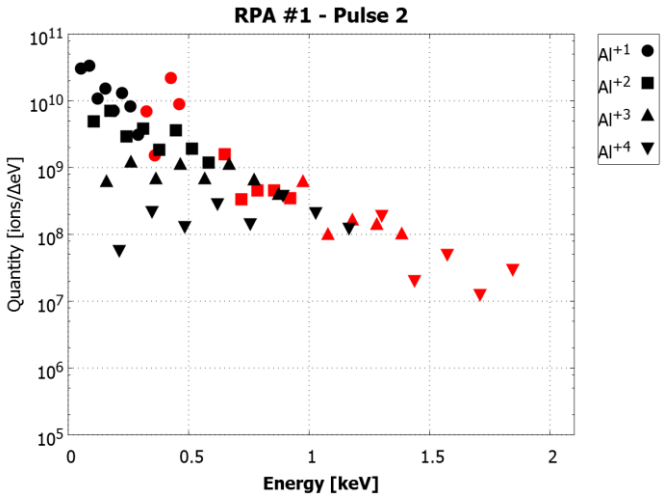

Fig. 222 RPA #1 Pulse 2 Energy Spectrum

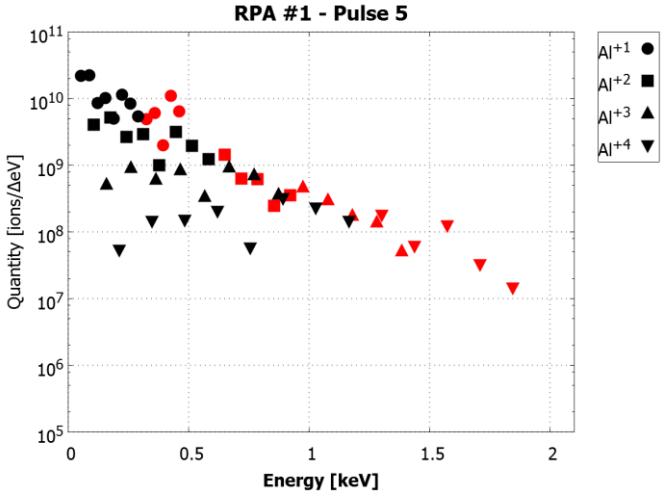

Fig. 223 RPA #1 Pulse 5 Energy Spectrum

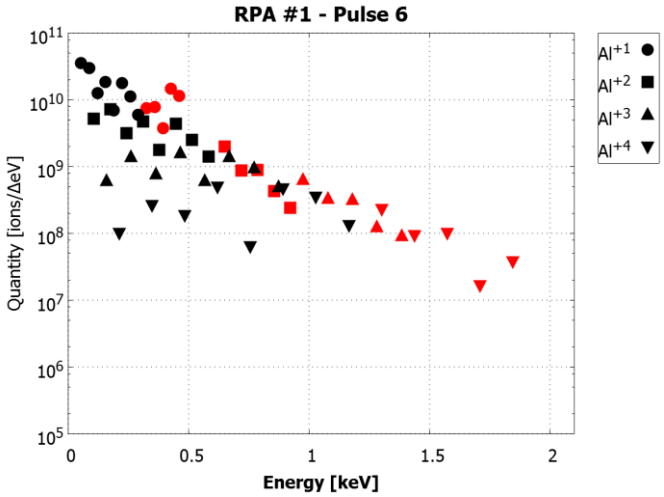

Fig. 224 RPA #1 Pulse 6 Energy Spectrum

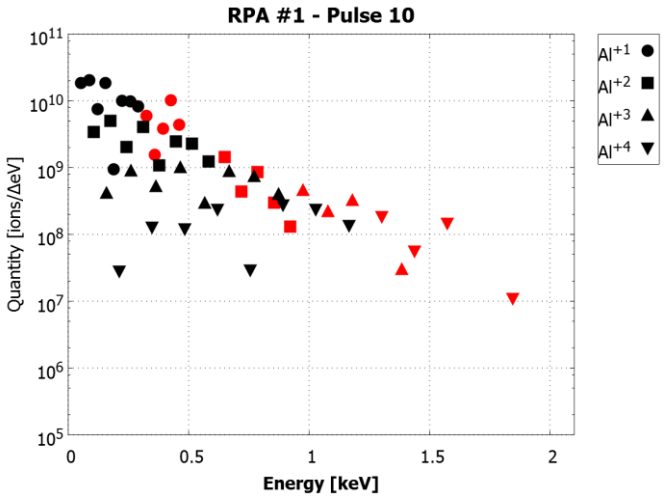

Fig. 225 RPA #1 Pulse 10 Energy Spectrum

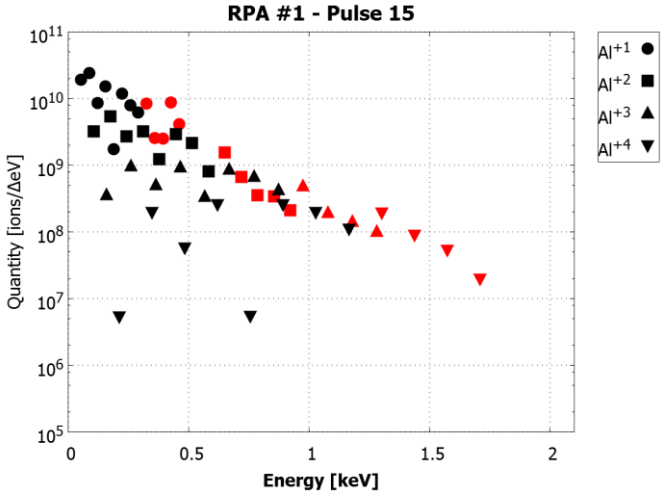

Fig. 226 RPA #1 Pulse 15 Energy Spectrum

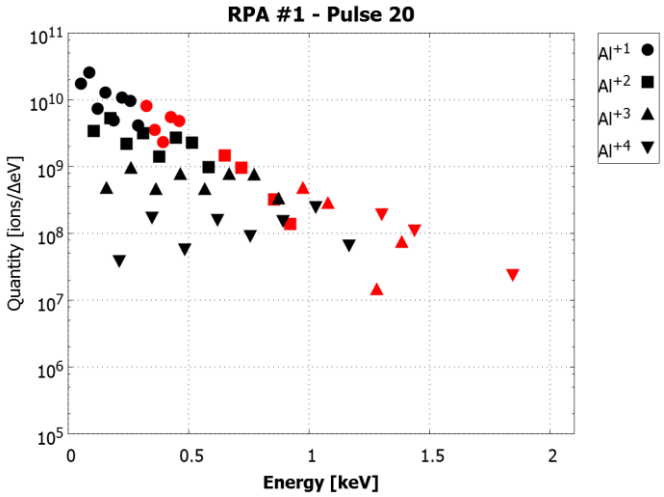

Fig. 227 RPA #1 Pulse 20 Energy Spectrum

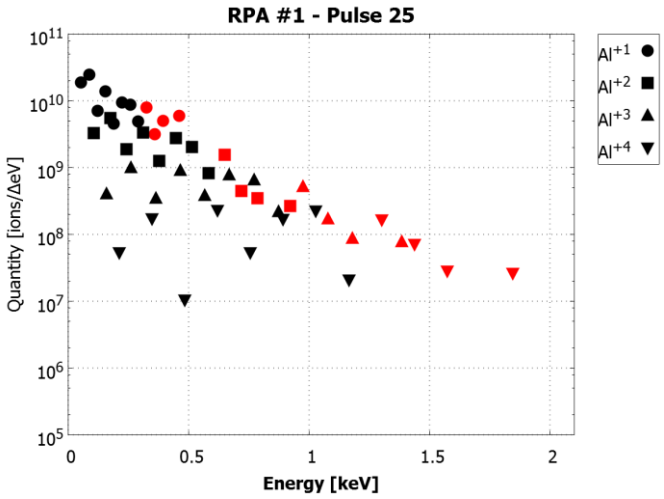

Fig. 228 RPA #1 Pulse 25 Energy Spectrum

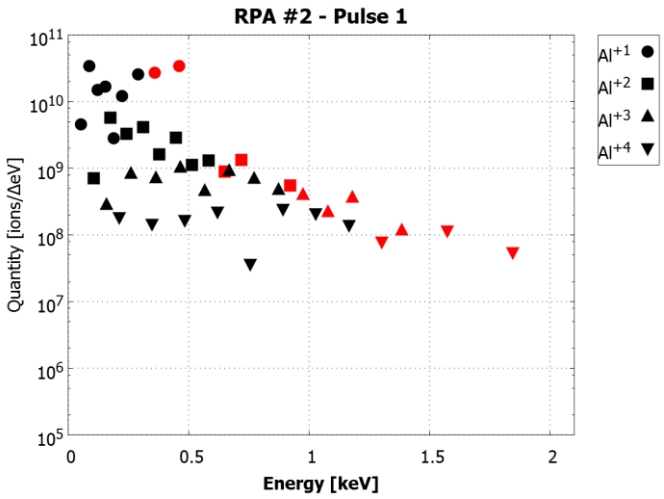

Fig. 229 RPA #2 Pulse 1 Energy Spectrum

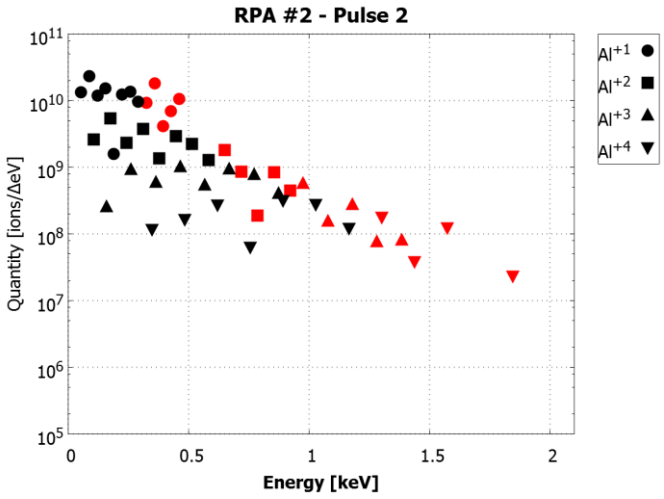

Fig. 230 RPA #2 Pulse 2 Energy Spectrum

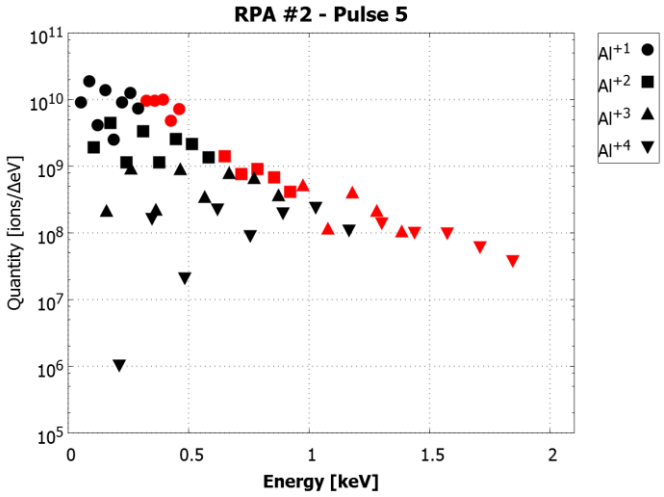

Fig. 231 RPA #2 Pulse 5 Energy Spectrum

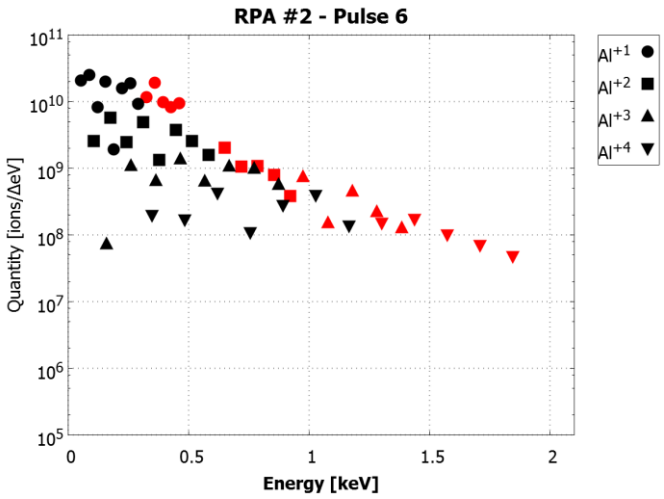

Fig. 232 RPA #2 Pulse 6 Energy Spectrum

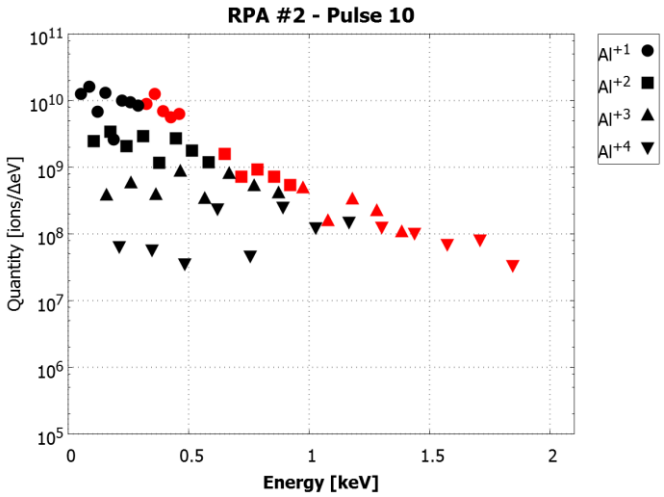

Fig. 233 RPA #2 Pulse 10 Energy Spectrum

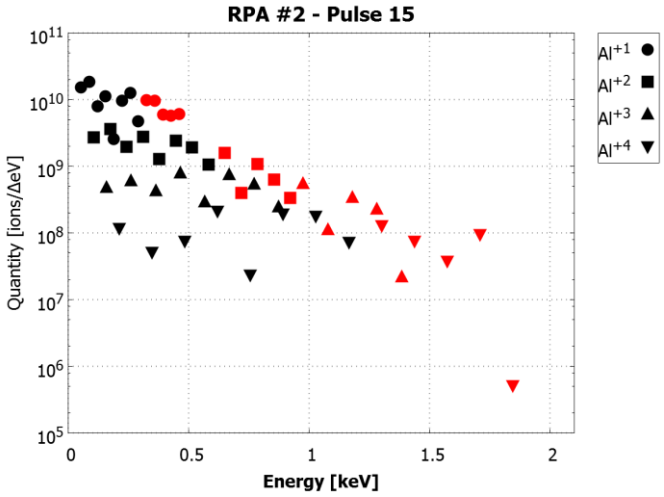

Fig. 234 RPA #2 Pulse 15 Energy Spectrum

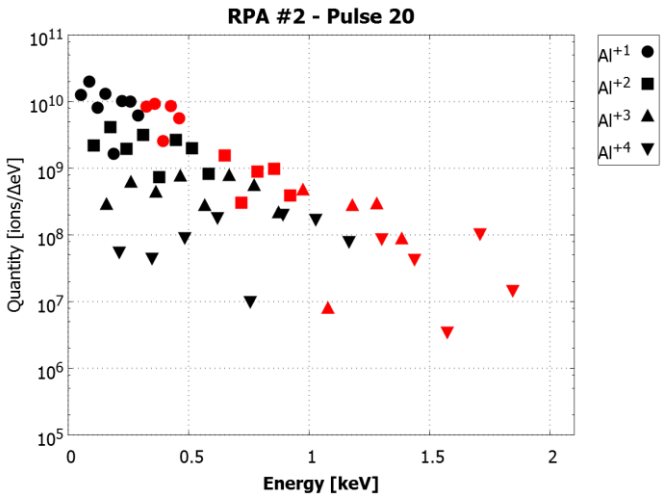

Fig. 235 RPA #2 Pulse 20 Energy Spectrum

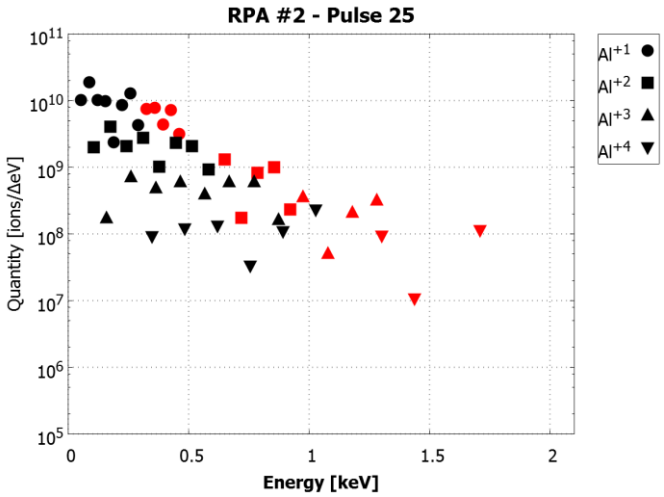

Fig. 236 RPA #2 Pulse 25 Energy Spectrum

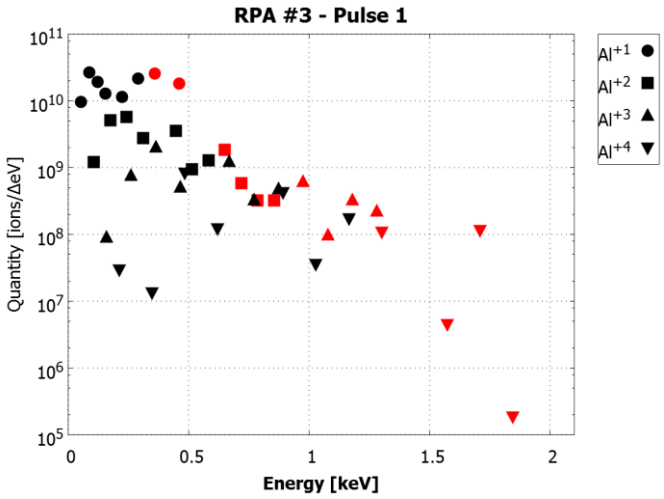

Fig. 237 RPA #3 Pulse 1 Energy Spectrum

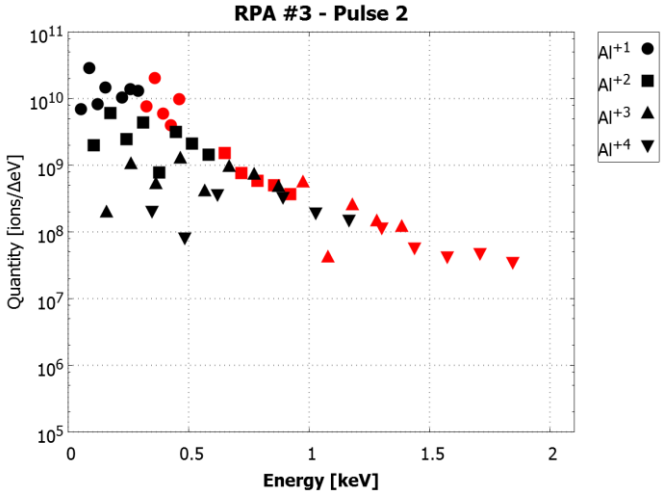

Fig. 238 RPA #3 Pulse 2 Energy Spectrum

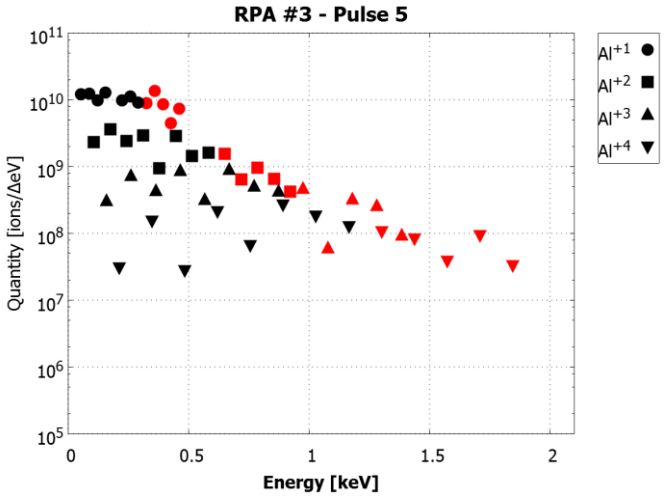

Fig. 239 RPA #3 Pulse 5 Energy Spectrum

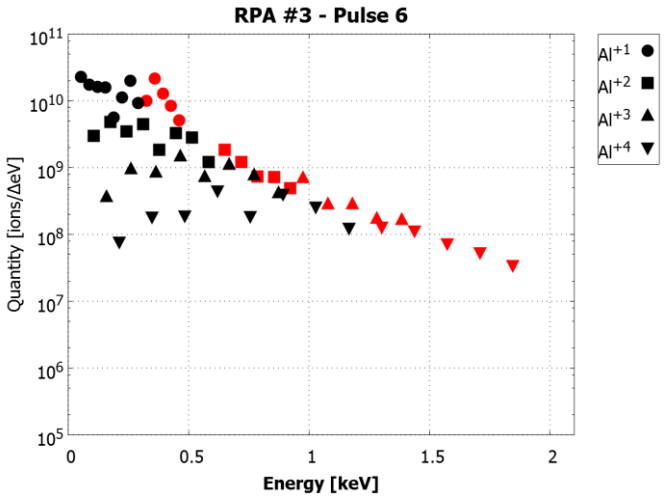

Fig. 240 RPA #3 Pulse 6 Energy Spectrum

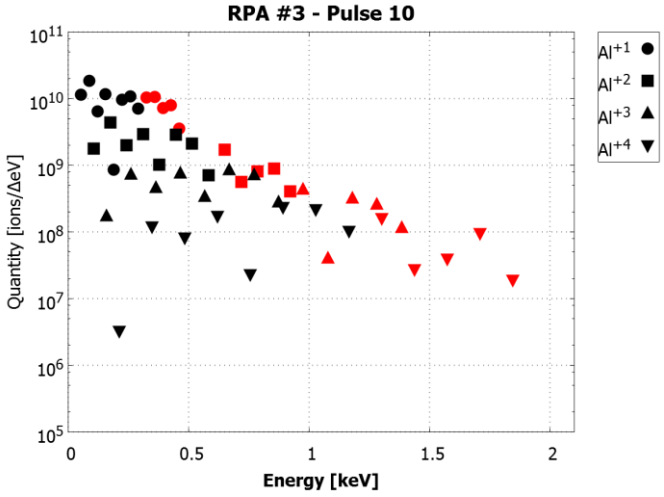

Fig. 241 RPA #3 Pulse 10 Energy Spectrum

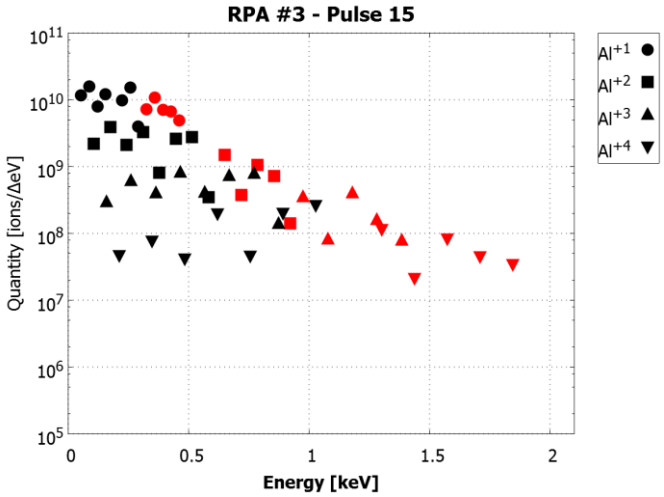

Fig. 242 RPA #3 Pulse 15 Energy Spectrum

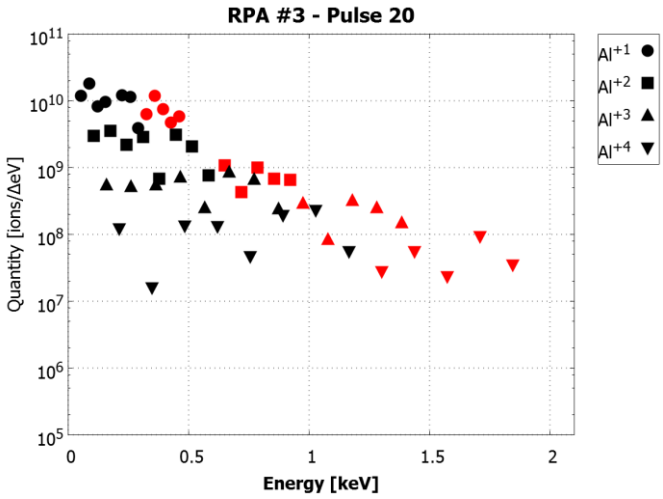

Fig. 243 RPA #3 Pulse 20 Energy Spectrum

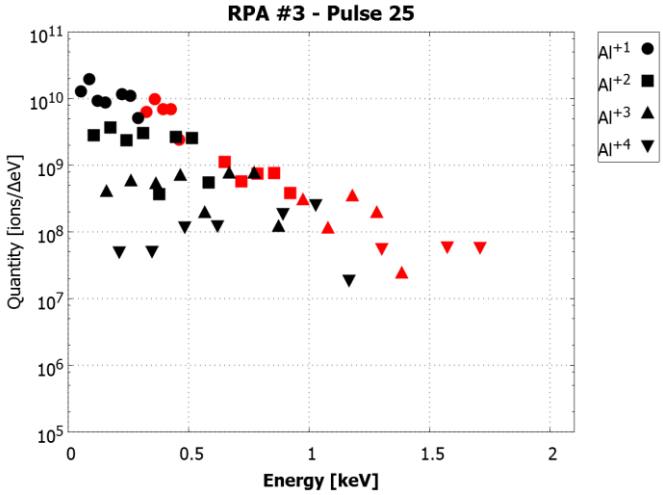

Fig. 244 RPA #3 Pulse 25 Energy Spectrum

A.5 Combined RPA & Spectrometer Energy Distribution Plots

These plots show the combination of data from RPA #1 (black) and Weak Focus #1 (red). The RPA data goes from 30 to 310 eV/e^-. The spectrometer data goes up from 310 eV/e^-.

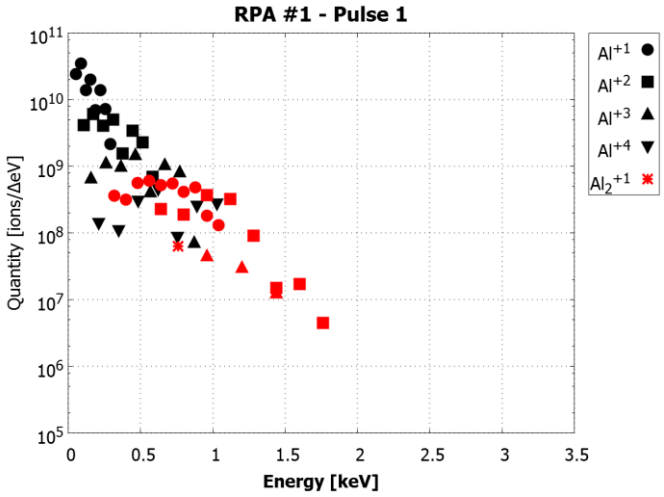

Fig. 245 Combined Pulse 1 Energy Spectrum

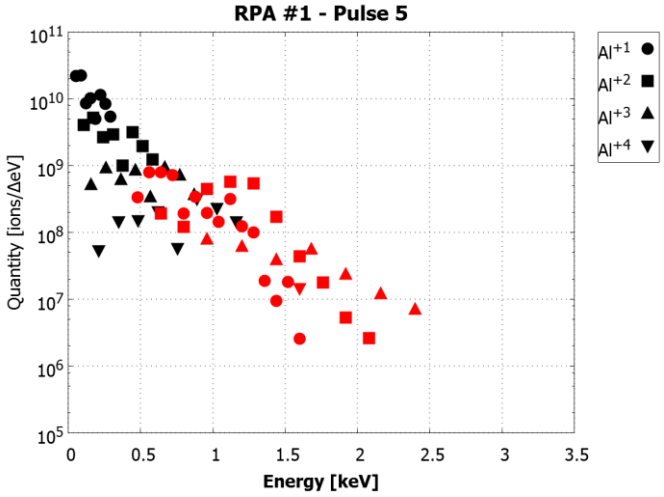

Fig. 246 Combined Pulse 5 Energy Spectrum

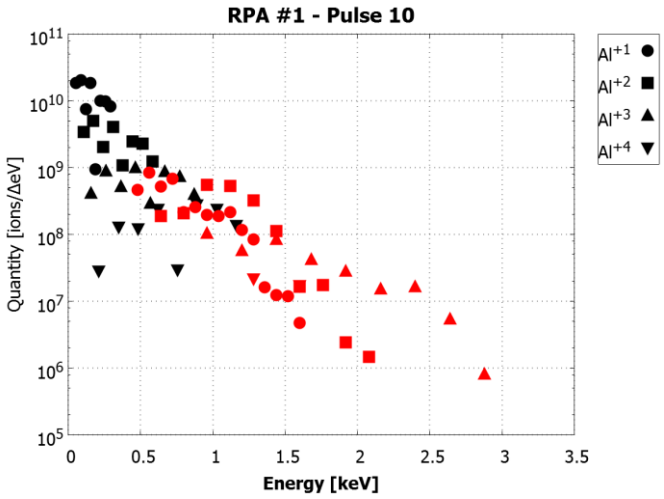

Fig. 247 Combined Pulse 10 Energy Spectrum

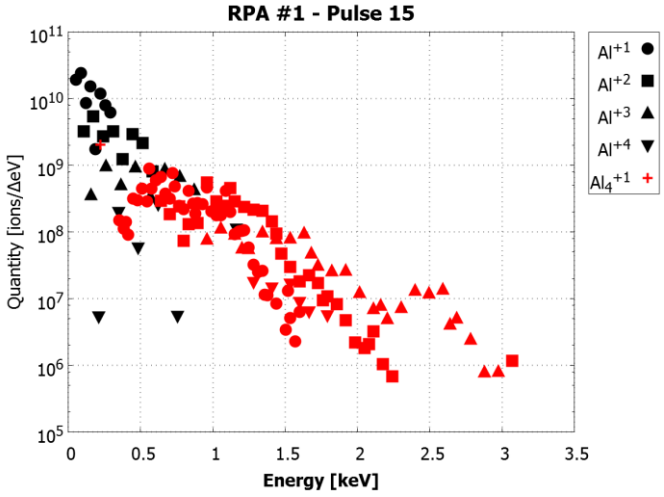

Fig. 248 Combined Pulse 15 Energy Spectrum

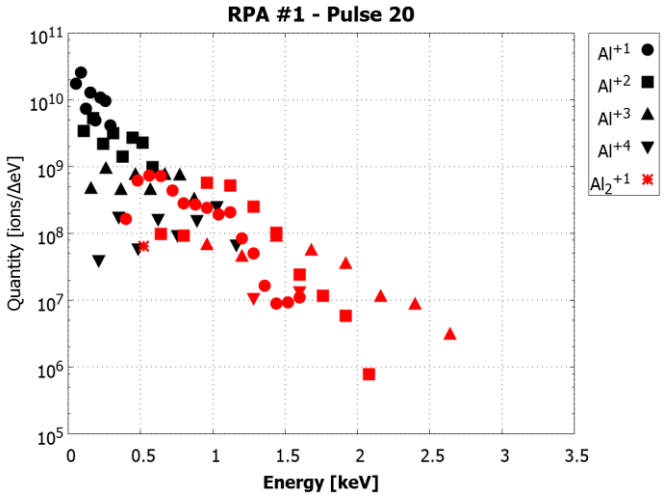

Fig. 249 Combined Pulse 20 Energy Spectrum

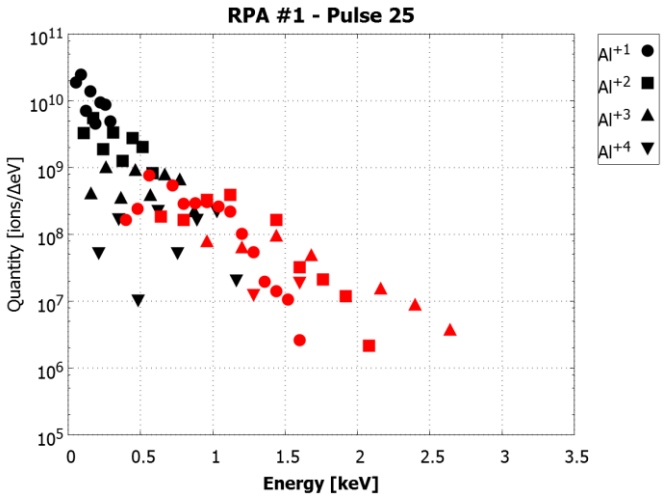

Fig. 250 Combined Pulse 25 Energy Spectrum

A.6 Ion Source Energy Sweep Plots

Table 11 System Biases For Plotted Ionic Liquid Sweeps

Liquid	Polarity	Secondary	V_{needle} [kV]	V_{det} [kV]	V_{scin}-V_{det} [kV]
EMI-BF_4	+	e^-	1.324	-5.007	5.007
EMI-BF_4	+	Al^+	1.324	-4.003	-3.711
EMI-BF_4	-	Al^+	-1.553	5.000	-5.000
EMI-BF_4	-	e^-	-1.553	4.008	3.888
EMI-Im	+	e^-	1.202	-5.039	5.039
EMI-Im	+	Al^+	1.262	-3.004	-5.014
EMI-Im	-	Al^+	-1.250	5.011	-5.011
EMI-Im	-	e^-	-1.346	4.006	4.072
EMI-$GaCl_4$	+	e^-	1.509	-4.998	4.998
EMI-$GaCl_4$	+	Al^+	1.614	-2.987	-4.852
EMI-$GaCl_4$	-	Al^+	-1.622	5.000	-5.000
EMI-$GaCl_4$	-	e^-	-1.298	4.012	3.657

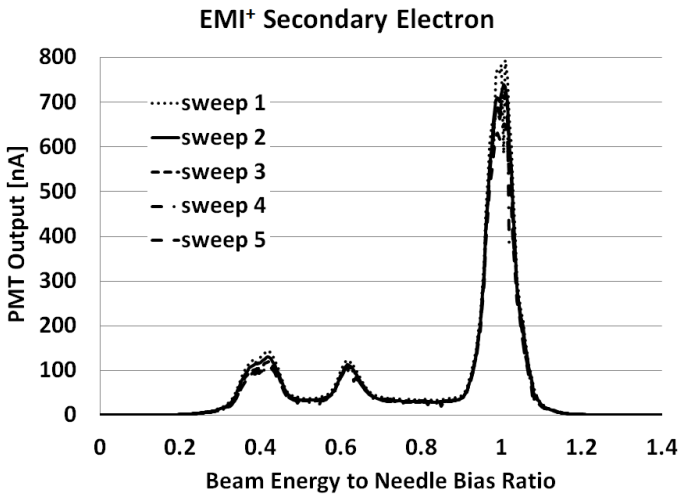

Fig. 251 EMI-BF_4, Positive Beam, Secondary Electron

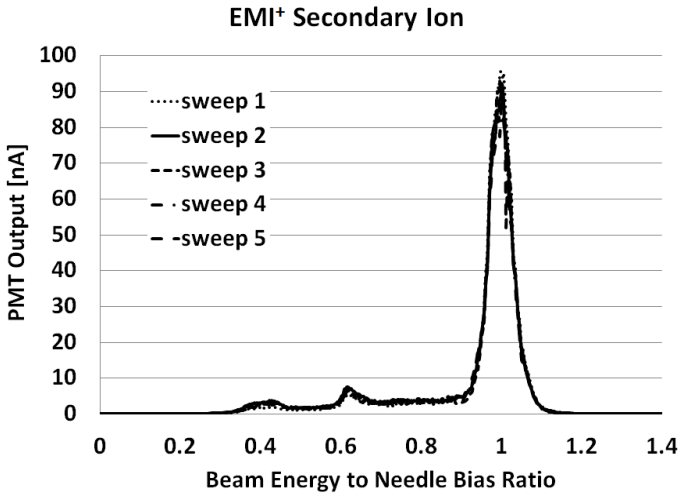

Fig. 252 EMI-BF_4, Positive Beam, Secondary Ion

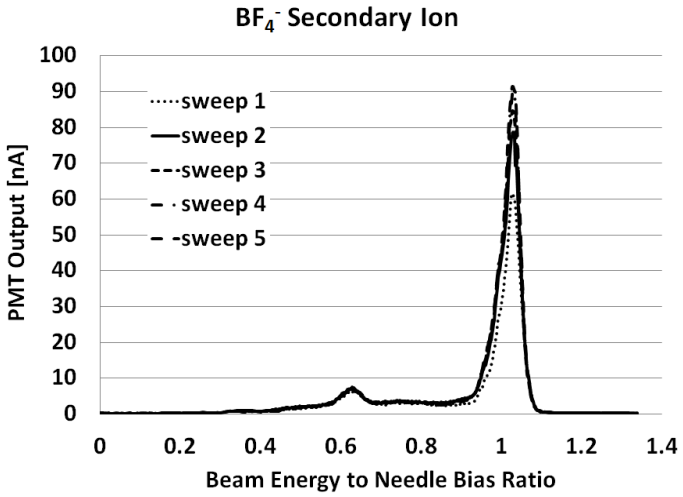

Fig. 253 EMI-BF_4, Negative Beam, Secondary Ion

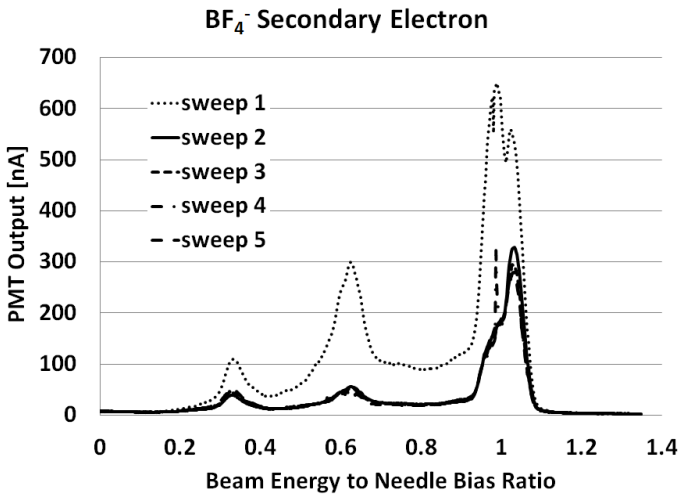

Fig. 254 EMI-BF_4, Negative Beam, Secondary Electron

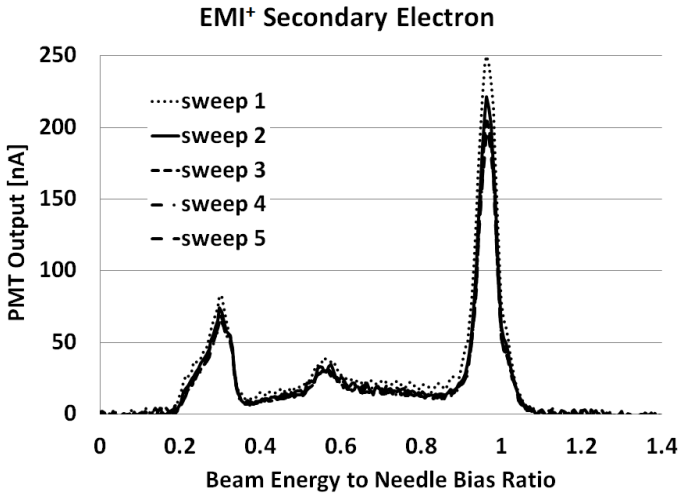

Fig. 255 EMI-Im, Positive Beam, Secondary Electron

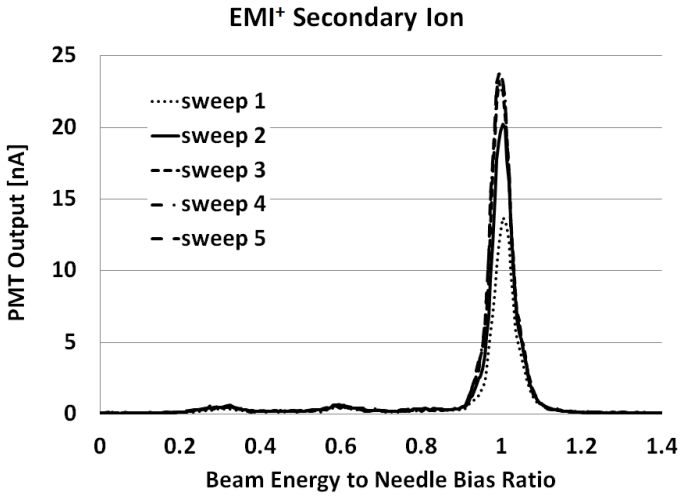

Fig. 256 EMI-Im, Positive Beam, Secondary Ion

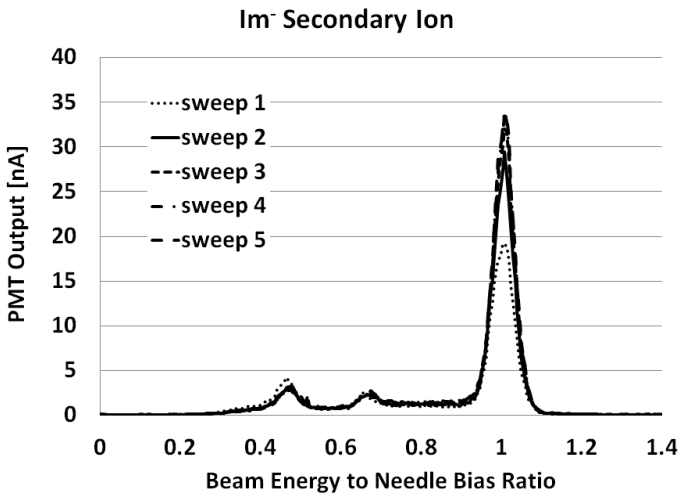

Fig. 257 EMI-Im, Negative Beam, Secondary Ion

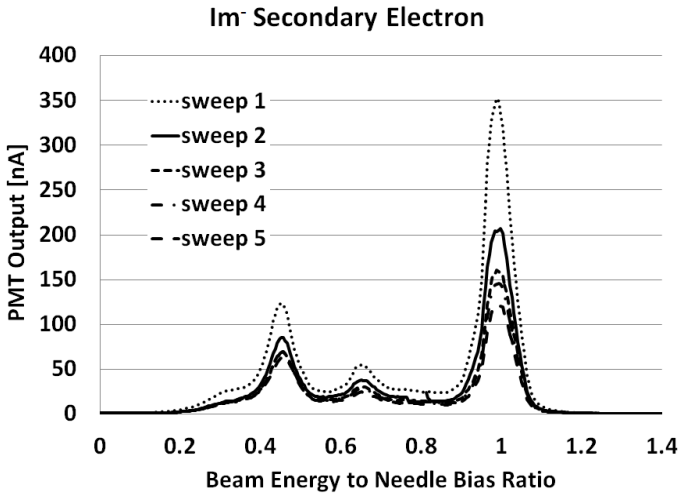

Fig. 258 EMI-Im, Negative Beam, Secondary Electron

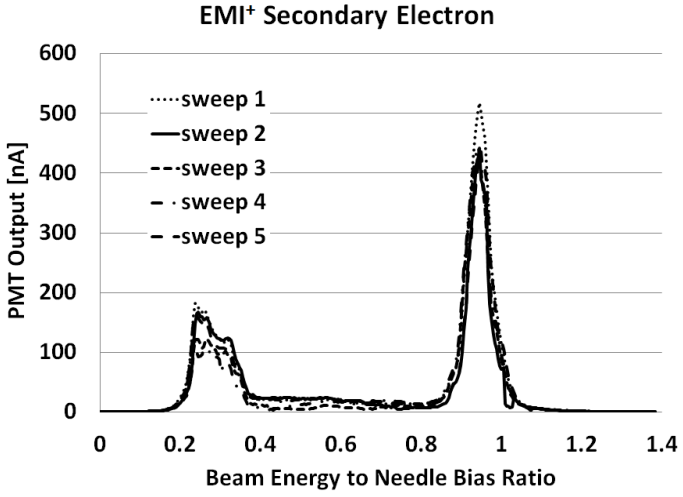

Fig. 259 EMI-$GaCl_4$, Positive Beam, Secondary Electron

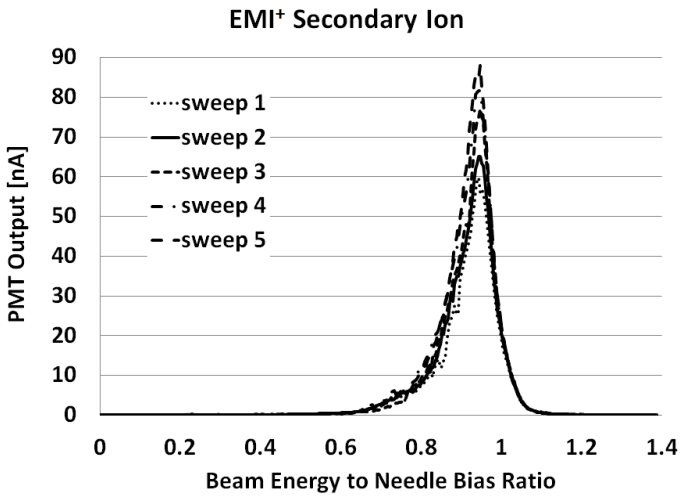

Fig. 260 EMI-$GaCl_4$, Positive Beam, Secondary Ion

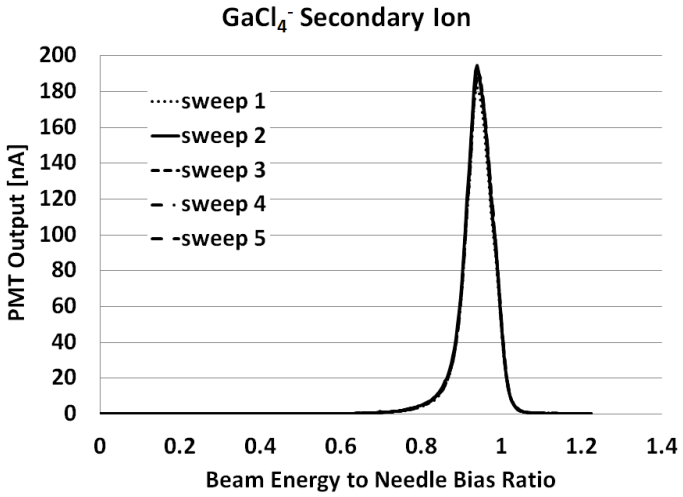

Fig. 261 EMI-$GaCl_4$, Negative Beam, Secondary Ion

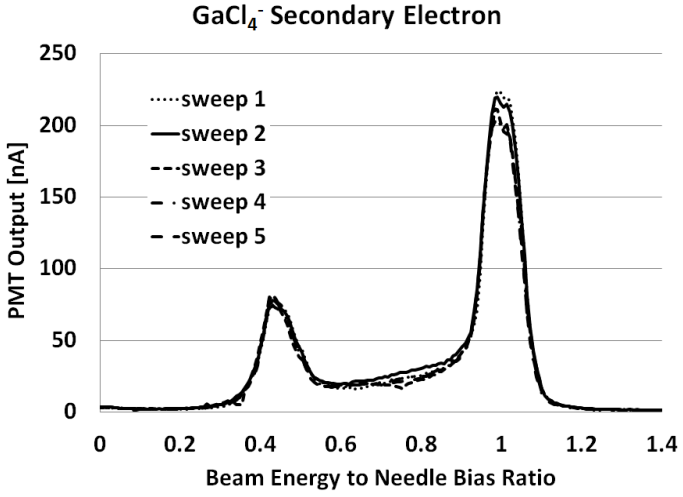

Fig. 262 EMI-$GaCl_4$, Negative Beam, Secondary Electron

Appendix B: Uncertainty Calculations

All uncertainties are calculated using the following formula.

$$\left(\sigma_{f(\bar{x})}\right)^2 = \sum_k \left[\left(\frac{\partial f}{\partial x_k}\sigma_k\right)^2\right] \tag{49}$$

B.1 Retarding Potential Analyzer (RPA)

The RPA was used to calculate the mass, momentum, and kinetic energy of the ablation plume for ion energy-per-charge less than 310V. The readout signal, *S(t)*, for a given RPA bias, V_j, is a time dependent voltage across a resistor, *R*, with parasitic capacitance, *C*. The uncertainty in this signal due variability of the ablation event is represented by a simple multiplier, A_j, and is independent for each RPA signal capture. The free flight length between the ablation site and RPA entry aperture, L_{TOF}, the solid angle of the RPA entry aperture, Ω, and the transparency for the RPA, *T*, are given in Table 12 along with their uncertainties. The uncertainty in the RPA bias is dominated by the step size between subsequent measurements. Typical uncertainties in mass, impulse, and kinetic energy are presented in Table 13.

Table 12 RPA Input Uncertainties

Quantity	Variable	Value	Uncertainty
Ablation variability	A_{bl}	1	20 %
RPA bias	V_j	variable	15 V
Readout resistance	R	2505 Ω	1 %
Readout capacitance	C	180 pF	11.1 %
Flight length	L_{TOF}	0.187 m	0.8 %
Transparency	T	0.137	12.2 %
Aperture solid angle	Ω	3.23 msr	1.6 %

Table 13 Typical RPA Metric Uncertainties

Quantity	Variable	Value	Uncertainty
Ablated mass (ionized)	m	220 pg/sr	17 %
Impulse	mv	6.5 nNs/sr	16.5 %
Kinetic Energy	E	120 μJ/sr	16.5 %
Average Velocity	v	30 km/s	16.5 %

The current, I, arriving at the RPA collector is given by Eq. (50).

$$I = \frac{S}{R} + C\frac{dS}{dt} \tag{50}$$

The current for a given energy level is calculated by subtracting the total current observed at neighboring energy levels, Eq. (51). The index j refers to the different RPA bias settings, V_j.

$$\Delta I_j(t) = I_{j-1}(t) - I_j(t) = A_j\left(\frac{1}{R}\left[S_{j-1}(t) - S_j(t)\right] + C\left[\dot{S}_{j-1}(t) - \dot{S}_j(t)\right]\right) \tag{51}$$

The performance metrics are then calculated from Eq. (52) through Eq. (54) , where n is the mass to charge ratio of each species in multiples of that for Al^{+1}.

$$\begin{aligned} m &= \frac{m_{Al}}{T\Omega}\sum_j\sum_n\left[A_j\int_{\tau(V_j,n)}^{\tau(V_j,n-1)}\frac{\Delta I_j(t)}{ne^-}dt\right] = \frac{m_{Al}}{e^-T\Omega}\sum_j\sum_n\left(A_j\left[\frac{1}{R}S_{m,j} + C\dot{S}_{m,j}\right]\right) \\ S_{m,j} &= \int_{\tau(V_j,n)}^{\tau(V_j,n-1)}\frac{\left[S_{j-1}(t) - S_j(t)\right]}{n}dt \quad , \quad \dot{S}_{m,j} = \int_{\tau(V_j,n)}^{\tau(V_j,n-1)}\frac{\left[\dot{S}_{j-1}(t) - \dot{S}_j(t)\right]}{n}dt \end{aligned} \tag{52}$$

$$\begin{aligned} mv &= \frac{m_{Al}}{T\Omega}\sum_j\sum_n\left[A_j\int_{\tau(V_j,n)}^{\tau(V_j,n-1)}\frac{\Delta I_j(t)}{ne}\left(\frac{L_{TOF}}{t}\right)dt\right] = \ldots \\ \ldots &= \frac{m_{Al}L_{TOF}}{eT\Omega}\sum_j\sum_n\left[A_j\left(\frac{1}{R}S_{mv,j} + C\dot{S}_{mv,j}\right)\right] \end{aligned} \tag{53}$$

$$S_{mv,j} = \int_{\tau(V_j,n)}^{\tau(V_j,n-1)}\frac{\left[S_{j-1}(t) - S_j(t)\right]}{nt}dt \quad , \quad \dot{S}_{mv,j} = \int_{\tau(V_j,n)}^{\tau(V_j,n-1)}\frac{\left[\dot{S}_{j-1}(t) - \dot{S}_j(t)\right]}{nt}dt$$

$$E = \frac{m_{Al}}{T\Omega}\sum_j\sum_n\left[A_j\int_{\tau(V_j,n)}^{\tau(V_j,n-1)}\frac{\Delta I_j(t)}{2ne}\left(\frac{L_{TOF}}{t}\right)^2 dt\right] = \ldots$$

$$\ldots = \frac{m_{Al}{L_{TOF}}^2}{2eT\Omega}\sum_j\sum_n\left[A_j\left(\frac{1}{R}S_{E,j} + C\dot{S}_{E,j}\right)\right] \tag{54}$$

$$S_{E,j} = \int_{\tau(V_j,n)}^{\tau(V_j,n-1)}\frac{\left[S_{j-1}(t) - S_j(t)\right]}{nt^2}dt \quad , \quad \dot{S}_{E,j} = \int_{\tau(V_j,n)}^{\tau(V_j,n-1)}\frac{\left[\dot{S}_{j-1}(t) - \dot{S}_j(t)\right]}{nt^2}dt$$

The integration bounds, Eq. (55), are calculated using Eq. (47) to get the flight time for singly charged aluminum. The formula is reduced to the free flight portion for uncertainty calculations.

$$\left(\frac{1}{\sqrt{4}}\right)t_{Al^{+1}} \le \tau \le \left(\sqrt{4}\right)t_{Al^{+1}}$$

$$\tau(U,N) = \frac{1}{\sqrt{N}}t_{Al^{+1}} \approx \frac{1}{\sqrt{N}}\frac{L_{TOF}}{\sqrt{2U}}\sqrt{\frac{m_{Al}}{e}} \tag{55}$$

Uncertainty due to the integration bounds between species is assessed via Leibniz's integral rule, Eq. (56).

$$\frac{d}{dx}\int_{a(x)}^{b(x)}f(x,t)dt = f(x,b(x))\frac{d}{dx}b(x) - f(x,a(x))\frac{d}{dx}a(x) + \int_{a(x)}^{b(x)}\frac{\partial}{\partial x}f(x,t)dt \tag{56}$$

The derivatives of the metrics *m*, *mv*, and *E* are given, unnumbered, in Appendix B.1.3. The average plume velocity is calculated by dividing the impulse by the mass. The velocity uncertainty is calculated from the mass and impulse uncertainties according to Eq. (57). The transparency and entry area cancel when calculating the velocity, so their uncertainties may be neglected when calculating the velocity uncertainty.

$$\frac{\sigma_v}{v} = \sqrt{\left(\frac{\sigma_{mv}}{mv}\right)^2 + \left(\frac{\sigma_m}{m}\right)^2} \tag{57}$$

B.1.1 RPA Aperture Solid Angle

The entry aperture solid angle is calculated from the aperture area and flight length. The aperture area is relatively well known compared to the flight length, so contributes negligibly.

$$\Omega = 2\pi\left(1-\cos\left[\tan^{-1}\left(\frac{r}{L_{TOF}}\right)\right]\right) \approx \pi\left(\frac{r}{L_{TOF}}\right)^2$$
$$\frac{\sigma_\Omega}{\Omega} = 2\left(\frac{\sigma_{L_{TOF}}}{L_{TOF}}\right) = 1.6\% \tag{58}$$

B.1.2 RPA Transparency

The transparency was calculated by comparing the spectrometer's aperture current signal and the lowest RPA signal near the peak of the signal, Eq. (59).

$$T \approx \frac{\Omega_{app} I_0(t_{\max})}{\Omega I_{app}(t_{\max})} \tag{59}$$

Both signals were averaged over multiple observations, giving an uncertainty of 11.5% for the average RPA signal and 4% for the average spectrometer aperture current. The uncertainty in readout resistance is low enough to be over powered by the RPA signal uncertainty. The uncertainty in capacitance may be ignored because the comparison focused on the peak of the signal, where its time derivative is zero. Uncertainty due to the entry area is also relatively small and may alternately be ignored because the major contributor, field-free flight length, is common to the two calculations. The uncertainty is calculated in Eq. (60).

$$\frac{\sigma_T}{T} = \sqrt{\left(\frac{\sigma_{I_0}}{I_0(t_{\max})}\right)^2 + \left(\frac{\sigma_{I_{app}}}{I_{app}(t_{\max})}\right)^2} = 12.2\% \tag{60}$$

B.1.3 Derivatives of the metrics

vs V_j

$$\frac{\partial m}{\partial V_j} = \frac{m_{Al}}{eT\Omega}\sum_n\left[A_j\frac{\Delta I_j\left(\tau\left(V_j,n-1\right)\right)}{n}\left(\frac{-1}{\sqrt{n-1}}L_{TOF}\left(2V_j\right)^{-\frac{3}{2}}\sqrt{\frac{m_{Al}}{e}}\right)\right]\ldots$$
$$\ldots-\frac{m_{Al}}{eT\Omega}\sum_n\left[A_j\frac{\Delta I_j\left(\tau\left(V_j,n\right)\right)}{n}\left(\frac{-1}{\sqrt{n}}L_{TOF}\left(2V_j\right)^{-\frac{3}{2}}\sqrt{\frac{m_{Al}}{e}}\right)\right]$$

$$\frac{\partial mv}{\partial V_j} = \frac{m_{Al}L_{TOF}}{eT\Omega}\sum_n\left[A_j\frac{\Delta I_j\left(\tau\left(V_j,n-1\right)\right)}{n\tau\left(V_j,n-1\right)}\left(\frac{-1}{\sqrt{n-1}}L_{TOF}\left(2V_j\right)^{-\frac{3}{2}}\sqrt{\frac{m_{Al}}{e}}\right)\right]\ldots$$
$$\ldots-\frac{m_{Al}L_{TOF}}{eT\Omega}\sum_n\left[A_j\frac{\Delta I_j\left(\tau\left(V_j,n\right)\right)}{n\tau\left(V_j,n\right)}\left(\frac{-1}{\sqrt{n}}L_{TOF}\left(2V_j\right)^{-\frac{3}{2}}\sqrt{\frac{m_{Al}}{e}}\right)\right]$$

$$\frac{\partial E}{\partial V_j} = \frac{m_{Al}{L_{TOF}}^2}{2eT\Omega}\sum_n\left[A_j\frac{\Delta I_j\left(\tau\left(V_j,n-1\right)\right)}{n\tau\left(V_j,n-1\right)^2}\left(\frac{-1}{\sqrt{n-1}}L_{TOF}\left(2V_j\right)^{-\frac{3}{2}}\sqrt{\frac{m_{Al}}{e}}\right)\right]\ldots$$
$$\ldots-\frac{m_{Al}{L_{TOF}}^2}{eT\Omega}\sum_n\left[A_j\frac{\Delta I_j\left(\tau\left(V_j,n\right)\right)}{n\tau\left(V_j,n\right)^2}\left(\frac{-1}{\sqrt{n}}L_{TOF}\left(2V_j\right)^{-\frac{3}{2}}\sqrt{\frac{m_{Al}}{e}}\right)\right]$$

vs L_{TOF}

$$\frac{\partial m}{\partial L_{TOF}} = \frac{m_{Al}}{eT\Omega}\sum_j\sum_n\left[A_j\frac{\Delta I_j\left(\tau\left(V_j,n-1\right)\right)}{n}\left(\frac{1}{\sqrt{n-1}}\frac{1}{\sqrt{2V_j}}\sqrt{\frac{m_{Al}}{e}}\right)\right]\ldots$$
$$\ldots-\frac{m_{Al}}{eT\Omega}\sum_j\sum_n\left[A_j\frac{\Delta I_j\left(\tau\left(V_j,n\right)\right)}{n}\left(\frac{1}{\sqrt{n}}\frac{1}{\sqrt{2V_j}}\sqrt{\frac{m_{Al}}{e}}\right)\right]$$

$$\frac{\partial mv}{\partial L_{TOF}} = \frac{m_{Al}}{eT\Omega}\sum_j\sum_n\left[A_j\left(\frac{1}{R}S_{mv,j} + C\dot{S}_{mv,j}\right)\right]\ldots$$
$$\ldots + \frac{m_{Al}L_{TOF}}{eT\Omega}\sum_j\sum_n\left[A_j\frac{\Delta I_j\left(\tau\left(V_j,n-1\right)\right)}{n\tau\left(V_j,n-1\right)}\left(\frac{1}{\sqrt{n-1}}\frac{1}{\sqrt{2V_j}}\sqrt{\frac{m_{Al}}{e}}\right)\right]\ldots$$
$$\ldots - \frac{m_{Al}L_{TOF}}{eT\Omega}\sum_j\sum_n\left[A_j\frac{\Delta I_j\left(\tau\left(V_j,n\right)\right)}{n\tau\left(V_j,n\right)}\left(\frac{1}{\sqrt{n}}\frac{1}{\sqrt{2V_j}}\sqrt{\frac{m_{Al}}{e}}\right)\right]$$

$$\frac{\partial E}{\partial L_{TOF}} = \frac{m_{Al}L_{TOF}}{eT\Omega}\sum_j\sum_n\left[A_j\left(\frac{1}{R}S_{E,j} + C\dot{S}_{E,j}\right)\right]\ldots$$
$$\ldots + \frac{m_{Al}{L_{TOF}}^2}{eT\Omega}\sum_j\sum_n\left[A_j\frac{\Delta I_j\left(\tau\left(V_j,n-1\right)\right)}{n\tau\left(V_j,n-1\right)^2}\left(\frac{1}{\sqrt{n-1}}\frac{1}{\sqrt{2V_j}}\sqrt{\frac{m_{Al}}{e}}\right)\right]\ldots$$
$$\ldots - \frac{m_{Al}{L_{TOF}}^2}{eT\Omega}\sum_j\sum_n\left[A_j\frac{\Delta I_j\left(\tau\left(V_j,n\right)\right)}{n\tau\left(V_j,n\right)^2}\left(\frac{1}{\sqrt{n}}\frac{1}{\sqrt{2V_j}}\sqrt{\frac{m_{Al}}{e}}\right)\right]$$

vs R

$$\frac{\partial m}{\partial R} = \frac{-m_{Al}}{eT\Omega R^2}\sum_j\sum_n\left[A_jS_{m,j}\right]$$

$$\frac{\partial mv}{\partial R} = \frac{-m_{Al}L_{TOF}}{eT\Omega R^2}\sum_j\sum_n\left[A_jS_{mv,j}\right]$$

$$\frac{\partial E}{\partial R} = \frac{-m_{Al}{L_{TOF}}^2}{2eT\Omega R^2}\sum_j\sum_n\left[A_jS_{E,j}\right]$$

vs C

$$\frac{\partial m}{\partial C} = \frac{m_{Al}}{eT\Omega}\sum_j\sum_n\left[A_j\dot{S}_{m,j}\right]$$

$$\frac{\partial mv}{\partial C} = \frac{m_{Al}L_{TOF}}{eT\Omega}\sum_j\sum_n\left[A_j\dot{S}_{mv,j}\right]$$

$$\frac{\partial E}{\partial C} = \frac{m_{Al} L_{TOF}^{\ 2}}{2eT\Omega} \sum_j \sum_n \left[A_j \dot{S}_{E,j} \right]$$

vs A_j, T, and Ω

$$\frac{\partial f}{\partial x} = \frac{f}{x}$$

B.2 Mass Spectrometer (MS)

The spectrometer was used to calculate the mass, momentum, and kinetic energy of the ablation plume for ion energy-per-charge greater than 310V. The uncertainties of input parameters are listed in Table 14. Typical uncertainties in the output metrics are listed in Table 15.

Table 14 Spectrometer Input Uncertainties

Quantity	Variable	Value	Uncertainty
Energy gate bias	V_i	variable	0.02 %
Ion-energy-to-gate-bias ratio	η	3.2	3.6 %
Flight length	L_{TOF}	0.269 m	0.8 %
Aperture solid angle	Ω	8.86 μsr	1.6 %
Ablation variability (PMT)	A_{bl}	1	32 %
PMT readout resistance	R	2505 Ω	1 %
PMT readout capacitance	C	125 pF	6.7 %
Ablation variability (aperture)	A_{bl2}	1	15 %
Aperture current resistance	R_{app}	2497 Ω	1 %
Aperture current capacitance	C_{app}	130 pF	7.7 %
Detector bias	V_{det}	5 kV	1.3%
Scintillator bias	V_{scin}	grounded	0 %
PMT gain control	V_{pmt}	4 V	2.5 %
Detection Efficiency	β_2	7000	16.6 %
Calibration data fitting error	*Fit*	1	2-4 %

Table 15 Typical Spectrometer Metric Uncertainties

Quantity	Variable	Value	Uncertainty
Ablated mass (ionized)	m	32 pg/sr	21 %
Impulse	mv	2.7 nNs/sr	21.5 %
Kinetic Energy	E	110 μJ/sr	22 %
Average Velocity	v	81 km/s	11 %

The readout signal, *S(t)*, for a given spectrometer gate bias, V_i, is a time dependent voltage across a resistor, *R*, with parasitic capacitance, *C*. Each spectrometer energy gate bias is identified by the index i and each ion species in the ablation plume is identified by the index n. The mass content (per eV), $M_{n,i}$, of each ion species at a given energy level, $KE_{n,i}$, is calculated by integrating the current pulses, index j, produced by the PMT as each species arrives, Eq. (61), and applying calibrations, β_k, from Chapter 4, Eq. (62). In these equations, a_j, b_j, and c_j are fit parameters for the j^{th} pulse, q_n is the charge of the n^{th} species, and m_n is the mass of a single ion of the n^{th} species. Uncertainties for the fit parameters are negligible compared to the overall variability of the ablation signal between cases, represented by A_{bl} in Table 14.

$$Q_{n,i} = A_{n,i} \sum_j \int \left[a_j \exp\left(\frac{\left(t - b_j\right)^2}{2{c_j}^2} \right) dt \right] = A_{n,i} \sum_j \left[a_j c_j \sqrt{2\pi} \right] \tag{61}$$

$$M_{n,i} = \prod_k [\beta_k] \frac{m_n Q_{n,i}}{q_n} \tag{62}$$

Derivatives of each calibration factor with resepct to the parameters in Table 14 are covered in subsections B.2.1 through B.2.8. They are combined with derivatives of the metrics with respect to $M_{n,i}$ and $M_{n,i-1}$ to get the derivative of the

metrics with each of the input parameters. Most of the corrections take a form like Eq. (63), so have a derivative like Eq. (64). A number of the corrections used to calculate $M_{n,i}$ are a constant for all spectrometer cases, and so their uncertainties may be neglected when comparing between spectrometer cases, as is the case for calculating the average velocity. This will be noted in the subsection for that specific correction.

The uncertainty in $M_{n,i}$ due variability of the ablation event is represented by a simple multiplier, $A_{n,i}$, and is independent for each species and each spectrometer capture.

$$\beta^{-1}(x) = f(x) \tag{63}$$

$$\frac{\partial \beta}{\partial x} = -\beta^2 \frac{\partial f}{\partial x} \tag{64}$$

The uncertainty contributions of the readout resistance and capacitance follow trivially from integrating Eq. (50) over time, provided the input signal and its time derivative, which are given by Eqs. (65) and (66). The signal is a reconstruction of the observed input, so the values of R, C, a, b, and c used in Eqs. (65) and (66) are exact – uncertainty comes only from the quality of the fit, which is much better than the inherent variability between ablation events.

$$\begin{aligned} S(t) = \exp\left(-\frac{t}{RC}\right)\sum_{i=1}^{N}\left[\sqrt{\frac{\pi}{2}}\frac{a_i c_i}{C}\exp\left(\frac{2RCb_i + c_i^{\,2}}{2R^2C^2}\right)\cdots\right. \\ \left.\cdots\left(\operatorname{erf}\left(\frac{RCb_i + c_i^{\,2}}{\sqrt{2}c_i RC}\right) - \operatorname{erf}\left(\frac{RC(b_i - t) + c_i^{\,2}}{\sqrt{2}c_i RC}\right)\right)\right] \end{aligned} \tag{65}$$

$$\dot{S}(t) = -\frac{S(t)}{RC} + \frac{1}{C}\sum_{i=1}^{N} a_i \exp\left(-\frac{(t-b_i)^2}{2c_i^{\,2}}\right) \tag{66}$$

The plume distribution, M, is built by linearly interpolating between observed energy levels, Eq. (67).

$$\begin{gathered} M_{n,i}(KE) = a_{n,i}\left(KE - KE_{n,i-1}\right) + M_{n,i-1} \\ a_{n,i} = \frac{M_{n,i} - M_{n,i-1}}{KE_{n,i} - KE_{n,i-1}} \quad , \quad KE_{n,i} = q_n \eta V_i \end{gathered} \tag{67}$$

Uncertainty in KE comes from the applied voltage, calibration with the ion source (0.9%, section 4.4.1), uncertainty in the entry angle (0.1°, section 3.2.1), and uncertainty from the spectrometer energy-per-charge passband width (3.3%, section 4.4.4). Using Eq. (23), the entry angle uncertainty leads to a kinetic energy uncertainty of 1.1%. Combining all these gives a total uncertainty in KE_i of 3.6%.

The mass, m, impulse, mv, and kinetic energy, E, of the ionized ablation plume are calculated by integrating the distribution M, leading to Eq. (68) through (70). Note that m is the observed mass in the plume, including all species, while m_n is the mass of a single ion of species n. The derivatives of the metrics m, mv, and E are given, unnumbered, in subsections B.2.9 through B.2.12. The velocity is calculated from the ratio of mv to m, as for the RPA, and uses the same uncertainty formula, Eq. (57).

$$m = \sum_n \sum_i \left[\left(KE_{n,i} - KE_{n,i-1}\right) \frac{\left(M_{n,i} + M_{n,i-1}\right)}{2} \right] \tag{68}$$

$$mv = \sum_n \sum_i \left[\frac{2a_{n,i}}{5} \sqrt{\frac{2e^-}{m_n}} \left(KE_{n,i}{}^{2.5} - KE_{n,i-1}{}^{2.5} \right) .. \right.$$
$$\left. ... + \frac{2}{3} \sqrt{\frac{2e^-}{m_n}} \left(M_{n,i-1} - a_{n,i} KE_{n,i-1} \right) \left(KE_{n,i}{}^{1.5} - KE_{n,i-1}{}^{1.5} \right) \right] \quad (69)$$

$$E = \sum_n \sum_i \left[\frac{e^- a_{n,i}}{3m_n} \left(KE_{n,i}{}^{3} - KE_{n,i-1}{}^{3} \right) .. \right.$$
$$\left. ... + \frac{e^-}{2m_n} \left(M_{n,i-1} - a_{n,i} KE_{n,i-1} \right) \left(KE_{n,i}{}^{2} - KE_{n,i-1}{}^{2} \right) \right] \quad (70)$$

B.2.1 β_1: Entry Area

This correction converts the total observed signal to a per-steradian value, based on the effective entry aperture area (sec 3.2.1). The entry aperture area in steradians is a function of flight length. This parameter is the same for all spectrometer cases, so its uncertainty can be ignored when comparing different spectrometer cases.

$$\beta_1{}^{-1} = \Omega \approx \frac{\Delta y \Delta z}{L_{TOF}{}^2}$$
$$\frac{\partial \beta_1}{\partial L_{TOF}} = \left(\beta^2 \right) \left(\frac{2\Omega}{L_{TOF}} \right) \quad (71)$$

B.2.2 β_2: Overall Detection Efficiency

This correction accounts for the overall detection efficiency (secondary particle yields, scintillator yield, etc.) for each primary ion at a reference primary and secondary particle impact energy and PMT gain (sec 4.15). The parameter is determined by fitting the spectrometer data to the RPA data above 300 V, focusing

near the maximum. The only new uncertainty contribution from this correction is the uncertainty of the peak of the 300V RPA signal. The RPA signal uncertainty is 11.5% after averaging. The RPA transparency adds another 12%. This parameter is the same for all spectrometer cases, so its uncertainty can be ignored when comparing different spectrometer cases.

$$\beta_2^{-1} = 7\times10^3$$

$$\frac{\sigma_{\beta_2}}{\beta_2} = \sqrt{0.115^2 + 0.12^2} = 16.6\% \tag{72}$$

$$\frac{\partial\beta_2}{\partial\beta_2^{-1}} = -\beta^2$$

B.2.3 β_3: Space Charge

This correction accounts for expansion of the beam within the spectrometer due to space charge (sec 4.14).

$$\beta_3 = \frac{A}{A_0} = 3.13\times10^8\left(\frac{\gamma}{\eta V_{gate}}\right)^{1.070} + 1$$

$$\gamma(t) = \frac{I_{app}(t)}{A_{app}}\frac{t}{L_{TOF}} \tag{73}$$

The area of the beam, A, is in m^2. The charge density at the entry aperture is represented by γ (changed from σ to avoid confusion with uncertainty) and expressed in C/m^3. The gate pass energy-per-charge, ηV_{gate}, is in Volts. Fitting the simulation results introduced an uncertainty, σ_{Fit}, of less than 4%. Uncertainty in the overall value of the multiplier is absorbed into β_2, the readout conversion factor. The charge density at the aperture is calculated from ion velocity, the aperture current, and the

aperture area. The aperture current and its uncertainty are calculated in the same way as for the RPA current, based on Eq. (50), including an inherent uncertainty due to ablation, represented in Table 14 by A_{bl2}. Uncertainties in the aperture area and arrival timing are negligible relative to flight length and aperture current. Derivatives due to the ion energy are grouped in Eq. (74) and derivatives due to charge density in Eq. (75).

$$\frac{\partial \beta_3}{\partial \eta} = -1.07 \times 3.13 \times 10^8 \left(\frac{1}{\eta^{2.070}} \right) \left(\frac{\gamma}{V_{gate}} \right)^{1.070}$$
$$\frac{\partial \beta_3}{\partial V_{gate}} = -1.07 \times 3.13 \times 10^8 \left(\frac{1}{V_{gate}^{2.070}} \right) \left(\frac{\gamma}{\eta} \right)^{1.070} \tag{74}$$

$$\frac{\partial \beta_3}{\partial R_{app}} = \left(1.07 \times 3.13 \times 10^8 \frac{\gamma^{0.07}}{(\eta V_{gate})^{1.07}} \right) \left[\left(\frac{t}{A_{app} L_{TOF}} \right) \left(\frac{S_{app}(t)}{R_{app}^{\ 2}} \right) \right]$$
$$\frac{\partial \beta_3}{\partial C_{app}} = \left(1.07 \times 3.13 \times 10^8 \frac{\gamma^{0.07}}{(\eta V_{gate})^{1.07}} \right) \left[\left(\frac{t}{A_{app} L_{TOF}} \right) \left(\dot{S}_{app}(t) \right) \right] \tag{75}$$
$$\frac{\partial \beta_3}{\partial A_{bl2}} = \left(1.07 \times 3.13 \times 10^8 \frac{\gamma^{0.07}}{(\eta V_{gate})^{1.07}} \right) (\gamma)$$

B.2.4 β_4: Defocusing in the accelerator

This corrects for defocusing of low energy ions when they are accelerated to the detector voltage in a single step (sec 4.3.2). This correction is unity for all ions above 350 eV/e-.

$$\beta_4^{-1} = 1.52\times10^{-3}\left(\eta V_{gate}\right) + 0.454 \qquad \eta V_{gate} < 350\frac{eV}{e^-}$$

$$\frac{\partial\beta_4}{\partial V_{gate}} = -\left(\beta_4^{\,2}\right)\left(1.52\times10^{-3}\eta\right) \tag{76}$$

$$\frac{\partial\beta_4}{\partial\eta} = -\left(\beta_4^{\,2}\right)\left(1.52\times10^{-3}V_{gate}\right)$$

B.2.5 β_5: Spectrometer Passband Shape

This correction converts from total ion content over time at a specific energy to total ion content per unit energy. It is assumed that the distribution is constant over the bandwidth of the spectrometer and that the spectrometer passband is Gaussian (sec 4.4.4). The only significant uncertainty comes from the gate pass energy-per-charge, U, whose uncertainty is 3.6%. For this calculation, ηV_{gate} is in Volts and q_n is in multiples of electron charge. The fit parameters a_j, b_j, and c_j are in amps, seconds, and seconds.

$$\beta_5^{-1} = \sqrt{2\pi}\,\frac{2q_n\eta V_{gate}}{\sum_j a_j c_j\sqrt{2\pi}}\left(\sum_j\left[a_j c_j\sqrt{2\pi}\,\frac{c_i}{b_i}\right]\right)$$

$$\frac{\partial\beta_5}{\partial\eta} = -\left(\beta_5^{\,2}\right)\left(\frac{\beta_5^{-1}}{\eta}\right) \tag{77}$$

$$\frac{\partial\beta_5}{\partial V_{gate}} = -\left(\beta_5^{\,2}\right)\left(\frac{\beta_5^{-1}}{V_{gate}}\right)$$

B.2.6 β_6: Detector impact energy

This corrects for differences in the detector bias and ion impact energy relative to the case for which β_2 was determined (sec 4.12.1). For this calculation,

ηV_{gate} and V_{det} are in kV and q_n is in multiples of electron charge. Uncertainty, σ_{Fit}, in the average value at each observed impact energy was approximately 4%. The correction is only applied for impact energies lower than 6.17 keV. The detector bias was the same for all cases, so its uncertainty (a small fraction of the uncertainty for this correction) won't affect comparisons between different spectrometer cases.

$$\beta_6^{-1} = 0.4122 \ln\left(q_n\left[\eta V_{gate} + V_{\det}\right]\right) + 0.2499$$

$$\frac{\partial \beta_6}{\partial \eta} = -\beta_6^{\,2}\left(\frac{0.4122 V_{gate}}{\eta V_{gate} + V_{\det}}\right) \quad , \quad \frac{\partial \beta_6}{\partial V_{gate}} = -\beta_6^{\,2}\left(\frac{0.4122 \eta}{\eta V_{gate} + V_{\det}}\right) \tag{78}$$

$$\frac{\partial \beta_6}{\partial V_{\det}} = -\beta_6^{\,2}\left(\frac{0.4122}{\eta V_{gate} + V_{\det}}\right) \quad , \quad \frac{\partial \beta_6}{\partial Fit} = -\beta_6^{\,2}\left(\beta_6^{-1}\right)$$

B.2.7 β_7: Secondary particle energy

This corrects for differences in the scintillator bias setting relative to the case for which β_2 was determined (sec 4.12.2). For this calculation, V_{scin} and V_{det} are in kV. Uncertainty, σ_{Fit}, in the average value at each observed secondary paritcle energy was approximately 2%. This parameter was the same for all cases, so can be ignored for comparisons between spectrometer cases.

$$\beta_7^{-1} = 0.0586\left(V_{scin} - \mathrm{V}_{\det}\right)^2 - 0.0857\left(V_{scin} - \mathrm{V}_{\det}\right) - 0.0368$$

$$\frac{\partial \beta_7}{\partial V_{scin}} = -\left(\beta_7^{\,2}\right)\left(0.1172\left[V_{scin} - V_{\det}\right] - 0.0857\right)$$

$$\frac{\partial \beta_7}{\partial V_{\det}} = \left(\beta_7^{\,2}\right)\left(0.1172\left[V_{scin} - V_{\det}\right] - 0.0857\right) \tag{79}$$

$$\frac{\partial \beta_7}{\partial Fit} = -\left(\beta_7^{\,2}\right)\left(\beta_7^{-1}\right)$$

B.2.8 β_8: Photomultiplier gain

This corrects for differences in PMT gain, expressed by the control voltage *P* in Volts, relative to the case for which β_2 was determined (sec 4.12.3). Uncertainty, $\sigma_{Fit,}$ in the average gain at each observed value of P was approximately 4%. This parameter was the same for all cases, so can be ignored for comparisons between spectrometer cases.

$$\begin{aligned} \beta_8^{-1} &= 1.01P - 2.98 \\ \frac{\partial \beta_8}{\partial P} &= -\left(\beta_8^{\,2}\right)(1.01) \\ \frac{\partial \beta_8}{\partial Fit} &= -\left(\beta_8^{\,2}\right)\left(\beta_8^{-1}\right) \end{aligned} \tag{80}$$

B.2.9 Derivatives of the metrics – a

Derivatives of a are provided here to simplify calculation and presentation of the derivatives of the metrics.

$$a_{n,i} = \frac{M_{n,i} - M_{n,i-1}}{KE_{n,i} - KE_{n,i-1}}$$

$$\frac{\partial a_{n,i}}{\partial M_{n,i}} = \frac{1}{KE_{n,i} - KE_{n,i-1}}$$

$$\frac{\partial a_{n,i}}{\partial M_{n,i-1}} = \frac{-1}{KE_{n,i} - KE_{n,i-1}}$$

$$\frac{\partial a_{n,i}}{\partial KE_{n,i}} = \frac{\left(M_{n,i} - M_{n,i-1}\right)}{\left(KE_{n,i} - KE_{n,i-1}\right)^2}$$

$$\frac{\partial a_{n,i}}{\partial KE_{n,i-1}} = \frac{-\left(M_{n,i} - M_{n,i-1}\right)}{\left(KE_{n,i} - KE_{n,i-1}\right)^2}$$

B.2.10 Derivatives of the metrics – Mass

$$m = \sum_n \sum_i \left[\left(KE_{n,i} - KE_{n,i-1} \right) \frac{\left(M_{n,i} + M_{n,i-1} \right)}{2} \right]$$

$$\frac{\partial m_{n,i}}{\partial KE_{n,i}} = \frac{M_{n,i} + M_{n,i-1}}{2}$$

$$\frac{\partial m_{n,i}}{\partial KE_{n,i-1}} = \frac{-\left(M_{n,i} + M_{n,i-1} \right)}{2}$$

$$\frac{\partial m_{n,i}}{\partial M_{n,i}} = \frac{KE_{n,i} - KE_{n,i-1}}{2}$$

$$\frac{\partial m_{n,i}}{\partial M_{n.i-1}} = \frac{-\left(KE_{n,i} - KE_{n,i-1} \right)}{2}$$

$$\left(\sigma_m \right)^2 = \sum_n \sum_i \left[\left(\frac{\partial m_{n,i}}{\partial M_{n,i}} \sigma_{M_{n,i}} \right)^2 + \left(\frac{\partial m_{n,i}}{\partial M_{n,i-1}} \sigma_{M_{n,i-1}} \right)^2 \ldots \right.$$
$$\left. \ldots + \left(\frac{\partial m_{n,i}}{\partial KE_{n,i}} \sigma_{KE_{n,i}} \right)^2 + \left(\frac{\partial m_{n,i}}{\partial KE_{n,i-1}} \sigma_{KE_{n,i-1}} \right)^2 \right]$$

B.2.11 Derivatives of the metrics – Impulse

Note: m_n is the mass of nth ion, not the value of the mass metric summed over index i.

$$mv = \sum_n \sum_i \left[\frac{2a_{n,i}}{5} \sqrt{\frac{2e^-}{m_n}} \left[{KE_{n,i}}^{2.5} - {KE_{n,i-1}}^{2.5} \right] .. \right.$$
$$\left. \ldots + \frac{2}{3} \sqrt{\frac{2e^-}{m_n}} \left[M_{n,i-1} - a_{n,i} KE_{n,i-1} \right] \left[{KE_{n,i}}^{1.5} - {KE_{n,i-1}}^{1.5} \right] \right]$$

$$\frac{\partial mv_{n,i}}{\partial a_{n,i}} = \frac{2}{5} \sqrt{\frac{2e^-}{m_n}} \left({KE_{n,i}}^{2.5} - {KE_{n,i}}^{2.5} \right) - \frac{2}{3} \sqrt{\frac{2e^-}{m_n}} KE_{n,i} \left({KE_{n,i}}^{1.5} - {KE_{n,i}}^{1.5} \right)$$

$$\frac{\partial mv_{n,i}}{\partial M_{n,i}} = \frac{\partial mv_{n,i}}{\partial a_{n,i}} \frac{\partial a_{n,i}}{\partial M_{n,i}}$$

$$\frac{\partial mv_{n,i}}{\partial M_{n,i-1}} = \frac{2}{3}\sqrt{\frac{2e^-}{m_n}}\left(KE_{n,i}{}^{1.5} - KE_{n,i-1}{}^{1.5}\right) + \frac{\partial mv_{n,i}}{\partial a_{n,i}} \frac{\partial a_{n,i}}{\partial M_{n,i-1}}$$

$$\frac{\partial mv_{n,i}}{\partial KE_{n,i}} = a_{n,i} KE_{n,i}{}^{1.5}\sqrt{\frac{2e^-}{m_n}} + KE_{n,i}{}^{0.5}\sqrt{\frac{2e^-}{m_n}}\left(M_{n,i-1} - a_{n,i} KE_{n,i-1}\right) + \frac{\partial mv_{n,i}}{\partial a_{n,i}} \frac{\partial a_{n,i}}{\partial KE_{n,i}}$$

$$\frac{\partial mv_{n,i}}{\partial KE_{n,i-1}} = -a_{n,i} KE_{n,i-1}{}^{1.5}\sqrt{\frac{2e^-}{m_n}} - KE_{n,i-1}{}^{0.5}\sqrt{\frac{2e^-}{m_n}}\left(M_{n,i-1} - a_{n,i} KE_{n,i-1}\right)...$$
$$...-\frac{2a_{n,i}}{3}\sqrt{\frac{2e^-}{m_n}}\left(KE_{n,i}{}^{1.5} - KE_{n,i-1}{}^{1.5}\right) + \frac{\partial mv_{n,i}}{\partial a_{n,i}} \frac{\partial a_{n,i}}{\partial KE_{n,i-1}}$$

$$\left(\sigma_{mv}\right)^2 = \sum_n \sum_i \left[\left(\frac{\partial mv_{n,i}}{\partial M_{n,i}}\sigma_{M_{n,i}}\right)^2 + \left(\frac{\partial mv_{n,i}}{\partial M_{n,i-1}}\sigma_{M_{n,i-1}}\right)^2 ...\right.$$
$$\left....+\left(\frac{\partial mv_{n,i}}{\partial KE_{n,i}}\sigma_{KE_{n,i}}\right)^2 + \left(\frac{\partial mv_{n,i}}{\partial KE_{n,i-1}}\sigma_{KE_{n,i-1}}\right)^2\right]$$

B.2.12 Derivatives of the metrics – Energy

Note: m_n is the mass of nth ion, not the value of the mass metric summed over index i.

$$E = \sum_n \sum_i \left[\frac{e^- a_{n,i}}{3m_n}\left[KE_{n,i}{}^3 - KE_{n,i-1}{}^3\right] + \frac{e^-}{2m_n}\left[M_{n,i-1} - a_{n,i} KE_{n,i-1}\right]\left[KE_{n,i}{}^2 - KE_{n,i-1}{}^2\right]\right]$$

$$\frac{\partial E_{n,i}}{\partial a_{n,i}} = \frac{e^-}{3m_n}\left(KE_{n,i}{}^3 - KE_{n,i-1}{}^3\right) - \frac{e^-}{2m_n} KE_{n,i-1}\left(KE_{n,i}{}^2 - KE_{n,i-1}{}^2\right)$$

$$\frac{\partial E_{n,i}}{\partial M_{n,i}} = \frac{\partial E_{n,i}}{\partial a_{n,i}} \frac{\partial a_{n,i}}{\partial M_{n,i}}$$

$$\frac{\partial E_{n,i}}{\partial M_{n,i-1}} = \frac{e^-}{2m_n}\left(KE_i{}^2 - KE_{i-1}{}^2\right) + \frac{\partial E_{n,i}}{\partial a_{n,i}}\frac{\partial a_{n,i}}{\partial M_{n,i-1}}$$

$$\frac{\partial E_{n,i}}{\partial KE_{n,i}} = \frac{e^- a_{n,i}}{m_n} KE_i{}^2 + \frac{e^-}{m_n} KE_i\left(M_{n,i-1} - a_{n,i}KE_{i-1}\right) + \frac{\partial E_{n,i}}{\partial a_{n,i}}\frac{\partial a_{n,i}}{\partial KE_{n,i}}$$

$$\frac{\partial E_{n,i}}{\partial KE_{n,i-1}} = \frac{-e^- a_{n,i}}{m_n} KE_{i-1}{}^2 - \frac{e^-}{m_n} KE_{i-1}\left(M_{n,i-1} - a_{n,i}KE_{i-1}\right)\ldots$$

$$\ldots - \frac{e^- a_{n,i}}{2m_n}\left(KE_i{}^2 - KE_{i-1}{}^2\right) + \frac{\partial E_{n,i}}{\partial a_{n,i}}\frac{\partial a_{n,i}}{\partial KE_{n,i-1}}$$

$$\left(\sigma_E\right)^2 = \sum_n \sum_i \left[\left(\frac{\partial E_{n,i}}{\partial M_{n,i}}\sigma_{M_{n,i}}\right)^2 + \left(\frac{\partial E_{n,i}}{\partial M_{n,i-1}}\sigma_{M_{n,i-1}}\right)^2 \ldots\right.$$

$$\left.\ldots + \left(\frac{\partial E_{n,i}}{\partial KE_{n,i}}\sigma_{KE_{n,i}}\right)^2 + \left(\frac{\partial E_{n,i}}{\partial KE_{n,i-1}}\sigma_{KE_{n,i-1}}\right)^2\right]$$

B.3 Combined Instrument Results

The mass, momentum, and kinetic energy metrics from the spectrometer (>310 V) and RPA (<310 V) were combined to get those metrics for the overall plume. Their combined uncertainty was calculated by a straight forward application of Eq. (49). Values relative to laser energy use the same formula, but add the laser uncertainty, 5.3% (sec 4.1). Typical uncertainties in the output metrics are listed in Table 16.

Table 16 Typical Combined Metric Uncertainties

Quantity	Variable	Value	Uncertainty
Ablated mass (ionized)	m	250 pg/sr	15 %
Impulse	mv	9.3 nNs/sr	13.5 %
Kinetic energy	E	230 μJ/sr	14 %
Average velocity[a]	v	33 km/s	13 %
Mass per energy[a]		410 ng/J	16 %
Momentum coupling[a]	C_m	14 μNs/J	14.5 %
Propulsive efficiency[a]	eff	31 %	15 %
Ionization fraction[a]		8 %	15 %
Specific Impulse[a]	I_{sp}	270 s	20 %

a) Adjusted for typical ablation plume profile (sec 5.3)

The combined velocity is an average of the two instruments weighed by ablated mass, Eq. (81). The average velocity for each instrument is calculated from the impulse and mass metrics, Eq. (82). Several uncertainties (noted in each uncertainties own section) are reduced because the calculation represents a comparison of observations from the same instrument. Those uncertainties enter into the velocity averaged over both instruments through the weighting factor for the average (the mass metric).

$$v_{MS} = \left(\frac{mv}{m}\right)_{MS}$$

$$\left(\frac{\sigma_v}{v}\right)_{MS} = \left(\sqrt{\left(\frac{\sigma_{mv}}{mv}\right)^2 + \left(\frac{\sigma_m}{m}\right)^2}\right)_{MS} \tag{81}$$

$$v = \frac{v_{MS}m_{MS} + v_{RPA}m_{RPA}}{m_{MS} + m_{RPA}}$$

$$\sigma_v = \sqrt{\left(\frac{\partial v}{\partial v_{MS}}\sigma_{v_{MS}}\right)^2 + \left(\frac{\partial v}{\partial v_{RPA}}\sigma_{v_{RPA}}\right)^2 + \left(\frac{\partial v}{\partial m_{MS}}\sigma_{m_{MS}}\right)^2 + \left(\frac{\partial v}{\partial m_{RPA}}\sigma_{m_{RPA}}\right)^2} \tag{82}$$

$$\frac{\partial v}{\partial v_{MS}} = \frac{m_{MS}}{m_{MS} + m_{RPA}} \quad , \quad \frac{\partial v}{\partial v_{RPA}} = \frac{m_{RPA}}{m_{MS} + m_{RPA}}$$

$$\frac{\partial v}{\partial m_{MS}} = \frac{v_{MS} - v}{m_{MS} + m_{RPA}} \quad , \quad \frac{\partial v}{\partial m_{RPA}} = \frac{v_{RPA} - v}{m_{MS} + m_{RPA}}$$

Specific impulse is calculated from the removed volume per pulse observed by a scanning electron microscope (converted to mass by the material density), m_{SEM}. The average plume velocity and the mass of the ionized portion of the plume are v_{ion} and m_{ion}.The typical value and uncertainty for m_{SEM} are 1.5 ng and 3% (sec 4.17).

$$I_{sp} = \frac{v_{ion}}{g0} \frac{m_{ion}}{m_{SEM}}$$

$$\sigma_{I_{sp}} = \sqrt{\left(\frac{\sigma_{v_{ion}}}{v_{ion}}\right)^2 + \left(\frac{\sigma_{m_{ion}}}{m_{ion}}\right)^2 + \left(\frac{\sigma_{m_{SEM}}}{m_{SEM}}\right)^2} \tag{83}$$

Bibliography

[2] Eric S. Smith, Raymond J. Sedwick, John F. Merk, et al., "Assessing the Potential of a Laser-Ablation-Propelled Tug to Remove Large Space Debris," Journal of Spacecraft and Rockets, vol. 50, no. 6, pp. 1268-1276, 2013. 10.2514/1.A32439

[3] John E. Sinko and Don A. Gregory, "CO2 Laser Ablation Impulse Generation with Polymer Propellants," Journal of Propulsion and Power, vol. 27, no. 5, pp. 1121-1130, 2011.

[4] John E. Sinko and Don A. Gregory, "Critical fluence effects in laser propulsion," Proc of SPIE: High-Power Laser Ablation VII, vol. 7005, 2008.

[5] R. A. Ganeev, U. Chakravarty, P. A. Naik, et al., "Pulsed laser deposition of metal films and nanoparticles in vacuum using subnanosecond laser pulses," Applied Optics, vol. 46, no. 8, pp. 1205 - 1210, 2007.

[6] A. W. Bailey and A. Modak, "Numerical Simulation of Laser Ablation with Cavity Reflections," Journal of Thermophysics, vol. 3, no. 1, 1988.

[7] Koji Suzuki, Keisuke Sawada, Ryota Takaya, et al., "Ablative Impulse Characteristics of Polyacetal with Repetitive CO2 Laser Pulses," JOURNAL OF PROPULSION AND POWER, vol. 24, no. 4, 2008.

[8] John E. Sinko, Nilesh B. Dhote, Jonathan S. Lassiter, et al., "Conical nozzles for pulsed laser propulsion," Proc. of SPIE: High Power Laser Ablation VII, vol. 7005, 2008.

[9] Karl-Heinz Leitz, Benjamin Redlingshofer, Yvonne Reg, et al., "Metal Ablation with Short and Ultrashort Laser Pulses," Physics Procedia, vol. 12, pp. 230-238, 2011.

[10] David Gomez and Igor Goenaga, "On the incubation effect on two thermoplastics when irradiated with ultrashort laser pulses: Broadening effects when machining microchannels," Applied Surface Science, vol. 253, pp. 2230-2236, 2006.

[11] P. T. Mannion, J. Magee, E. Coyne, et al., "The effect of damage accumulation behaviour on ablation thresholds and damage morphology in ultrafast laser micro-machining of common metals in air," Applied Surface Science, vol. 233, pp. 275-287, 2004.

[12] Wenqian Hu, Yung C. Shin, and Galen King, "Modeling of multi-burst mode pico-second laser ablation for improved material removal rate," Applied Physics A, vol. 98, pp. 407-415, 2010.

[13] S. M. Pershin, "Nonlinear increase in the interaction efficiency of a second pulse with a target upon excitation of a plasma by a train of pulses from a Nd:YAG laser," Quantum Electronics, vol. 39, no. 1, pp. 63-67, 2009.

[14] Hideyuki Horisawa, Tadaki Shinohara, and Kazuyoku Tei, "Development of Compact High-Power Laser System for Laser-Electric Hybrid Propulsion System," 46th AIAA/ASME/SAE/ASEE Joint Propulsion Conference & Exhibit, 2010.

[15] Peter J. Cumpson, Jose F. Portoles, Anders J. Barlow, et al., "Accurate argon cluster-ion sputter yields: Measured yields and effect of the sputter threshold in practical depth-profiling by x-ray photoelectron spectroscopy and secondary ion mass spectrometry," Journal of Applied Physics, vol. 114, pp. 124313, 2013.

[16] T. Seki, T. Murase, and J. Matsuo, "Cluster size dependence of sputtering yield by cluster ion beam irradiation," Nuclear Instruments and Methods in Physics Research B, vol. 242, no. 1-2, pp. 179 - 181, 2006.

[17] M. P. Seah, "Universal Equation for Argon Gas Cluster Sputtering Yields," Journal of Physical Chemistry C, vol. 117, pp. 12622 - 12632, 2013.

[18] C. Guillermier, S. Della Negra, R. D. Rickman, et al., "Influence of massive projectile size and energy on secondary ion yields from organic surfaces," Applied Surface Science, vol. 252, pp. 6529-6532, 2006.

[1] S N Srivastava, B K Sinha, and K P Rohr, "Ions and ion-energy spectra of a collisional laser plasma produced from multi-species targets of aluminium and titanium," Journal of Physics B: Atomic, Molecular and Optical Physics, vol. 39, pp. 3073-3086, 2006. 10.1088/0953-4075/39/14/014

[19] O. Benavides, L. del la Cruz May, and A. Flores Gil, "A comparative study on reflection of nanosecond Nd-YAG laser pulses in ablation of metals in air and in vacuum," Optics Express, vol. 21, no. 11, pp. 13068-13074, 2013. 10.1364/OE.21.013068

[20] Lukas Urech, Thomas Lippert, Claude R. Phipps, et al., "Polymers as Fuel for laser plasma thrusters. A correlation of thrust with material and plasma properties by mass spectrometry," Proc of SPIE: High-Power Laser Ablation VI, vol. 6261, 2006.

[21] A. S. Rubin, S. H. Zaidi, and R. B. Miles, "Thrust vectoring of laser-ablated aluminum plasma using permanent magnets," 50th AIAA Aerospace Sciences Meeting including the New Horizons Forum and Aerospace Exposition, 2012.

[22] Kohei Anju, Keisuke Sawada, Akihiro Sasoh, et al., "Time-Resolved Measurements of Impulse Generation in Pulsed Laser-Ablative Propulsion," Journal of Propulsion and Power, vol. 24, no. 2, pp. 322-329, 2009.

[23] C. Phipps, J. Luke, D. Funk, et al., "Laser impulse coupling at 130 fs," Applied Surface Science, vol. 252, pp. 4838-4844, 2006.

[24] Andrew V. Pakhomov, Jun Lin, and M. Shane Thompson, "SPECIFIC IMPULSE OF ABLATIVE LASER PROPULSION," 42nd AIAA Aerospace Sciences Meeting and Exhibit, 2004.

[25] Muddassir M S Gualini, Shakeel A. Khan, and Salman Iqbal, "Comparative Study of Plastics as Propellants for Laser Ablation Plasma Thrusters," JOURNAL OF PROPULSION AND POWER, vol. 25, no. 5, 2009.

[26] S. S. Harilal, M. S. Tillack, B. O'Shay, et al., "Confinement and dynamics of laser-produced plasma expanding across a transverse magnetic field," Physical Review E, vol. 69, 2004.

[27] Atsushi Matsuda, Takeharu Sakai, and Akihiro Sasoh, "Ablation impulse characteristics by laser pulse irradiation," 47th AIAA Aerospace Sciences Meeting Including The New Horizons Forum and Aerospace Exposition, 2009.

[28] Koichi Mori, Akihiro Sasoh, Kimiya Komurasaki, et al., "Preliminary experiments of a double-beam technique for laser-ablative-impulse enhancement," 47th AIAA Aerospace Sciences Meeting Including The New Horizons Forum and Aerospace Exposition, 2009.

[29] Shigeaki Uchida, Kazuo Imasaki, Xianglin Zhou, et al., "Enhancement of momentum coupling efficiency using repetitive pulse ablation," Proc. of SPIE: High Power Laser Ablation III, vol. 4065, pp. 495-501, 2000.

[30] Z. Zhang, P. A. VanRompay, J. A. Nees, et al., "Multi-diagnostic comparison of femtosecond and nanosecond pulsed laser plasmas," Journal of Applied Physics, vol. 92, no. 5, pp. 2867-2874, 2002.

[31] B. Rethfeld, K. Sokolowski-tinten, D. Von Der Linde, et al., "Timescales in the response of materials to femtosecond laser excitation," Applied Physics A: Materials Science & Processing, vol. 79, pp. 767-769, 2004.

[32] J. K. Chen, D. Y. Tzou, and J. E. Beraun, "A semiclassical two-temperature model for ultrafast laser heating," International Journal of Heat and Mass Transfer, vol. 49, pp. 307-316, 2006.

[33] W. S. Fann, R. Storz, H. W K Tom, et al., "Electron thermalization in gold," Physical Review B, vol. 46, no. 20, 1992.

[34] W. S. Fann, R. Storz, H. W K Tom, et al., "Direct Measurement of Nonequilibrium Electron-Energy Distributions in Subpicosecond Laser-Heated Gold Films," Physical Review Letters, vol. 68, no. 18, 1992.

[35] B. N. Chichkov, C. Momma, S. Nolte, et al., "Femtosecond, picosecond and nanosecond laser ablation of solids," Applied Physics A: Materials Science & Processing, vol. 63, pp. 109-115, 1996.

[36] N. N. Nedialkov, P. A. Atanasov, S. Amoruso, et al., "Laser ablation of metals by femtosecond pulses: Theoretical and experimental study," Applied Surface Science, vol. 253, pp. 7761-7766, 2007.

[37] P. A. Atanasov, N. N. Nedialkov, S. E. Imamova, et al., "Laser ablation of Ni by ultrashort pulses: molecular dynamics simulation," Applied Surface Science, vol. 186, pp. 369-373, 2002.

[38] Changrui Cheng and Xianfan Xu, "Mechanisms of decomposition of metal during femtosecond laser ablation," Physical Review B, vol. 72, 2005.

[39] V. Schmidt, W. Husinsky, and G. Betz, "Ultrashort laser ablation of metals: pump–probe experiments, the role of ballistic electrons and the two-temperature model," Applied Surface Science, vol. 197-198, pp. 145-155, 2002.

[40] Mikhail E. Povarnitsyn, Tatiana E. Itina, Pavel R. Levashov, et al., "Simulation of ultrashort double-pulse laser ablation," Applied Surface Science, vol. 257, pp. 5168-5171, 2011.

[41] Nadezhda M. Bulgakova and Igor M. Bourakov, "Phase explosion under ultrashort pulsed laser ablation: modeling with analysis of metastable state of melt," Applied Surface Science, vol. 197-198, pp. 41-44, 2002.

[42] Quanming Lu, Smuel S. Mao, Xianglei Mao, et al., "Delayed phase explosion during high-power nanosecond laser ablation of silicon," Applied Physics Letters, vol. 80, no. 17, pp. 3072-3074, 2002.

[43] Jing Huang, Yuwen Zhang, and J. K. Chen, "Superheating in liquid and solid phases during femtosecond-laser pulse interaction with thin metal film," Applied Physics A: Materials Science & Processing, vol. 103, pp. 113-121, 2011.

[44] Laurent J. Lewis and Danny Perez, "Laser ablation with short and ultrashort laser pulses: Basic mechanisms from molecular-dynamics simulations," Applied Surface Science, vol. 255, pp. 5101-5106, 2009.

[45] Carsten Schafer, Herbert M. Urbassek, and Leonid V. Zhigilei, "Metal ablation by picosecond laser pulses: A hybrid simulation," Physical Review B, vol. 66, 2002.

[46] Xianfan Xu, "Fundamentals of Phase Change Processes in Laser-Materials Interaction," 37th AIAA Thermophysics Conference, 2004.

[47] Takeharu Sakai, Katsuhiro Ichihashi, Naoya Ogita, et al., "Ablative Impulse Performance of Polyacetal Using Pulsed CO2 laser," 42nd AIAA Plasmadynamics and Lasers Conference, 2011.

[48] Wolfgang O. Schall, Hans-Albert Eckel, Jochen Tegel, et al., "Characterization of the Absorption Wave Produced by CO2 Laser Ablation of a Solid Propellant," Final Report for EOARD Grant, 2005.

[49] Jurgen Ihlemann, Frank Beinhorn, Henning Schmidt, et al., "Plasma and plume effects on UV laser ablation of polymers," Proceedings of SPIE: High-Power Laser Ablation V, vol. 5448, 2004.

[50] Changrui Cheng and Xu Xianfan, "Mechanisms of decomposition of metal during femtosecond laser ablation," Physical Review B, vol. 72, 2005.

[51] Mikhail E. Povanitsyn, Konstantin V. Khishchenko, and Pavel R. Levashov, "Phase transitions in femtosecond laser ablation," Applied Surface Science, vol. 255, pp. 5120-5124, 2009.

[52] S. Mahmood, R.S. Rawat, S.V. Springham, et al., "Plasma dynamics and determination of ablation parameters using the near-target magnified imaging during pulsed laser ablation," Applied Physics A, vol. 101, pp. 701-705, 2010.

[53] T. V. Kononenko, P. Alloncle, V. I. Konov, et al., "Shadowgraphic imaging of laser transfer driven by metal film blistering," Applied Physics A: Materials Science & Processing, vol. 102, pp. 49-54, 2011.

[54] S. Sonntag, C. Trichet Paredes, J. Roth, et al., "Molecular dynamics simulations of cluster distribution from femtosecond laser ablation in aluminum," Applied Physics A: Materials Science & Processing, vol. 104, pp. 559-565, 2011.

[55] X. Zeng, X. L. Mao, R. Greif, et al., "Experimental investigation of ablation efficiency and plasma expansion during femtosecond and nanosecond laser ablation of silicon," Applied Physics A, vol. 80, pp. 237-241, 2005.

[56] Annemie Bogaerts and Zhaoyang Chen, "Effect of laser parameters on laser ablation and laser-induced plasma formation: A numerical modeling investigation," Spectrochimica Acta Part B, vol. 60, pp. 1280-1307, 2005.

[57] J. Konig, S. Nolte, and A. Tunnermann, "Plasma evolution during metal ablation with ultrashort laser pulses," Optics Express, vol. 13, no. 26, 2005.

[58] Takeharu Sakai, Katsuhiro Ichihashi, Naoya Ogita, et al., "Ablative Impulse Performance of Polyacetal Using Pulsed CO2 Laser," 42nd AIAA Plasmadynamics and Lasers Conference, 2011.

[59] John E. Sinko and Don A. Gregory, "Vaporization - Driven Impulse Generation for Laser Propulsion," 43rd AIAA/ASME/SAE/ASEE Joint Propulsion Conference & Exhibit, 2007.

[60] L. V. Zhigilei, "Dynamics of the plume formation and parameters of the ejected clusters in short-pulse laser ablation," Applied Physics A: Materials Science & Processing, vol. 76, pp. 339-350, 2003.

[61] S. Amoruso, R. Bruzzese, M. Vitiello, et al., "Experimental and theoretical investigations of femtosecond laser ablation of aluminum in vacuum," Journal of Applied Physics, vol. 98, 2005.

[62] Andrew V. Pakhomov, M. Shane Thompson, and Don A. Gregory, "Ablative Laser Propulsion Efficiency," 33rd Plasmadynamics and Lasers Conference, 2002.

[63] Andrew V. Pakhomov, M. Shane Thompson, and Don A. Gregory, "Ablative Laser Propulsion: A Study of Specific Impulse, Thrust and Efficiency," Beamed Energy Propulsion: First International Symposium on Beamed Energy Propulsion, 2003.

[64] J. Vincenc Obona, V. Ocelik, J.Z.P. Mitko, et al., "On the surface topography of ultrashort laser pulse treated steel surfaces," Applied Surface Science, vol. 258, pp. 1555-1560, 2011.

[65] Jincheng Wang and Chunlei Guo, "Ultrafast dynamics of femtosecond laser-induced periodic surface pattern formation on metals," Applied Physics Letters, vol. 87, 2005.

[66] S. Nolte, C. Momma, H. Jacobs, et al., "Ablation of metals by ultrashort laser pulses," Journal of Optical Society America B, vol. 14, no. 10, 1997.

[67] R. Le Harzic, D. Breitling, M. Weikert, et al., "Pulse width and energy influence on laser micromachining of metals in a range of 100 fs to 5 ps," Applied Surface Science, vol. 249, pp. 322-331, 2005.

[68] Shigeaki Uchida, Xianglin Zhou, Kazuo Imasaki, et al., "Study on momentum coupling efficiency of laser ablation for space debris removal," Proc of SPIE: High-Power Laser Ablation II, 2000.

[69] R. LE Harzic, D. Breitling, M. Weikert, et al., "Ablation comparison with low and high energy densities for Cu and Al with ultra-short laser pulses," Applied Physics A: Materials Science & Processing, vol. 80, pp. 1589-1593, 2005.

[70] J. Yang, Y. Zhao, and X. Zhu, "Theoretical studies of ultrafast ablation of metal targets dominated by phase explosion," Applied Physics A, vol. 89, pp. 571-578, 2007.

[71] Sven Doring, Soren Richter, Stefan Nolte, et al., "In situ imaging of hole shape evolution in ultrashort pulse laser drilling," Optics Express, vol. 18, no. 19, 2010.

[72] Qiang Li, Huiying Lao, Jia Lin, et al., "Study of femtosecond ablation on aluminum film with 3D two-temperature model and experimental verifications," Applied Physics A: Materials Science & Processing, vol. 105, pp. 125-129, 2011.

[73] J. Cheng, W. Perrie, S. Tao B. Wu, et al., "Ablation mechanism study on metallic materials with a 10 ps laser under high fluence," Applied Surface Science, vol. 255, pp. 8171-8175, 2009.

[74] A. V. Mazhukin, V. I. Mazhukin, and M. M. Demin, "Modeling of femtosecond ablation of aluminum film with single laser pulses," Applied Surface Science, vol. 257, pp. 5443-5446, 2011.

[75] Mikhail E. Povarnitsyn, Tatiana E. Itina, Konstantin V. Khishchenko, et al., "Multi-material two-temperature model for simulation of ultra-short laser ablation," Applied Surface Science, vol. 253, pp. 6343-6346, 2007.

[76] Benxin Wu and Yung C. Shin, "A simplified predictive model for high-fluence ultra-short pulsed laser ablation of semiconductors and dielectrics," Applied Surface Science, vol. 255, pp. 4996-5002, 2009.

[77] V. Oliveira and R. Vilar, "Finite element simulation of pulsed laser ablation of titanium carbide," Applied Surface Science, vol. 253, pp. 7810-7814, 2007.

[78] S. I. Anisimov, N. A. Inogamov, Yu. V. Petrov, et al., "Interaction of short laser pulses with metals at moderate intensities," Applied Physics A, vol. 92, pp. 939-943, 2008.

[79] N. A. Inogamov, V. V. Zhakhovskii, S. I. Ashitkov, et al., "Nanospallation Induced by an Ultrashort Laser Pulse," Journal of Experimental and Theoretical Physics, vol. 107, no. 1, pp. 1-19, 2008.

[80] Sylvie Noel and Jorg Hermann, "Reducing nanoparticles in metal ablation plumes produced by two delayed short laser pulses," Applied Physics Letters, vol. 94, 2009.

[81] Sylvie Noel, Jorg Hermann, and Tatiana Itina, "Investigation of nanoparticle generation during femtosecond laser ablation of metals," Applied Surface Science, vol. 253, pp. 6310-6315, 2007.

[82] Takeharu Sakai, Katsuhiro Ichihashi, Atsushi Matsuda, et al., "Calculation of Pulsed Laser-Ablative Impulse on Polyacetal," 40th AIAA Plasmadynamics and Lasers Conference, 2009.

[83] Zhaoyang Chen and Samuel S. Mao, "Femtosecond laser-induced electronic plasma at metal surface," Applied Physics Letters, vol. 96, 2008.

[84] Xinwei Wang, "Thermal and Thermomechanical Phenomena in Picosecond Laser Copper Interaction," Journal of Heat Transfer, vol. 126, pp. 355-364, 2004.

[85] Thomas Lippert, Marc Hauer, Claude Phipps, et al., "Polymers Designed for Laser Applications - Fundamentals and Applications," Proceedings of the SPIE: High-Power Laser Ablation, vol. 4760, pp. 63-71, 2002.

[86] Mikhail E. Povarnitsyn, Tatian E. Itina, Konstantin V. Khishchenko, et al., "Simulation of DoublePulse Laser Ablation," International Symposium on High Power Laser Ablation 2010, 2010.

[87] A.Y. Vorobyev, V.M. Kuzmichev, N.G. Kokody, et al., "Residual thermal effects in Al following single ns- and fs- laser pulse ablation," Applied Physics A, vol. 82, pp. 357-362, 2006.

[88] Amir Ahmad and V. K. Tripathi, "Nonlinear absorption of femtosecond laser on a metal surface embedded by metallic nanoparticles," Applied Physics Letters, vol. 89, 2006.

[89] G. Cristoforetti, S. Legnaioli, V. Palleschi, et al., "Crater drilling enhancement obtained in parallel non-collinear double-pulse laser ablation," Applied Physics A: Materials Science & Processing, vol. 98, pp. 219-225, 2010.

[90] Michael F. Modest, "Effects of Multiple Reflections on Hole Formation During Short-Pulsed Laser Drilling," Journal of Heat Transfer, vol. 128, 2006.

[91] Nadezhda M. Bulgakova, Anton B. Evtushenko, Yuri G. Shukov, et al., "Role of laser-induced plasma in ultradeep drilling of materials by nanosecond laser pulses," Applied Surface Science, vol. 257, pp. 10876-10882, 2011.

[92] V. I. Eremin, A. V. Korzhimanov, and A. V. Kim, "Relativistic self-induced transparency effect during ultraintense laser interaction with overdense plasmas: Why it occurs and its use for ultrashort electron bunch generation," Physics of Plasmas, vol. 17, 2010.

[93] Oleg Plaksin, Yoshihiko Takeda, Hiroshi Amekura, et al., "Saturation of nonlinear optical absorption of metal-nanoparticle composites," Journal of Applied Physics, vol. 103, 2008.

[94] Keiko Watanabe, Koichi Mori, and Akihiro Sasoh, "Ambient Pressure Dependence of Laser-Induced Impulse onto Polyacetal," Journal of Propulsion and Power, vol. 22, no. 5, 2006.

[95] A. E. Wynne and B. C. Stuart, "Rate dependence of short-pulse laser ablation of metals in air and vacuum," Applied Physics A: Materials Science & Processing, vol. 76, pp. 373–378, 2003.

[96] Takeharu Sakai, "Impulse Generation on Aluminum Target Irradiated with Nd:YAG Laser Pulse in Ambient Gas," JOURNAL OF PROPULSION AND POWER, vol. 25, no. 2, 2009.

[97] Dilawar Ali, M. Z. Butt, and M. Kahaleeq-ur-Rahman, "Ablation yield and angular distribution of ablated particles from laser-irradiated metals: The most fundamental determining factor," Applied Surface Science, vol. 257, pp. 2854-2860, 2011.

[98] J. Hermann, L. Mercadier, E. Mothe, et al., "On the stoichiometry of mass transfer from solid to plasma during laser ablation of brass," Spectrochimica Acta Part B, vol. 65, pp. 636-641, 2010.

[99] J. P. Colombier, E. Audouard, P. Combis, et al., "Controlling energy coupling and particle ejection from aluminum surfaces irradiated with ultrashort laser pulses," Applied Surface Science, vol. 255, pp. 9597-9600, 2009.

[100] J. C. Alonso, R. Diamant, P. Castillo, et al., "Thin films of silver nanoparticles deposited in vacuum by pulsed laser ablation using a YAG:Nd laser," Applied Surface Science, vol. 255, pp. 4933 - 4937, 2009.

[101] U. Chakravarty, P. A. Naik, C. Mukherjee, et al., "Formation of metal nanoparticles of various sizes in plasma plumes produced by Ti:sapphire laser pulses," Journal of Applied Physics, vol. 108, 2010.

[102] John E. Sinko, "Laser Ablation Propulsion Tractor Beam System," Journal of Propulsion and Power, vol. 26, no. 1, pp. 189-191, 2010.

[103] John E. Sinko and Clifford A. Schlecht, "Reversed-Thrust Laser Propulsion and Astronaut Retrieval," Journal of Propulsion and Power, vol. 27, no. 5, pp. 1114-1120, 2011.

[104] C. R. Phipps, J. R. Luke, T. Lippert, et al., "Micropropulsion using laser ablation," Applied Physics A: Materials Science & Processing, vol. 79, pp. 1385-1389, 2004.

[105] Takeharu Sakai, "Impulse Generation on Aluminum Target Irradiated with Nd:YAG Laser Pulse in Ambient Gas," JOURNAL OF PROPULSION AND POWER, vol. 25, no. 2, 2009.

[106] C. R. Phipps and J. P. Reilly, "ORION: Clearing near-Earth space debris in two years using a 30-kW repetitively-pulsed laser," , .

[107] Wolfgang O. Schall, "Laser requirements for the removal of space debris from orbit," SPIE, vol. 3574, 1998.

[108] Claude Phipps, "Orion: Challenges and Benefits," SPIE Conference on High-Power Laser Ablation, vol. 3343, 1998.

[109] Andrew V. Pakhomov, M. Shane Thompson, Wesley Swift Jr., et al., "Ablative Laser Propulsion: Specific Impulse and Thrust Derived from Force Measurements," AIAA JOURNAL, vol. 40, no. 11, 2002.

[110] Andrew V. Pakhomov, Jun Lin, Timothy Cohen, et al., "TWO-PULSED ABLATION OF GRAPHITE AND OTHER ELEMENTARY PROPELLANTS FOR ABLATIVE LASER PROPULSION," 34th AIAA Plasmadynamics and Lasers Conference, 2003.

[111] O. Batishchev, J. L. Cambier, and A. Batishcheva, "Ultrafast Laser Ablation for Space Propulsion," 44th AIAA/ASME/SAE/ASEE Joint Propulsion Conference & Exhibit, 2008.

[112] Richard J. Thompson and Trevor M. Moeller, "MACH2 Simulations of a Micro-laser Ablation Plasma Thruster with Nozzles," 46th AIAA/ASME/SAE/ASEE Joint Propulsion Conference, 2010.

[113] Hiroyuki Koizumi, Takayoshi Inoue, Yoshihiro Arakawa, et al., "Dual Propulsive Mode Microthruster Using a Diode Laser," JOURNAL OF PROPULSION AND POWER, vol. 21, no. 6, 2005.

[114] J. R. Luke, C. R. Phipps, and G. G. McDuff, "Laser plasma thruster," Applied Physics A: Materials Science & Processing, vol. 77, pp. 343-348, 2003.

[115] T. Moeller and Young-Keun Chang, "MACH2 simulations of a micro laser ablation plasma thruster," Aerospace Science and Technology, vol. 11, pp. 481-489, 2007.

[116] John K. Ziemer, "Laser Ablation Microthruster Technology," 33rd Plasmadynamics and Lasers Conference, 2002.

[117] Claude Phipps, Mitat Birkan, Willy Bohn, et al., "Review: Lasesr-Ablation Propulsion," Journal of Propulsion and Power, vol. 26, no. 4, pp. 609-637, 2010.

[118] Claude Phipps and James Luke, "Diode Laser-Driven Microthrusters: A New Departure for Micropropulsion," AIAA Journal, vol. 40, no. 2, 2002.

[119] G. Cristoforetti, G. Lorenzetti, P. A. Benedetti, et al., "Effect of laser parameters on plasma shielding in single and double pulse configurations during the ablation of an aluminium target," Journal of Physics D: Applied Physics, vol. 42, 2009.

[121] S. H. Zaidi, T. W. Smith, R. Murray, et al., "Magnetically Guided Laser Ablation for High Specific Impulse Thrusters," 43rd AIAA Aerospace Sciences Meeting and Exhibit, 2005.

[122] J. S. Lash, R. M. Gilgenback, and C. H. Ching, "Laser-ablation-assisted-plasma discharges of aluminum in a transvers-magnetic field," Applied Physics Letters, vol. 65, no. 5, 1994.

[123] A. M. Rubenchik, C. P J Barty, R. J. Beach, et al., "Laser Systems for Orbital Debris Removal," International Symposium on High Power Laser Ablation 2010, pp. 347-353, 2010.

[124] James Mason, Jan Stupl, William Marshall, et al., "Orbital Debris-Debris Collision Avoidance," Preprint submitted to Advances in Space Research, 2011.

[125] Jonathan W. Campbell, Charles R. Taylor, Larry L. Smalley, et al., "Laser/space material uncooperative propulsion for orbital debris removal and asteroid, meteoroid, and comet deflection," Space Technology and Applications International Forum - 1999, 1999.

[126] N. G. Basov, E. M. Zemskov, R. I. Il'kaev, et al., "Laser System for Observation and Removal of Space Debris," SPIE, vol. 3574, 1998.

[127] Jonathan W. Campbell, "Using Lasers in Space: Laser Orbital Debris Removal and Asteroid Deflection," Center for Strategy and Technology @ Air War College, 2000.

[128] Jonathan W. Campbell, Claude Phipps, Larry Smalley, et al., "The Impact Imperative: Laser Ablation for Deflecting Asteroids, Meteoroids, and Comets from Impacting the Earth," Beamed Energy Propulsion: First International Symposium on Beamed Energy Propulsion, 2003.

[129] Sang-Young Park and Daniel D. Mazanek, "DEFLECTION OF EARTH-CROSSING ASTEROIDS/COMETS USING RENDEZVOUS SPACECRAFT AND LASER ABLATION," 2004 Planetary Defense Conference: Protecting Earth from Asteroids, 2004.

[130] Akihiro Sasoh, Shingo Suzuki, and Atsushi Matsuda, "Wall-Propelled, In-Tube Propulsion with Repetitive-Pulse Laser Ablation," Journal of Propulsion and Power, vol. 25, no. 2, 2009.

[131] Jordin T. Kare, "Laser Launch - The Second Wave," Beamed Energy Propulsion: First International Symposium on Beamed Energy Propulsion, 2003.

[132] Claude Phipps, James Luke, and Wesley Helgeson, "Laser Space Propulsion Overview," Proc of SPIE: XVI International Symposium on Gas Flow, Chemical Lasers, and High-Power Lasers, vol. 6346, 2007.

[133] Catherine Miller, "On the Stability of Complex Ions in Ionic Liquid Ion Sources," Massachusetts Institute of Technology Libraries, 2015.

[134] Paulo Lozano and Manuel Martinez-Sanchez, "Ionic liquid ion sources: characterization of externally wetted emitters," Journal of Colloid and Interface Science, vol. 282, pp. 415-421, 2005. 10.1016/j.jcis.2004.08.132

[135] Catherine E. Miller and Paulo C. Lozano, "Measurement of the Fragmentation Rates of Solivated Ions in Electrospray Thrusters," 52nd AIAA/SAE/ASEE Joint Propulsion Conference, AIAA Propulsion and Energy Forum, 2016. 10.2514/6.2016-4551

[136] N. R. Daly, "Scintillation Type Mass Spectrometer Ion Detector," Review of Scientific Instruments, vol. 31, no. 264, pp. 264 - 267, 1960.

[137] Walt A. de Heer and Paolo Milani, "Large ion volume time-of-flight mass spectrometer with position and velocity sensitive detection capabilities for cluster beams," Review of Scientific Instruments, vol. 62, no. 3, pp. 670-677, 1991. 10.1063/1.1142066

[138] M. N. Akhtar, Bashir Ahmad, and Shoaib Ahmad, "Low energy heavy ion detection with the plastic scintillator NE102E," Nuclear Instruments and Methods in Physics Research B, vol. 207, pp. 333-338, 2003.

[139] ELJEN Technology, "EJ-212 Plastic Scintillator," datasheet, 2007.

[140] Anne-Marie Frelin, Jean-Marc Fontbonne, Gilles Ban, et al., "Comparative Study of Plastic Scintillators for Dosimetric Applications," IEEE Transactions of Nuclear Science, vol. 55, no. 5, pp. 2749-2756, 2008. 10.1109/TNS.2008.2002888

[141] National Institute of Standards and Technology, "Stopping-power and range tables for electrons (ESTAR)," https://physics.nist.gov/PhysRefData/Star/Text/ESTAR.html, Mar. 11, 2018.

[142] W. Baumann and L. Reimer, "Comparison of the Noise of Different Electron Detection Systems Using a Scintillator-Photomultiplier Combination," Scanning, vol. 4, pp. 141-151, 1981.

[143] R. D. Rickman, S. V. Verkhoturov, G. J. Hager, et al., "Multi-ion emission from large and massive keV cluster impacts," International Journal of Mass Spectrometry, vol. 245, pp. 48 - 52, 2005.

[144] Ranran Liu, Qiyao Li, and Lloyd M Smith, "Detection of Large Ions in Time-of-Flight Mass Spectrometry: Effect of Ion Mass and Acceleration Voltage on Microchannel Plate Detector Response," Journal of American Society for Mass Spectrometry, vol. 25, pp. 1374-1383, 2014. 10.1007/s13361-014-0903-2

[145] S. Yagi, T. Nagata, M. Koide, et al., "Relative counting efficiencies of ion charge-states by microchannel plate," Nuclear Instruments and Methods in Physics Research B, vol. 183, pp. 476-486, 2001.

[146] ELJEN Technology, "Light Guides and Acrylic Plastic," datasheet, 2016.

[147] E. Parilis, "Sweeping-out-electrons effect under impact of large molecules and clusters," Nuclear Instruments and Methods in Physics Research B, vol. 193, pp. 240-247, 2002.

[148] Jochen Maul, "Measurement of nanoparticle mass distributions by laser desorption/ionization time-of-flight mass spectrometry," Journal of Physics: Condensed Matter, vol. 19, pp. 176216, 2007.

[149] Virendra N. Mahajan, "Uniform versus Gaussian beams: a comparison of the effects of diffraction, obscuration, and aberrations," Journal of Optical Society America A, vol. 3, no. 4, pp. 470-485, 1986.

[150] Helmut Liebl, "Applied Charged Particle Optics," Springer, 2008. ISBN 978-3-540-71924-3

[151] Andre Anders and Gera Yu. Yushkov, "Measurements of secondary electrons emitted from conductive substrates under high-current metal ion bombardment," Surface and Coatings Technology, vol. 136, pp. 111-116, 2001.

[152] Yasushi Yamauchi and Ryuichi Shimizu, "Secondary Electron Emission from Aluminium by Argon and Oxygen Ion Bombardment below 3 keV," Japanese Journal of Applied Physics, vol. 22, no. 4, pp. L227-L229, 1983.

[153] Casey C. Farnell, Cody C. Farnell, Shawn C. Farnell, et al., "Electrostatic Analyzers with Application to Electric Propulsion Testing," Journal of Propulsion and Power, vol. 33, no. 3, pp. 638-658, 2017. 10.2514/1.B35413

[154] Hamamatsu, "Photomultiplier Tube R9880U Series," datasheet, 2010.

[155] Hamamatsu, "Photomultiplier Tubes Basics and Applications Third Edition," Hamamatsu Photonics, 2007.

[156] E Buttini, A Thum-Jager, and K Rohr, "The mass dependence of the jet formation in laser-produced particle beams," Journal of Physics D: Applied Physics, vol. 31, pp. 2165-2169, 1998.

[157] B. Thestrup, B. Toftmann, J. Schou, et al., "Ion dynamics in laser ablation plumes from selected metals at 355 nm," Applied Surface Science, vol. 197-198, pp. 175-180, 2002.

[158] Dilawar Ali, M.Z. Butt, and Saad Butt, "The fundamental determining factor of angular emission of multiple charged ions ejected by laser ablation of different metals and their binary alloys," Materials Chemistry and Physics, vol. 137, pp. 147-153, 2012. 10.1016/j.matchemphys.2012.08.065

[159] Ian C. Lyon, "MALDI analysis of presolar nanodiamonds: Mass spectrometric determination of the mass distribution of nanodiamonds from meteorites and a technique to manipulate individual nanodiamonds," Meteoritics & Planetary Science, vol. 40, no. 7, pp. 981-987, 2005. 10.1111/j.1945-5100.2005.tb00168.x